Old Dominion University

ODU Digital Commons

Fall 12-2020

Advances in the Understanding of Sourcing and Fate of Pyrogenic Organic Matter in the Environment

Aleksandar Ivaylov Goranov
Old Dominion University, agora001@odu.edu

ADVANCES IN THE UNDERSTANDING OF SOURCING AND FATE OF

PYROGENIC ORGANIC MATTER IN THE ENVIRONMENT

by

Aleksandar Ivaylov Goranov
B.S. June 2017, Ramapo College of New Jersey

A Dissertation Submitted to the Faculty of
Old Dominion University in Partial Fulfillment of the
Requirements for the Degree of

DOCTOR OF PHILOSOPHY

CHEMISTRY

OLD DOMINION UNIVERSITY
December 2020

Approved by:

Patrick G. Hatcher (Director)

Andrew S. Wozniak (Member)

James W. Lee (Member)

Balasubramanian Ramjee (Member)

Sandeep Kumar (Member)

ABSTRACT

ADVANCES IN THE UNDERSTANDING OF SOURCING AND FATE OF PYROGENIC ORGANIC MATTER IN THE ENVIRONMENT

Aleksandar Ivaylov Goranov
Old Dominion University, 2020
Director: Dr. Patrick G. Hatcher

With higher occurrences of forest fires worldwide, there has been an increase in scientific interest surrounding the chemistry of pyrogenic organic matter (pyOM). The main structural components of pyOM, the condensed aromatic compounds (ConAC), exhibit intriguing physico-chemical properties and have been one of the main focuses of biogeochemical research. The overwhelmingly large number of scientific articles regarding pyOM and ConAC are guided by the assumption that ConAC in the environment are *exclusively* of pyrogenic origin, even though some recent studies have suggested that some of these ConAC could also be derived from non-pyrogenic radical-driven processes. To evaluate this controversial proposition, two wood samples exposed to Fenton chemistry through iron nails are evaluated using several qualitative and quantitative techniques. Presented is quantitative evidence that ConAC can be produced non-pyrogenically from terrestrial biomass upon exposure to reactive oxygen species. Evidence from this study directly challenges the dogmatic assumption that ConAC are solely pyrogenic and implores that the global estimates of the contributions of fire-derived organic matter to both terrestrial and aquatic ecosystems must be re-evaluated.

During rain events, significant amounts of pyOM enter the aquatic environment by dissolution and become known as dissolved pyOM (pyDOM). Then, degradative processes driven by sunlight and microbes can alter its composition. Using advanced analytical techniques, the structural and molecular changes that occur to pyDOM after photo-irradiation and microbial incubation were evaluated. Multiple new insights into the photochemical degradation of pyDOM were uncovered, including the evolution of new structural entities, the development of a photo-transformation pathway, and the attribution of photo-reactivity to fire temperature and pyrolyzed biomass type. The bio-incubation of

pyDOM with soil microbes indicated that a portion of pyDOM has been incorporated into microbial biomass which vastly differed for each different incubation. The lability and observed diversity in composition of the microbially produced compounds indicate that pyDOM contributes to the large complexity and diversity of natural organic matter in the environment.

Results from this Dissertation advance our understanding of pyOM, pyDOM, and ConAC in the environment, and reveal that the sourcing and degradation (fate) of ConAC (and, therefore, of pyOM/pyDOM) are much more complex than originally perceived.

This Dissertation is dedicated to my mentors, who created the scientist I am today, as well as to the army of family and friends behind my back, who have always supported me in any adventure I decided to pursue.

ACKNOWLEDGEMENTS

The completion of this Dissertation and any of the associated scientific publications would have not been possible without the contribution and support of many, and I find it extremely difficult to express my gratitude in such a short format.

First and foremost, I would like to thank my advisor Dr. Patrick G. Hatcher. From the very first time we communicated in October 2016, he made it clear that I will have a great experience in his research group and that I will accomplish the numerous goals I had set for myself during my doctoral education. Since then, we have had what I would call the perfect "advisor-student relationship", and every moment of my graduate education at ODU has been a happy one. Dr. Hatcher allowed me to be an independent researcher while guiding me through my amazing PhD journey. I was supported in designing and executing experiments myself and in deciding what kind of analytical tools to use. I could mature, develop my critical thinking, and, of course, make mistakes along the way, becoming the scientist I am today. He even supported me in pursuing my own research ideas, which I recognize to have been an essential component of fostering my own research interests for my post-doctoral career. Although Dr. Hatcher is a very busy researcher, he always found ways to make time for me and have a chat over the phone, look at my extensive PowerPoint reports, edit my manuscripts, or just determine if the idea I had the night before at 4 AM was good or bad. I will be forever grateful for the opportunities I was given and for the relationship we established.

Secondly, I would like to acknowledge Dr. Andrew S. Wozniak, currently an assistant professor at University of Delaware, who also had highly significant contributions to my doctoral education. Dr. Wozniak was a member of the Hatcher group, and he and I physically overlapped for just about a month. The very first experiments I ran, and the very first time I used the FT-ICR-MS and liquid-state NMR spectrometer, took place with his assistance. Working with him in person, although for a very short time, really jump-started my PhD education. After he left to pursue his faculty position, Dr. Wozniak and I have been in constant communication, a collaboration that was an essential component to my PhD education. As I come from a strictly chemical

background, I would often tailor a discussion section of a manuscript towards the analytical side of the technique, or just go on an analytical tangent unrelated to the goals of the project. Dr. Wozniak has a much different environmental background, and he would often ask me "Why is this important?" or "How is this environmentally relevant?". While I pride myself to be an analytical environmental chemist, if I want to be a scientist, these are the questions that I should be able to answer. I believe our collaboration resulted in creating an important reality-check component of my education here, and Dr. Wozniak's guidance was significant in transforming me from an analyst/technician to a critically thinking PhD-worthy scientist. Working with him has been a genuine pleasure.

Throughout my graduate education I had the opportunity to communicate and work with several other scientists, who all collectively contributed to my education and productivity. I would like to express gratitude to the other so-far unmentioned doctoral committee members, Drs. James W. Lee, Sandeep Kumar, and Balasubramanian Ramjee, for contributing positively to my education, and for providing feedback, critiques, and suggestions towards my research. Additionally, I would like to thank my collaborators, Drs. Andrew R. Zimmerman (University of Florida), Siddhartha Mitra (East Carolina University), Kyle W. Bostick (was at University of Florida, now at Fugro GeoServices Ltd.), Danielle R. Schlesinger (was at Princeton University, now at Johns Hopkins University), Satish Myneni (Princeton University), and Dobromir "Dobri" Yordanov (was at Google LLC, now at Facebook Inc.). These researchers have very different backgrounds and expertise to mine, and collaborating was not easy, but was highly educational and fruitful. I am thankful for their contributions to this work and the various discussions we have had.

While I worked with many scientists from distance, several within our own research group must be acknowledged. First, Dr. Hongmei Chen, who turned out to be a night-owl like me, and I was never alone in the office and lab. Whenever I had a question or wanted to take a break with a friendly chat, she was always there. If I needed help, Dr. Chen would immediately drop whatever she was doing and help me – she would make the time to assist me even when her schedule allowed for little time to spare. Dr. Chen was the one who showed me the beauty of programming earlier in my PhD and motivated me to learn MATLAB – a common programing language used in the environmental sciences. Another person who I must thank is Dr. Rachel L. Sleighter who was also always

magically available to help others. While she is extremely involved with her full-time research position, growing family, and dozens of collaborations, she was always willing to chat about statistics, test one of my new MATLAB codes, or just talk about science and life in general. Another close colleague of mine who had significant contributions towards my education here was Dr. Derek C. Waggoner. Through our shared passion for analytical chemistry, Dr. Waggoner assisted me in learning to use many of the instruments in the Hatcher lab and the COSMIC facility. He was always willing to discuss anything, or show me something in the lab, such as replacing the filament of the source of our GCxGC-MS. I would also like to thank Dr. Amanda M. Tadini, a visiting post-doctoral scholar from Brazil, for the fruitful collaborations we have had during my last year at ODU. Lastly, I would like to specially acknowledge our two outstanding undergraduate research assistants, Alicia C. Bryan and Scarlet Z. Aguilar-Martinez, who contributed to some of my side projects and enhanced the productivity of our research group.

My PhD experience was such a great one because I had spectacular mentors during my undergraduate and graduate studies. These individuals educated me, guided me, and significantly shaped my research and career interests. Besides the individuals mentioned, several others need to be acknowledged. Namely, these were Drs. Jane Williamson and Louise Tosetto (Macquarie University, Sydney, Australia), Andrea Murray (was at Center for Marine Resource Studies, Cockburn Harbour, Turks and Caicos Islands, now at Washington University in St. Louis), Heidi Hertler (Center for Marine Resource Studies, Cockburn Harbour, Turks and Caicos Islands), Sasha J. Wagner (was at Skidaway Institute of Oceanography, now at Rensselaer Polytechnic Institute), Aron Stubbins (was at Skidaway Institute of Oceanography, now at Northeastern University), and Loraine T. Tan (Ramapo College of New Jersey). My undergraduate coursework at Ramapo College of NJ, along with these individuals' mentorship through various research experiences, were essential to prepare me for my PhD and my post-doctoral career. They not only taught me the critical technical skills, but also how to manage my time, work effectively, how to do research (following all steps of the scientific method), do an effective literature review, and, very importantly, "Work Smart, Not Hard". They gave me a very solid base of knowledge and skills which I started using from day one of my PhD. It is their mentorship that allowed me to complete this Dissertation in short order, and to foster

my research interests that I will be pursuing in my career. I owe everything to them and will be forever grateful for their guidance.

While I worked quite independently on my main projects and did not work closely with individuals not listed so far, I cannot omit the fact that many others were essential for keeping me a happy, motivated, and productive student. I do thank for that the rest of the members of the Hatcher research group, the COSMIC staff, and the rest of the students, faculty, and staff of our department and college. Namely, I must mention Megan A. Hept and Andriana "Andrea" Chrysovalanti Zourou for the numerous amazing moments during my time at ODU, and for being family in the moments of need.

None of my research would have been possible without the funding from the National Science Foundation (proposal numbers EAR-1451452, EAR-1451367, and CHE-1610021) and the Frank Batten Endowment Fund to Dr. Patrick G. Hatcher (ODU). The Dominion Scholar Fellowship from the College of Sciences at ODU which I received for the 2018-2019 and 2019-2020 academic years was, I believe, another critical factor contributing to my high productivity and fast completion of this Dissertation.

Last but not the least, I would like to thank my family and friends for their continuous love and support during this incredible journey. Given that many of them are an ocean away, it has been very difficult to stay in touch, but through social media and travel we managed to stay connected and have a great time. I would like to namely thank one of my closest friends, Katerina "Kate" V. Djambazova (Chemistry PhD candidate at Vanderbilt University). She contributed significantly to the completion of my PhD not only by just being one of my closest friends, but by always being available to read and comment on my manuscripts (or anything really), discuss career choices, post-doctoral positions, developments in instrumentation, or just invite me for a drink after a stressful week. I love you, Kate!

There is a stigma that PhD students are miserable and getting a PhD is a terrible experience. The individuals above contributed to my life in such ways that these 3½ years were amazing, and I was happy during every single second of them. I accomplished many things during my PhD, contributed to so many projects, learned a lot and gained the skills I needed to become the scientist I am today. It was not easy, but I made the most out of it, and I will be forever grateful that I was given this opportunity to learn and enjoy it all.

NOMENCLATURE

1D	one-dimensional
2D	two-dimensional
3D	three-dimensional
δ	NMR chemical shift (in ppm)
$\delta^{13}C$	stable carbon isotopic composition (in ‰)
$\Delta^{14}C$	radiocarbon isotopic composition (in ^{14}C years)
ε	molar absorptivity (in $L \cdot mol^{-1} \cdot cm^{-1}$)
λ_{MAX}	wavelength of maximum emission (in nm)
π	bonding molecular orbital
π^*	antibonding molecular orbital
τ	TOCSY mixing time (in ms)
ANOVA	analysis of variance
BACon	BPCA aromatic condensation index
BBI	double-resonance broadband z-gradient inverse liquid-state NMR probe
BPCA	benzenepolycarboxylic acid(s)
CCAM	carboxyl-rich aliphatic molecules
cat	catalyst(s)
CDOM	chromophoric (or colored) dissolved organic matter
ConAC	condensed aromatic compound(s)
COSMIC	ODU College of Sciences Major Instrumentation Cluster facility
CRAM	carboxyl-rich alicyclic molecules
Da	Dalton (unified atomic mass unit in mass spectrometry)
DNA	deoxyribonucleic acid
DOM	dissolved organic matter
EEM(s)	excitation-emission matrix/matrices
EM	exponential multiplication (function)
ESI	electrospray ionization (source)

F_1	first dimension in multi-dimensional NMR
F_2	second dimension in multi-dimensional NMR
FDOM	fluorophoric (or fluorescent) dissolved organic matter
FID	free induction decay
FT-ICR-MS	Fourier transform – ion cyclotron resonance – mass spectrometer/spectrometry
GCxGC-MS	2D gas chromatography (GC by GC) – mass spectrometer/spectrometry
GFF	glass-fiber filter
hv	photo-excitation
IHSS	International Humic Substances Society
inh	inhibitor(s)
IUPAC	International Union of Pure and Applied Chemistry
k	rate constant
CHN reactor	reactor for measuring carbon, hydrogen, and nitrogen contents of compounds/mixtures (in elemental analyzers)
CHO formula	molecular formula containing only carbon, hydrogen, and oxygen
Kel-F	Kellogg (trade name for polychlorotrifluoroethylene)
KM	Kendrick Mass (in Da)
KMD	Kendrick Mass Defect (in Da)
KNM	Kendrick Nominal Mass (in Da)
LC-MS	liquid chromatography – mass spectrometry
LMW	low molecular weight
LOD	limit of detection
m/z	mass-to-charge (in Da)
MAS	magic angle spinning
MATLAB	matrix laboratory (a multi-paradigm programming environment and language)
MLEV-17	17-step Malcolm Levitt composite decoupling scheme (in NMR spectroscopy)

mlevgpphw5	gradient-enhanced (gp) phase-sensitive (ph) TOCSY NMR analysis with MLEV-17 and W5-WATERGATE elements
MultiCPMAS	multi-pulse cross-polarization (CP) magic angle spinning (MAS) (type of solid-state NMR analysis)
MW	molecular weight (in Da)
MWord	Mega-word (number of FID transient points)
NMR	nuclear magnetic resonance (spectroscopy)
OC	organic carbon
ODU	Old Dominion University
p-value	probability of statistical significance
PAH(s)	polycyclic aromatic hydrocarbon(s)
PARAFAC	parallel factor analysis
PEW5	perfect echo - water suppression element with gradient-tailored excitation
PEW5shapepr	1D ^{1}H NMR analysis with PEW5 and shaped presaturation (shapepr) water suppression elements
PhD	Doctor of Philosophy
PPL	styrene – divinylbenzene copolymer
ppm	parts per million
PTFE	polytetrafluoroethylene (also known as Teflon)
pyOM	pyrogenic organic matter
pyDOM	pyrogenic dissolved organic matter (dissolved pyOM)
QSINE	squared sine function, $\sin^2 x$ (in NMR spectroscopy)
R	secondary reactant
R^2	coefficient of determination (also known as goodness of fit)
RCNJ	Ramapo College of New Jersey
ROS	reactive oxygen species
RU	Raman unit(s)
sic	*sic erat scriptum* (Latin); "just as" or "thus was written" (English)
SRNOM	Suwannee River natural organic matter
SSB	shifted sine bell (in NMR spectroscopy)

T_1	spin-lattice relaxation time (in NMR spectroscopy)
TOC	total organic carbon (quantity in $mgC \cdot L^{-1}$ units)
TOCSY	total correlation spectroscopy (type of NMR analysis)
UV-A	ultraviolet type-A electromagnetic radiation (315 – 400 nm)
UV-VIS	ultraviolet-visible (spectrum/spectroscopy)
v	rate of a chemical reaction (e.g., rate of photo-degradation)
vK	van Krevelen (diagram)
W5-WATERGATE	five-pulse element in NMR pulse sequences for water suppression using gradient-tailored excitation
WACS	Western Atlantic Climate Study project
WDW	window function
wt.%	weight percentage

Peak labels in fluorescence Excitation-Emission-Matrix (EEM) spectra

B_1	Tyrosine or tyrosine-like fluorophores (1st band)
B_2	Tyrosine or tyrosine-like fluorophores (2nd band)
T_1	Tryptophan or tryptophan-like fluorophores (1st band)
T_2	Tryptophan or tryptophan-like fluorophores (2nd band)

Mechanisms/Pathways

D	decarboxylation
KET	keto-enol tautomerism
OX	oxygenation
OX_1	direct photolysis
OX_2	oxygen-mediated direct photolysis
OX_3	radical-mediated oxygenation
RMR	radical-mediated reactions

Ultrahigh Resolution Mass Spectrometric Metrics

AI_{MOD}	modified aromaticity index
DBE	double bond equivalency (also known as degree of unsaturation)
DBE/C	carbon-normalized DBE
DBE-O	oxygen-corrected DBE
H/C	hydrogen-to-carbon ratio
H/N	hydrogen-to-nitrogen ratio
N/C	nitrogen-to-carbon ratio
NOSC	nominal oxidation state of carbon
O/C	oxygen-to-carbon ratio
O/N	oxygen-to-nitrogen ratio

Chemical Compounds/Functionalities

$^1O_2$	singlet oxygen
$(CH_3)_2CH-OH$	isopropanol
$(NH_4)_2SO_4$	ammonium sulfate
Aryl-O	oxygenated aryl (aromatic) functionalities
B5	benzenepentacarboxylic acid
B6	benzenehexacarboxylic (mellitic) acid
C	carbohydrate
C=C	olefin
C=C-OH	enol
$C_{12}H_{22}O_{11}$	sucrose
$-CH_2-$	methylene
CH_3-	methyl
CH_3-CH_2-	ethyl
$CH_3-CH_2-COO^-$	propionate
CH_3-CH_2-OH	ethanol
$CH_3-CO-CH_3$	acetone
CH_3-COO^-	acetate

CH_3O-	methoxy group
CH_3OH	methanol
CH_4	methane
$-CHO$	aldehyde group
CO	carbon monoxide
CO_2	carbon dioxide
CO_3^{2-}	carbonate
$ConAC^{+\bullet}$	ConAC-cation radical
$-COOH$	carboxyl group
D_2O	deuterated/heavy water (i.e., deuterium oxide)
Fe	iron
Fe^{3+}	iron (III) cation
H_2	hydrogen
H_2O	water
HCl	hydrochloric acid
HCO_3^-	bicarbonate
$HCOO^-$	formate
$H-C_\beta-C_\alpha-X$	β-hydrogen to a heteroatom (X)
KH_2PO_4	potassium dihydrogen phosphate
L	lignin
NH_3	ammonia
NH_4^+	ammonium
NO_3^-	nitrate
O_2	oxygen
$O_2^{-\bullet}$	superoxide
$O_{2(aq)}$	dissolved oxygen
$O-alkyl$	oxygenated alkyl group
$-OH$	hydroxyl group (alcohol)
$^{\bullet}OH$	hydroxyl radical
R	alkyl group
TMSP	sodium 2,2,3,3-tetradeutero-3-trimethylsilylpropanoate

TABLE OF CONTENTS

Page

APPENDICES

LIST OF TABLES

LIST OF FIGURES

CHAPTER I

INTRODUCTION

Wildfires are phenomena that have been occurring in the geological record since the evolution of terrestrial plants, and even nowadays there are massive uncontrollable fires that cause devastating damage to terrestrial ecosystems (Bowman et al., 2009). The residue that is left after biomass pyrolysis (of trees, grasses, etc.) is referred to as black carbon, charcoal, soot, and others, but collectively is known as pyrogenic organic matter (pyOM). In recent years, the scientific community has recognized that pyOM can chemically alter our ecosystems. Furthermore, there is a growing interest in using pyOM as a soil supplement in agriculture (e.g., Spokas et al., 2012), for carbon sequestration (e.g., Lehmann, 2007), and for water decontamination (e.g., Abdel-Fattah et al., 2015; Dai et al., 2019). Because these natural and anthropogenic activities contribute to the distribution of massive amounts of pyOM in the environment, examining the sources and environmental fate of pyOM is of utmost scientific concern. The goal of this Dissertation is to advance the understanding of the origins and fate of pyOM in the environment using novel molecular and structural approaches.

PyOM is a bi-phasic mixture of graphene-like condensed aromatic compounds (ConAC) and a pool of poorly characterized aliphatic molecules (Hockaday et al., 2007; Bostick et al., 2018; Wozniak et al., 2020). ConAC in soils and sediments have been studied extensively (Masiello, 2004; Czimczik and Masiello, 2007; Bird et al., 2015; Santín et al., 2016a), and until very recently, they were thought to be exclusively of pyrogenic origin (e.g., Goldberg, 1985; Glaser et al., 1998). Using that assumption, it has been estimated that fire-derived ConAC comprise ~14 % of soil organic matter (Bird et al., 1999; Hammes et al., 2007; Cusack et al., 2012; Reisser et al., 2016) and ~10% of the globally fluxed riverine dissolved organic matter (DOM) to the oceans (Jaffé et al., 2013).

This Dissertation is formatted based on the journal *Geochimica et Cosmochimica Acta*.

While there is no question that ConAC are produced by combustion, recent studies report that ConAC can be created from non-pyrogenic radical-based processes (Chen et al., 2014; Waggoner et al., 2015). As all ConAC in the aquatic environment are assumed to be pyrogenic, it is likely that the global estimates of export of pyOM to the oceans or their incorporation into soil organic matter are over-estimated. The reports of Chen et al. (2014) and Waggoner et al. (2015) have been questioned by the scientific community, with the argument that observed non-pyrogenically produced ConAC are an experimental or analytical artifact. The main critique is that these studies have not employed quantitative analytical techniques for ConAC quantification, namely the benzenepolycarboxylic acids (BPCA) analysis (Wagner et al., 2018). The BPCA method is a chemical marker technique currently viewed as the gold standard for quantifying ConAC in environmental matrices, even though questions exist regarding its specificity (Zimmerman and Mitra, 2017; Chang et al., 2018; Gerke, 2018). It utilizes a concentrated nitric acid digestion to degrade ConAC into BPCA molecular markers (benzenehexa- and benzenepentacarboxylic acids) which are quantified chromatographically, and the total BPCA concentration is used as a proxy for ConAC concentration. The proposed non-pyrogenic pathway for formation of ConAC is through radical-induced molecular re-arrangement (electrocyclization) of lignin (Waggoner et al., 2015), the second most abundant biopolymer in the environment (Thevenot et al., 2010). Chapter II of this Dissertation will include a study of two wooden boards that have been exposed to Fenton chemistry through the association with iron nails embedded in them. The wood specimens were exposed for over a decade to environmental conditions such as wetting and drying cycles induced by rain and sun, simulating the kind of exposure that fresh plant materials experience in soil litter layers. After the decade of exposure, a visual charcoalification of the wood material in zones adjacent to iron nails has been observed. **I hypothesize that the Fenton reaction produced ConAC from woody biomass after a decade-long exposure to yield the charcoalified product.** The observed changes due to exposure to the Fe nail will be evaluated quantitatively using the BPCA method to provide a quantitative proof of the non-pyrogenic formation of ConAC, validating this hypothesis. This study contributes to the increasingly growing concern that the measured ConAC in

the environment via the BPCA method do not entirely correspond to pyOM, which would have important implications to the knowledge of sourcing of ConAC in the environment.

For many years it was thought that this highly condensed solid pyOM was very stable and that it accumulated for millennia in soils and sediments without much impact to the environment (e.g., Goldberg, 1985; Glaser et al., 1998). It has been recently recognized that some portion of this pyOM can be leached by water (e.g., rain) and can enter the aquatic environment (Hockaday et al., 2007; Dittmar and Paeng, 2009; Dittmar et al., 2012; Jaffé et al., 2013; Stubbins et al., 2015; Bostick et al., 2018). Research has shown that dissolved pyOM (pyDOM) contributes significantly to the global carbon cycle (Druffel, 2004; Lehmann, 2007; Riedel et al., 2016), constituting an average of 10% of the total globally exported organic matter from rivers to the ocean (Jaffé et al., 2013). However, the estimated annual production of pyOM from forest fires exceeds the estimates of pyOM in terrestrial environments (Kuhlbusch and Crutzen, 1996; Schmidt and Noack, 2000; Czimczik et al., 2003; Forbes et al., 2006). The fact that one does not observe massive accumulation of pyOM in soils suggests that there are degradative and/or transport pathways that alter pyOM cycling and fluxes in the environment (Masiello, 2004; Bostick et al., 2018). It is known that solar photo-irradiation is highly destructive to ConAC, and photochemistry has been identified as the most significant sink in the environment for these compounds (Stubbins et al., 2012). However, while it is known that some of them photo-mineralize (mainly to CO and CO_2), the photo-transformation pathway and the chemical structures of the molecular by-products remain uncertain. **I hypothesize that the structural and molecular changes occurring after photo-irradiation can be discerned by applying advanced analytical techniques.** I aim to validate this hypothesis by applying ultrahigh resolution mass spectrometry and multidimensional nuclear magnetic resonance spectroscopy to pyDOM samples before and after photo-irradiation**.** Chapter III of this Dissertation will therefore include a study showing numerous new insights to the photochemistry of pyDOM, including observation of new structural moieties, development of a photo-transformation pathway, and evaluation of the photo-reactivity of pyDOM as a function of fire temperature and pyrolyzed biomass type.

While photochemical degradation is a very important process for sunlit environments, a large fraction of pyDOM is also cycled through soil porewater and groundwater systems. In these dark environments the fate of organic matter is mainly controlled by microorganisms such as bacteria and fungi. Previous studies have shown that microbes can utilize pyOM as food (e.g., Zimmerman, 2010), however, the molecular details of this degradation are unknown. Furthermore, to date, there are no studies in the literature of pyDOM that have evaluated its bio-degradability without priming the systems with labile molecules (e.g., sucrose). Because studies have determined that microbial degradation of terrestrial DOM can be fully respired to CO_2 with no photochemical facilitation (e.g., Ward et al., 2013; Fasching et al., 2014), evaluating the bio-reactivity of pyDOM is needed. Thus, Chapter IV of this Dissertation will be on the microbial degradation of pyDOM. **I hypothesize that significant molecular changes to pyDOM will be observed after biotic incubations with microbes.** My study will evaluate the types of molecules that are bio-degraded and bio-produced, determine the effect of production temperature and photochemistry, and provide new insights on the involvement of pyDOM within the global carbon and nitrogen cycles.

The three studies shown in this Dissertation will contribute greatly to the knowledge of pyOM in the environment. They provide novel insights on the sourcing of the condensed component (ConAC) of pyOM, and on the photochemical and microbial fate of its water-soluble fraction (pyDOM). Given the highly complex nature of this type of environmental matrix, a variety of analytical platforms have been utilized to accomplish comprehensive analysis. Chapter V will conclude this Dissertation and provide future directions for the wildfire biogeochemistry community. The novel insights into the chemistry of pyOM that are presented in this document will bring more pieces to the mysterious complexity of carbon cycling and will provide a better understanding of what the consequences of forest fires, or related anthropogenic activities, are to the aquatic environment.

CHAPTER II

DECADE-LONG FENTON DEGRADATION OF WOOD LEADS TO NON-PYROGENIC FORMATION OF CONDENSED AROMATIC COMPOUNDS

1. INTRODUCTION

Pyrogenic organic matter (pyOM), or black carbon, is the solid residue left after combustion (e.g., forest fires, fossil fuel usage), and such substances have been a focus of research for several decades now. There is an overwhelming number of studies that report of: its pyrogenic formation (e.g., Hedges et al., 2000; Baldock and Smernik, 2002; Santín et al., 2016b), abundance in various environmental matrixes such as soils and sediments (Masiello, 2004; Czimczik and Masiello, 2007; Bird et al., 2015; Reisser et al., 2016; Santín et al., 2016a), aerosols (Wozniak et al., 2008; Bao et al., 2017), and dissolved organic matter (e.g., Wagner et al., 2018). It is now well recognized that pyOM plays an important role in the global carbon cycle due to its presumed recalcitrance. For example, it has been estimated that 14% of soil organic carbon, a major terrestrial reservoir of organic carbon on Earth, is fire-derived (Bird et al., 1999; Hammes et al., 2007; Cusack et al., 2012; Reisser et al., 2016). Another important finding is that large quantities of condensed aromatic compounds (ConAC) of combustion-derived pyOM in soils (Jaffé et al., 2013; Jones et al., 2020) are annually exported by rivers to the world's oceans.

There is a growing concern that the ConAC used to assess the existence of pyOM may not be exclusively of pyrogenic origin. Recent studies by ultrahigh resolution mass spectrometry and NMR suggest that ConAC in the environment can be produced non-pyrogenically through radical polymerization of ligninaceous molecules. The first evidence for this proposition came from Fe-rich systems (Chen et al., 2014; Waggoner et

al., 2015) where hydroxyl radicals were iron-generated via photochemistry or the Fenton reaction (Fenton, 1894; Walling, 1975). This induced well-known ring-opening of aromatic structures and subsequent production of carboxyl-containing olefins that can initiate the formation of ConAC through electrocyclization reactions like the Diels-Alder reaction (Diels and Alder, 1928). Another recent study also observed non-pyrogenic formation of ConAC, this time in the aerobic microbial incubation of wheat straw (Chen et al., 2020), another example of a system rich in active radicals from exoenzymes. However, these studies have been questioned by the scientific community and "warrant further investigation using quantitative methods such as the benzenepolycarboxylic acids method [sic]" (Wagner et al., 2018). The benzenepolycarboxylic acids (BPCA) method is currently used extensively to quantify ConAC in various environmental matrixes. Originally developed for quantification of ConAC in soil matrices (Glaser et al., 1998), it employs an oxidation by nitric acid at highly degradative conditions (high temperature and pressure). After this thermochemolytic digestion, the graphene-like ConAC are degraded into BPCA compounds. These marker molecules are then quantified chromatographically and quantitatively related back to total ConAC concentration in the digested sample using various mathematical approaches (Glaser et al., 1998; Dittmar, 2008; Ziolkowski et al., 2011; Stubbins et al., 2015; Kappenberg et al., 2016). Most researchers assume that ConAC can only be created by exposure to high temperatures. One of the most recent studies on ConAC revealed using stable carbon isotopic measurements that oceanic ConAC are not of riverine or terrestrial origin (Wagner et al., 2019a). This finding contrasts with many of the previous studies that assume a land-derived origin of ConAC in the oceans (e.g., Dittmar and Koch, 2006; Jaffé et al., 2013). The finding of Wagner et al. (2019a) also suggests that oceanic ConAC can be produced by non-pyrogenic processes in the ocean, especially considering the high photo-degradability of ConAC during sunlit riverine export and the likelihood of ConAC not reaching the mouths of rivers whatsoever.

In this Chapter, I present the first quantitative evidence for the previously proposed formation of non-pyrogenic ConAC in the terrestrial environment employing the BPCA assay. I have collected two pine wood boards from decks attached to residential houses. The decks were assembled with iron nails more than 10 years ago and were exposed to wetting and drying events by the natural weathering processes. Upon recent dismantling

of the decks, the obtained boards were observed to have undergone a charring-like process ("charcoalification") in the contact zone between the boards in close proximity to the Fe nails used to connect the boards. Figure 1 shows photographs of the observed charcoalification next to the iron nails in both wood samples (Pine 1 and 2). Because the charcoalification was limited to the junction of two boards, the observed transformation occurred under dark conditions and photochemistry was eliminated as being responsible for the alteration. Portions of the boards remote from Fe nails appeared to be virtually intact mainly indicating that microbial decomposition of the wood has been retarded. It appears that the charcoalification is catalyzed by Fe and very likely due to Fenton chemistry. To evaluate the chemical changes that have occurred, material from two locations has been obtained for each sample – the blackened solid, hereafter referred to as a "Fe-exposed sample" and trimmings of wood far from the nail, referred to as a "control". In contrast with previous studies by Chen et al. (2014) and Waggoner et al. (2015), large amounts of sample were available which allows for the application of numerous analytical techniques and performing "comprehensive analysis". If ConAC were created during the decade-long exposure to nails, understanding of this non-pyrogenic process and unveiling its by-products would be critical for properly constraining the fluxes and accumulation of pyrogenic organic matter in the environment.
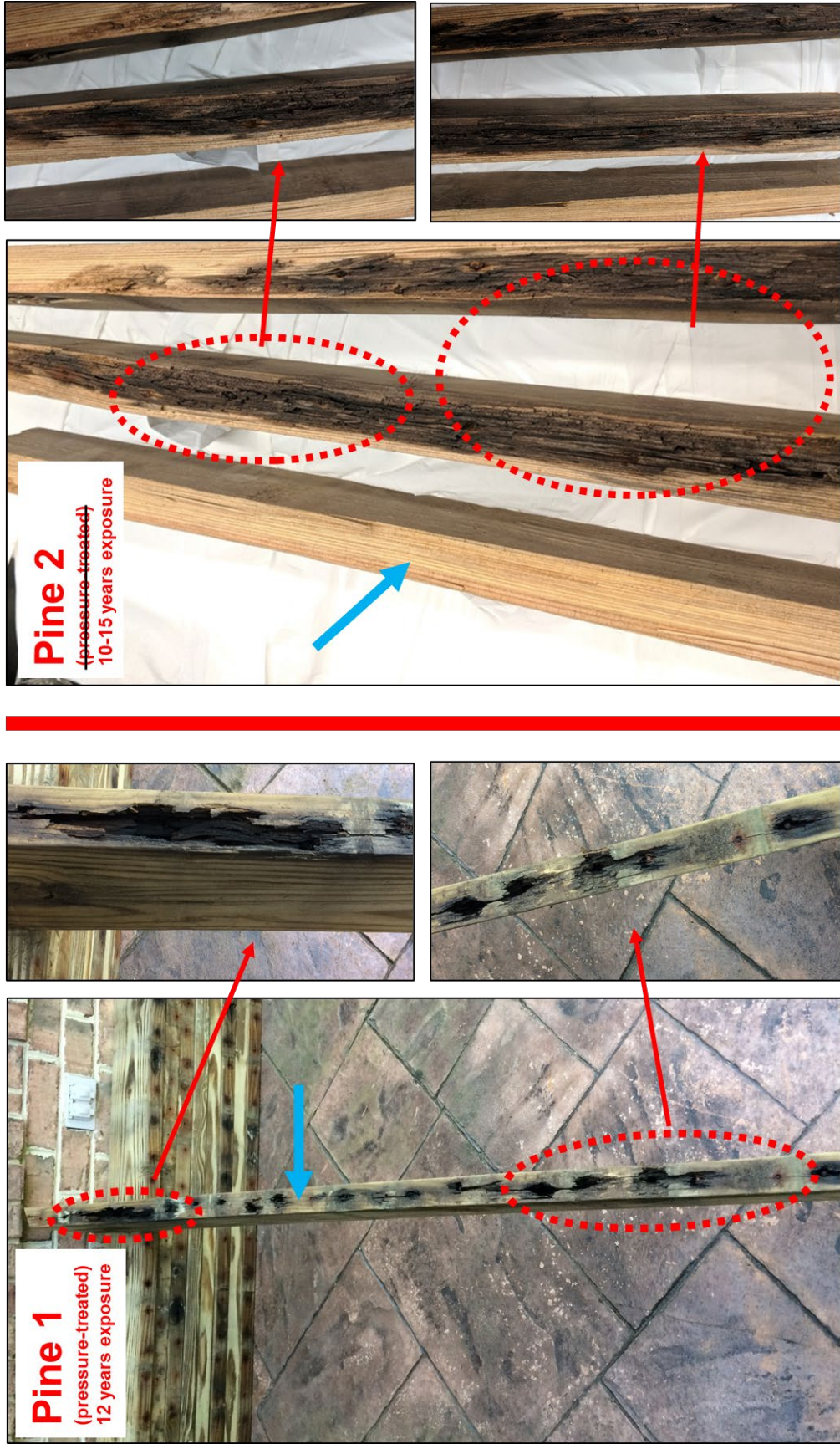
Figure 1. Charcoalification of fresh pine wood boards through exposure to iron nails. The **blue** arrows indicate zones with no visible charcoalification which were sampled to serve as representative controls.

2. MATERIALS AND METHODS

2.1. Sample Extraction

Wood specimens were rinsed with laboratory-grade MilliQ water (18.1 mΩ) and air dried under cover. Charcoalified wood pieces from the areas in close proximity to the nails were sampled with pre-combusted tweezers. Wood samples remote from the nail were sampled using a pre-combusted wood scraper. Sampling was done from numerous "control" and "Fe-exposed" zones to obtain representative samples. All samples were ground and sieved (Mesh #80, 0.177 mm opening) to fine powders.

2.2. Elemental analysis

Elemental analysis for carbon (C%), hydrogen (H%), and nitrogen (N%) was performed using a Thermo Finnigan FlashEA 1112 elemental analyzer fitted with a CHN column. Samples were analyzed in triplicate and calibrated to a five-point external calibration curve of nicotinamide (CE Elantech, Inc.). Empty tin capsules were analyzed as blanks and to evaluate for sample carryover.

Metal (Cu% and Fe%) analysis was performed after ashing 20-30 mg solid samples at 600 ^{O}C in a temperature-controlled oven for 24 hours. The solid residue was then digested with 5 mL aqua regia (HNO_3:HCl = 1:3 molar ratio) for 12 hours, and the acid was evaporated in a sand bath at 70 ^{O}C. Then, 5 mL 65% HNO_3 were added and allowed to digest for 6 hours, after which the acid was again evaporated in a sand bath at 70°C. HNO_3 was added once more and evaporated after the digestion. Lastly, 5 mL 2% HNO_3 and ~1 mg of $La(NO_3)_3$ were added, and the nitrates formed during the digestions were dissolved with the assistance of a 10-minute sonication. The solutions were filtered using 0.2 μm PTFE filters and immediately analyzed.

Metal quantification was performed on a Shimadzu AA-7000 atomic absorption spectrometer using a flame atomizer. Copper nitrate (1000 ppm, Acros Organics) and iron nitrate (10000 ppm, ASSURANCE) were used for external calibration. Instrument and procedural blanks were used to evaluate for contamination and sample carryover.

2.3.   Solid-state Nuclear Magnetic Resonance (NMR) analysis

NMR analysis was performed with untreated dried powdered samples. Samples were packed in a 4 mm Zirconia (ZrO_2) rotor with a polychlorotrifluoroethylene (Kel-F) cap. Analysis was performed on a 400 MHz (9.4 Tesla) Bruker BioSpin AVANCE II spectrometer fitted with a 4 mm HCN MAS probe at the College of Sciences Major Instrumentation Cluster (COSMIC) facility at Old Dominion University (Norfolk, VA). One-dimensional quantitative ^{13}C spectra were acquired using the recently developed multi-pulse cross-polarization (MultiCPMAS) pulse program (Johnson and Schmidt-Rohr, 2014). Samples were spun at the magic angle at 14 kHz and analyzed using relaxation delay of 1 s, 5000 scans, 5 cross-polarization segments, and a total contact time of 3.30 ms. The obtained spectra were phased, calibrated to an external adamantane standard (Earl and Vanderhart, 1982), and multiplied by an exponential window function (EM) of 50 Hz. Spectra were then baseline-corrected and integrated in the following ranges: Methyl: 0 – 20 ppm, Methylene: 20 – 45 ppm, O-Alkyl: 45 – 90 ppm, di-O-Alkyl: 90 – 110 ppm, Aryl: 110 – 146 ppm, Aryl-O: 146 – 165 ppm, Carboxyl/Ester (COO): 165 – 184 ppm, Carbonyl (CO): 184 – 220 ppm.

2.4.   Benzenepolycarboxylic acids (BPCA) analysis

Dried powdered samples, no more than 5 mg carbon-equivalents (Kappenberg et al., 2016), were weighed in 25-mL glass ampules. Concentrated nitric acid (2 mL, 65% HNO_3, J.T. Baker, trace metal grade) was added and the ampules were allowed to demineralize for 15 min (Wagner et al., 2017a). Then, they were flame sealed and thermolyzed in a programmable oven for 9 hours at 170 ^{O}C. After the digestion, the nitric acid was evaporated at 60 ^{O}C in a sand bath under a gentle stream of ultrapure N_2 gas (Airgas, UHP300). The BPCA-containing residue was then dissolved in 2 mL of 0.6 M phosphoric acid and filtered using a 0.2 μm PTFE filter into an autosampler vial. Only benzenehexa- (B6) and benzenepentacarboxylic (B5) acid markers were quantified as these markers have been found to be most reliable as being produced only by ConAC molecules (Stubbins et al., 2012; Wagner et al., 2018). In contrast, benzenetri- and

benzenetetracarboxylic acids can be produced after the nitric acid oxidation of ligninaceous molecules (Kappenberg et al., 2016; Bostick et al., 2018). B6 and B5 were quantified chromatographically on an Agilent 1100 high-performance liquid chromatography (HPLC) system. Separation was achieved utilizing an organic-free gradient of 0.6 M phosphoric acid (pH = 1) and phosphate buffer (20 mM, pH = 6) on an Agilent Poroshell 120 Phenyl-Hexyl (4.6 x 150 mm, 2.7 μm) column following procedures outlined by Wagner et al. (2017a). Injection volumes were varied from 5 – 20 μL and the separated compounds were detected spectrophotometrically at 254 nm at ambient temperature. The B5 and B6 peaks eluted at characteristic times and were quantified using external calibration curves. The concentration of these two markers (in nM) were related to the initial concentration of ConAC (in μM carbon-equivalents) following Eq. 1 below (Stubbins et al., 2015).

$$ConAC = 0.0891 \times (B5 + B6)^{0.9175}$$
<div align="right">Eq. 1</div>

The calculated ConAC content is then normalized to the amount of organic carbon (OC) that was oxidized to result in a ConAC/OC value (in weight percentage, wt.%). ConAC contents quantified using this approach are directly comparable to the recent pyrogenic organic matter literature (e.g., Dittmar et al., 2012; Jaffé et al., 2013; Wagner and Jaffé, 2015; Wagner et al., 2015a, 2019a,b; Drake et al., 2020). The method was evaluated using the Suwannee River natural organic matter standard (SRNOM, 1R101N) from the International Humic Substances Society (IHSS) and BPCA recoveries were comparable to previously published values (Wagner et al., 2017a).

2.5.　Base-solubilization of organic matter

Base-extraction was selected as the method for obtaining a representative liquid extract of the solid wood samples. It was performed using sodium hydroxide (Fisher, Certified grade) at pH = 12 at a ratio of 0.5 g sample/100 mL extractant. Suspensions were vigorously stirred on a shaker plate for 24 hours. Then, the supernatant is removed and substituted with new 100 mL of extractant. The extraction was done three times over

3 x 24 hours to result in a total of 300 mL base-extract of each sample. Base-extracts were then filtered through pre-combusted 0.7 μm glass-fiber filters (GFF, Whatman, 47 mm diameter) and cation-exchanged using a Dowex 50Wx8 resin (Acros Organics). A procedural blank of just sodium hydroxide was processed the same way. All extractions were performed under an inert (N_2) atmosphere. The procedure followed the IHSS guidelines and is evaluated and described in greater detail elsewhere (Hatcher et al., 2019). Carbon content of the final extracts was quantified using a Shimadzu Scientific total organic carbon analyzer (TOC-V_{CPH}) with potassium hydrogen phthalate (Nacalai Tesque, JIS special grade) external calibration curves.

2.6.   Ultrahigh resolution mass spectrometry (FT-ICR-MS)

Cation-exchanged base-extracts were diluted to 50 mg·L^{-1} carbon-equivalents (50 mgC·L^{-1}) and then further diluted with methanol (CH_3OH, Fisher Scientific, Optima LC-MS grade) to give 1:1 CH_3OH:H_2O mixtures. Samples were analyzed on a Bruker Daltonics 12-Tesla Apex Qe FT-ICR-MS housed in the COSMIC facility. The instrument is calibrated daily with a polyethylene glycol standard and instrument blanks are analyzed in-between samples to assure for no sample carryover. Samples are infused into the Apollo II electrospray ionization (ESI) source at flow rate of 120 μL/h and molecules are ionized in negative mode. Ionization voltages are optimized on a per-sample basis to assure for uniform spray currents across the dataset. The ionized molecules are collected in a hexapole, filtered by a quadrupole for a mass range of 200-1200 m/z, pre-concentrated in a second hexapole, and transferred into the ICR cell where 300 transients were collected. They were co-added, and the resultant free induction decay is zero-filled and sine-bell apodized. After a fast Fourier transformation, spectra are calibrated to naturally abundant fatty acids, dicarboxylic acids, and compounds belonging to the CH_2-homologous series (Sleighter et al., 2008). Peaks with signal-to-noise above 3 were exported to MATLAB where salt, blank, and ^{13}C isotopologue peaks were removed from each spectrum. Molecular formulas were assigned to each mass list using the Molecular Formula Calculator from the National High Magnetic Field Laboratory (Tallahassee, FL). Formulas were restricted to elemental composition of $^{12}C_{5-\infty}$, $^{1}H_{0-100}$, $^{16}O_{0-50}$, $^{14}N_{0-10}$, $^{32}S_{0-}$

4, and $^{31}P_{0-2}$, and the obtained formulas were refined following previously published criteria (Kujawinski and Behn, 2006; Koch et al., 2007; Stubbins et al., 2010). No ambiguous assignments were left in the final formula lists (i.e., for each mass spectral peak there was only one molecular formula). For simplicity, only formulas containing carbon, hydrogen, and oxygen elements are used hereafter (i.e., CHO formulas).

Molecular formulas are further classified based on their modified aromaticity index (AI$_{MOD}$), a measurement of the double-bond density in a molecule (Koch and Dittmar, 2006, 2016). Compounds with AI$_{MOD}$ = 0 are classified as "aliphatic". Molecules with 0 < AI$_{MOD}$ < 0.5 have either an aromatic moiety that is highly functionalized with aliphatic groups or have olefinic/alicyclic bonds. Molecules with 0.5 ≤ AI$_{MOD}$ < 0.67 are classified as "aromatic". Formulas with AI$_{MOD}$ ≥ 0.67 (Koch and Dittmar, 2006, 2016) and number of C-atoms ≥ 15 (Osterholz et al., 2016) are classified as condensed aromatic (ConAC). The calculation for this index is shown below.

$$AI_{MOD} = \frac{1 + C - \frac{1}{2}O - S - \frac{1}{2}(N + P + H + Cl)}{C - \frac{1}{2}O - N - S - P}$$

Eq. 2

3. RESULTS

3.1. Structural characterization using one-dimensional NMR spectroscopy

Bulk structural characteristics of the two samples before and after exposure to Fenton chemistry were determined using one-dimensional nuclear magnetic resonance (NMR) spectroscopy. Solid-state ^{13}C NMR analysis is a classical approach for evaluating solid environmental matrices (Simpson and Simpson, 2009; Mao et al., 2017), and utilizing the ^{13}C multi-pulse cross-polarization magic angle spinning technique (^{13}C MultiCPMAS, Johnson and Schmidt-Rohr, 2014) allows for quantitative reporting of the total content of the various ^{13}C functionalities in the studied samples. Figure 2 shows the results obtained for the two samples.

Figure 2. One-dimensional solid-state ^{13}C NMR analysis of whole wood samples (control colored in **orange** and Fe-exposed in **brown**). Left panels show the obtained spectra, with chemical functionality labels (top) and peak labels (bottom panel). Carbohydrate and Lignin resonances, along with the corresponding carbon numbers, are shown in **red** (**C** and *L*, respectively). Right panels show the integrated chemical shift regions, with percent change in functionality abundance shown under each label in the x-axis.

The obtained ^{13}C MultiCPMAS NMR spectra for the control samples were highly characteristic for woody samples (Gil and Neto, 1999). Lignin and carbohydrate signatures are easily identified and seem to predominate in the spectra, as these biopolymers are of high abundance in woody biomass (Hedges et al., 1985). Lignin's presence is identified by the peaks associated with its methoxy (**C**H$_3$O-, 56 ppm) and phenolic (aryl-O, 147 ppm) functionalities. Cellulose's glycosidic units present seven peaks in the area between 60 and 110 ppm (C$_1$-C$_6$,). There are several peaks in the region of 0 – 45 ppm, which is where methyl (**C**H$_3$-) and methylene (-**C**H$_2$-) functionalities usually resonate. These are generally associated with acetylated glucose units in hemicelluloses and resinous substances. Pine 1 is a pressure-treated wood, thus it is also expected that some of aliphatic resonances to originate from alkyl groups in the quaternary ammonium ligands of the pressure-treatment reagent (Freeman and McIntyre, 2008). The peak at 172 ppm is associated with carboxyl groups (-**C**OOH) or derivatives (-**C**OOR) such as amides or esters. It is likely that this peak corresponds to acetyl esters of hemicellulose, cellulose lactones, and carboxyl groups of gluconic and glucuronic acids of oxidized cellulose.

Nearly all peaks found in the Fe-exposed samples are present in the control samples, which is expected as both samples are from the same parent source. The distribution (peak intensity) of carbon moieties has changed after the long-term Fenton oxidation – carbonyl, carboxyl, aryl-O, and aryl increase showing that the exposure to Fe in the nail over decade-long exposure period has enriched the two exposed samples in aromatic structures at the expense of degradation of cellulosic materials (as evident by decrease in di-O-alkyl and O-alkyl resonances). Carbohydrates are labile towards oxidative processes and their degradation pathways via Fenton reaction has been previously studied (Moody, 1963; Morelli et al., 2003). This is in agreement with the presented data. It must be noted that the abundance of iron in the exposed samples (and copper in the Pine 1 samples) may have quenched some of the aromatic signals (Pfeffer et al., 1984; Botto et al., 1987), thus the abundance of aromatic carbons in the Fe-exposed samples is likely much greater.

3.2. Quantification of condensed aromatic compounds (ConAC)

The obtained solid samples were subjected to nitric-acid digestion for BPCA quantitative assays along with elemental analyses (Table 1).

Table 1. Elemental analysis and benzenepolycarboxylic acids (BPCA) quantification of condensed aromatic compounds (ConAC) in the two pine wood samples.

Sample	C (wt.%)	H (wt.%)	H/C (mol/mol)	ConAC/OC (wt. %)	Fe (wt.%)	Cu (wt.%)
Pine 1 Control	46.2 ± 0.6	5.8 ± 0.2	1.49 ± 0.06	0.23 ± 0.02	Below LOD	0.347 ± 0.015
Pine 1 Exposed	50.1 ± 0.6	5.2 ± 0.1	1.23 ± 0.03	1.02 ± 0.03	4.413 ± 0.650	0.775 ± 0.017
Pine 2 Control	46.1 ± 0.4	6.0 ± 0.1	1.55 ± 0.03	0.25 ± 0.01	Below LOD	0.026 ± 0.002
Pine 2 Exposed	47.0 ± 2.0	5.2 ± 0.2	1.33 ± 0.03	1.12 ± 0.02	4.733 ± 0.153	0.050 ± 0.003

*LOD = limit of detection

The bulk elemental analysis reveals an enrichment in carbon and dehydrogenation, which results in the decrease of H/C ratio for both samples (14% and 17% decrease, respectively) indicative of aromatization of the samples after exposure to Fenton chemistry in agreement with the presented NMR data earlier. To quantify any ConAC in these samples, the BPCA analysis was employed. While it certainly has limitations, it is currently considered to be the best quantitative tool for quantifying ConAC in environmental matrixes (Hammes et al., 2007; Wagner et al., 2018). Here, the ConAC quantity (ConAC/OC in weight %) is reported after scaling the B6 and B5 concentrations (Stubbins et al., 2015) and normalizing the data to organic carbon in the sample. Interestingly, there are detectable amounts of ConAC in both control samples. Given that the boards of both decks were exposed to natural conditions over 10+ years, it is likely that some of the Fenton-produced ConAC has diffused throughout the boards or that

ConAC are produced in the control samples at low abundances. It is observed that both Fe-exposed samples contain about 1% of ConAC, which is low given the extent of charcoalification determined by visual inspection (Figure 1). Regardless, the increase of ConAC in these samples indicated that ConAC have been produced during the decade-long exposure of wood to the nails, a truly non-pyrogenic process.

An alternative explanation is that due to carbohydrate mineralization (or other radical-labile molecules) by Fenton chemistry, the ConAC that was already present in the unexposed zones became concentrated in the regions of Fe-exposure. However, occurrence of ConAC in the unexposed regions of the wood could have only resulted via copper Fenton-like chemistry (Pham et al., 2013). While sorption of aerosol-derived ConAC into the wood is possible (Bao et al., 2017; Wagner et al., 2019b), no ConAC has been observed in fresh wood as measured by the BPCA analysis in a recent study (Bostick et al., 2018). Thus, because the control of Pine 2 also has ConAC of 0.25%, and is poor in Cu (Table 1), Copper Fenton-like chemistry is very unlikely to be the source of it. Thus, it is much more plausible that ConAC from the Fe-exposed regions became redistributed through the woods with the assistance of water dissolution throughout the decade-long exposure.

3.3. Molecular Characterization using Ultrahigh Resolution Mass Spectrometry (FT-ICR-MS)

To investigate the 12-year exposure on the molecular level, ultrahigh resolution mass spectrometry (FT-ICR-MS) was performed. This technique has become extremely popular in organic geochemistry as it is able to resolve the thousands of molecules in complex environmental samples and evaluate their composition (Hertkorn et al., 2007; Sleighter and Hatcher, 2007; Hertkorn et al., 2008; Zhang et al., 2020). While this instrument only measures mass-to-charge values for all ionized molecules in a sample, its ultrahigh precision allows for a unique molecular formula to be assigned to each mass peak. While not quantitative, it is another common tool for detecting the presence of ConAC in various samples (Hockaday et al., 2007; Wagner et al., 2018). Similar to the assumption employed for the BPCA method, formulas with modified aromaticity index

$AI_{MOD} \geq 0.67$ (Koch and Dittmar, 2006, 2016) are often labeled as black carbon (e.g., (Stubbins et al., 2010, 2017; Roth et al., 2019), and if they contain a N or S atom, they are even referred to as black nitrogen (Wagner et al., 2015b) and black sulfur (Hertkorn et al., 2016), respectively. Given that the utilized FT-ICR-MS instrument did not have an ionization source suitable for analyzing solid samples, the four samples of this study were base-extracted using dilute sodium hydroxide. This is a classical extraction technique in the study of solid environmental matrices such as soils, and it has been shown that it does not alter the structural composition of the evaluated sample (Hatcher et al., 2019). Figure 3 shows the molecular formulas obtained for each wood sample before and after Fenton exposure. The formulas are classified using a presence/absence approach (Sleighter et al., 2012) in three categories: Fenton-labile (formulas present in the control samples); Fenton-resistant (formulas present in both samples); and Fenton-produced (formulas present in the Fenton-exposed sample).
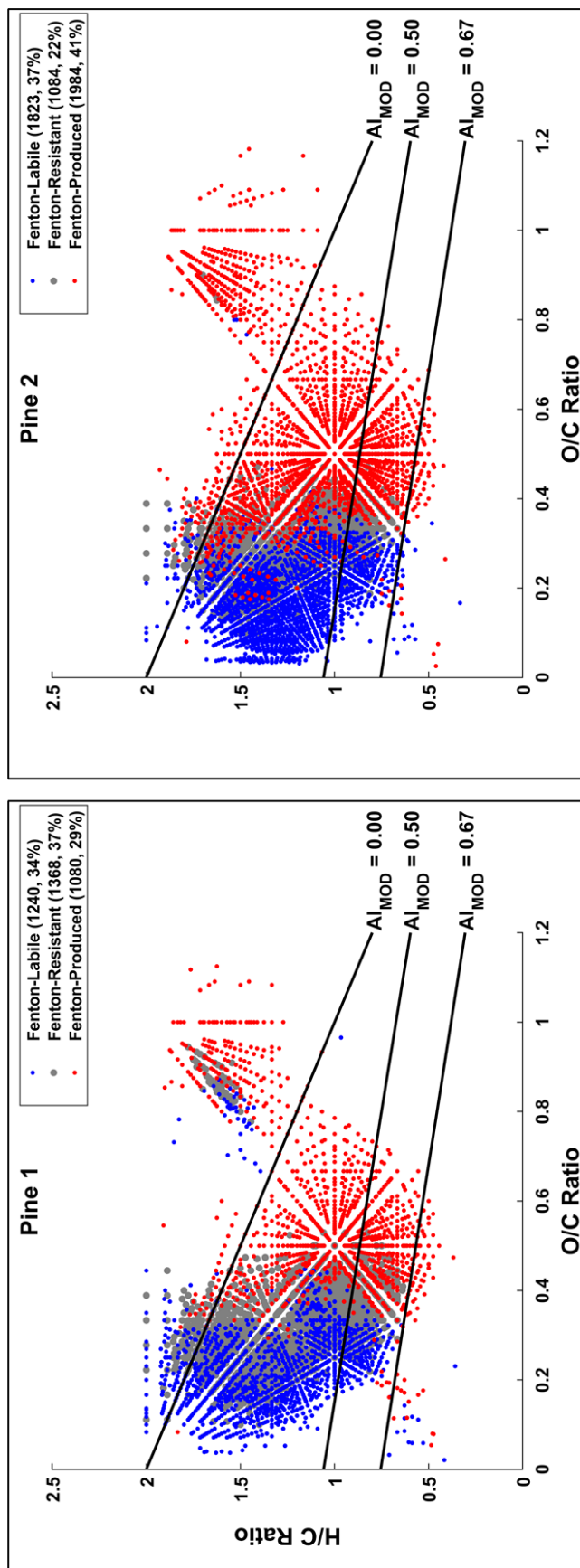
Figure 3. Van Krevelen diagrams (H/C vs O/C) of FT-ICR-MS formulas identified only in the control (**Fenton-Labile**), only in the Fenton-exposed (**Fenton-Produced**), or in both samples (**Fenton-Resistant**) using a presence/absence approach (Sleighter et al., 2012). The number of formulas of each class (and corresponding percentages) are given in parentheses in the legends. The van Krevelen space is separated based on modified aromaticity index (AI_{MOD}) thresholds (Koch and Dittmar, 2006, 2016).

After exposure to Fenton chemistry there are clear shifts in molecular composition. For both samples, molecular formulas with higher O/C ratio and lower H/C ratio evolve, which is also accompanied by loss of numerous aliphatic/olefinic compounds (blue markers). The compounds are likely carboxyl-containing aliphatic molecules (CCAM) recently found and proposed to be important in the formation of aromatic and condensed aromatic compounds in soils (DiDonato et al., 2016; DiDonato and Hatcher, 2017). The newly formed Fenton-produced molecules are lignin-like, but there are also some ConAC formulas ($AI_{MOD} \geq 0.67$) formed. If this data is interpreted using the traditional approaches in the literature (e.g., Stubbins et al., 2010, 2017; Roth et al., 2019), it can be concluded that ConAC are being produced after Fenton exposure. This data complements the trends presented earlier using BPCA analysis and is in agreement with the previously published mechanisms for formation of ConAC from lignin (Chen et al., 2014; Waggoner et al., 2015). The observed changes are also consistent with humification reactions in soils (Stevenson, 1994; Guggenberger, 2005) which are known to produce aromatic and condensed aromatic structures (Chang et al., 2018; Gerke, 2019). This likely validates the hypothesis made previously by DiDonato et al. (2016) that the most stable fraction of soil organic matter, the humic acid, is derived from lignin which has been processed via radical electrocyclization reactions. However, a more in-depth analysis of these samples using humic acid extractions must be done to fully evaluate this proposition. A recent study determined that microbe-induced humification produces condensed moieties (Chen et al., 2020), also in agreement with that presented here in which Fenton exposure leads to humification.

Additional evidence for the observed molecular changes can be obtained by evaluating the common formulas among the two samples being compared in each of the woods. Plots of the relative mass spectrometric abundance of individual peaks that are common to the Fe-exposed samples versus those in the control samples are indicative of how much these molecules are affected by the Fenton reaction (Figure 4). A correlation with a high coefficient of determination (R^2) would indicate that these peaks are not affected by the Fenton oxidation (Sleighter et al., 2012). The low R^2 values of Pine 1 and Pine 2 (0.0395 and 0.0185, respectively) indicate that there are significant changes in the molecular abundance of these molecules.
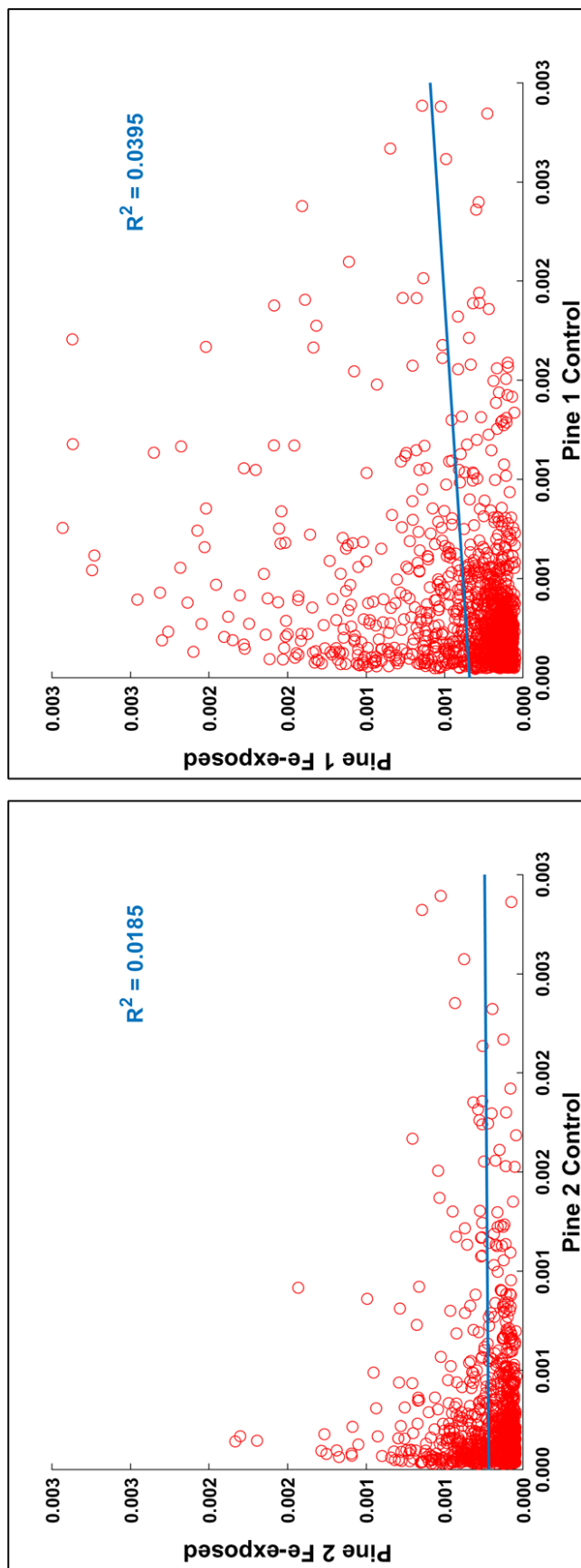
Figure 4. Mass spectrometric abundance scatterplots of the Fenton-resistant formulas of Pine 1 (left) and Pine 2 (right panel). A low R^2 value is indicative of a significant change in mass spectrometric abundance of the common formulas among the two samples being compared (Sleighter et al., 2012).

Thus, while the common formulas among the control and Fe-exposed samples of each wood specimen are operationally classified as "resistant" to Fenton-exposure, solely because they are detected in both samples, a closer inspection reveals significant changes in their mass spectrometric abundances. It is possible that the Fenton-induced changes are insufficient to cause them to disappear and be counted as formulas that are Fenton-labile or Fenton-produced. Additional evaluation using three-dimensional van Krevelen diagrams allows for observing these changes in better detail (Figures 5 and 6). Shifts of the mass spectrometric abundance of the common formulas is easily depicted by the percent change plots on the right panels indicating that the molecular composition shifts to higher oxygenation and lower hydrogenation. These trends parallel with what is observed above (Figure 3) using only unique formulas for each sample, and with the quantitative solid-state ^{13}C NMR data (Figure 2), further validating my observations.
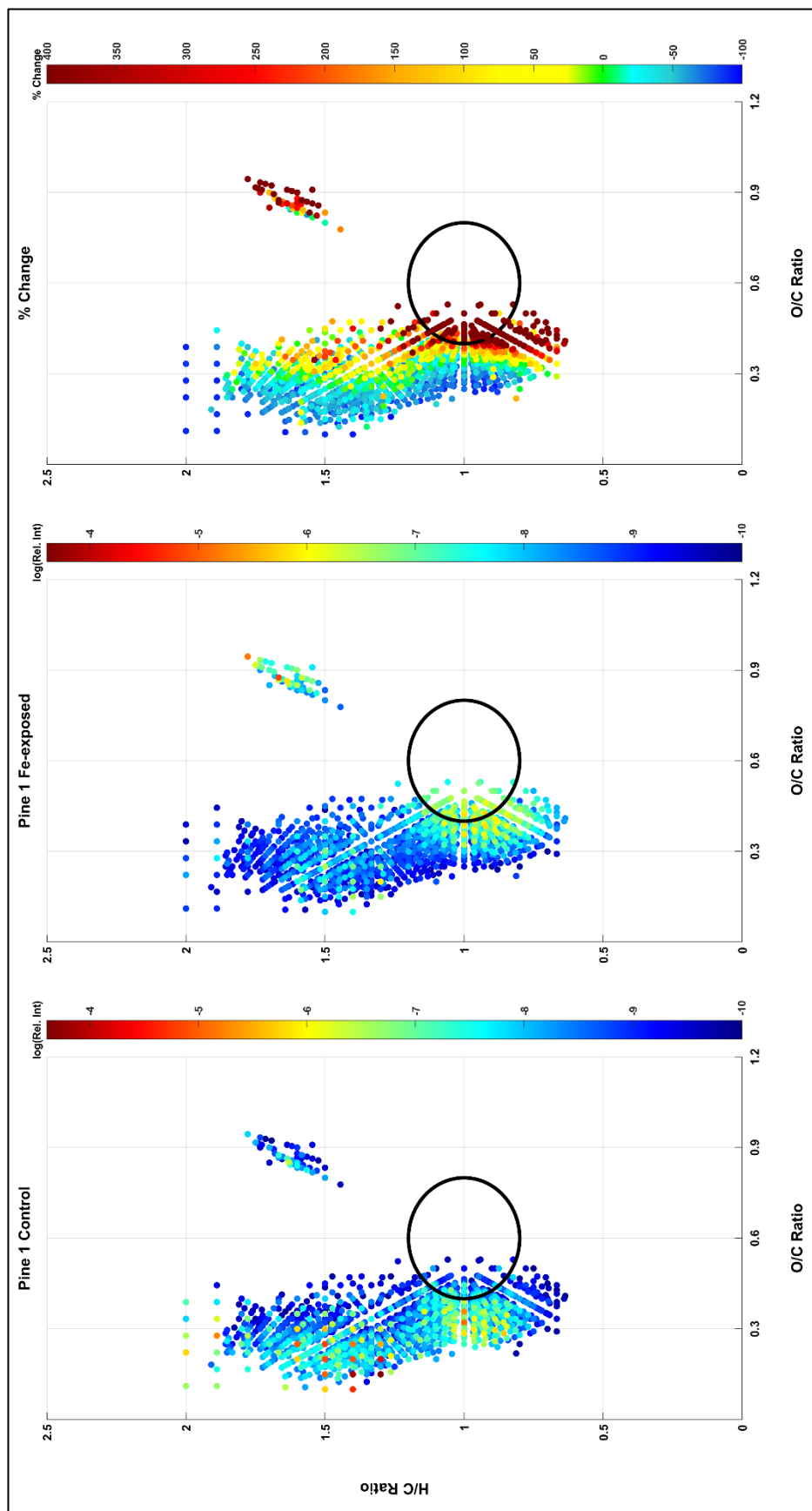
Figure 5. 3D van Krevelen diagrams of Pine 1 before (left) and after (middle) Fenton exposure. A comparison using % change in relative magnitude of each formula is shown on the right panel. The black circle is set as a visual reference for comparisons.
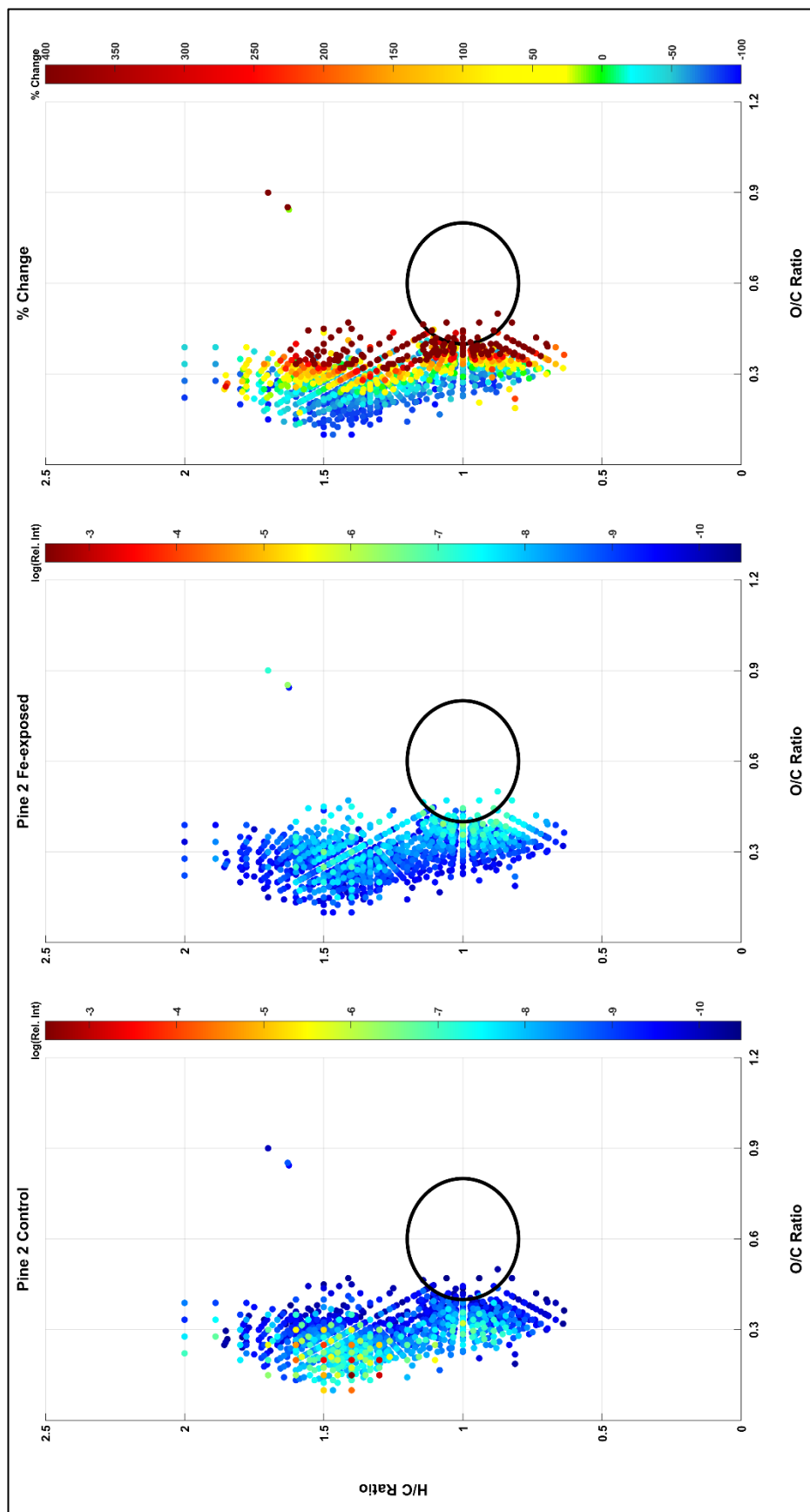
Figure 6. 3D van Krevelen diagrams of Pine 2 before (left) and after (middle) Fenton exposure. A comparison using % change in relative magnitude of each formula is shown on the right panel. The black circle is set as a visual reference for comparisons.

4. DISCUSSION

4.1. Non-pyrogenic formation of ConAC in the environment

The evident non-pyrogenic formation of ConAC, and the fact that none of the wood boards have never been exposed to combustion, is strong evidence that ConAC in the environment can also originate from non-pyrogenic sources, validating previously made propositions (Chen et al., 2014; Waggoner et al., 2015). It must be noted that one of the woods presented here (Pine 1) had been pressure-treated, and one may argue that the chemical used (typically copper complexes with alkylated quaternary ammonium ligands, Freeman and McIntyre, 2008) is responsible for the observed trends. However, the close association of the charcoalification in close proximity to emplaced Fe nails suggests that Fenton reactions driven by Fe was dominant in the locality of the nails. Perhaps a Cu-driven Fenton oxidation (Pham et al., 2013) was occurring throughout and in the remainder of the wood remote from nails – the control. This could possibly explain the existence of BPCAs in the control of that sample. While there is no unambiguous knowledge if Pine 2 had been pressure treated, analysis of nitrogen using elemental analysis revealed no detectable amounts of N (data not shown). Additionally, copper measurements (using atomic absorption spectroscopy) of Pine 2 revealed that the copper content is comparable to that of untreated wood (Etiégni and Campbell, 1991) providing additional evidence that this sample has not been pressure-treated (Table 1). Thus, unless the sample was treated with a highly unusual reagent, Pine 2 can be considered to be untreated. This validates the observed trends for Pine 1 proving that the observed compositional changes are not induced by its pressure treatment.

Additional evidence for this non-pyrogenic process is provided by a recently acquired wood sample of maple (Figure 7), which has been exposed for one year to iron nails and it is known that this wood plank has <u>not</u> been pressure-treated. While there is not enough material to perform BPCA analysis and quantitatively confirm the formation of ConAC, it is clear that even after a year visual charcoalification has occurred.
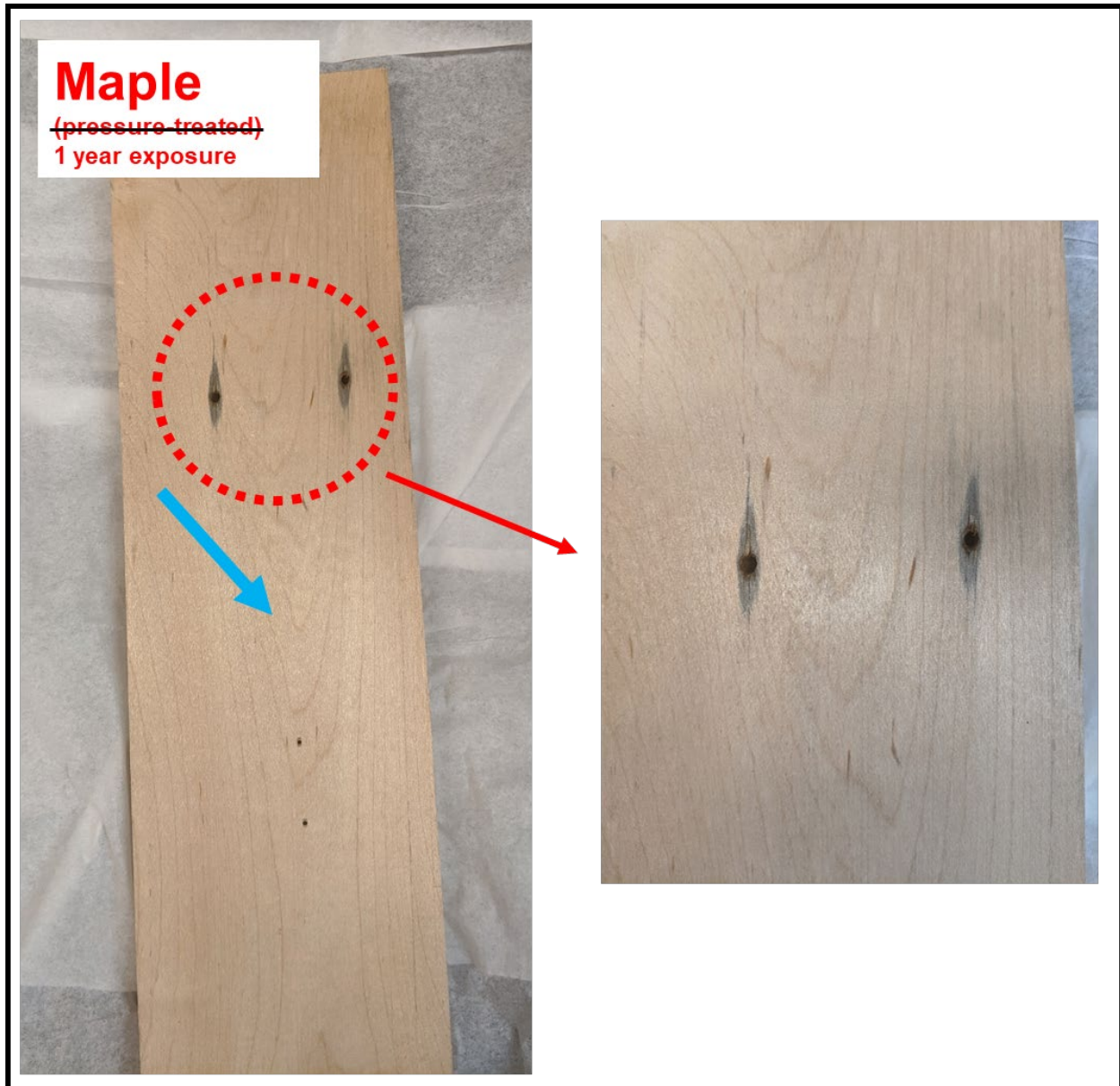
Figure 7. Charcoalification of fresh maple wood through exposure to iron nails. The **blue** arrow indicates a zone with no visible charcoalification. The red arrows show where exposure to Fe nails has occurred over a period of one year.

The evidence shown in this Chapter has significant implications to the wildfire biogeochemistry community, because for over 20 years much of the research is based on the assumption that all ConAC observed in the environment are *exclusively* derived from combustion processes (mainly forest fires, but also various anthropogenic activities). Previous evaluations of the BPCA methodology have raised concerns that this method may falsely identify ConAC as being pyrogenic (Hammes et al., 2007; Zimmerman and Mitra, 2017), and the data presented here verifies this argument. As previously suggested (Chang et al., 2018), the BPCA method is an excellent technique for quantifying ConAC, but it cannot distinguish between pyrogenic (from pyOM) and non-pyrogenic ConAC. Thus, when this method is utilized, I strongly advise for a careful data interpretation and determination if non-pyrogenic sourcing of ConAC is possible in the particular study. However, it is likely that this may not be fully possible, and more complex techniques involving isotopic measurements may need to be employed (e.g., Wagner et al., 2017a).

This finding complements recent observations which also raise concerns about the generally simplistic model of pyDOM cycling proposed by Jaffé et al. (2013). A recent study made the surprising discovery that ConAC found in the global ocean have a different stable-carbon isotopic (δ^{13}C) signature than that of ConAC from terrestrial vegetation exported by rivers. The researchers employed a method which determines the δ^{13}C-value of BPCAs (Wagner et al., 2017a), allowing them to evaluate the source of ConAC. The surprising statistically-significant difference between riverine and oceanic ConAC carbon isotopic signature contrasts with the many previous published studies implying that oceanic ConAC are sourced by rivers (Dittmar and Koch, 2006; Hockaday et al., 2006; Dittmar and Paeng, 2009; Dittmar et al., 2012; Jaffé et al., 2013; Wang et al., 2016; Marques et al., 2017; Coppola et al., 2019; Jones et al., 2020). Oceanic ConAC turn out to have a carbon isotopic signature similar to that of phytoplankton-produced biomass, as well as marine particulate and dissolved organic carbon (Beaupré, 2014) suggesting that the ConAC are sourced from a non-pyrogenic process in the ocean. The research presented in this Chapter signifies and provides quantitative evidence of the proposed Fe-stimulated electrocyclization reactions (Chen et al., 2014; Waggoner et al., 2015) which could be a possible pathway for a non-pyrogenic formation of ConAC in oceanic environments. This has been recently suggested as an important process in

hydrothermal vents zones (Estes et al., 2019), but studies have yet to evaluate the carbon isotopic composition and to analytically constrain the fluxes and sourcing of ConAC in the global ocean from such sources.

Clearly, the long-held assumption that "all condensed aromatic organic matter (i.e., ConAC) in the environment is *exclusively* pyrogenic" is questionable in light of the findings presented here, and this must be considered in the future research of wildfire and terrestrial/oceanic biogeochemistry. While the study of this Chapter reports only of ~1% of ConAC being produced over 10+ years, this can be a significant fraction of the 10% ConAC in rivers (Jaffé et al., 2013) and the 14% of ConAC in soils (Bird et al., 1999; Hammes et al., 2007; Cusack et al., 2012; Reisser et al., 2016). It is likely that this relatively low abundance of ConAC in these visually charcoalified samples is a consequence of a majority of ConAC being washed over time from these areas Unfortunately, the data presented in this chapter is insufficient to quantify the potential overestimation of pyOM in the soil and aquatic environments, and future studies need to address this process using quantitative techniques and evaluate its significance. Non-pyrogenic ConAC and fire-produced ConAC ("black carbon") do not seem to be distinguishable with the traditional techniques for identifying ConAC in the environment (FT-ICR-MS and BPCA quantification) which creates a serious challenge for geochemists who study pyrogenic organic matter. It is essential that future studies focus on exploring these substances, evaluate their structures, isotopic signatures, heteroatomic content, and fluxes in the environment. The presence of this non-pyrogenic ConAC creates a serious challenge to the current views on cycling of lignin and pyOM/pyDOM in the environment. This must be overcome in the future by advances in the chemistry and analysis of organic molecules the environment in order to fully understand the how pyOM and pyDOM are involved in the global biogeochemical cycles.

4.2. Constant reworking of fresh plant litter by reactive oxygen species into steady fluxes of aromatic and condensed aromatic molecules

Reactive oxygen species (ROS) are well known to hydroxylate and cleave the monolignol units of lignin during plant litter degradation (also known as humification)

yielding muconic acids (Umezawa et al., 1983; Umezawa and Higuchi, 1987; Higuchi, 1990, 1993), species that are highly reactive due to the presence of olefinic bonds (C=C) in their structures. These acids can then participate in cyclization reactions that yield aromatic compounds (including ConAC), as Waggoner et al. (2015) described. The shift of molecular composition from aliphatic to aromatic presented earlier is in agreement with their proposed Diels-Alder-like reactions. ROS are highly ubiquitous in soils, and it is suggested that they are essentially important in the processing of soil organic matter. Trusiak et al. (2018) recently observed that hydroxyl radicals are produced in Arctic soils coincident with rain events that supply dissolved oxygen to the soil surface. They suggest that Fe^{2+} reacts with dissolved oxygen to produce hydroxyl radicals through Fenton chemistry yielding Fe^{3+}. The oxidized Fe^{3+} is then reduced back to Fe^{2+} at the expense of organic matter which is being oxidized. In another study of rot in fruits, Morelli et al. (2003) suggest that oxygen reacts with Fe^{2+} ligated to organic matter to produce a superoxide radical that can abstract hydrogens from water or organic matter to form hydrogen peroxide. H_2O_2 can then react with Fe^{2+} yielding hydroxyl radicals, which can then attack organic matter constituents of fruits such as carbohydrates and proteins. These studies show that oxidation of soil organic matter with oxygen-containing radicals is continuous, with ROS radicals being constantly regenerated at the expense of the organic matter being oxidized. These findings have an implication that radical-driven processes are continuous in the environment, and can constantly produce aromatic substances, as well as non-pyrogenic ConAC, for prolonged periods of time. Because the exposure to Fenton chemistry is an oxidative process, oxygenation of organic matter is inevitable, thus enabling the solubilization of organic matter. It has been found that a similar oxidative process of charcoal, photo-oxidation, can produce and leach dissolved ConAC from particulate charcoal (Roebuck et al. 2017). Thus, it is expected that Fenton chemistry not only produces ConAC, but also facilitates its dissolution and transport to the aquatic environment. Once mixed with fire-derived ConAC in the global pool of dissolved organic matter, there is no current way of analytically distinguishing non-pyrogenic from pyrogenic ConAC, which can bias measurements and lead to over-estimations of fire-derived organic matter in the different environmental reservoirs.

My proposition of constant formation of non-pyrogenic ConAC in soils can possibly explain recent unusual findings in the wildfire biogeochemistry literature. A study evaluating ConAC concentrations and radiocarbon age across the Amazon River (Coppola et al., 2019) identified significant fluctuations in the radioisotopic composition of ConAC. Their study, in parallel with many others (Jaffé et al., 2013; Güereña et al., 2015; Wang et al., 2016; Wagner et al., 2017b) reported that rivers globally export dissolved ConAC at a constant rate. Other studies have found that the riverine export of ConAC is constant and is not affected by fire history (Dittmar et al., 2012; Ding et al., 2013; Marques et al., 2017). These studies report of no correlation between the production of charcoal in the upstream catchments and corresponding ConAC concentrations in rivers downstream indicative that the ConAC flux is independent of how long ago a fire had occurred. If these ConAC were truly sources by pyOM, their concentrations should increase immediately after a forest fire, and this was not observed. Another study also reports of a lack of correlation between ConAC in soils and fire history of these regions (Kane et al., 2010), which is also raising questions, because it is expected that soils with previous exposure to fire will be enriched in ConAC.

While these studies attempted to evaluate the export and environmental dynamics of pyOM and pyDOM, they are basing their findings on the assumption that the measured ConAC using the employed BPCA analysis is *exclusively* of pyrogenic origin. Based on the findings presented in this Chapter, it is likely that the aforementioned studies have quantified both fire-derived ConAC ("black carbon") and non-pyrogenic (Fenton and microbial-derived) ConAC that are both leached from soils and sediments. Specifically, the reports by Ding et al. (2013) and Kane et al. (2010) that ConAC quantities are unaffected by recent fire events raise concerns as a recent fire event must increase the ConAC contents (in riverine DOM and soil organic matter, respectively). I hypothesize that the reported ConAC in these studies is actually Fenton-derived that is continuously being produced during plant litter degradation of soils by microbes or Fenton chemistry, and then continuously transported in rivers. The fire-derived ConAC flux that Ding et al. (2013) targeted to measure was likely masked, I hypothesize, by a larger constant flux of non-pyrogenic ConAC. The observation of relatively low abundance of ConAC (~1%) in the wood samples of my study after Fenton exposure is possibly a result of such a

constant formation and leaching of ConAC from the wood planks into the soil beneath the two houses. This would result in a continuous ConAC flux as reported by Ding et al., 2013. In a recent study observing the non-pyrogenic formation of ConAC in soils by microbes (via similar radical-based reactions to those discussed here here) it was estimated that non-pyrogenic pathways may be annually producing 3 – 12 % of ConAC in soils (Chen et al., 2020). Thus, it is likely that Fenton-derived ConAC are significantly contributing to the globally active pool of ConAC, a finding that is significantly at odds with the many studies implying a combustion history.

5. CONCLUSIONS

While it is without a doubt that ConAC are produced in pyrolytic processes, here I present quantitative evidence for an abiotic non-pyrogenic process that can be important to the sourcing of pyrogenic organic matter in the environment. Results from this study indicate that ligninaceous aromatics and aliphatic compounds (such as CCAM) can contribute to the formation of non-pyrogenic ConAC in soils and a fraction of the presumed charcoal-derived pyOM in soils may be Fenton-derived. Results from this study also validate the previous propositions by Chen et al. (2014) and Waggoner et al. (2015) and indicate that the sources of ConAC in the environment must be re-evaluated in future studies to account for any non-pyrogenic contributions.

CHAPTER III

PHOTOCHEMISTRY AFTER FIRE: STRUCTURAL TRANSFORMATIONS OF PYROGENIC DISSOLVED ORGANIC MATTER ELUCIDATED BY ADVANCED ANALYTICAL TECHNIQUES

PREFACE

The contents of this chapter have been published in 2020 in the journal *Geochimica et Cosmochimica Acta*. The data included in this chapter have been published in the data repository *Mendeley.* Full citations for the manuscript and data are provided below. The formatting of the manuscript has been slightly altered to fit it in the continuity of this Dissertation. Copyright permission has been obtained from the publisher (Elsevier) and is provided in Appendix A.

Goranov, A.I., Wozniak, A.S., Bostick, K.W., Zimmerman, A.R., Mitra, S. and Hatcher, P.G. (2020) Photochemistry after fire: Structural transformations of pyrogenic dissolved organic matter elucidated by advanced analytical techniques. *Geochim Cosmochim Ac* **290**, 271-292.

Goranov, A.I., Wozniak, A.S., Bostick, K.W., Zimmerman, A.R., Mitra, S. and Hatcher, P.G. (2020) Photochemistry after fire: Structural transformations of pyrogenic dissolved organic matter elucidated by advanced analytical techniques. *Mendeley Data*, V1, doi: 10.17632/sc9ftvtcxn.1

1. INTRODUCTION

Pyrogenic organic matter (pyOM) is the pool of compounds that are by-products of incomplete combustion of natural organic matter (Goldberg, 1985). A significant fraction of pyOM consists of condensed aromatic compounds (ConAC), also commonly referred to as "black carbon". This fraction is a highly complex mixture of molecules with variable molecular weight, degree of condensation, degree of oxygenation, and solubility in aqueous media (Masiello, 2004; Wagner et al., 2018; Wozniak et al., 2020). Upon biomass pyrolysis (such occurs in oxygen-limited wildfire environments), a large fraction of the organic matter is volatilized into the atmosphere, and the graphene-like solid products are accumulated, and eventually buried in various environmental matrices. This solid residue has been presumed to be recalcitrant to further degradation (e.g., Skjemstad et al., 2002), and to store carbon for millennia (e.g., Masiello and Druffel, 1998; Ziolkowski and Druffel, 2010). Thus, pyOM may effectively sequester carbon, and mediate the levels of CO_2 in the atmosphere, the primary driver of climate change (Lorenz and Lal, 2014).

Oxygen-functionalized pyOM molecules, including oxygenated ConAC, can be leached by rain and transported to aquatic environments as pyrogenic dissolved organic matter (pyDOM, Hockaday et al., 2007; Dittmar and Paeng, 2009; Jaffé et al., 2013; Stubbins et al., 2015). Pyrogenic inputs into the various dissolved organic matter (DOM) pools have been identified as important components of the globally active cycle of organic matter (Druffel, 2004; Lehmann, 2007; Riedel et al., 2016). Thus, elucidating the chemistry of pyDOM is paramount to understanding its role and behavior in the environment. Furthermore, the estimated annual production of pyOM from forest fires is more than enough to account for its build-up in terrestrial environments (Kuhlbusch and Crutzen, 1996; Schmidt and Noack, 2000; Czimczik et al., 2003; Forbes et al., 2006). The fact that one does not observe massive accumulation of pyOM in soils suggests that there are degradative and/or transport pathways that alter the cycling and fluxes of pyOM in the environment (Masiello, 2004; Bostick et al., 2018).

ConAC have been shown to be highly photo-labile (Bostick et al., 2020b), and this has been identified as an important pathway for their degradation in the environment (Stubbins et al., 2010, 2012). Using size-exclusion chromatography, Wagner and Jaffé

(2015) found that ConAC in natural DOM are photo-degraded into smaller compounds. This likely renders them more susceptible to bio-degradation (Mopper and Kieber, 2002; Bruun et al., 2008; Wagner and Jaffé, 2015; Wagner et al., 2018). However, while previous studies have provided valuable information on the cycling of ConAC in the environment, they have strictly dealt with natural DOM samples, a highly complex mixture of natural and pyrogenic compounds that have aged in the environment for an unknown length of time. Environmental aging alters the chemical properties of pyOM, which, for example, affects its stability towards oxidative processes (Ascough et al., 2011) as might be expected from photo-irradiation by natural sunlight.

Biochars, which are biomass pyrolyzed under controlled laboratory conditions, offer another avenue for studying environmental processes affecting pyOM without introducing confounding variables from environmental aging or admixture with DOM from non-pyrogenic sources. For example, biochars have been used to study the photochemical (Ward et al., 2014; Fu et al., 2016) as well as microbial (Zimmerman, 2010; Zimmerman et al., 2011) stability of pyOM. Only a few studies have examined the photochemistry of biochar-derived pyDOM (Ward et al., 2014; Fu et al., 2016; Wang et al., 2020). These studies have shown agreement in trends with previous photochemical studies on environmentally exposed ConAC (Stubbins et al., 2010, 2012; Wagner and Jaffé, 2015). In these studies, ConAC were photo-transformed into smaller, more aliphatic molecules as well as inorganic carbon via photo-mineralization. Fu et al. (2016), Li et al. (2019), and Wang et al. (2020) also showed that upon light-excitation, biochar-derived pyDOM produces reactive oxygen species (ROS), which are highly reactive photo-transients that are involved in various degradative processes (e.g., Scully et al., 2003; McNally et al., 2005; Porcal et al., 2013). These aforementioned studies, however, focused on chars produced over narrow temperatures (400 or 450 ^{O}C), and fire in nature occurs over a much wider range of temperatures yielding chars with properties that vary along a combustion continuum (Masiello, 2004; Wagner et al., 2018; Wozniak et al., 2020). Previous studies have shown that pyrolysis temperature and biomass type have a significant effect on the molecular composition of pyDOM (Schneider et al., 2010; Santín et al., 2016b; Bostick et al., 2018; Wozniak et al., 2020), thus it is likely that they will sequentially impact its photo-reactivity.

To evaluate the photo-degradation of pyDOM and assess its dependence on production temperature and parent feedstock, aqueous extracts from a temperature series of biochars were subjected to photo-degradation in a custom-built solar simulator. As forest fire temperatures are generally in the 300-500 ^{O}C range, but more pronounced structural changes to pyOM occur above 600 ^{O}C (Santín et al., 2015, 2016b), oak wood chars prepared at lower (250 and 400 ^{O}C) and higher (525 and 650 ^{O}C) temperatures were used to representatively evaluate the combustion continuum. A parallel study, Bostick et al. (2020b), examined the photo-degradative impacts on total organic carbon (TOC), benzenepolycarboxylic acids (BPCA) molecular markers for ConAC, and operationally defined optical pyDOM fractions (chromophoric and fluorophoric pyDOM) for the same samples. It was observed that 5 – 18 % of the organic carbon was mineralized over a 5-day photo-irradiation, with the photo-lability of pyDOM increasing with the production temperature (250 < 400 < 525 < 650 ^{O}C) of the parent oak char. It was determined that the ConAC content was the primary factor for controlling the photo-lability of pyDOM, and the degree of condensation of ConAC was a secondary factor. A comparison of oak versus grass pyDOM from parent chars prepared at the same pyrolysis temperature (650 ^{O}C) revealed that parent feedstock also has a critical role in pyDOM photochemistry. To characterize the photo-transformations at the molecular level, these aqueous extracts were examined via Fourier transform – ion cyclotron resonance – mass spectrometry (FT-ICR-MS) and nuclear magnetic resonance (NMR) spectroscopy. These two parallel studies have allowed us to gain new insights on the photo-reactivity of pyDOM leached from chars produced at varied temperatures, as well as to identify the by-products and pathways of the pyDOM components that are susceptible to photo-degradation.

2. MATERIALS AND METHODS

2.1. Preparation of char leachates and photo-irradiation

Chars in this study were obtained by pyrolyzing laurel oak wood (*Quercus hemisphaerica*, 1 cm x 1 cm x 5 cm pieces) either under full atmosphere (250 ^{O}C) or

under nitrogen gas flow at 400, 525, and 650 ^{O}C in a custom-made pyrolyzer. Dwarf Fakahatchee grass sheaths (*Tripsacum floridanum*) were also charred under N_2 flow at 650 ^{O}C. Characteristics and details of the production of these solids have been published previously (Zimmerman, 2010; Mukherjee et al., 2011; Bostick et al., 2018, 2020b; Wozniak et al., 2020). After grinding and sieving to 0.25 – 2.00 mm size particles, about 10 g of solid biochar material was leached in 400 mL of MilliQ laboratory-grade water (18.1 mΩ) for two days in amber vials under dark conditions. A leachate of the parent oak biomass was also prepared using shavings of the wood to allow for a representative extraction of reference wood DOM. The produced leachates are denoted hereafter with the parent biomass preceding the pyrolysis temperature (e.g., Oak 525, Grass 650). Further details of the preparation and composition of these leachates can be found in their previous studies (Bostick et al., 2018, 2020b; Wozniak et al., 2020).

Leachates were filtered using mixed acetylated and nitrated cellulose filters (0.45 μm) and diluted to avoid self-shading effects (leachate absorbance at 340 nm as following: Oak Biomass: 0.068, Oak 250: 0.130, Oak 400: 0.138, Oak 525: 0.064, Oak 650: 0.040, and Grass 650: 0.120). The leachates were then spiked with $HgCl_2$ to prevent bio-degradation. Preliminary experiments determined that the addition of $HgCl_2$ does not interfere with the utilized NMR or FT-ICR-MS analyses. Leachates were transferred to quartz tubes (3-cm diameter) arranged horizontally for photo-irradiation in a custom-built photo-incubation chamber. Q-Lab Corporation UV-A lamps were installed to produce UV-A light (295 – 365 nm, λ_{MAX} = 340 nm, 40 watt). This band of the solar spectrum is what passes through the ozone layer in the stratosphere, and therefore is the main driver for photochemistry in the tropospheric environment (e.g., Mopper and Kieber, 2000, 2002; Stubbins et al., 2008). Irradiation was conducted over a period of five days (120 hours) though light outputs were approximately 1.2 times more intense than natural sunlight, and natural light/dark cycles were not replicated. Thus, while irradiations were not intended to replicate natural conditions, the total light exposure was equivalent to that experienced over ~12 days (assuming 12 light hours per day). PyDOM samples were collected at time 0 ("Day 0") and at the termination of the irradiation ("Day 5") for all samples except Oak 400 pyDOM which was sampled at 0 ("Day 0"), 24 ("Day 1"), 48 ("Day 2"), and 120 ("Day

5") hours of irradiation. A more detailed description of sample preparation and photo-irradiation is provided in the parallel study (Bostick et al., 2020b).

2.2. Nuclear magnetic resonance (NMR) spectrometry

NMR analysis was performed without pre-concentration and minimal sample modification. Samples were diluted volumetrically with deuterated water (Acros Organics, 100% D) to produce a 90:10 $H_2O:D_2O$ solution. Sodium 2,2,3,3-tetradeutero-3-trimethylsilylpropanoate (TMSP, Acros Organics, 98% D) was added to a final concentration of 0.83 µM to serve as an internal reference. Liquid-state analyses were performed at room temperature (24.9 ± 0.1 ^OC) on a 400 MHz (9.4 Tesla) Bruker BioSpin AVANCE III spectrometer fitted with a double-resonance broadband z-gradient inverse (BBI) probe at the College of Sciences Major Instrumentation Cluster (COSMIC) facility at Old Dominion University (Norfolk, VA). Data were processed using the Bruker TopSpin software. NMR assignments and predictions were performed using the ACD/Labs ChemSketch and NMR predictors (Advanced Chemistry Development, Inc.) and cross-referenced following Silverstein et al. (2005).

One-dimensional (1D) ^1H spectra were acquired using the PEW5shapepr pulse program, which utilizes Perfect Echo - WATERGATE and shaped presaturation elements for water suppression (Adams et al., 2013; Whitty et al., 2019). Relaxation delay of 4 seconds was used to allow for a more quantitative observation of certain resonances (aryl and olefinic functionalities, as well as some low molecular weight compounds, Vlahov, 1999; Alexandri et al., 2017). The obtained free induction decay (FID) of 10k summed transients was zero-filled to a 16k-sized dataset, and apodized using a 3-Hz Lorentzian window function (WDW = EM). Spectra are internally calibrated to the sharp distinguishable singlet of methanol at $\delta = 3.34$ ppm (Gottlieb et al., 1997), phased, and baseline-corrected. Spectra are then blank-corrected by normalizing them to a spectrum of a procedural blank using the TMSP peak ($\delta \approx -0.02$ ppm). Spectral integration was then performed over chemical shifts that are specific for the different ^1H chemical environments. Integrals are converted to C-basis (Decesari et al., 2007) and normalized to total spectral intensity. Further details regarding ^1H NMR data treatment can be found

in Section 1 of Appendix B. Due to certain alterations in sample preparation and instrumental parameters, there are slight differences between the data for the fresh (control) leachates presented here and in Bostick et al. (2018), as discussed in Section 2 of Appendix B.

Two-dimensional (2D) ^{1}H-^{1}H total correlation spectroscopy (TOCSY) spectra were acquired using the phase-sensitive gradient-enhanced mlevgpphw5 pulse program. It includes a 17-step Malcolm Levitt (MLEV-17) composite decoupling scheme (Bax and Davis, 1985) and a W5-WATERGATE element for water suppression (Liu et al., 1998). Long-range spin-spin couplings were allowed to evolve over a mixing time of 100 ms. Spectra were acquired with 2048 and 128 points in the F_2 and F_1 dimensions, respectively, with 512 transients per increment. The acquired data were then zero-filled to a 4096 x 1024 matrix, which is processed with a π/2-shifted (SSB = 2) sine-squared window function (WDW = QSINE). Linear prediction to 256 points was used in the F_1 dimension. Spectra are calibrated to the methanol peak (δ = 3.34 ppm, Gottlieb et al., 1997), phased, and baseline-corrected in both dimensions. To eliminate T_1 noise, a common artifact in 2D spectra, a one-dimensional positive projection was calculated based on rows with no significant resonances. The projection was then subtracted from each row in the 2D spectrum, canceling out T_1-noise resonances to a large extent. The same manipulation was applied on all columns to clean-up the spectra in the F_2 dimension (Klevit, 1985).

2.3. Ultrahigh resolution mass spectrometry (FT-ICR-MS)

Prior to mass spectrometric analysis, fractions of the photo-irradiated samples and their corresponding controls (the fresh leachates) were adjusted to pH = 2 by addition of HCl, and solid-phase extracted using 3-mL PPL cartridges (Agilent Technologies, Bond Elut PPL, 100 mg styrene divinyl copolymer) as previously described (Dittmar et al., 2008). This step was necessary to remove the high amounts of inorganic salts in the pyDOM matrices that would interfere with ionization during the FT-ICR-MS analysis (Stenson et al., 2002). Cartridges were eluted with methanol (Fisher Scientific, Optima LC-MS grade), and eluents were diluted with water (Fisher Scientific, Optima LC-MS

grade) to obtain 1:1 $CH_3OH:H_2O$ mixtures. Samples were infused (120 µL/h) into an Apollo II electrospray ionization (ESI) source interfaced with a Bruker Daltonics 12-Tesla Apex Qe FT-ICR-MS housed in the COSMIC facility. Prior to analysis, the instrument was externally calibrated with a polyethylene glycol polymer standard to assure accurate m/z measurements over the desired mass range (300 – 800 Da). External calibration was performed every 6 hours to check for instrumental drift during the time of the analysis. Instrument blanks were measured between samples to assure for no carryover. Ionization was performed in negative mode, and ESI voltages were optimized per each sample to assure for consistent spray currents in order to make the samples in the dataset comparable. Ionized molecules are collected in a hexapole, sorted by a quadrupole, preconcentrated in a second hexapole, and transferred to the ICR cell where 300 transients are collected using a 4 MWord time domain. The data were co-added, and the resultant FID was zero-filled and sine-bell apodized. The Bruker Daltonics Data Analysis software then performed a fast Fourier transformation. Each obtained mass spectrum was then internally calibrated to naturally abundant fatty acids, dicarboxylic acids, and compounds belonging to the CH_2-homologous series, as previously described (Sleighter et al., 2008). Then, using an in-house MATLAB script, salt, blank, and isotopologue (^{13}C, ^{37}Cl) peaks were identified and removed. Molecular formulas within ± 0.5 ppm error were assigned to peaks (S/N ≥ 3) in the FT-ICR-MS spectra using the Molecular Formula Calculator from the National High Magnetic Field Laboratory (Tallahassee, FL). Formula assignments were restricted to elemental compositions of $^{12}C_{5-∞}$, $^{1}H_{0-100}$, $^{16}O_{0-30}$, $^{14}N_{0-5}$, $^{32}S_{0-2}$, $^{31}P_{0-2}$, and $^{35}Cl_{0-4}$, constraints previously evaluated and verified for pyDOM from the biochars of this project (Wozniak et al., 2020). Molecular formulas that did not adhere to previously established rules for molecular composition (Stubbins et al., 2010) were discarded. For cases when one m/z peak had multiple molecular formula assignments, inclusion within homologous series (CH_2, H_2, COO, CH_2O, O_2, H_2O, NH_3, HCl) was used to refine the assignments (Kujawinski and Behn, 2006; Koch et al., 2007). In the final data for all samples, at least 80% of the mass spectral peaks were assigned with unambiguous molecular formulas.

To evaluate the bulk composition of pyDOM, various averaged metrics based on molecular formula lists were used. The following parameters were calculated for all

formulas and then averaged without intensity-weighing: N/C ratio, nominal oxidation state of carbon (NOSC), double bond equivalency (DBE) and carbon-normalized DBE (DBE/C), and modified aromaticity index (AI$_{MOD}$). For each metric, a brief description and calculation (if necessary) are shown below:

- N/C - used to characterize the heteroatomic (N-containing) formulas in the studied samples.

- DBE is a well-established measure of the total unsaturations + alicyclic rings in a molecule (e.g., Bae et al., 2011). It is calculated as following:

$$\mathrm{DBE} = 1 + \frac{1}{2}(2\mathrm{C} - \mathrm{H} + \mathrm{N} + \mathrm{P} - \mathrm{Cl}) \hspace{2cm} \mathrm{Eq.\ 3}$$

  DBE/C is the DBE-value normalized to the number of C-atoms in the molecule. This metric can serve as a proxy for the aromaticity of molecules (Hockaday et al., 2006).

- Modified aromaticity index (AI$_{MOD}$) – While DBE is only a measure of the quantity of double bonds/alicyclic rings in a molecular structure, AI$_{MOD}$ is a value that measures the double-bond density in a molecule (Koch and Dittmar, 2006, 2016). This index and its mathematical definition are described earlier in Section 2.6 of Chapter II.

- The molecular weight (MW) metric is the average molecular weight of all molecular formulas. This number is corrected for the loss of a H-atom during ionization in negative ESI mode. While MW for all formulas in each sample is reported, the MW of the ConAC is reported separately.

- NOSC is the average oxidation state of all carbons in the molecule based on its elemental composition. This parameter can be a proxy for polarity, solubility, biogeochemical reactivity, and bioavailability of substances (Kroll et al., 2011; LaRowe

and Van Cappellen, 2011). For example, it has been used to study the alteration of DOM by polyvalent cations (Riedel et al., 2012). It is calculated as shown below:

$$\text{NOSC} = 4 - \frac{4C + H - 3N - 2O - 2S + 5P - Cl}{C} \qquad \text{Eq. 4}$$

3. RESULTS

3.1. One-dimensional ^{1}H NMR Analysis

Based on one-dimensional structural NMR analysis it is evident that the major functionalities of pyDOM (aryl, olefin, oxygenated alkyl (O-alkyl) and alkyl) were altered significantly (Figure 8) by photo-irradiation. While aromatic and olefinic moieties appear to be degraded (mineralized and/or transformed to other functionalities), oxygenated and aliphatic spectral signals (alkyl & O-alkyl) increased after photoirradiation. Photochemical exposure also resulted in a significant loss of organic carbon (5 – 18%, Bostick et al., 2020b) due to formation of CO_2 (and/or corresponding HCO_3^-/CO_3^{2-}), carbon monoxide (Stubbins et al., 2008), or volatile organic compounds such as CH_4 (Bange and Uher, 2005). This is also in agreement with mechanistic studies that, using mass-spectrometry, determined that oxidation of polycyclic aromatic hydrocarbons (PAHs) ultimately yields long-chain alkanes and CO_2 (Zeng et al., 2000b, a). After the five-day photo-irradiation experiment in this study, the various pyDOM samples had ample resonances for O-alkyl as well as measurable olefinic and aryl moieties (Figure 8), which suggests that the photo-degradation of pyDOM was not complete, as one would expect from complete conversion to CO_2.
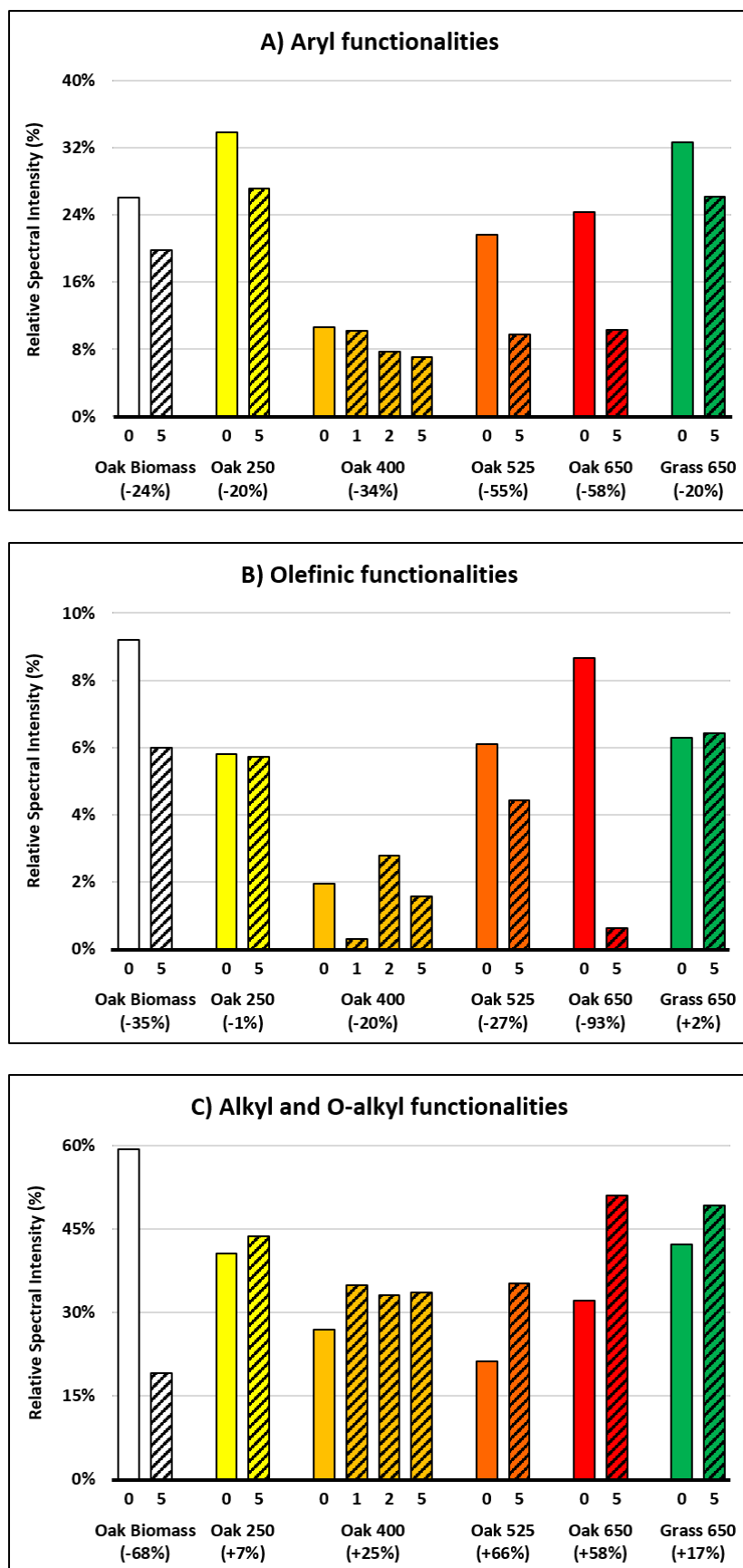
Figure 8. Distribution of main chemical functionalities in fresh (open) and photo-irradiated pyDOM leachates (crosshatched bars) from 1D ^{1}H NMR. Data is presented on a C-basis (after Decesari et al., 2007) for the three main functionality groups: a) aryl (6.50 – 8.30 ppm), b) olefinic (5.00 – 6.50 ppm), and c) combined alkyl and oxygenated alkyl (O-alkyl) protons (0.60 – 4.40 ppm). The number immediately under the bars indicates the day of photo-irradiation. Changes in each functionality after the five-day irradiation relative to the fresh leachate (see Eq. B1) are shown as percentages under each leachate label.

The relative abundance of the aryl signal is reduced to a large extent after irradiation of all pyDOM samples (Figure 8a), which is consistent with previous studies of ConAC in DOM (Stubbins et al., 2010, 2012; Wagner and Jaffé, 2015), as well as of ConAC from biochar-derived pyDOM (Ward et al., 2014; Fu et al., 2016; Bostick et al., 2020b). In the parallel study examining the same samples using the BPCA method, Bostick et al. (2020b) observed large ConAC losses (75 – 94%) over the 5-days of photo-degradation, which parallels the aryl loss presented here, and is in agreement with the proposed idea that the primary factor for sample photo-lability is the increasing ConAC content. Using a BPCA Aromatic Condensation (BACon) index (Ziolkowski and Druffel, 2010; Bostick et al., 2018), a proxy for degree of condensation of ConAC, Bostick et al. (2020b) also determined that the degree of condensation of ConAC is a secondary factor determining the photo-lability of pyDOM. Both of these properties of the samples relate to light absorptivity of the samples, which is well-known to drive the photochemical degradation of natural DOM (e.g., Bertilsson and Tranvik, 2000).

Olefinic moieties of pyDOM (resonating in the region of 5.00 – 6.50 ppm, and not reported previously) decreased in relative abundance after irradiation (Figure 8b). The most notable peak in the olefinic region of the upper temperature leachates (Oak 400, Oak 525, and Oak 650) is a sharp singlet at δ = 5.97 – 5.99 ppm (Figure 9), characteristic of a polysubstituted olefinic bond (i.e., having no neighboring H-atoms that would cause peak splitting (also known as multiplicity, Silverstein et al., 2005).
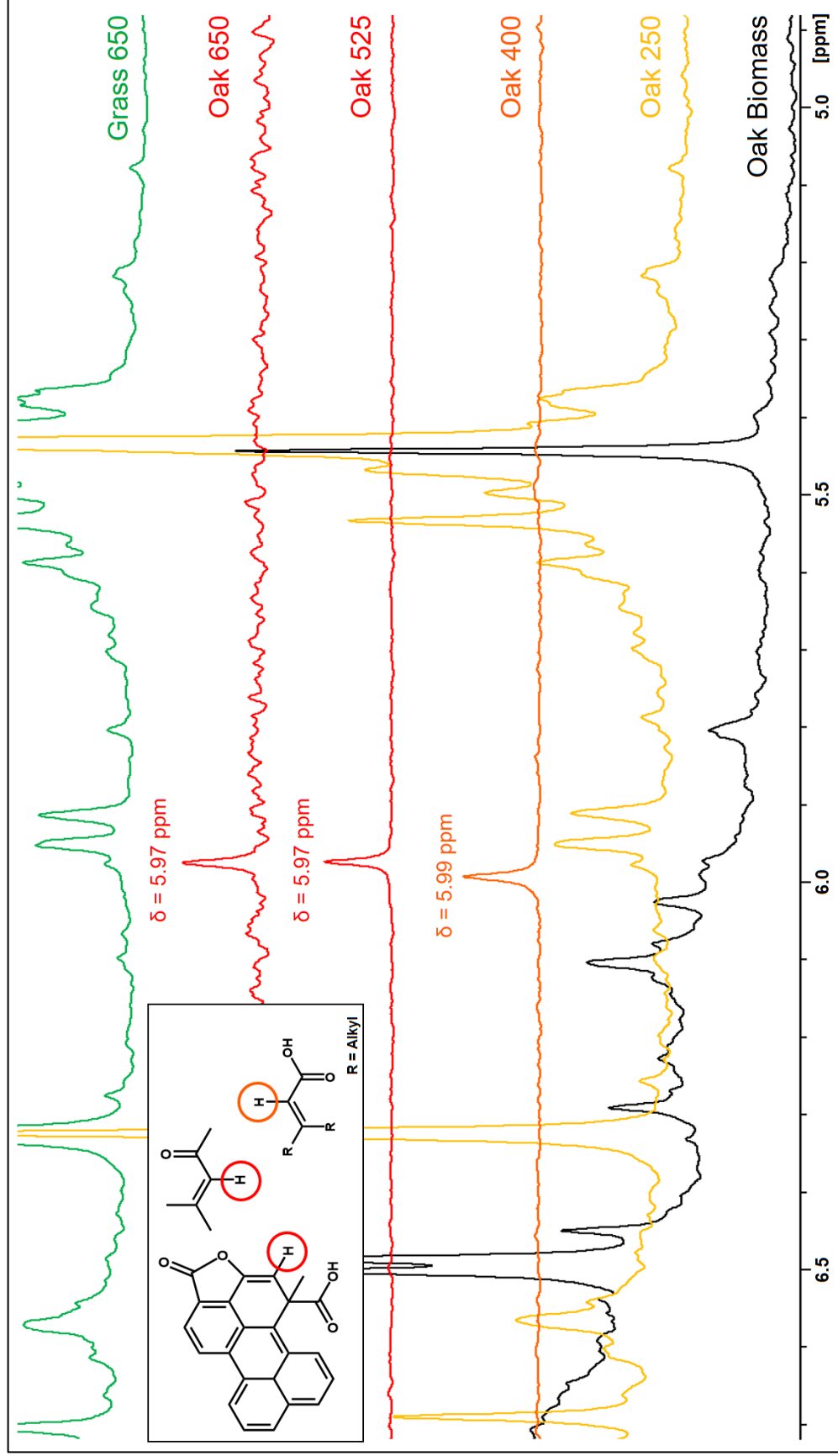
Figure 9. Olefinic resonances (5.00 – 6.50 ppm) of fresh leachates. Peaks indicative of a ^{1}H-nucleus of a polysubstituted olefinic bond are labeled with their corresponding chemical shifts. Hypothetical structures are shown in the insert, and their olefinic protons that would resonate at δ = 5.97 and δ = 5.99 ppm are circled with **red** and **orange**, respectively.

The hypothetical structures (generated using ACD/Labs NMR predictor software) shown in the insert of Figure 9 indicate that the olefinic bond may originate from either 1) the aromatic fraction of pyDOM (condensed or ligninaceous aromatic molecules) or 2) its poorly characterized aliphatic fraction. The decrease in olefinic spectral signal after photo-degradation (Figure 8b) demonstrates that these functionalities are also photo-degraded. Photochemical processes are known to primarily degrade aromatic compounds to produce aliphatic compounds which suggests that the olefinic groups may be part of ConAC, but more in-depth structural NMR and/or mass spectrometric work is planned in future studies to reveal the origin of this functionality in pyDOM, as it cannot be distinguished using the currently employed analytical approaches. With increasing thermal maturity of the parent char, the olefinic functionalities of the upper temperature chars (Oak 400, Oak 525, and Oak 650) become increasingly photo-labile (20 % loss in Oak 400 vs. 93% loss in Oak 650 pyDOM, Figure 8b). In comparison with the high temperature oak char pyDOM, Oak Biomass, Oak 250, and Grass 650 show olefinic resonances with very different chemical shifts and multiplicities, suggesting that these structural entities are associated with components that are perhaps ligninaceous, and do not exist after pyrolysis at higher temperatures. Interestingly, the olefins of Grass 650 pyDOM show a strong similarity to those of Oak 250, and the observed resonances for high temperature char leachates from oak (singlets at δ = 5.97 and δ = 5.99 ppm, Figure 9) are present in neither Oak 250 nor Grass 650 pyDOM. This is another indication that these resonances are likely associated with ConAC which would be produced at higher temperatures. The similarity between Oak 250 and Grass 650 pyDOM is also evident in the relative abundance of the major functional groups and their change after photo-irradiation (Figure 8). This indicates that Oak 250 and Grass 650 are of similar composition and photo-reactivity. The different olefinic signatures between Oak Biomass and Oak 250/Grass 650 suggest that upon pyrolysis lignin is structurally modified and can persist in some altered form at higher temperatures (e.g., 650 ^{O}C). Wozniak et al. (2020) observed a high number of lignin-like compounds present in the FT-ICR-MS data for Grass 650 pyDOM, which supports the hypothesis that the observed olefinic resonances of Grass 650 pyDOM are primarily ligninaceous.

While aromatic and olefinic functionalities were degraded, alkyl- and O-alkyl functionalities were produced by increased photo-degradation (Figure 8c). These alkyl and O-alkyl groups are known photo-products (e.g., Stubbins et al., 2010), but also exist in pyDOM prior to photo-irradiation. It has been determined that pyOM is a bi-phasic system of ConAC and aliphatic fractions (Hockaday et al., 2007; Wozniak et al., 2020), but the pyrogenic aliphatic compounds have been overlooked in the pyOM/pyDOM literature, and their structural composition has not been extensively studied. Thus, I employed additional analyses in an attempt to provide more information on their structure and photo-reactivity.

3.2. Two-dimensional ^{1}H-^{1}H Total Correlation Spectroscopy (TOCSY) NMR Analysis

Total correlation NMR spectroscopy (TOCSY) is a technique well-suited for examining aliphatic moieties associated with sp^3-hybridized carbon. This technique provides information on the connectivity in molecules by detecting the interactions between ^{1}H-nuclei that are 2-6 covalent bonds away from each other. These interactions, also known as couplings, result in peaks off the diagonal line in the TOCSY spectra, and are known as cross-peaks. Thus, if two peaks on the diagonal have a cross-peak, their corresponding protons are nearby in the corresponding structure(s) and are in a "coupling network". It must be noted that nuclei that 1) are separated by a heteronuclear functionality (e.g., an ether group), 2) have small J-coupling constants (i.e., their protons have weak interactions), or 3) have broadened resonances, will not produce cross-peaks (Gheysen et al., 2008; Simpson et al., 2011). These limitations introduce challenges in the interpretation of TOCSY data, but they are usually a small downside relative to the high sensitivity of the technique (due to detection based on ^{1}H-nuclei). TOCSY is capable of providing a wealth of structural information (e.g., Kaiser et al., 2003; Hertkorn et al., 2006; Powers et al., 2019), but unfortunately the challenging pyDOM samples of this project did not produce spectra of high quality (for reasons described in Section 3 of the Appendix B). However, numerous novel observations were obtained as described below.
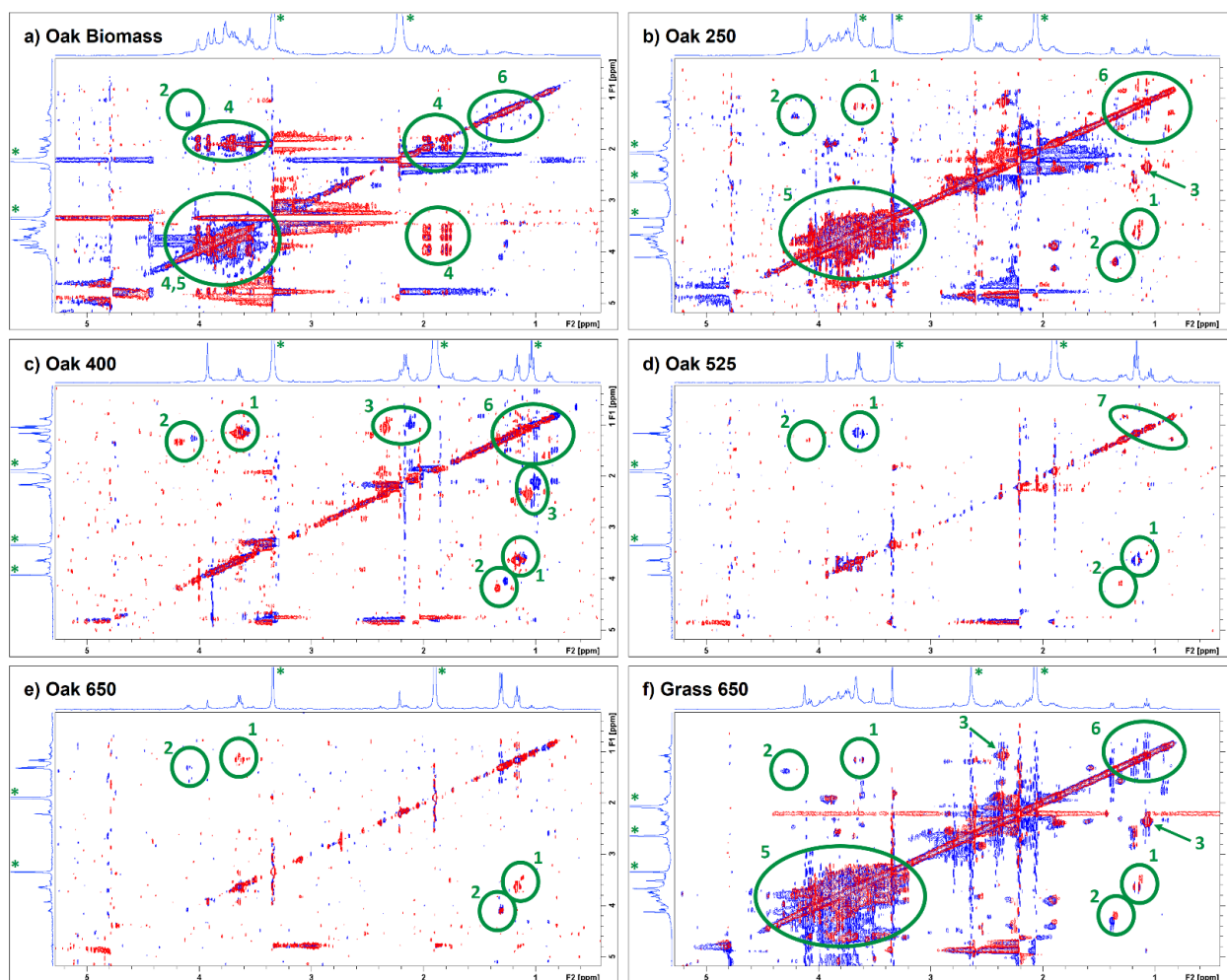
Figure 10. Data from 2D ^{1}H-^{1}H Total Correlation Spectroscopy (TOCSY) NMR for fresh (**blue**) and photo-degraded (**red**) leachates in the alkyl and O-alkyl regions (0 – 5 ppm). The whole TOCSY spectra (0 – 10 ppm) can be seen in Figure 10. The 1D ^{1}H spectra of the fresh leachates are displayed as F_1 and F_2 projections. The green asterisks (*) indicate peaks that are off-scale. Peak groups are referred to as panel and peak number (e.g., a_3, d_1, etc.). Peak labels correspond to: 1 = ethanol (C$\underline{H}_3$-C$\underline{H}_2$-OH), 2 = isopropanol ((C$\underline{H}_3$)$_2$C$\underline{H}$-OH), 3 = propionate (C$\underline{H}_3$-C$\underline{H}_2$-COO$^-$), 4 = carbohydrates, 5 = lignin, 6 = methyl (C$\underline{H}_3$-) and methylene (-C$\underline{H}_2$-) groups, and 7 = ethyl group (C$\underline{H}_3$-C$\underline{H}_2$-).
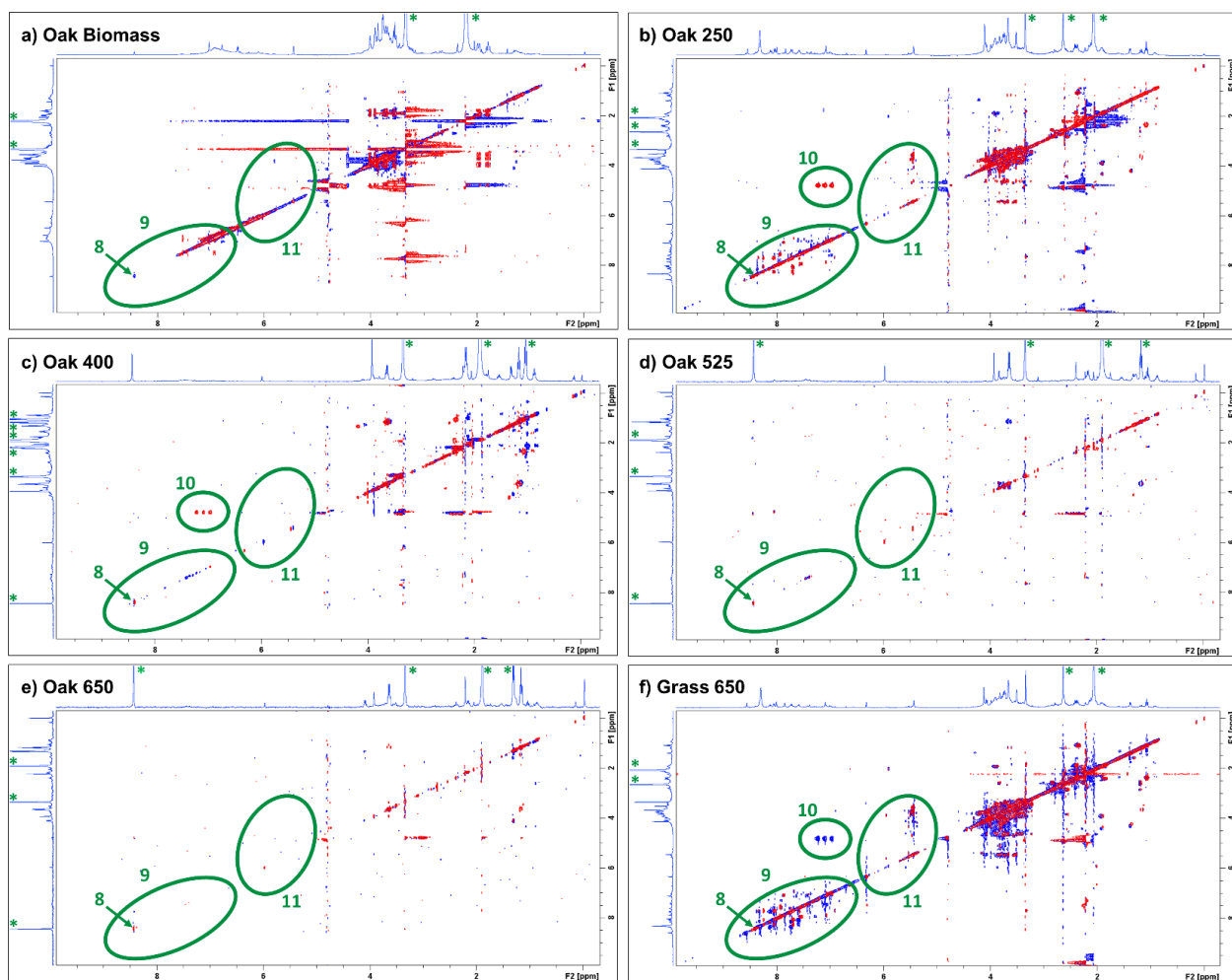
Figure 11. Whole 2D ^{1}H-^{1}H TOCSY NMR spectra for control (**blue**) and photo-degraded leachates (**red**). The 1D ^{1}H spectra of the control leachates are displayed as F_1 and F_2 projections. The green asterisk (*) indicates peaks that are off-scale. Peaks/peak groups are referred to as panel label and peak number (e.g., a_3, d_1, etc.). Peak labels correspond to: 8 = formate (<u>H</u>COO$^-$), 9 = Aryl-<u>H</u>, 10 = N<u>H</u>$_4^+$, 11 = Olefins and their coupling with O-alkyl functionalities.

The Oak Biomass leachate (Figure 10a) displayed typical signatures of a woody extract, with characteristic resonances of cellulose (a_4) and lignin (a_5) (Liitiä et al., 2003; Kapaev and Toukach, 2016). There is a significant overlap in the resonances in the a_4 and a_5 regions, however, upon photo-irradiation the lignin coupling networks were reduced and the cellulosic peaks became more pronounced, although the carbohydrates also appeared to be slightly photo-modified. The methyl (-C$\underline{H}_3$) and methylene (-C$\underline{H}_2$-) resonances (a_6) in this sample also appear to be photo-degraded. No cross-peaks were observed for the aromatic protons in this sample (Figure 11, peak group a_9) indicative of a high degree of substitution of the aromatic rings. A cross-peak is observed upon photo-degradation that suggests a ring-substituent cleavage such as removal of methoxy groups (-OCH$_3$).

Upon char formation with increasing temperatures, carbohydrate signatures gradually disappear from the spectra of the leachates, and new aliphatic coupling networks are created (peak groups b_6, c_6, f_6). The latter functionalities also appear to be photo-produced, with a positive identification of an ethyl functionality (C$\underline{H}_3$-CH$_2$-, $\delta = 0.85$, triplet, and CH$_3$-C$\underline{H}_2$-, $\delta = 1.27$, quartet) being produced upon photo-irradiation (d_7) as exemplified by Oak 525 pyDOM. These observations are in contrast with the findings of Fu et al. (2016) who observed photo-degradation of methyl groups (CH$_3$-) in pyDOM from a bamboo shavings char (prepared at 400 ^{O}C). The lignin O-alkyl resonance networks (a_5 and b_5) in Oak Biomass and Oak 250 are no longer visible in Oak 400 pyDOM. This is expected, because lignin is readily degraded at temperatures above 400 ^{O}C (Laird et al., 2008). However, lignin's methoxy resonances (-OC$\underline{H}_3$, $\delta = 3.92$, singlet) are present in all samples, in agreement with the fact that lignin is a major precursor of pyDOM (e.g., Richter and Howard, 2000). Methoxy groups appear to degrade upon photo-irradiation, as observed previously (Stubbins et al., 2008), and are likely the source of methanol in the photo-degraded leachates (C$\underline{H}_3$OH, $\delta = 3.34$, singlet). The spectrum of Grass 650 pyDOM (Figure 10f) exhibited a high diversity of structures as evident by the numerous cross-peaks, with high similarity to Oak 250, and in contrast to Oak 650. Many of these cross-peaks are characteristic for lignin, as it was suggested by the evaluation of olefinic resonances in Section 3.1 above. The preservation of lignin at 650 ^{O}C suggests that pyro-

transformative processes are highly dependent on the composition of the starting feedstock, as Wozniak et al. (2020) also concluded.

In all samples, resonances of low molecular weight (LMW) compounds can be identified by their characteristic NMR signatures. These include acetate (C$\underline{H}_3$-COO$^-$), formate ($\underline{H}$-COO$^-$), methanol (C$\underline{H}_3$OH), ethanol (C$\underline{H}_3$-C$\underline{H}_2$-OH), acetone (C$\underline{H}_3$-CO-C$\underline{H}_3$), propionate (C$\underline{H}_3$-C$\underline{H}_2$-COO$^-$), isopropanol ((C$\underline{H}_3$)$_2$C$\underline{H}$-OH), and ammonium (N$\underline{H}_4^+$). Such substances have been previously observed in pyOM (Spokas et al., 2011) and pyDOM (Smith et al., 2016). Upon photo-degradation, some of these peaks exhibited a slight change in their chemical shift position. This is likely due to changes in the pH of the system, to which certain peaks, like acetate, are sensitive (Tynkkynen et al., 2009). The observed changes in abundance for formate, methanol, and acetate were variable, with no clear trend with production temperature (Figure 12). For example, upon photo-irradiation, acetate increased in Oak 250 and Oak 650, but its apparent concentration (based on relative NMR peak area) decreased in the other leachates. When a LMW compound is lost during photo-irradiation, it is likely that it acted as a radical scavenger (e.g., Buxton et al., 1988; Clifton and Huie, 1989) since none of these compounds are photo-degradable by direct UV-A photolysis. If its relative concentration increases, it likely is a photo-product of side-chain cleavage reactions of a larger pyDOM compound (e.g., Walling, 1975; Wetzel et al., 1995; Goldstone et al., 2002). While the data for LMW compounds can be evaluated in greater detail, interpretation of the photochemical reactions within pyDOM would be limited, because no measurements of ROS species have been conducted. These data suggest that both ROS and LMW species are involved in mediating the photochemical transformation pathways of pyDOM and DOM, which indicates the necessity of their evaluation in future studies.
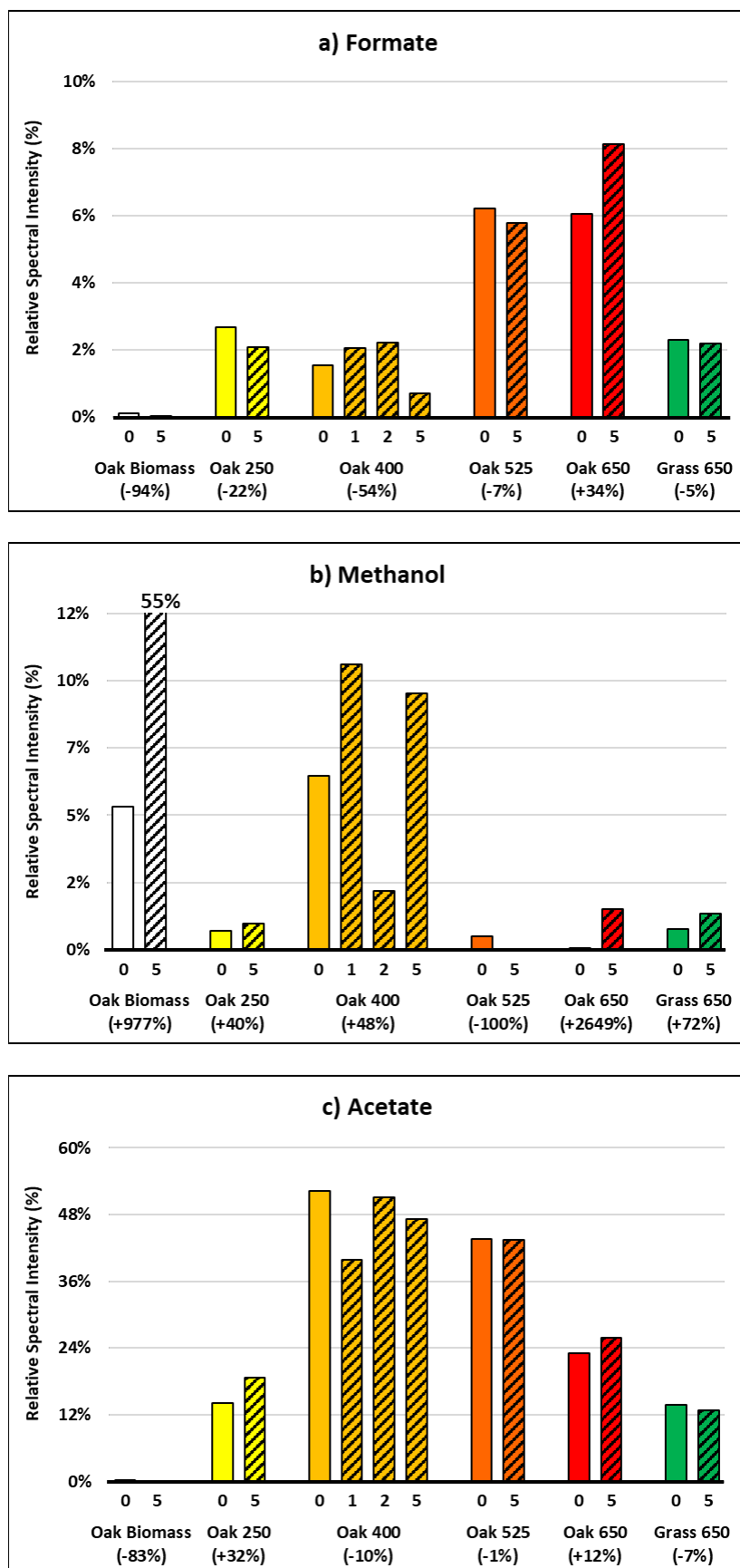
Figure 12. Distribution of low molecular weight compounds for fresh (open bars) and photo-irradiated pyDOM leachates (crosshatched bars) from 1D ^{1}H NMR. Data is presented on a C-basis (after Decesari et al., 2007) for the three main LMW species: a) formate ($\underline{H}COO^-$, $\delta \approx 8.3$ ppm), b) methanol ($C\underline{H}_3OH$, $\delta = 3.34$ ppm), and c) acetate ($C\underline{H}_3COO^-$, $\delta \approx 1.9$ ppm). The number immediately under the bars indicates the day of photo-irradiation. Changes in each functionality after the five-day irradiation relative to the fresh leachate are shown as percentages under each leachate label (calculation shown in Eq. B1 of Appendix B). Please note that the y-axis scale of each panel is different.

3.3. Ultrahigh Resolution Mass Spectrometric Analysis (FT-ICR-MS)

The FT-ICR-MS technique allows for studying the molecular-level elemental composition of natural samples (e.g., Sleighter and Hatcher, 2007; Hertkorn et al., 2008), and has proved valuable in the study of environmental processes (e.g., Kim et al., 2006). To visualize molecular composition changes after photo-irradiation, O/C and H/C ratios of assigned molecular formulas are plotted on van Krevelen (vK) diagrams (Van Krevelen, 1950; Kim et al., 2003). As has been done previously (e.g., Stubbins et al., 2010), the pyDOM formulas are classified into three groups:

- Photo-labile – molecular formulas that are unique to the control non-irradiated samples (fresh pyDOM leachates). These formulas may have been lost either via complete photo-mineralization to inorganic carbon (or volatile organic gases), or were photo-transformed to other compounds;

- Photo-resistant – formulas that are present in both the control and its corresponding photo-irradiated sample. While termed "resistant", they are not necessarily impervious to photo-transformation;

- Photo-produced – formulas that are unique to the photo-irradiated samples and were not detected in their corresponding control leachates. These are the products of photo-transformation of photo-labile and perhaps, to some extent, photo-resistant compounds. These newly detected peaks may also represent compounds that have low ionization efficiencies whose ionization was suppressed due to competition with other ions in the control leachates. It is possible that due to the loss of the photo-labile compounds, more ESI charge was available for molecules with low ionization efficiency. Despite this analytical caveat, these newly detected compounds are very likely true photo-products as the mass spectrometric data presented here are consistent with quantitative NMR data for these samples (Figure 8), as well as previous findings in the photochemistry literature (Kujawinski et al., 2004; Gonsior et al., 2009; Stubbins et al., 2010; Rossel et al., 2013; Riedel et al., 2016; Gomez-Saez et al., 2017; Yuan et al., 2019; Miranda et al., 2020).
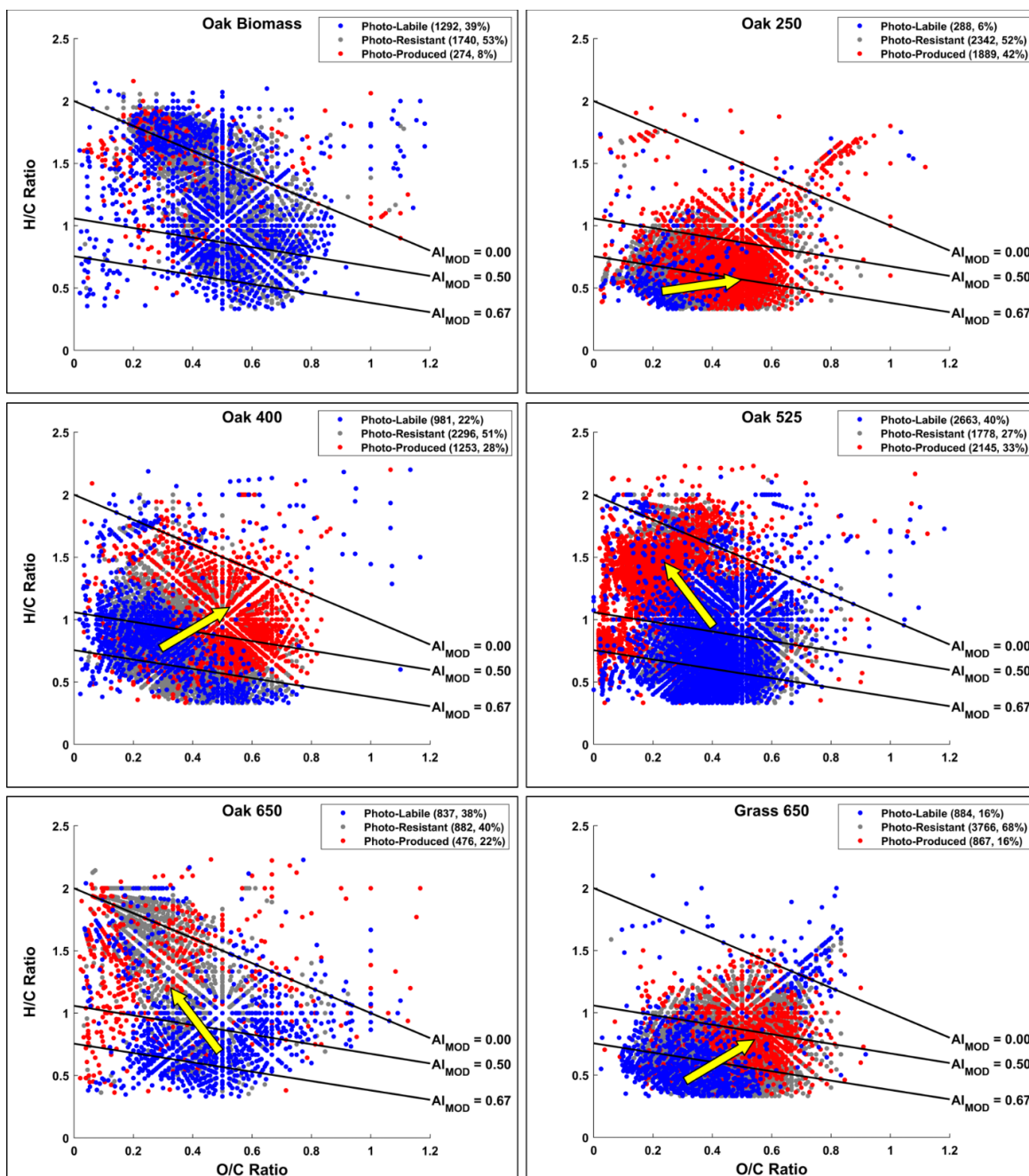
Figure 13. Van Krevelen (vK) diagrams of pyDOM leachates before and after photo-irradiation. Molecular formulas are separated into three classes using a presence/absence approach: Photo-labile (**blue**), Photo-resistant (**gray**), and Photo-produced (**red**). The yellow arrows indicate the general shift of molecular composition due to photo-irradiation. The number of molecular formulas of each pool (and corresponding percentages) are given in parentheses in the legends. The black lines separate the vK space based on the modified aromaticity index (AI_{MOD}, Koch and Dittmar, 2006, 2016). vK diagrams of individually plotted photo-labile and photo-produced formulas are shown on Figures B2-3 in Appendix B, respectively. Photo-resistant formulas are individually plotted on Figure 14.

Based on the abundance of photo-labile and photo-produced compounds, it is evident that different pyDOM samples behave dissimilarly upon photo-irradiation (Figure 13). Most broadly, upon photo-irradiation, low temperature (Oak 250 and Oak 400) and Grass 650 pyDOM showed shifts toward higher O/C and H/C ratios, while those produced from higher temperature (Oak 525 and Oak 650) shifted toward lower O/C and higher H/C ratios. But there were subtle differences among all the samples.

Oak 250 pyDOM composition clearly shifted to being characterized by compounds with higher O/C and H/C ratios, as noted by a removal of photo-labile compounds at H/C ratios of 0.3 – 0.6 and O/C ratios of 0.1 – 0.3, coupled with an evolution of photo-produced formulas at H/C ratios of 0.3 – 1.2 and O/C ranging 0.2 – 0.7. Similar observations were made for photo-exposed ConAC-rich mangrove porewater exported to adjacent estuaries (Tremblay et al., 2007). Because Oak 250 pyDOM is rich in ligninaceous molecules, it is likely that many of the observed photo-labile and photo-produced species are thermally modified lignin molecules. A similar trend in changes of molecular composition was observed for ligninaceous samples after transformation by ROS (Waggoner et al., 2015, 2017; Waggoner and Hatcher, 2017). Oak 400 pyDOM also showed a shift towards a more aliphatic and oxygenated composition, as determined by the evolution of photo-produced compounds that are more H-rich (H/C from 0.5 to 1.75) and O-rich (O/C from 0.4 to 0.8). Similar photo-induced changes in composition have been observed for DOM from the Cape Fear River Estuary (North Carolina, USA), a watershed influenced by industry, urban areas, forests, and some agricultural areas (Gonsior et al., 2009). Oak 525 pyDOM shows a much different response to photo-irradiation, with its composition shifting to high H/C (0.5 – 2) and low O/C (0 – 0.5), evident by the formation of highly aliphatic structures, as previously observed for biochar-derived pyDOM (Ward et al., 2014), and DOM from the Congo River (Stubbins et al., 2010) which is rich in ConAC (Wagner et al., 2017a; Drake et al. 2020). Thus, it is likely that these structures are ConAC photo-degradation products. Oak 650 degraded similarly to Oak 525 suggesting that their pyDOM are of similar composition. However, using quantitative approaches, Bostick et al. (2020b) determined that Oak 650 was more photo-labile than Oak 525. Another important observation from the FT-ICR-MS data is that the proportion of photo-labile compounds increased over the oak pyDOM temperature gradient. While only 6% of Oak

250 pyDOM formulas were removed by photo-irradiation, nearly half of Oak 525 and Oak 650 pyDOM formulas were no longer detected (40% and 38%, respectively). In contrast to Oak 650, the FT-ICR-MS data of Grass 650 show a photo-labile pool of molecular formulas at low H/C and O/C ratios, and a pool of photo-produced compounds at higher ratios indicating similarities with the photo-transformation of Oak 250 and Oak 400. These observations indicate that both production temperature and biomass feedstock control the photo-reactivity of pyDOM.

Molecular formulas present in both the photo-degraded and corresponding control samples of each pyDOM are conventionally labeled photo-resistant (e.g., Stubbins et al., 2010), but the magnitude distribution of these formulas changes significantly after photo-irradiation as well. Using abundance-colored vK diagrams (Figure 14), it is evident that the shifts in abundance of the photo-resistant compounds before and after photo-irradiation are identical to the shifts observed using photo-labile and photo-produced compounds shown with yellow arrows in Figure 13 above. Furthermore, while Oak 650 does not photo-produce as many new aliphatic compounds as Oak 525 (Oak 525 = 2145 (33%), Oak 650 = 476 (22%)), it is clear that for both samples the aliphatic photo-resistant compounds increase significantly in abundance after photo-degradation. Thus, it is also possible that many of the 837 photo-labile compounds of Oak 650 are converted to already existing aliphatic "photo-resistant" formulas. In difference, Oak Biomass, Oak 250, and Grass 650 do not show any significant shifts in their magnitude distributions.

Scatterplots of relative abundance (for both control and photo-degraded pyDOM samples) were prepared in order to quantitatively evaluate the change of composition of the photo-resistant formulas (Figure 15). If the coefficient of determination (R^2) is close to 1.00, the two samples being compared have a compositionally similar pool of photo-resistant compounds (Sleighter et al., 2012). The abundance of the photo-resistant molecules for the oak char leachates changes drastically after photo-irradiation (all $R^2 <$ 0.1) with the exception of Oak 250 pyDOM ($R^2 \approx 0.80$). The significant decrease in R^2 for the upper temperature chars is another indication that the composition of their pyDOM is more susceptible to irradiation-induced changes. The small change in magnitude distribution in Oak Biomass, Oak 250, and Grass 650 ($R^2 > 0.80$) is also indicative of the low susceptibility of these samples to photo-transformation.
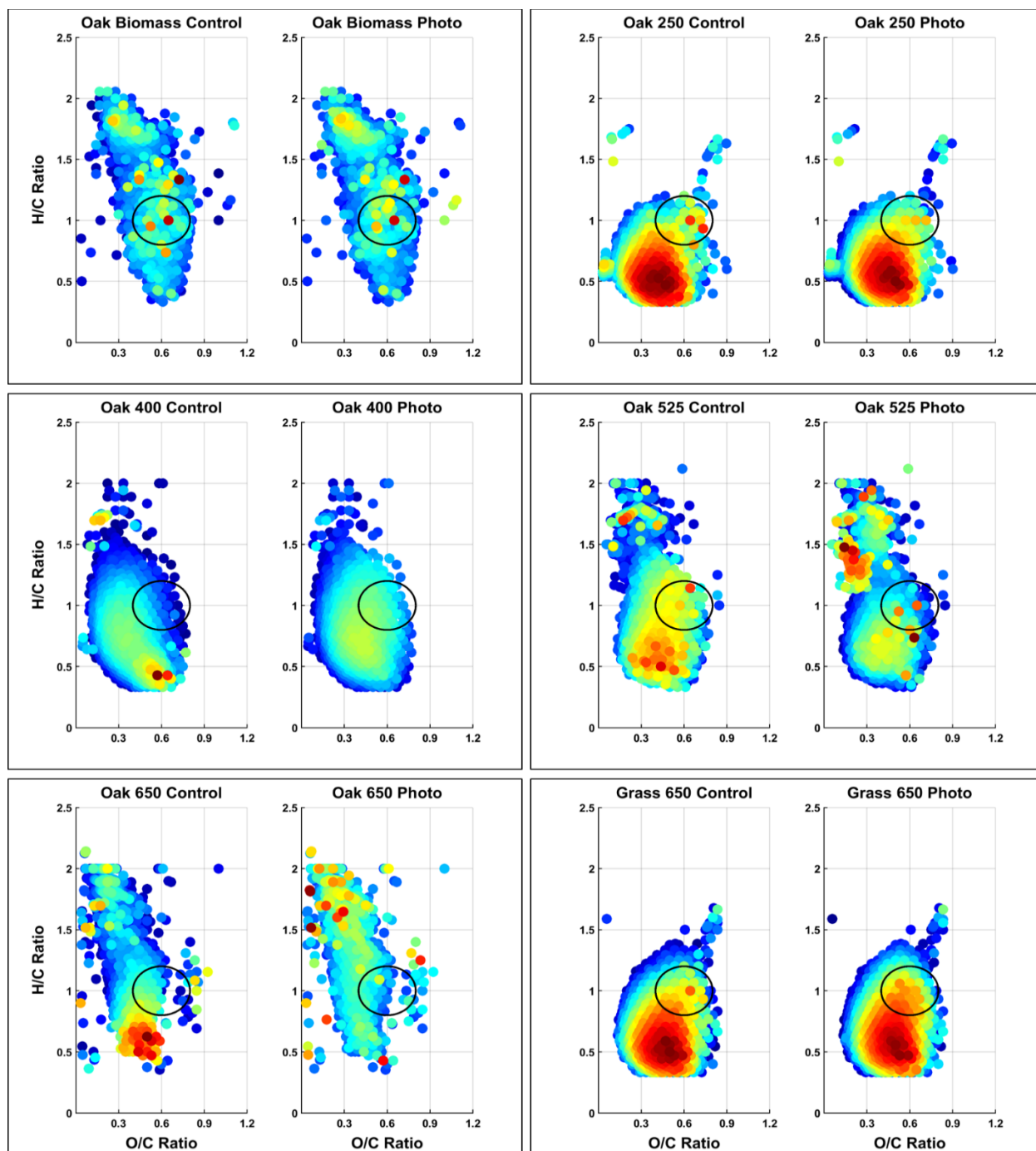
Figure 14. 3D Van Krevelen diagrams of for photo-resistant molecules in each leachate (molecular formulas that have been found common to both control and 5-day photo-irradiated leachate). Color code corresponds to relative magnitude, with **red** being the most abundant, and **blue** being with least. Color schemes are the same for each photo-control pair, but different for each leachate. The black circle serves as a visual reference for comparisons.
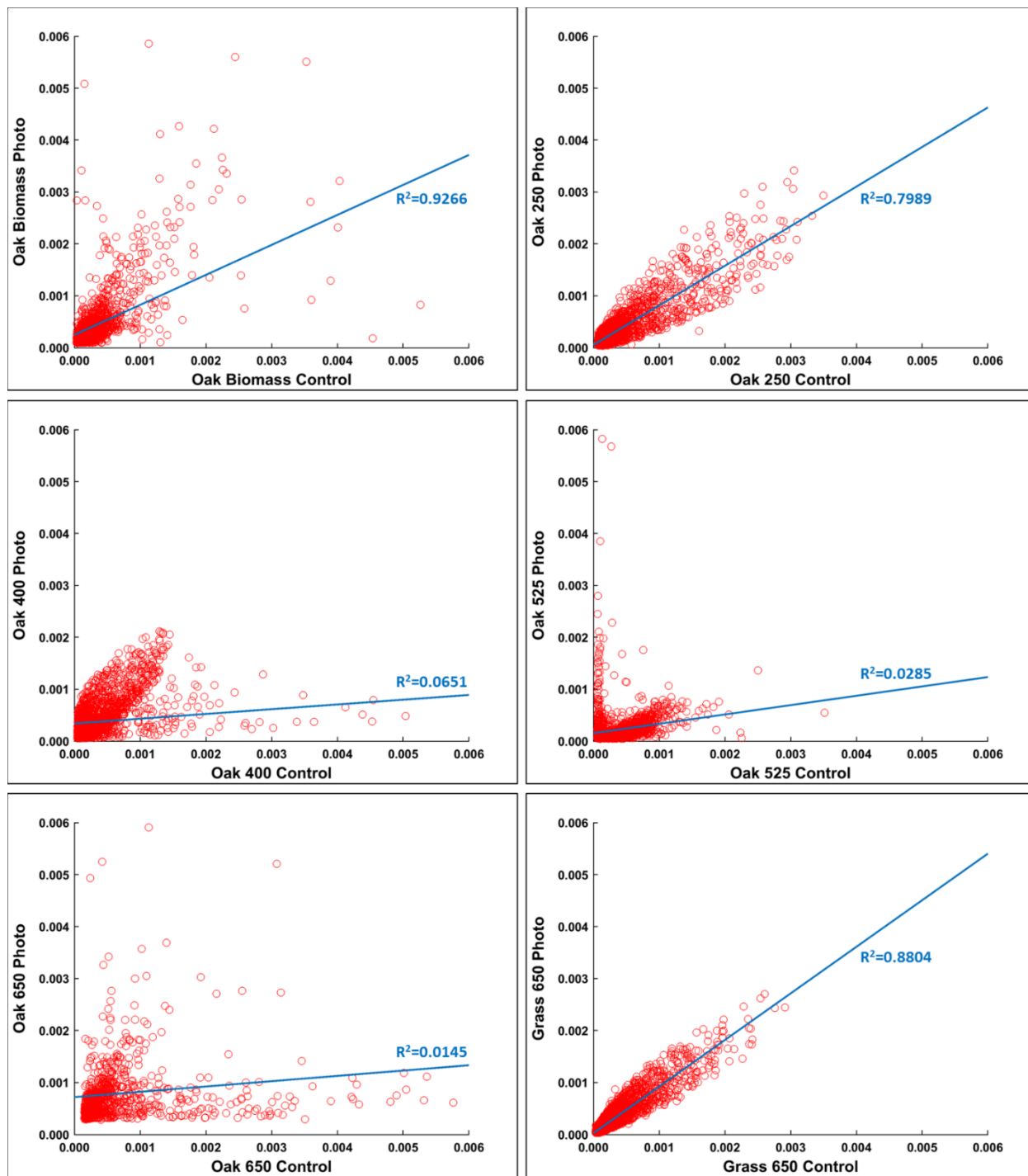
Figure 15. Abundance scatterplots of the photo-resistant formulas. A high R^2 value indicates a high similarity in the abundance composition of the common formulas in the compared samples (Sleighter et al., 2012).

The water-extract of the parent oak biomass had a significantly different photo-degradation pattern from all of the pyDOM leachates. It showed a uniform removal of photo-labile compounds across the vK diagram space (Figure 13) and a formation of a small pool of photo-produced aliphatic compounds (274, 8%). This was an unexpected result, because previous studies of woody biomass (Derbyshire and Miller, 1981; George et al., 2005) or ligninaceous samples (Tremblay et al., 2007; Gonsior et al., 2009; Waggoner et al., 2015, 2017; Waggoner and Hatcher, 2017) have observed substantial changes upon oxidation.

The leachate of Oak 400 was also sampled for analyses at Days 1 and 2 to obtain time-resolved information on the shifts of molecular composition across the five-day photo-irradiation experiment (Figure 16).
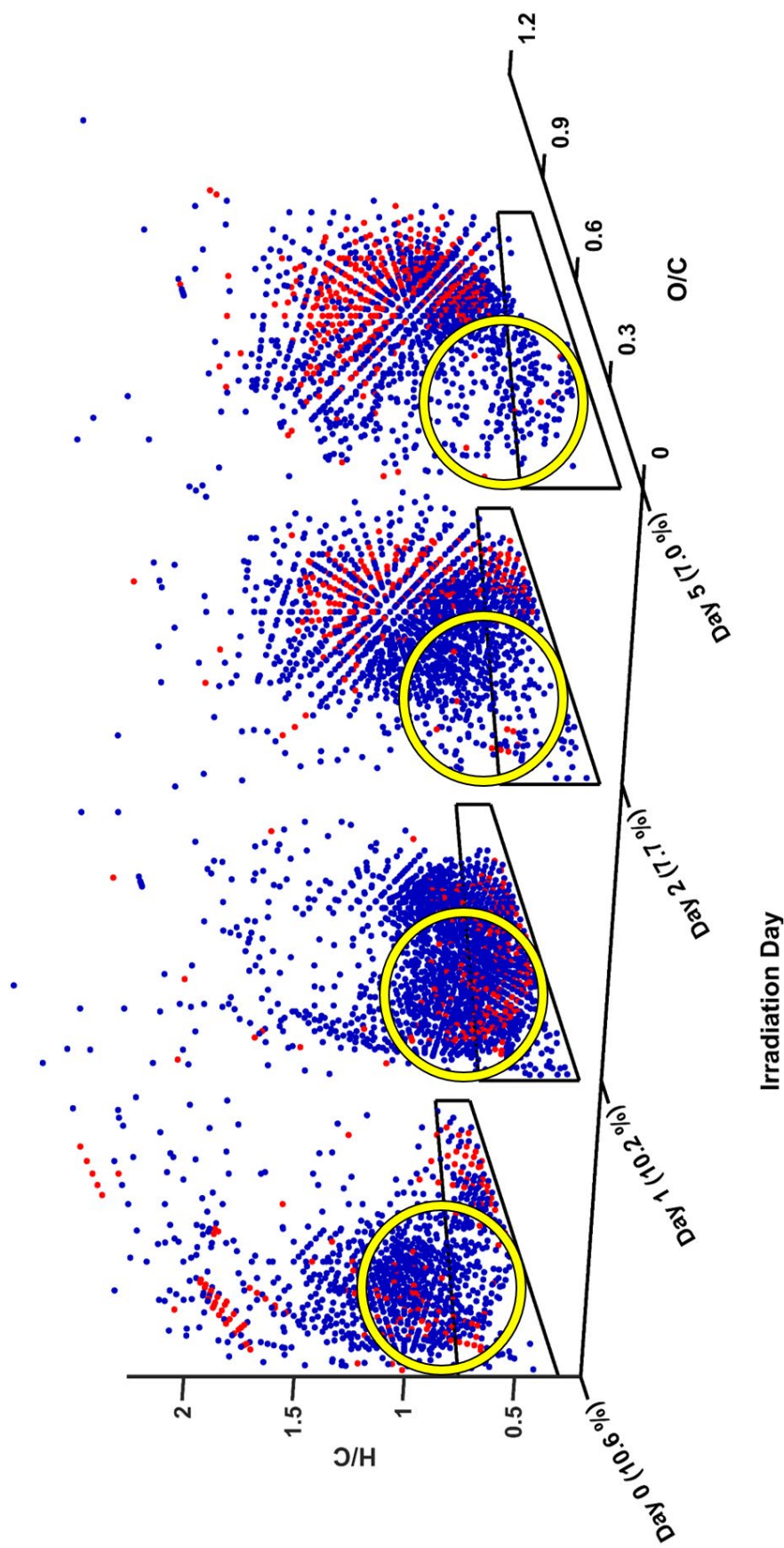
Figure 16. Van Krevelen (vK) diagrams of photo-degradation time series study of Oak 400 pyDOM. ConAC formulas fall into the boxed region ($AI_{MOD} \geq 0.67$). For clarity, formulas that were common to all four time points are not shown (can be seen on Figure 17). The most abundant formulas are colored in red. The yellow circle serves as a constant visual reference. NMR signal (rel.% in C-basis following Decesari et al., 2007) for aryl functionalities in each sample is shown in parentheses on the x-axis.

During the first day of the irradiation, the number of ConAC formulas increased. While photo-production of ConAC has been observed for certain aquatic systems (Chen et al., 2014), this likely did not occur here because there was no increase in aryl functionalities observed via NMR (Day 0 = 10.6 %, Day 1 = 10.2 %), nor in compounds yielding BPCA molecular markers (decrease of 22%, Bostick et al., 2020b). It is likely that unfunctionalized ConAC (i.e., PAHs) present in Oak 400 pyDOM at Day 0, undetected by the ESI-FT-ICR-MS, were photo-oxygenated, thus entered the analytical window to be detected at Day 1. Already observed ConAC at Day 0 also likely became oxidized and contributed to the shift in molecular composition. This suggests differences in the analytical windows of ESI-FT-ICR-MS, NMR, and BPCA analyses, which needs to be considered in future studies, as previously noted by Wozniak et al. (2020).

The molecular composition of Oak 400 pyDOM on Day 1 was similar to previous mass spectrometric measurements of biochar leachate (Ward et al., 2014), as well as of DOM from fire-influenced sites (Hockaday et al., 2007; Gonsior et al., 2009; Stubbins et al., 2010). After further photo-irradiation, on Day 2 there was a loss of molecules with low H/C ratios (inside the yellow circle) and a production of formulas at high O/C and H/C ratios, similar to the trend of Oak 250. There was also a significant loss of aryl functionalities (from 10.2% to 7.7%). By Day 5, there was a major loss of ConAC as observed by FT-ICR-MS, NMR, TOC and BPCA molecular markers (Bostick et al., 2020b) as well as a production of more oxygenated and aliphatic compounds as described above (Figure 13 and corresponding section). By evaluating the abundance distribution of the formulas that were present among the four Oak 400 samples of the time series study (Figure 17), identical shifts in composition were observed. These non-linear changes over the time series suggest a sequence of different photo-transformation reactions that occur throughout the five-day photo-irradiation.
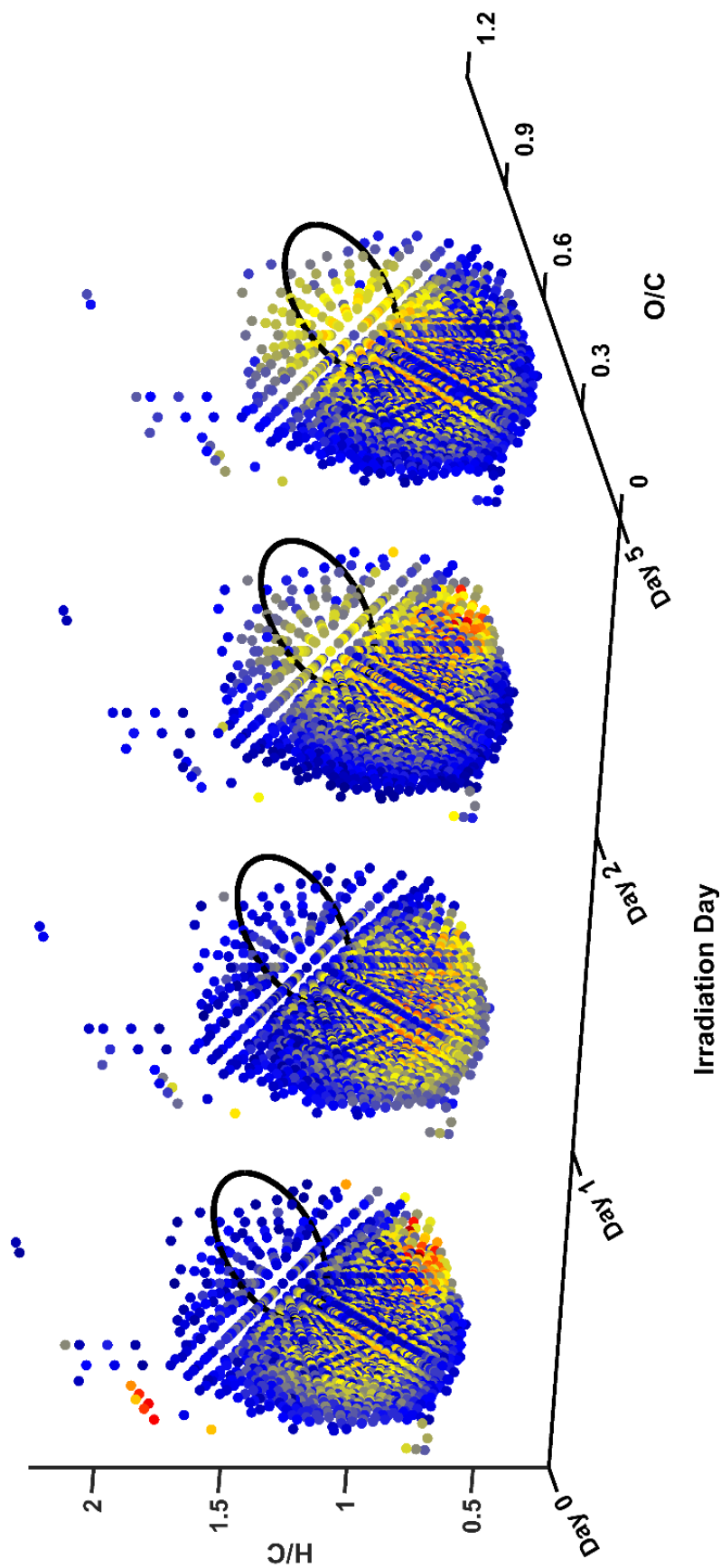
Figure 17. 3D Van Krevelen diagrams of formulas that were present in all four samples of the Oak 400 pyDOM time series. The **blue** color represents formulas with the lowest spectral magnitude, and **red** the ones with the highest. The black ovals serve as visual references for comparisons.

Metrics derived from FT-ICR-MS data (nominal oxidation state of carbon, AI_{MOD}, carbon-normalized double bond equivalency, and molecular weight) allow for an assessment of how bulk pyDOM composition changes after photo-irradiation, and supplements the trends shown above using van Krevelen diagrams. While there is a significant degradation observed for these leachates, the average MW of the molecules in these leachates does not show large differences (Figure 18a). This is likely due to the simultaneous destruction of aryl/olefinic and formation of alkyl/O-alkyl functionalities. Previous studies of pyDOM have mainly focused on ConAC and have determined that larger ConAC are photochemically degraded to smaller molecules as determined using the BPCA analysis, size-exclusion chromatography (Wagner and Jaffé, 2015), and UV-VIS spectroscopy (Stubbins et al., 2012). Bostick et al. (2020b) also report a decrease in the MW of ConAC from Oak 400 and Oak 650 pyDOM upon photo-degradation (as determined by UV spectroscopy and BPCA analysis). The FT-ICR-MS data presented here does not show a significant change in MW of pyDOM for both Oak 400 and Oak 650. This discrepancy is due to the different analytical windows of the utilized instrumentation. Bostick et al. (2020b) used the slope ratio UV-VIS-spectroscopic measurement, a proxy of the MW changes of optically active compounds within UV absorbance of 275 – 400 nm (Helms et al., 2008), as well as the BACon index, also derived solely from ConAC. The FT-ICR-MS has a much larger analytical window detecting all ionizable compounds in negative-ion mode ESI, including many aliphatic compounds that would not be detected using UV-VIS spectroscopy. However, when MW only for ConAC is evaluated (Figure 18b), the observed decreases in MW agree with Stubbins et al. (2012), Wagner and Jaffé (2015), and Bostick et al. (2020b).

In agreement with previous photochemical studies, DBE (Figure 18c), C-normalized DBE (Figure 18d), and AI_{MOD} (Figure 18e) decrease after photo-irradiation. Decreases in these metrics are indicative of destruction of conjugated (ConAC) or olefinic sp^2 systems, in agreement with the degradation of ConAC and ligninaceous aromatic molecules. In contrast, many of these metrics (MW, MW ConAC, DBE) increase for Oak 250 pyDOM and for the first day of irradiation of Oak 400 pyDOM. This is likely due to oxygenation of unfunctionalized ConAC, which are undetectable in the control samples,

but their oxygenated products were detectable, as proposed earlier for the observed trends on Figure 16.

The nominal oxidation state of carbon (NOSC) is a useful parameter for evaluating changes in oxidation state (Kroll et al., 2011; LaRowe and Van Cappellen, 2011). An increasing NOSC is indicative of oxidation (i.e., molecules become more oxygenated), while decreasing NOSC signifies reduction (molecules become more aliphatic). Oak Biomass, Oak 525, and Oak 650 show a decreasing NOSC indicative of these samples becoming more aliphatic after the five-day photo-irradiation, while the other samples seem to become oxygenated due to their positively changing NOSC (Figure 18f). This data parallels the observations made earlier using the van Krevelen diagrams above.

Lastly, changes in N/C ratios before and after photo-irradiation are indicative of the photochemistry nitrogen-containing pyDOM molecules. For Oak Biomass, Grass 650, and the lower temperature oak char leachates (Oak 250 and Oak 650), a decrease in nitrogen is evident after photo-irradiation. This is likely due to photo-degradation of nitrogen-containing molecules. The observed evolution of ammonium peaks using 2D TOCSY NMR (peak group 10 in Figure 11) in these samples agrees with this proposition suggesting a deamination pathway. The absence of NH_4^+ peaks in the Oak Biomass spectra indicate that the nitrogen-containing ligninaceous molecules photo-degrade through a different mechanism. The increase in N/C for the higher temperature char leachates (Oak 525 and Oak 650) indicates a preservation of nitrogen into the photochemical by-products. This suggests that these photo-products may be of higher bio-lability and marine-like composition.
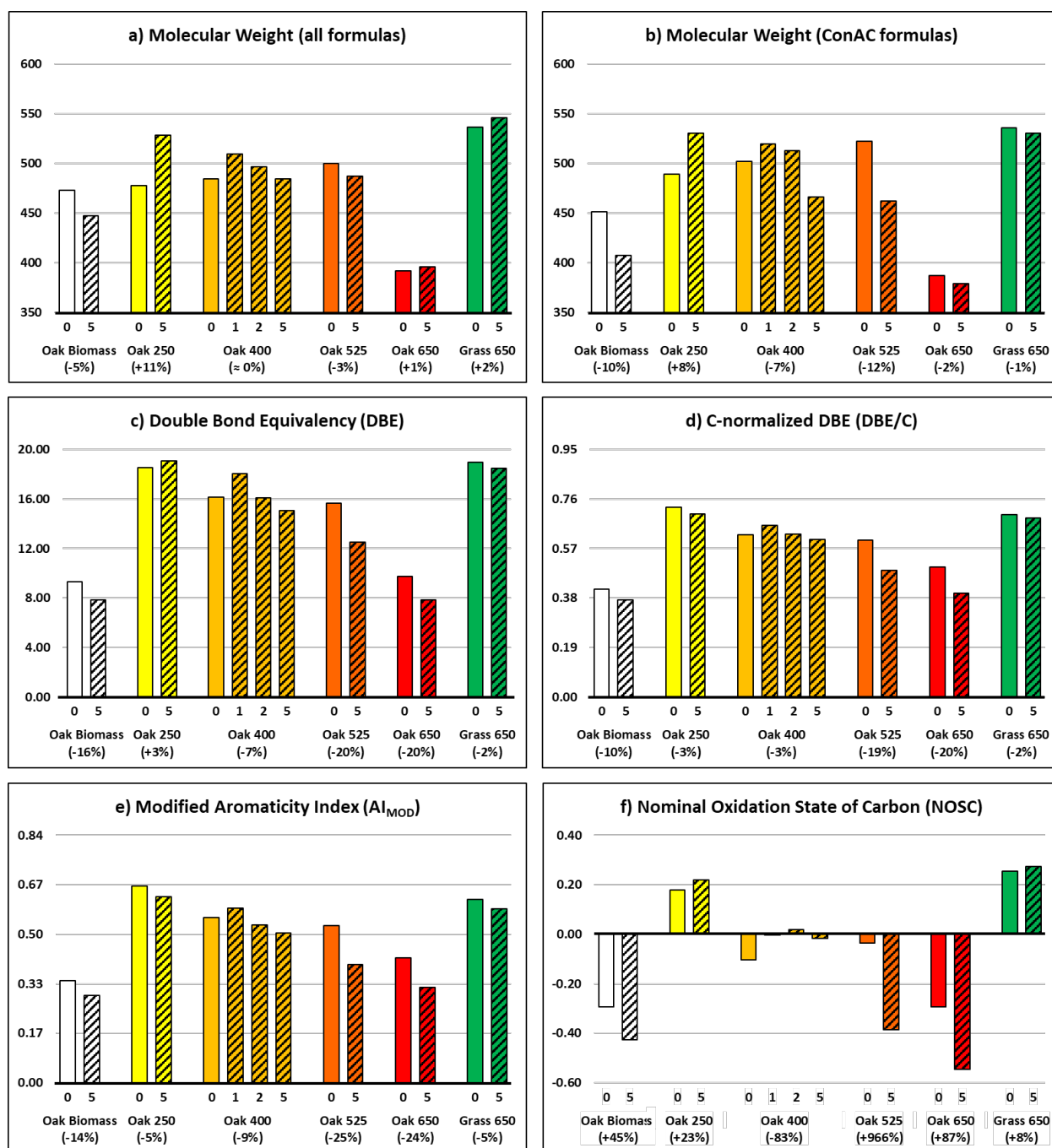
Figure 18. FTMS metrics for the control (open) and photo-irradiated pyDOM leachates (crosshatched bars). The number immediately under the bars indicates the day of photo-irradiation. Changes in each metric for each leachate after the five-day photo-irradiation relative to the control leachate are shown as percentages under each leachate label. Please note that the y-axis scale of each panel is different.
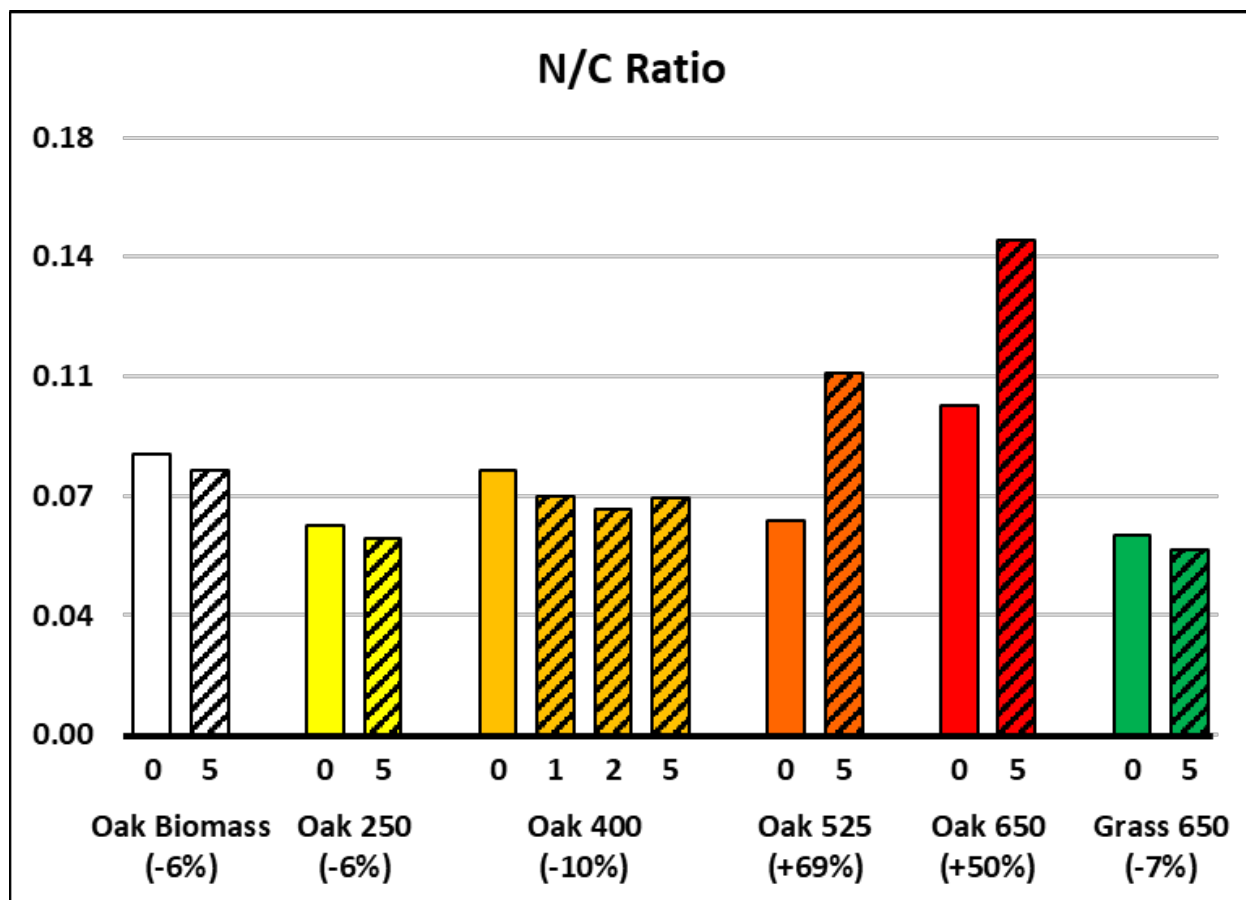
Figure 19. Average nitrogen-to-carbon (N/C) ratios for the control (open) and photo-irradiated pyDOM leachates (crosshatched bars). The numbers immediately under the bars indicate the day of photo-irradiation. Percent change in N/C for each leachate after photo-irradiation relative to the control leachate are shown under each leachate label.

4. DISCUSSION

4.1. Photo-lability of the pyDOM structural and molecular components of pyDOM as a function of production temperature

The decreases in aryl functionalities are indicative of the photo-lability of aromatic functional groups, and this agrees with previous observations for both pyDOM (Ward et al., 2014; Fu et al., 2016; Bostick et al., 2020b) and DOM in general (Kujawinski et al., 2004; Gonsior et al., 2009; Stubbins et al., 2010; Rossel et al., 2013; Riedel et al., 2016; Gomez-Saez et al., 2017; Yuan et al., 2019; Miranda et al., 2020). While it is not possible to directly differentiate between aryl groups from lignin versus those of ConAC using ^{1}H NMR, the presented data suggest that aryl functionalities from ConAC are more photo-labile than ligninaceous aryl groups, as evident from the data for Oak Biomass and Oak 250 leachates in comparison to the leachates of higher temperature chars (Figure 8). Previously it was determined that Oak Biomass DOM is ConAC-free (Bostick et al., 2018), and that Oak 250 pyDOM contains both condensed and ligninaceous aromatic compounds (Bostick et al., 2018; Wozniak et al., 2020). These two samples show higher initial aromatic content relative to the higher temperature char pyDOM samples (Figure 8) perhaps due to the higher solubility of lignin. However, smaller proportions of aromatic functionalities are lost from these samples after photo-degradation. It is evident that the aryl groups associated with ConAC in Oak 400, Oak 525, and Oak 650 (lignin-poor chars) are more photo-labile (34 – 58% loss) than the aryl groups associated with the lignin-rich Oak Biomass DOM and Oak 250 pyDOM (20 – 24% loss). While lignin has been shown to be photo-labile (Opsahl and Benner, 1998; Spencer et al., 2009), its monolignol units contain only a single aromatic ring, thus are less photo-reactive at the utilized irradiation wavelengths (295 – 365 nm, λ_{MAX} = 340 nm). Therefore, lignin is expected to be less photo-labile than ConAC. It is well-established in organic spectroscopy that with the increasing number of conjugated rings (i.e., number of conjugated π-bonds), the energy gap between the bonding molecular orbital (π) and antibonding molecular orbital (π*) narrows. This allows for radiation of higher wavelengths (and therefore lower energy) to be absorbed and excite the molecule through a π → π* transition. Moreover, the molar

absorptivity (ε) increases, allowing the molecule to absorb higher quantities of radiation (e.g., Mamy et al., 2015). This increased susceptibility to molecular excitation and radiation absorption explains the greater photo-lability of ConAC relative to ligninaceous aromatic compounds. This is also in good agreement with previous photochemical studies (Stubbins et al., 2010, 2012; Wagner and Jaffé, 2015), as these works have also observed that larger ConAC have higher photo-lability. Furthermore, photochemical studies of model pyrogenic compounds, polycyclic aromatic hydrocarbons (PAHs), in organic-solvent (Guieysse et al., 2004), soil (Marquès et al., 2016), and surface water (Jacobs et al., 2008) media have also reported that larger PAHs are more readily photo-degraded than smaller ones.

This study also reports on the photo-reactivity of another, previously uncharacterized functionality of pyDOM – olefins. The observed olefinic peaks at $\delta = 5.97$ and 5.99 ppm in higher temperature leachates via 1D ^{1}H NMR (Figure 9) may originate from both the aromatic and non-aromatic components of pyDOM, indicating that future structural NMR studies should evaluate the source of this functionality in greater detail. These functionalities appear to be only present in higher temperature char leachates (Oak 400, Oak 525, Oak 650) indicating that they are associated with structures formed at higher temperatures, possibly ConAC. The data presented in this Chapter show that this functionality degrades upon photo-irradiation (Figure 8b), and its lability increases with the production temperature of the parent char. Linear polyenes are optically absorptive much like ConAC. However, only alkenes having five or more conjugated double bonds are capable of absorbing UV-A radiation, and such compounds are unlikely to be a part of the composition of pyDOM due to their hydrophobic character. Thus, I conclude that the degradation pathway for the olefins of pyDOM is not based on their ability to absorb light. Rather, olefins are likely degraded through radical-mediated reactions. Reactive oxygen species (ROS) are produced upon photo-excitation of PAHs (Penning et al., 1999; Yu et al., 2006) and ConAC from biochar-derived pyDOM (Fu et al., 2016; Li et al., 2019; Wang et al., 2020). Olefinic groups are easily ruptured and substituted by ROS, yielding oxygenated and aliphatic structures. A recent study, however, evaluating the composition of terrestrial and marine DOM upon permanganate oxidation (Laszakovits et al., 2020) did not observe degradation of olefins, and it was concluded that these functionalities

were hindered (and therefore preserved) in the hydrophobic DOM pockets. While DOM molecules are amphipathic (Wershaw, 1999) and radical activity is lowered in the internal regions of their aggregates (Latch and McNeill, 2006), it seems that the olefins in the pyDOM samples were easily accessible, especially in pyDOM from chars produced at higher temperatures. Given that more thermally mature pyDOM is richer in LMW compounds (Bostick et al., 2018), and such substances promote disaggregation (Simpson, 2002), it is likely that pyDOM has different conformational properties than natural DOM, thus the olefinic functional groups of pyDOM seem to be easily accessible by ROS.

The reason for the greater extent of photo-degradation of olefinic moieties in pyDOM from higher thermal maturity chars is unknown. It may be that either 1) more ROS species are produced by photo-degradation of more thermally mature pyDOM, thus more ROS would be available to degrade more olefinic bonds, or 2) there are more olefinic moieties per molecule in more thermally mature pyDOM, therefore these olefins degrade faster because of higher pyDOM degradation rates at higher thermal maturity. The implication of the presence of this olefinic functionality in pyDOM and its controlled photo-reactivity by thermal maturity may be important for the chemistry and cycling of pyDOM, because the olefinic bond is much less energetic than the delocalized aromatic bond, which means that these olefinic moieties are much more susceptible to attacks by radicals. While these olefinic functionalities are 2 – 9% of pyDOM (as measured by ^{1}H NMR, Figure 8b), they are likely important mediators in the transformative processes of pyDOM. Furthermore, the lability of olefins towards radical attacks will allow for the degradation of olefin-containing pyDOM structures in soil/sedimentary environmental matrices (i.e. "dark" environments) or areas rich in ROS (such as the Fe-rich blackwater swamps, Chen et al., 2014), which would contradict with the assumed persistence of pyOM in dark environments. Finally, olefins can undergo electrocyclic condensation reactions such as the Diels-Alder reaction, and it has been shown in Chapter II that such reactions can form non-pyrogenic ConAC in the environment. This has important implications to the sourcing of ConAC and the use of BPCAs to quantify pyOM in the environment. My observations here show that olefinic moieties of pyDOM are potentially

important to the biogeochemistry of pyOM, and natural organic matter in general, and therefore should be thoroughly evaluated in future studies.

The TOCSY data (Figures 10 and 11) demonstrate that cellulose was removed at lower temperatures (below 250 ^{O}C) while lignin was present in the leachates of oak chars of up to 400 ^{O}C. This is in agreement with solid-state ^{13}C NMR and FT-ICR-MS data for these biochars reported previously by Wozniak et al. (2020). Several LMW compounds such as isopropanol, propionate, acetate, acetone, methanol, and ammonia, were also observed and showed non-linearly changing abundances (Figure 12). This suggests that different radical processes occur in the different leachates upon photo-degradation. The NMR data also allow for the identification of methoxy (-OCH$_3$) residues in all pyDOM leachates, as well as a photo-produced ethyl (-CH$_2$CH$_3$) residue in Oak 525 pyDOM revealing some of the structural motifs of pyDOM and its photo-products.

The FT-ICR-MS data for the Oak Biomass leachate (Figures 13 and 14) and TOCSY data (Figures 10 and 11) indicate that the water-soluble oak wood organic matter contains mostly ligninaceous and cellulosic molecules, as observed previously for this leachate (Wozniak et al., 2020). Similar observations were also made using the water-soluble organic matter from white oak after FT-ICR-MS analysis (He et al., 2019). After photo-irradiation, this leachate lost 1292 formulas (39%) uniformly throughout the vK space (Figure 13), which contrasts with previous oxidative studies of lignin that observed high degrees of molecular alteration (Chen et al., 2014; Waggoner et al., 2015, 2017; Waggoner and Hatcher, 2017). The ^{1}H NMR data provide an explanation for this unexpected result (Figure 20). It is evident that the fresh leachate contained a significant amount of acetone (C$\underline{H}_3$-CO-C$\underline{H}_3$, δ = 2.21 ppm, singlet, 35% spectral magnitude), which is a known radical scavenger (Liu et al., 2015). After photo-exposure, the spectral magnitude attributed to this compound represented only ~1% of the total spectral intensity. The monolignol aromatic rings of lignin are not highly absorptive of the employed radiation (295 – 365 nm, λ$_{MAX}$ = 340 nm), therefore, it is expected that most of the changes in this sample would have happened through radical-mediated reactions. Thus, it is likely that ROS were quenched by the presence of acetone, and more substantial changes in composition that were observed in previous studies (Chen et al., 2014; Waggoner et al., 2015, 2017; Waggoner and Hatcher, 2017) would have occurred

after a longer photo-exposure of Oak Biomass and complete depletion of the present radical-quenching species. It is likely that its photo-labile compounds were mostly photo-mineralized, converted to compounds undetectable by ESI-FT-ICR-MS (as indicated by the low number of photo-produced compounds – 274 formulas, Figure 13), or converted to already existing (photo-resistant) compounds. The ^{1}H NMR data (Figure 20) also showed the formation of a large quantity of methanol (C$\underline{H}_3$OH, δ = 3.34 ppm, singlet, 55% spectral intensity), which is indicative of demethoxylation (cleavage of methoxy groups, -OCH$_3$), a known process in the oxidative degradation of lignin (Crawford, 1981; Waggoner and Hatcher, 2017; Waggoner et al., 2017).
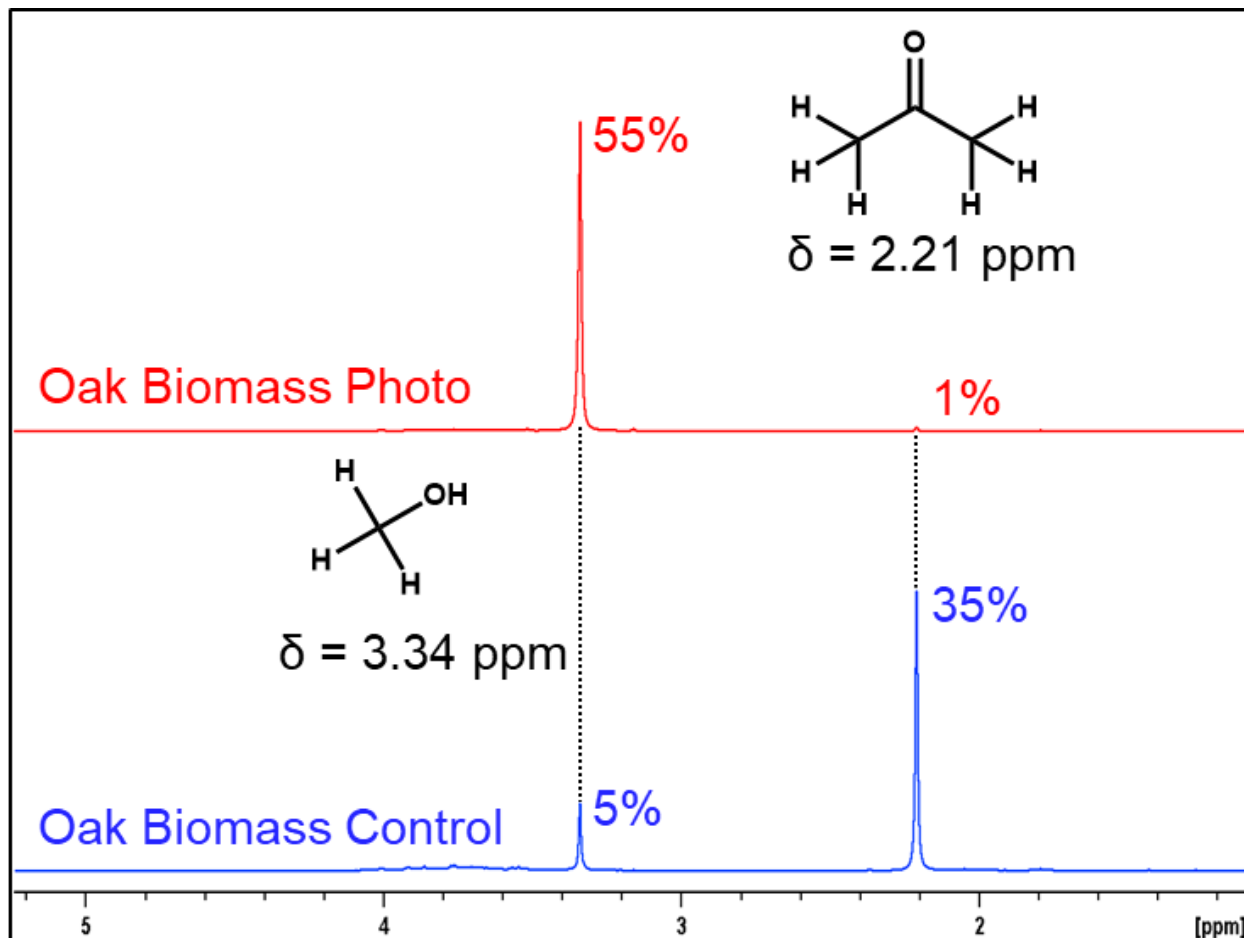
Figure 20. Production of methanol (δ = 3.34 ppm) and destruction of acetone (δ = 2.21 ppm) after photo-irradiation of Oak Biomass DOM as evident by 1D ^{1}H NMR.

The 2D NMR data (Figure 10) also support this finding of degradation by showing that aliphatic functionalities of this woody water-extract (a_6) were photo-degraded (as their spectral intensities decreased), and by the observation of a new cross-peak between aryl functionalities in the TOCSY data (Figure 11, peak group a_9). It is likely that the lost aliphatic resonances were associated with side-chains of lignin, and their disappearance after photo-irradiation also suggests side-chain cleavage and formation of LMW compounds. Another indication of an ROS-driven degradation in this sample is the decrease in carbohydrate functionalities. Sugars are not optically absorptive, therefore cannot be degraded by direct photolysis at UV-A wavelengths. However, studies have found that ROS species such as hydroxyl radicals are destructive to sugars (Moody, 1963; Morelli et al., 2003).

From this study, it is clear that 1) the examined oak wood DOM and pyDOM samples degrade very differently from each other and 2) the structural moieties of pyDOM exhibit different photo-lability that appears to be heavily controlled by the production temperature and parent feedstock. Bostick et al. (2020b) determined that ConAC concentration in each leachate, and the degree of condensation of ConAC, are the main factors controlling the photo-degradation of pyDOM. Both of these factors are directly related to the production temperature of the parent char (Schneider et al., 2010; Santín et al., 2016b; Bostick et al., 2018; Wozniak et al., 2020). Generally, with increasing thermal maturity, more aliphatic compounds and inorganic carbon (or volatile gasses) are produced at the expense of photo-labile ConAC (Bostick et al., 2020b). However, it is yet little understood how feedstock is related to the photo-degradation of pyDOM.

4.2. Photochemical degradation rate and the influence of parent feedstock

The photo-degradation trend of Grass 650 pyDOM was unexpected and reveals that the nature of the parent biomass used for biochar formation also has a significant impact on the photo-degradation of the leached pyDOM. Bostick et al. (2018) determined that both Oak 650 and Grass 650 contained similar quantities of ConAC (based on BPCA quantification), and ConAC were of similar degrees of condensation (based on the BACon

index). Thus, based on the findings of Bostick et al. (2020b) that ConAC concentration and degree of condensation are the main controls of the photo-degradation extent, pyDOM of both Oak 650 and Grass 650 should degrade in a similar manner. While ConAC (based on BPCA measurements) in Oak 650 and Grass 650 did degrade in similar quantities over the five-day experiment (Oak 650 = 94% loss vs. Grass 650 = 90% loss), their bulk pyDOM mineralized to much different extents (18% and 7% TOC loss, respectively), and multiple compositional differences after photo-degradation were observed between these samples. This suggests that there are other factors controlling the photochemistry of pyDOM affecting its photo-degradation rate.

Rates of chemical reactions (*v*) are dependent on many factors including the order of the reaction, concentration of reactants, temperature, solvent, and the presence of catalysts or inhibitors. Thus, the photo-degradation rate of pyDOM (*v*) can be expressed by the equation shown on Figure 21.

Figure 21. Generic expression of kinetic rate of photo-degradation of pyDOM.

This kinetic equation is highly generic but shows the influence of three major factors to the photo-degradation rate of pyDOM: 1) concentration of reactant(s), 2) rate constant (*k*), and 3) secondary sample matrix components such as catalysts (*cat*) and inhibitors (*inh*). As Bostick et al. (2020b) determined, the extent of degradation of pyDOM

is controlled by the concentration of ConAC in the original leachate, therefore the reaction is at least of first order, and the ConAC fraction is considered a primary reactant. However, as photo-irradiation of ConAC creates high fluxes of ROS (Fu et al., 2016; Li et al., 2019; Wang et al., 2020) and many of the photochemical processes of pyDOM involve radical-mediated reactions, it is possible that ROS participate as secondary reactants (R) and impact the reaction mechanism by increasing the reaction order. This would sequentially impact the rate of photo-degradation of pyDOM. Considering, however, that the concentrations of ROS in natural waters are at steady-state, and the photochemical reactions are typically of first order (Zepp, 1979; Blough and Zepp, 1995; Fasnacht and Blough, 2002; Goldstone et al., 2002; Pullin et al., 2004), it is possible that dilution during terrestrial-to-marine export will alter the photochemical kinetics in natural systems, and this must be considered in future photochemical studies of pyDOM.

The photochemical rate is also largely dependent on the rate constant (k), which is heavily dependent on structure of the reactant(s), as well as on how they interact. Structurally for ConAC, this parameter will be a function of the number of condensed rings, heteroatomic content (N, S, Cl), and presence/absence of functional groups (aldehyde, quinone, carboxyl groups, etc.). For the samples of this study, Bostick et al. (2020b) determined, based on their measured BACon index, that the degree of condensation of ConAC also influences the extent of photo-degradation.

The third factor that is likely to explain the vast difference between the extents of degradation of Oak 650 pyDOM and Grass 650 pyDOM is the presence of substances that can catalyze (*cat*) or inhibit (*inh*) the reaction rate. It is possible that the isopropanol and propionate that are identified in Grass 650 pyDOM using TOCSY NMR (Figure 10) act as photo-degradation inhibitors by scavenging ROS (Watts et al., 2017) and consequently slow its photo-degradation rate. Conversely, it is also possible that the oak char leachates contain a photo-accelerant, such as iron species, as previously found in wood ash (Etiégni and Campbell, 1991). Silicates can also act as photo-accelerants (Badr et al., 2008), and such species have been also previously measured in a biochar made of bamboo shavings (Fu et al., 2016).

The effect of matrix constituents must be important to the formation of pyOM and the consequent photochemistry of its pyDOM. The observation that Grass 650 pyDOM is

characterized with high abundance of apparent ligninaceous resonances and lignin-like molecules is unexpected, as lignin is thought to be highly thermo-labile above 400 $^{\circ}$C (Laird et al., 2008). No data is available to explain what is stabilizing the lignin and protecting it from the pyro-transformative reactions at high temperatures, but it is possible that it interacts with, for example, a mineral from the grass matrix, and is stabilized via chelation. It is also unknown if and how the non-aromatic component of pyDOM is involved in the photo-transformation of ConAC. These feedstock-induced differences in composition alter the photo-chemical degradation rates of its different constituents, as well as the degradation pathway. This is also suggested by the observation that methyl (-CH$_3$) groups in Oak 400 pyDOM are photo-produced while the same functionality is photo-degraded in a bamboo shavings char (400 $^{\circ}$C) leachate (Fu et al., 2016). As chars are produced in the environment from a variety of different feedstocks, the way their properties affect the chemistry of pyDOM must be evaluated and considered to account for the variability in photochemistry of pyDOM.

4.3. Proposed ConAC photo-degradation pathway

The trends in molecular composition identified using FT-ICR-MS show that ConAC in each pyDOM leachate degraded differently. By coupling the data from this chapter with studies of model pyrogenic compounds, PAHs, a master degradation pathway for ConAC in sunlit aquatic environments can be proposed (Figure 22) after adaptations and modifications from previous mechanistic studies (Zeng et al., 2000a,b; Fasnacht and Blough, 2003a,b; and references therein).
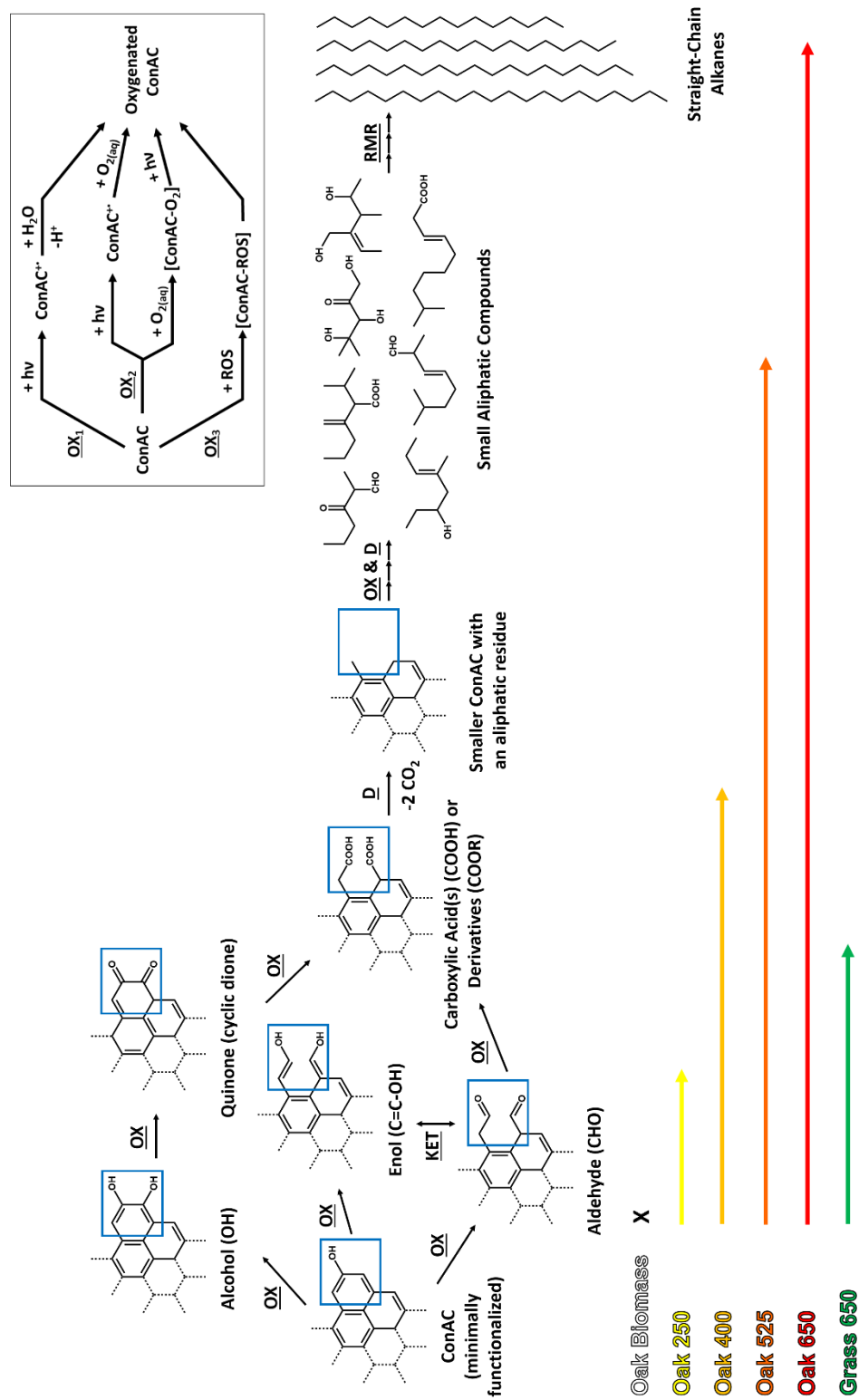
Figure 22. Proposed mechanism for ConAC photo-transformation adapted from Zeng et al. (2000a,b), Fasnacht and Blough (2003a,b), and references therein. The starting molecule is a generic structure for ConAC, and it can be of varied degree of condensation (as denoted by the dashed lines). Reactions are labeled as follows: OX = Oxygenation, KET = Keto-Enol Tautomerism, D = Decarboxylation, and RMR = Radical-Mediated Reactions. **Blue** boxes serve as visual references. The insert shows the three different oxygenation pathways (OX₁, OX₂, and OX₃). The colored arrows on the bottom correspond to a relative measure of the extent to which each leachate's ConAC are photo-transformed during the five-day photo-irradiation experiment.

Starting with freshly produced minimally functionalized ConAC (e.g., Wagner et al., 2017b), the first step is <u>oxygenation (OX)</u>. There are a number of proposed pathways in the PAH photo-degradation literature (e.g., Fasnacht and Blough, 2003b), and with regard to ConAC in the environment, there is no study to our knowledge that explores these in-depth. There are three main mechanisms proposed previously: <u>OX$_1$: Direct photolysis</u>, in which ConAC are photo-excited (hv) and produce ConAC-cation radicals (ConAC$^{+\cdot}$), which extract hydroxyl groups (-OH) from water molecules (Sigman et al., 1991); <u>OX$_2$: Oxygen-mediated direct photolysis</u>, whereby upon excitation (hv), ConAC react with dissolved oxygen (O$_{2(aq)}$) to produce oxygenated ConAC (Sigman et al., 1998; Fasnacht and Blough, 2003a,b; Kahan and Donaldson, 2007); and <u>OX$_3$: Radical-mediated oxygenation</u>, in which ROS attack ConAC and oxygenate them with no involvement of light in the reaction (Neff, 1979; Psillakis et al., 2004). Hydroxyl radicals ($\cdot$OH) produced from ozone (Beltrán et al., 1998; Rivas et al., 2009) or Fenton chemistry (Laurent et al., 2012; Lemaire et al., 2013) are known to be highly effective in degrading ConAC. ConAC themselves are also known to produce a significant amount of ROS when irradiated (Fu et al., 2016; Li et al., 2019; Wang et al., 2020), but studies have suggested that steady-state concentrations of ROS species in most natural waters are too low to compete with light-induced mechanisms (Zepp, 1979; Blough and Zepp, 1995; Fasnacht and Blough, 2002; Goldstone et al., 2002; Pullin et al., 2004). The parallel study of these samples also showed that the photo-degradation of ConAC is mainly driven by their light absorptivity properties (Bostick et al., 2020b), therefore ConAC in sunlit environments are degraded through a direct photolysis mechanism (OX$_1$ or OX$_2$), as previously suggested by Stubbins et al. (2008). However, it must be noted that the radical-mediated oxygenation mechanism (OX$_3$) is certainly important for ConAC transformation/degradation in dark environments, such as peats, soils, sediments (Page et al., 2012, 2013; Tong et al., 2016; Trusiak et al., 2018), and in ROS-rich aquatic environments such as Fe-rich blackwater swamps (Chen et al., 2014). Data generated by this study suggest that ROS species are most important for the degradation of the non-aromatic component of pyDOM, as hypothesized by Bostick et al. (2020b). Besides photo-oxidizing ConAC already present in pyDOM and DOM, these oxidative pathways are also responsible for photo-oxidizing

unfunctionalized ConAC in solid pyOM to result in their photo-dissolution (Roebuck et al., 2017; Li et al., 2019).

The oxygenation step (OX) of ConAC yields functional groups such as alcohol (-OH), enol (C=C-OH), aldehyde (-CHO), quinone (cyclic diones) and carboxylic acids (-COOH) (e.g., Yu et al., 2006; Fu et al., 2016). Other oxygen-containing functionalities, such as ethers, carboxylic acid derivatives, or more exotic groups (such as acetals) are also possible, but not shown in Figure 22 for simplicity. Formation of O-containing functionalities also often involves disruption of the aromatic sp^2-structure of ConAC, resulting in formation of aldehydes/enols (e.g., Wischmann and Steinhart, 1997; Yu et al., 2006; Fu et al., 2016). Mechanistically, ring-opening can be induced by light (Pullen et al., 1998; Toteva and Richard, 2011; Arruda et al., 2013) or ROS (Stenson et al., 2003; Waggoner et al., 2015, 2017; Waggoner and Hatcher, 2017; and references therein). When enols are formed, they easily rearrange to aldehydes through keto-enol tautomerism (KET). Aldehydes and quinones are highly labile even to mild oxidants, thus are easily converted to carboxyl groups (e.g., Dalcanale and Montanari, 1986; Sato et al., 2000; Travis et al., 2003). From the proposed master pathway, it is clear that the manner in which oxygenation of ConAC occurs can be highly variable, yet it is poorly understood for ConAC in the environment. Based on the variety of potential oxygenation mechanisms and the multiple unknowns in the photochemistry of pyOM, further work should focus on a detailed evaluation of the photo-induced pyDOM oxygenation mechanisms and characterization of their products.

The end-products of ConAC oxygenation are carboxyl groups, which can also exist as their derivatives (amides, esters, lactones, etc.). The COOH group is typically cleaved and volatilized as inorganic carbon (CO_2). Decarboxylation (D) generally requires thermal exposure, but photochemical (e.g., Griesbeck et al., 1999; Li et al., 2011) and radical pathways (e.g., aqueous Barton decarboxylation, Mangin et al., 2015) at ambient conditions do exist. Thus, carboxyl-containing molecules can be decarboxylated, yielding CO_2 and an aliphatic residue (methyl in this instance). This cycle of oxidation and ring-cleavage can repeat multiple times until all aromatic rings are destroyed, and small aliphatic compounds are produced. Zeng et al. (2000a,b) confirmed this mass spectrometrically for the oxidation of pyrene and benzo[α]pyrene by observing similar

compounds being produced. These compounds were also enriched in nitrogen (Figure 19), suggesting that pyDOM photochemistry may produce aliphatic marine-like compounds (Benner et al., 1992; Sleighter and Hatcher, 2008; Hertkorn et al., 2013). Zeng et al. (2000a,b) also determined that these small aliphatic molecules can be further polymerized through <u>radical-mediated reactions (RMR)</u> to yield larger aliphatic structures, as other studies have also suggested (Matsumoto et al., 1996; Matsumoto et al., 1998; Yu et al., 2006; Waggoner et al., 2015). Ultimately, all oxygen-containing functionalities are removed, and all alkyl residues are converted to straight-chain alkanes. In the mechanism proposed by Zeng et al. (2000a,b) the ultimate products of ConAC oxidation are CO_2 and long-chain alkanes, both of which would disappear from the ESI-FT-ICR-MS analytical window.

The proposed mechanistic pathways are supported by the trends observed using the advanced analytical techniques employed in this study. The aromatic species in Oak 250 pyDOM were oxygenated but did not transform into highly aliphatic molecules as the aromatic species in Oak 525 and Oak 650 pyDOM did (Figure 13). This is because this leachate is not rich in ConAC, and its constituent molecules are of relatively low degree of condensation (as determined quantitatively by BPCA analysis, Bostick et al., 2018, 2020b). Because ConAC contents and degree of condensation mainly controlled the rate of photo-transformation, Oak 250 pyDOM photo-mineralized slowly, with a corresponding TOC loss of only 11% (Bostick et al., 2020b). The ConAC of Oak 250 would have likely required a longer photo-exposure to reach a higher degree of photo-transformation. The leachate of Oak 400, which had undergone greater thermal lignocellulosic transformation than that of Oak 250, was more photo-labile. Its degradation can be readily tracked through the time series experiment for this sample (Figures 16 and 17), supporting the proposed sequential oxidation and decarboxylation steps of this pathway. In Oak 525 pyDOM, the formation of aliphatic compounds is observed (shown in Figure 13) indicating that many more molecules in this sample have undergone ring-opening reactions, and within five days, have proceeded much further on the proposed pathway, as also observed by Ward et al. (2014) in pyDOM from a char of tealeaf willow-feather moss mixture made at 450 ^{O}C. I hypothesize that if the Oak 400 time series were extended

further, the ConAC of Oak 400 would have also reached the extent of photo-transformation of Oak 525 and Oak 650.

The photo-degradation of Oak 650 pyDOM is intriguing because not many new aliphatic formulas were photo-produced as in Oak 525 pyDOM (Oak 525 = 2145 (33%), Oak 650 = 476 (22%), Figure 13). Oak 525 also produced more alkyl and O-alkyl functionalities than Oak 650 (66% and 58% increase, respectively, Figure 8c). However, Oak 650 pyDOM has been quantitatively determined to be most susceptible to degradation, losing almost all of its ConAC (94% loss, Bostick et al., 2020b). This enhanced photo-lability can be explained by the fact that it had the greatest concentration and degree of condensation of ConAC in its fresh leachate (Bostick et al., 2018, 2020b). The last step of the pathway, conversion of small aliphatic compounds to linear alkanes, is proposed to be radical-mediated. Formation of alicyclic molecules is unlikely as there were no evident cross-peaks for these functionalities in the TOCSY spectra (Figure 10), and Zeng et al. (2000a,b) did not observe any cyclic alkanes using mass spectrometry. In the FT-ICR-MS data there are also no carboxyl-rich alicyclic molecules (CRAM) observed, which are substances common to marine DOM (Hertkorn et al., 2006). The presence of radicals is necessary for the polymerization to straight-chain alkanes that are hypothesized here, and ConAC photo-degradation is known to produce ROS (Fu et al., 2016; Li et al., 2019; Wang et al., 2020). It is likely that the photo-irradiation of Oak 650 produces a high flux of such radicals, which allows for the nearly complete removal of the small oxygenated intermediates resulting in the complete photo-transformation of its ConAC pool into alkanes. If this is the case, the long-chain alkane by-products would not be ionizable by the electrospray ionization source and would therefore be undetectable by the mass spectrometric analysis. While such sp^3-carbon-rich compounds are highly detectable by 1D and 2D NMR, it may be that, due to their hydrophobic character, these molecules clustered as colloids or particles and precipitated on the walls of the irradiation/storage vessels, and therefore were not detectable by the following NMR analyses. As there is no direct evidence presented for the formation of these alkanes in this study, alternatively, the small aliphatic molecules could have also been mineralized by ROS into gaseous species. Clearly, the degradation pathways of ConAC and pyDOM are not linear, and unfortunately, the conclusions here are based mainly on a "before and

after" approach that is unable to capture these non-linear transformations. While the Oak 400 time series experiment does support the proposed pathway, future photochemical work of pyDOM should include a high resolution time series, as well as a variety of auxiliary measurements (ROS, metals, LMW compounds, etc.) to fully decipher the seemingly complex photochemistry of pyDOM.

4.4. Implications of pyDOM structural photo-transformations to biogeochemical cycling of organic matter

ConAC and pyDOM photochemistry are important to global carbon cycling in many ways. The proposed oxidative pathways of ConAC (Figure 22) likely control photo-dissolution of pyOM, a process of high environmental significance thought to influence the leaching of pyOM in aquatic environments (Roebuck et al., 2017; Li et al., 2019). While large amounts of ConAC are annually exported by rivers to the global ocean, ConAC concentrations change during export, likely due to degradative processes during transport (Jaffé et al., 2013; Wang et al., 2016; Marques et al., 2017; Coppola et al., 2019; Jones et al., 2020). It has also been determined that rivers export highly aromatic and young (<500 ^{14}C years old) dissolved ConAC to the marine environment (Ziolkowski and Druffel, 2010; Wang et al., 2016; Coppola et al., 2019). Open ocean DOM samples were found to contain less aromatic and very old ConAC (~18,000 ^{14}C years), which is explained by preferential photo-degradation of the high molecular weight ConAC, preserving the LMW ConAC (Santschi et al., 1995; Ziolkowski and Druffel, 2010). Another more recent study evaluating δ^{13}C signatures of ConAC in global rivers and the open ocean also suggests that photo-degradative processes during export can be significant to the cycling of and source-identification of ConAC in the environment (Wagner et al., 2019a). Additionally, using a conservative mass balance approach, Bostick et al. (2018) estimated that over 86% of the leached pyDOM may be lost in transit, with ConAC photo-degradation being one of the main suspected reasons. The study presented in this Chapter, among others in the published literature, show that photochemistry has indeed a significant impact on the quality and quantity of pyDOM in the biogeochemical cycles.

Determining the structural changes associated with pyDOM photochemistry is important for better understanding the reactions occurring in natural systems. For example, the comparison between Oak 650 pyDOM and Grass 650 pyDOM photo-degradation clearly indicates that the kinetics of degradation for these two samples are different, and evaluating the structural changes may be a key for determining how these two types of pyDOM differ. The abundance of different matrix components (e.g., Fe^{3+}, NO_3^-) and structural moieties (e.g., heterocyclic N) may also affect photochemical kinetics, which in turn will have implications to cycling of organic matter in sunlit environments. These differences in pyDOM types may also explain some contradicting interpretations in the literature. For example, Stubbins et al. (2012) suggested that ConAC mainly photo-mineralize to CO and CO_2, while Ward et al. (2014) argued that ConAC mainly photo-transform to small aliphatic molecules. These two studies have utilized completely different types of samples (ConAC from the deep ocean versus ConAC from a biochar leachate, respectively), have slightly different photo-irradiation apparatuses, and utilized different analytical techniques. Thus, while the discrepancy in their conclusions may be due to the different analytical windows of the utilized analyses, as Ward et al. (2014) suggests, it is also likely that the relative degree of photo-transformation versus photo-mineralization also varies for ConAC in different samples.

This study also brings new pieces of information to the long-running effort to explain the changes land-derived DOM occurring to terrestrial DOM during terrestrial-to-marine export, and the sourcing and chemistry of marine DOM (Hedges et al., 1997). The proposed pathway for photochemical degradation of ConAC (Figure 22) suggests that, once solubilized, and if exposed to light for sufficient amounts of time, ConAC degrade to small aliphatic structures, which have the potential to be polymerized to larger long-chain alkanes. These small aliphatic compounds are mainly observed in the pyDOM of Oak 525 and Oak 650 after photo-irradiation (Figure 13), and poor in number of unsaturations (Figure 18), and rich in nitrogen (Figure 19). These characteristics are common for marine DOM (Benner et al., 1992; Sleighter and Hatcher, 2008; Hertkorn et al., 2013), thus, it appears that photo-degradation shifts pyDOM to a marine-like molecular composition, and pyDOM photo-degradation products may be mislabeled as being derived from marine sources. Such an observation was made by Rossel et al. (2013) who compared the

molecular composition of deep ocean DOM to a photo- and microbially degraded leachate of a vascular plant and found a high degree of similarity. While terrestrial and marine DOM can be distinguished by their $\delta^{13}C$-signatures (Raymond and Bauer, 2001), it is known that photochemical and biotic transformation of DOM can alter the molecules' isotopic composition (Macko and Estep, 1984; Vähätalo and Wetzel, 2008). Thus, it is unknown if pyDOM photo-products and marine-derived DOM can be separated without further advancements in the development of specialized pyDOM-specific molecular markers. The convergence of pyDOM photochemistry with the numerous other sources of organic matter into the aquatic environment is likely a contributing reason to the high isomeric complexity of natural DOM (Hertkorn et al., 2007).

The last step of the proposed pathway, formation of long-chain alkanes, has not been previously observed in the environment. It has only been reported in laboratory studies in sterile conditions (Zeng et al., 2000a,b). The photo-produced small aliphatic molecules are of composition that would render them to be bio-labile (Spencer et al., 2015) and they will likely be consumed by biota as a food source. Thus, I hypothesize that the formation of the long-chain alkanes through radical-mediated reactions is likely to happen only in sterile laboratory experiments. In the environment, it is likely that the small aliphatic compounds produced towards the last stage of photo-degradation (Figure 22) are rapidly consumed by biota as a food source to produce marine DOM. Thus, pyDOM photo-degradation products may be important to riverine and marine food webs. This would be another observation of a photo-enhanced bio-lability, a well-studied phenomenon for DOM (Kieber et al., 1989; Lindell et al., 1995; Wetzel et al., 1995; Benner and Biddanda, 1998; Moran and Covert, 2003; Qualls and Richardson, 2003; Obernosterer and Benner, 2004; Abboudi et al., 2008; Chen and Jaffé, 2014; Antony et al., 2018) that has been proposed previously for pyDOM (Wagner and Jaffé, 2015). Thus, future work involving biotic incubations should be done to evaluate the biotic fate of pyDOM and its photo-degradation products.

5. CONCLUSIONS

This study examined the molecular composition and the photochemical changes of leachates from chars produced at different temperatures and from different parent biomass types. Using ^{1}H NMR, it was shown that aryl and olefinic functionalities of pyDOM were photo-labile, and alkyl and O-alkyl functionalities were photo-produced. The extent of degradation was controlled by the production temperature and parent feedstock of the parent chars. The photo-degradation of ConAC from the different leachates proceeded to different stages, which allowed for the development of a photo-transformation pathway for ConAC. The rate of photo-degradation was attributed to differences in starting ConAC concentrations in the leachates, as well as to the degree of condensation of ConAC. This study also found that the presence of one or more matrix components that catalyze/inhibit the rate of photo-transformation is another factor for consideration.

As ConAC are produced at a variety of temperatures and feedstocks in the environment, natural pyDOM will be of a highly variable composition. However, the proposed pathway here suggests if this variable pyDOM is subjected to photo-irradiation, ConAC are oxygenated, decarboxylated, and marine-like smaller aliphatic N-rich molecules are produced. In sterile laboratory conditions these molecules can be polymerized by ROS to a pool of long-chain alkanes, however in aquatic systems the small aliphatic molecules may be biotically labile and be metabolized by heterotrophs. Thus, pyDOM photochemistry may turn out to be a significant food source for biota that supports the production of marine DOM.

CHAPTER IV

LABILIZATION AND DIVERSIFICATION OF PYROGENIC DISSOLVED ORGANIC MATTER BY MICROBES

PREFACE

The data included in this chapter have been published in the data repository *Mendeley* (citation below).

Goranov, A.I., Wozniak, A.S., Bostick, K.W., Zimmerman, A.R., Mitra, S. and Hatcher, P.G. (2020) Labilization and diversification of pyrogenic dissolved organic matter by microbes. *Mendeley Data*, V1, doi: 10.17632/kjkhy3tfys.1

1. INTRODUCTION

Pyrogenic organic matter (pyOM), the carbonaceous solid residue that is left after biomass burning (e.g., forest fires, biochar production), has been gaining attention in recent years as an important active component of the global biogeochemical cycles. Compositionally, pyOM is mainly comprised of condensed aromatic compounds (ConAC) of various degrees of condensation and functionalization (Masiello, 2004; Schneider et al., 2010; Wagner et al., 2018). These molecules have been found in various environmental matrices such as soils and sediments (Schmidt and Noack, 2000; Skjemstad et al., 2002; Reisser et al., 2016) and atmospheric aerosols (Wozniak et al.,

2008; Bao et al., 2017). In these environmental matrices, ConAC were originally thought to be exclusively stable ("recalcitrant") due to their highly condensed character (Goldberg, 1985; Masiello and Druffel, 1998). However, more and more studies report the presence of pyrogenic molecules in different aquatic environments (Hockaday et al., 2006; Dittmar and Paeng, 2009; Roebuck et al., 2017; Wagner et al., 2017; Li et al., 2019). These studies support the estimates that riverine systems annually export large amounts of pyrogenic dissolved organic matter (pyDOM) to the global ocean (Dittmar et al., 2012; Jaffé et al., 2013; Wang et al., 2016; Marques et al., 2017; Jones et al., 2020). During export, pyDOM is likely altered by various processes resulting in degradation and alteration of its physico-chemical characteristics (Masiello, 2004; Coppola et al., 2019; Wagner et al., 2019). Using laboratory-prepared chars and conservative assumptions, Bostick et al. (2018) approximated that 86% of the leached pyDOM is degradable (e.g., mineralizable to CO_2), which indicates that pyDOM is a very active component within the global carbon cycle, as previously suggested (Druffel, 2004; Lehmann, 2007; Riedel et al., 2016).

In sunlit aquatic environments, photo-degradation is the most significant sink for the ConAC fraction of pyDOM (Stubbins et al., 2012). The photochemistry of ConAC and pyDOM has been studied utilizing either laboratory-prepared pyDOM (Ward et al., 2014; Fu et al., 2016; Li et al., 2019; Bostick et al., 2020b; Goranov et al., 2020; Wang et al., 2020) or ConAC-rich natural organic matter (Stubbins et al., 2010, 2012; Wagner and Jaffé, 2015). These studies have reported that ConAC are exceptionally photo-labile and they degrade through a series of oxygenation, ring-opening, and decarboxylation reactions leading to a pool of smaller aliphatic by-products. Additionally, pyDOM photochemistry has been associated with the production of high fluxes of reactive oxygen species (ROS), important transients involved in the photo-degradation of pyDOM (Fu et al., 2016; Li et al., 2019; Goranov et al., 2020; Wang et al., 2020). These studies have contributed to a better understanding of the biogeochemical cycling of pyDOM in the presence of sunlight in the environment. Microbial (biotic) pathways are another degradative pathway with high potential for altering and/or mineralizing pyDOM, but they are far less understood.

Biotic reworking of organic molecules is a key mechanism for producing the diverse molecular composition of natural organic matter (Lechtenfeld et al., 2015; Hach et al., 2020). Due to the highly condensed character of pyOM, it is often regarded as bio-recalcitrant, though several studies have shown that a fraction (about 0.5 to 10 %) is indeed bio-degradable (Kuzyakov et al., 2009, 2014; Zimmerman, 2010; Zimmerman et al., 2011). PyOM is mainly comprised of ConAC (Bostick et al., 2018; Wozniak et al., 2020), which contributes to its low bio-degradability (Zimmerman, 2010). By contrast, pyDOM is highly heterogeneous (Wozniak et al., 2020), and in addition to ConAC, it contains numerous low molecular weight (LMW) species (e.g., acetate, methanol, formate; Bostick et al., 2018; Goranov et al., 2020) as well as various pyrogenic aliphatic compounds and inorganic nutrients (Hockaday et al., 2007; Mukherjee and Zimmerman, 2013; Goranov et al., 2020; Wozniak et al., 2020). The very solubility of pyDOM is imparted by the greater abundance of polar functional groups, which would also allow for greater microbial accessibility. To date, there is no study that evaluates the molecular-scale bio-degradability of pyDOM. It is unknown whether and how (e.g., mechanistic pathways, kinetic rates) these different compound groups are bio-degraded.

Additionally, there are concerns that leachates of fire-derived substances may be toxic due to the presence aromatic molecules. It has been shown that cellulose- and pinewood-derived biochar water-extracts (pyDOM of laboratory-made charcoals) inhibit the growth of cyanobacteria while pyDOM of lignin-derived biochar has no inhibitory effects (Smith et al., 2016). The toxicity has been mainly attributed to polysubstituted phenols in the above-mentioned biochars. In natural systems, however, it is likely that other pyDOM components also play a role in controlling the bio-reactivity of pyDOM. An important very recent finding is that pyOM and pyDOM contain organochlorine compounds (both aliphatic and aromatic; Wozniak et al., 2020), which may enhance the toxicity of these pyrogenic substances. Thus, biotic incubations of pyDOM are needed to reveal if microbial growth can be sustained in a pyDOM/ConAC-rich environment.

To explore these questions, aqueous biochar leachates were incubated with a soil-derived microbial consortium and the compositional changes to pyDOM were evaluated using numerous analytical techniques. Laboratory-produced biochars can be considered model pyrogenic substances as they are similar to what is produced during forest fires in

the environment (Santín et al., 2017) but have not experienced environmental aging which impacts their physico-chemical properties (Ascough et al., 2011). Here, oak wood was used to produce biochars because most of riverine dissolved organic matter (DOM) is exported from forested catchments (Hedges et al., 1997). Pyrolysis was performed at two different temperatures (400 and 650 ^{O}C) representative of those in forest fires (Santín et al., 2015, 2016). As photochemistry has been shown to increase the bio-lability of various types of DOM (Kieber et al., 1989; Lindell et al., 1995; Wetzel et al., 1995; Benner and Biddanda, 1998; Moran and Covert, 2003; Qualls and Richardson, 2003; Obernosterer and Benner, 2004; Abboudi et al., 2008; Chen and Jaffé, 2014; Antony et al., 2018), pyDOM that had been photo-irradiated was also incubated with microbes. Previous studies of these pyDOM samples showed significant compositional and structural changes after photo-irradiation, which certainly implies different bio-reactivity (Bostick et al., 2020b; Goranov et al., 2020).

In a parallel study of the same samples (Bostick et al., 2020a), total organic carbon (TOC) loss and respired CO_2 were quantified, and the changes to the bulk structural composition was determined by one-dimensional ^{1}H nuclear magnetic resonance (NMR) spectroscopy. Additionally, in that study, benzenepolycarboxylic acids (BPCA) molecular markers were used to quantify the changes specific to the condensed (ConAC) fraction of pyDOM. It was found that pyDOM leachates derived from biochars of higher pyrolysis temperature (650 ^{O}C) were less bio-degradable than those from lower temperature (400 ^{O}C) leachates, and photo-irradiation increased the bio-lability of pyDOM. Over the 96-day incubation, up to 48% of the carbon was respired to CO_2 following first-order kinetics, with LMW compounds (e.g., acetate, formate, methanol) being preferentially degraded. To elucidate the molecular-level changes taking place during the bio-incubation of pyDOM, and probe the various molecules that are being degraded or produced by soil biota, these samples were examined using ultrahigh resolution mass spectrometry (Fourier transform – ion cyclotron resonance – mass spectrometry, FT-ICR-MS), two-dimensional NMR, and fluorescence spectroscopy. The collective results from these two studies improve the understanding of the degradative pathways of pyDOM and ConAC in the environment and allow for better interpretations pertaining to terrigenous-to-marine transfers and global cycling of organic matter.

2. MATERIALS AND METHODS

2.1. Preparation of pyDOM samples

Two biochars were prepared by heating laurel oak wood (*Quercus hemisphaerica*) under N_2 atmosphere at 400 and 650 $^{\circ}C$ for 3 hours. After grinding and sieving to particles of uniform size (0.25 - 2.00 mm), the chars were leached in 18.1 mΩ MilliQ laboratory-grade water (5 g in 500 mL) over 50 hours on a shaker table. The obtained pyDOM leachates, hereafter referred to as "Oak 400 Fresh" and "Oak 650 Fresh", were filtered using 0.2 μm Millipore GSWP mixed cellulose ester filters. Physico-chemical characteristics of similarly-produced solid chars and their leachates were reported in several previous studies (Zimmerman, 2010; Mukherjee et al., 2011; Bostick et al., 2018; Wozniak et al., 2020). A fraction of each leachate was also subjected to photo-irradiation for 5 days in a custom-made solar simulator equipped with Q-Lab Corporation UV-A lamps (295 – 365 nm, λ_{MAX} = 340 nm, 40 watt) equivalent to natural photo-irradiation of 12 days. Photo-transformation rates, structural changes, photo-irradiation apparatus design, and other relevant information has been published previously (Bostick et al., 2020b; Goranov et al., 2020). Photo-irradiated pyDOM samples will be hereafter referred to as "Oak 400 Photo" and "Oak 650 Photo". The four samples were diluted to a uniform TOC concentration of 4.7 mgC·L^{-1} prior to microbial incubations.

2.2. Incubation of pyDOM

Microbial incubations were performed using a soil-derived microbial consortium as an inoculum. Soil from the Austin Cary Memorial Forest (Gainesville, FL) was chosen, because this area is frequently subjected to prescribed burns (Johns, 2016), and its soil microbes likely interact with pyOM and pyDOM on a regular basis. Taxonomic details of its soil microbial characteristics have been published previously (Khodadad et al., 2011). The collected soil was treated to remove roots and detritus, and its water-extract was centrifuged to obtain a pellet. The pellet was then dissolved in 10 mL MilliQ laboratory-grade water to obtain an inoculate, 100 μL of which was used to spike 50 mL of each

pyDOM substrate. Additionally, microbial nutrients (KH_2PO_4 and $(NH_4)_2SO_4$) were provided following Zimmerman (2010) to support a healthy growth medium. Samples were incubated in gas-sealed amber vials on a shaker table at 28 ± 5 ^{O}C for 10 days in the dark. Using a double-needle assembly, CO_2-free air (Airgas, Zero Air) was flushed through the samples on days 0, 2, 5, and 10, which oxygenated the samples and removed dissolved inorganic carbon for its measurement, and is reported by Bostick et al. (2020a). A procedural blank and control samples were prepared in the exact same way but were poisoned with $HgCl_2$ immediately following the mixing of the different components (pyDOM, inoculate, nutrients). Additionally, a solution of sucrose (0.5 g $C_{12}H_{22}O_{11}$ in 40 mL MilliQ laboratory-grade water) was also incubated in the same manner. All incubated samples were poisoned with $HgCl_2$ to terminate microbial activity before shipment to Old Dominion University (Norfolk, VA) for spectroscopic and spectrometric analyses. Prior to spectroscopic analysis (see Section 2.3 below) or spectrometric analysis (see Section 2.4 below), samples were filtered using acid-washed 0.1 μm Teflon (PTFE) syringe filters. Further details about sample preparation can be found in the parallel study (Bostick et al., 2020a).

2.3. Analysis of chromophoric and fluorophoric dissolved organic matter

Chromophoric DOM (CDOM) measurements were performed on a Thermo Scientific Evolution 201 ultraviolet-visible (UV-VIS) spectrophotometer operated in a double-beam mode. A matched Starna quartz cuvette with MilliQ water was used as a reference during all spectral measurements. Spectra were recorded from 230 – 800 nm using a 1 nm step, 0.12 s integration time, and 500 nm/min scan speed. In addition to the double-beam referencing, the average noise in the 700-800 nm spectral region was subtracted from the spectra to correct for any instrument baseline drifts, temperature fluctuations, as well as scattering and refractive effects (Green and Blough, 1994; Helms et al., 2008). After consecutive procedural-blank corrections, the spectra (kept in decadic units) were normalized to the cuvette path length (1.0 cm) and the TOC content (in mgC·L$^-$^{1}) to convert them to specific absorbance (L·mgC^{-1}·cm^{-1}; Weishaar et al., 2003). CDOM

was quantified by integrating the spectra from 250 – 450 nm (Helms et al., 2008) and is reported in L·mgC^{-1}·cm^{-1}·nm units.

Fluorophoric DOM (FDOM) measurements were performed on a Shimadzu RF-6000 spectrofluorometer operated in 3D acquisition mode. Samples were analyzed without dilution as no sample yielded absorbance at 230 nm above 0.07 (Miller et al., 2010). Samples were excited from 230 – 500 nm (5 nm step) and emission was recorded over 250 – 650 nm (5 nm steps) to obtain excitation-emission matrices (EEMs). Additionally, five replicate water Raman scans were acquired on MilliQ water in 2D emission mode by exciting the sample at 350 nm and fluorescence intensity was monitored over 365 – 450 nm (0.5 nm steps). All measurements were done with 5 nm slit widths of the monochromators, 600 nm/min scan speed, and in high-sensitivity mode.

EEMs were processed in MATLAB using the drEEM toolbox (version 0.4.0.) using previously published routines (Murphy et al., 2010, 2013). Briefly, using the FDOMcorrrect.m function, the raw EEMs were adjusted for instrumental bias, blank-corrected using an EEM of the procedural blank, and scaled to adjust for any inner-filter effects using the raw UV-VIS spectra (Kothawala et al., 2013). This function also normalized the EEMs to Raman units (RU) after the area of the water Raman peak (peak maximum at 397 nm) had been determined by the ramanintegrationrange.m function (Murphy, 2011) on the averaged water Raman spectrum. The EEMs were then processed using the smootheem.m function to remove 1st and 2nd order Rayleigh signals and Raman scattering. EEMs are visualized and difference plots are generated using an in-house MATLAB script.

2.4. Fourier transform - ion cyclotron resonance - mass spectrometry (FT-ICR-MS)

Procedural blank, control, and incubated samples were loaded onto solid-phase extraction cartridges (Agilent Technologies Bond Elut PPL, 100 mg styrene divinyl copolymer) as previously described (Dittmar et al., 2008). Cartridges were eluted with methanol (Fisher Scientific, Optima LC-MS grade) and infused into an Apollo II electrospray ionization (ESI) source interfaced with a Bruker Daltonics Apex Qe FT-ICR-

MS operating at 10 T and housed in the College of Sciences Major Instrumentation Cluster (COSMIC) facility at Old Dominion University (Norfolk, VA). The instrument is externally calibrated daily with a polyethylene glycol standard, and a surrogate laboratory pyDOM standard was analyzed before and after pyDOM analyses to verify for the lack of instrumental drift. Additionally, an instrumental blank of methanol was analyzed between samples to verify for the absence of sample carryover. ESI spray voltages were optimized for each sample to assure for consistent spray currents among the samples. For each sample, 300 transients with a 4MWord time domain were collected, co-added, and the resultant free induction decay was zero-filled and sine-bell apodized. After fast Fourier transformation, internal calibration of the resultant mass spectra was performed using naturally abundant fatty acids, dicarboxylic acids, and compounds belonging to the CH_2-homologous series as previously described (Sleighter et al., 2008). Then, using an in-house MATLAB script, salt, blank, and isotopologue (^{13}C, ^{37}Cl) peaks were removed. Molecular formulas within ± 1 ppm error were assigned to FT-ICR-MS spectral peaks (S/N ≥ 3) using the Molecular Formula Calculator from the National High Magnetic Field Laboratory (Tallahassee, FL). Formula assignments were restricted to elemental composition of $^{12}C_{5-\infty}$, $^{1}H_{1-\infty}$, $^{14}N_{0-5}$, $^{16}O_{0-30}$, $^{32}S_{0-2}$, $^{31}P_{0-2}$, and $^{35}Cl_{0-4}$, and were refined using previously established rules (Stubbins et al., 2010). Any ambiguous peak assignments were refined by inclusion within homologous series (CH_2, H_2, COO, CH_2O, O_2, H_2O, NH_3, HCl) following Kujawinski and Behn (2006) and Koch et al. (2007). For all samples, at least 80% of the mass spectral peaks were assigned, and they accounted for at least 93% of the mass spectral magnitude. Molecular composition was evaluated by plotting the molecular formulas on van Krevelen (vK) diagrams, scatterplots of the formulas' hydrogen to carbon (H/C) versus oxygen to carbon (O/C) ratios (Van Krevelen, 1950; Kim et al., 2003). Formulas were further categorized using the modified aromaticity index (AI_{MOD}) as described previously in Section 2.6 of Chapter II. Additionally, N-containing formulas falling in the ranges of 1.5 ≤ H/C ≤ 2 and 0.1 ≤ O/C ≤ 0.67 were classified as peptide-like. Statistical evaluation using one-way analysis of variance (ANOVA) of means was performed in MATLAB using the "anova1" function. Post-hoc Scheffé's assessments were performed using the "multcompare" function in the same software. For the Kendrick Mass Defect (KMD) series analysis (described later in this Chapter), Kendrick Mass (KM)

was first calculated using the molecular weight of each compound (i.e., calculated mass from its molecular formula) following Eq. 5. Then, the Kendrick Nominal Mass (KNM) was calculated as the rounded integer (no decimals) of the Kendrick Mass (KM) as shown in Eq. 6. The Kendrick Nominal Mass (KMD) is the difference between KM and KNM, i.e., the decimals (Eq. 7). This analysis was performed for oxygen (O), carbonyl (CO), and carboxyl (COO) series.

$$\text{KM} = \text{Molecular Weight} \times \text{constant} \qquad\qquad \text{Eq. 5}$$

$$\text{constant} = \frac{15.9949146}{16.0000000} \text{ for O}; \quad \frac{27.9949146}{28.0000000} \text{ for CO}; \text{ and } \frac{43.9898292}{44.0000000} \text{ for COO series}$$

$$\text{KNM} = \text{integer of KM} \qquad\qquad \text{Eq. 6}$$

$$\text{KMD} = \text{KM} - \text{KNM} \qquad\qquad \text{Eq. 7}$$

2.5. Nuclear Magnetic Resonance (NMR) spectroscopy

One-dimensional ^{1}H NMR spectra of the samples of this project were published and evaluated in the parallel study (Bostick et al., 2020a). For the study reported in this Chapter, a select sample was analyzed using two-dimensional ^{1}H-^{1}H total correlation spectroscopy (TOCSY) to further evaluate several functional groups of interest. Analyses were performed on a 400 MHz (9.4 Tesla) Bruker BioSpin AVANCE III spectrometer fitted with a double-resonance broadband z-gradient inverse (BBI) probe in the COSMIC facility. Samples were analyzed without pre-concentration and volumetrically diluted with deuterated water (D_2O, Acros Organics, 100% D) to obtain a 90:10 H_2O:D_2O solution. To obtain ultraclean NMR spectra, NMR tubes were soaked with aqua regia, rinsed extensively with ultrapure water, and individually tested as blanks to verify that no background peaks are present. While ^{1}H spectra were originally processed using an exponential multiplication function (line broadening) of 5 Hz to obtain higher signal-to-noise for a more accurate and precise integration (Bostick et al., 2020a), here they were re-processed using a multiplication function of 1.5 Hz to better observe the splitting (multiplicity) patterns of the peaks of interest. TOCSY spectra were acquired using the

phase-sensitive gradient-enhanced mlevgpphw5 pulse program. It utilizes a 17-step Malcolm Levitt (MLEV-17) composite scheme (Bax and Davis, 1985) for magnetization transfer between any coupled nuclear spins, and a W5-WATERGATE element for water suppression (Liu et al., 1998). Both short-range and long-range spin-spin couplings were observed using 30 ms and 100 ms mixing times, respectively. The data were then zero-filled to a 4096 x 1024 matrix and then fitted with a π/2-shifted (SSB = 2) sine-squared window function. Linear prediction to 256 points was used in the F_1 dimension. All spectra were internally calibrated to the sharp distinguishable methanol singlet at 3.34 ppm (Gottlieb et al., 1997), and then were phased and baseline-corrected. T_1-noise removal was performed by calculating the positive projection of rows with no resonances and the summed projections were subtracted from all rows in the spectrum (Klevit, 1985). The same procedure was performed for all columns (F_2 dimension).

3. RESULTS

3.1. Molecular degradation of pyDOM

Ultrahigh resolution mass spectrometric analysis of the bio-incubated and corresponding control pyDOM leachates revealed significant changes in molecular composition after the 10-day incubation (Fig. 23). The identified molecular formulas for these samples were classified into one of three groups using a presence-absence approach (Stubbins et al., 2010; Sleighter et al., 2012). This approach identifies any common formulas among the two samples being compared (control and bio-incubated), as well as any formulas that are unique to each sample. It is important to note that the electrospray ionization (ESI) source is prone to biases, and the analytical window of FT-ICR-MS depends most critically on it. Thus, it may not identify compounds that are present if they are not ionizable (Stenson et al., 2002; Patriarca et al., 2020). Therefore, it is essential that observations by FT-ICR-MS are always paired with supplementary quantitative techniques (optical analyses, NMR, etc.) in order to determine if the identified trends are real or an artifact of ESI charge competition (D'Andrilli et al., 2020).
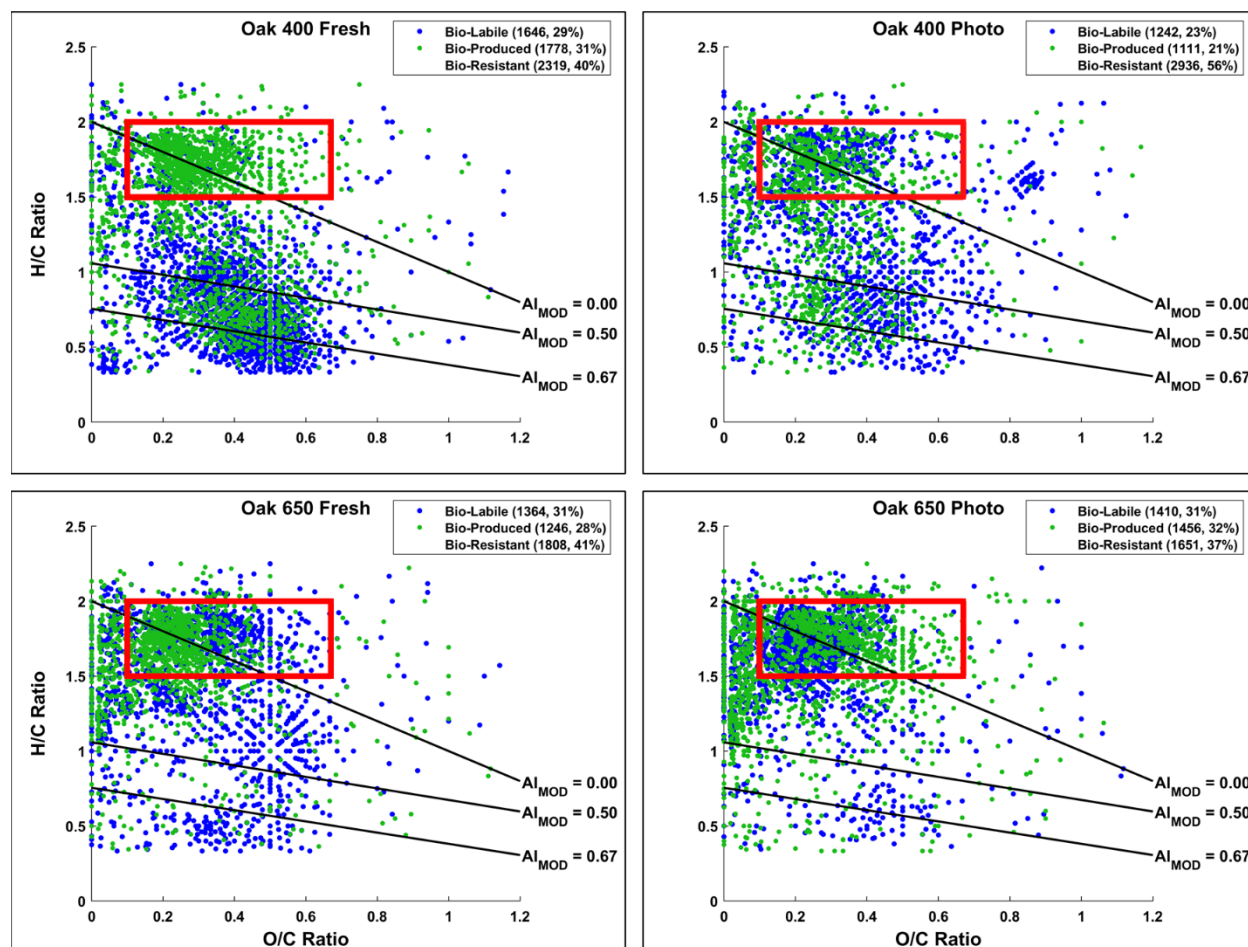
Figure 23. Van Krevelen (vK) diagrams of 10-day microbially incubated pyDOM leachates. Formulas are classified as **bio-labile** (molecular formulas only found in the "killed" control pyDOM leachates) and **bio-produced** (formulas that are only found in the bio-incubated samples). Formulas that are present in both the control and bio-incubated samples are operationally classified as bio-resistant and not shown for clarity. These three classes of molecules are separately plotted on vK diagrams and shown in Section 1 of Appendix C. The number of formulas found in each of these pools is listed in the legends along with corresponding percentages (relative to total number of formulas in the two samples being compared). The black lines indicate modified aromaticity index cutoffs (AI_{MOD}; Koch and Dittmar, 2006, 2016), and the red box indicates the peptide region (valid only for N-containing formulas).

In all samples, nearly a third of the formulas (23 – 31%) present in the control samples were not observed after the biotic incubations, which is proportional to the organic carbon losses observed by Bostick et al. (2020a). Interestingly, for all leachates the degraded ("bio-labile") molecules were not from a specific area of the vK diagrams but rather represent a broad range of H/C and O/C ratios and compound types (see Figure C1 in Appendix C). This variety of compound characteristics among bio-labile molecules suggests that the degradation pathway may not be from microbial consumption alone. It would be unlikely for the soil microorganisms to utilize organic matter compounds as food indiscriminately. Most interestingly, it is evident that large numbers of aromatic ($AI_{MOD} \geq$ 0.50) and some ConAC ($AI_{MOD} \geq 0.67$) formulas are lost, in agreement with observed losses in CDOM (Figure 24), as well as aryl functional groups (measured by ^{1}H NMR) and ConAC (measured by BPCA analysis) reported in the parallel study (Bostick et al., 2020a). Losses of specific compound classes, especially ConAC (due to their low ionizability) might be considered an artifact due to competition processes in the ESI source (Stenson et al., 2002; Patriarca et al., 2020). The agreement between FT-ICR-MS and other quantitative data (UV-VIS, NMR, TOC, BPCA), however, confirms the interpretation of degradation.
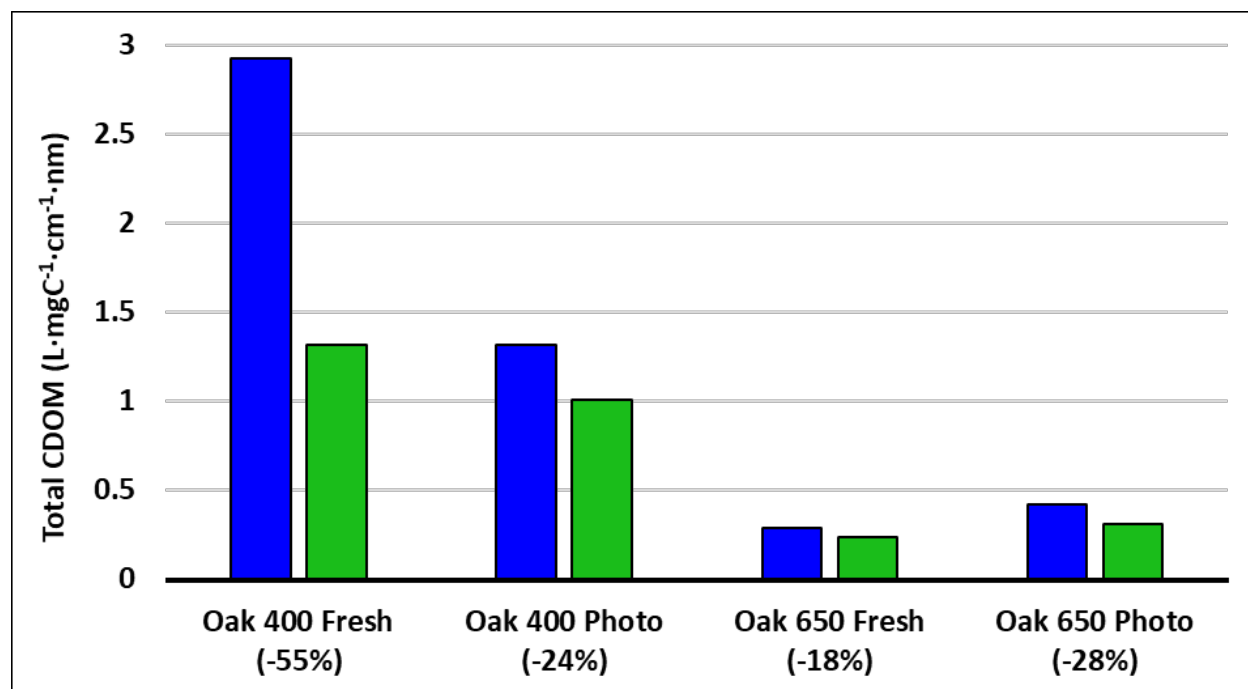
Figure 24. Total chromophoric dissolved organic matter (CDOM) content of pyDOM leachates before (**blue**) and after (**green**) 10-day biotic incubations. CDOM content is reported as the integrated carbon-normalized absorbance from 250 – 450 nm (Helms et al., 2008). The percent loss of CDOM for each leachate is shown as percentage under the label of each leachate.

Approximately half of the formulas (37 – 56%) in the original pyDOM leachates are classified, using the presence/absence approach, as bio-resistant (observed before and after biotic degradation). These formulas are located in all areas of the vK diagram (Figure C2 in Appendix C), showing variable oxygenation and aromaticity. Furthermore, the relative peak magnitudes of these formulas did not change significantly ($R^2 > 0.95$, Figure 25; Sleighter et al., 2012), suggesting that a wide variety of pyDOM molecules appear to be recalcitrant to microbial degradation. Using the available molecular data, it is not possible to attribute the observed recalcitrance to any molecular property. Therefore, it is likely that some of these molecules are still bio-labile and would have degraded in due time if the incubations were sampled at later time points. Longer biotic incubations should be conducted in future studies to fully differentiate between labile and recalcitrant pyDOM molecules.
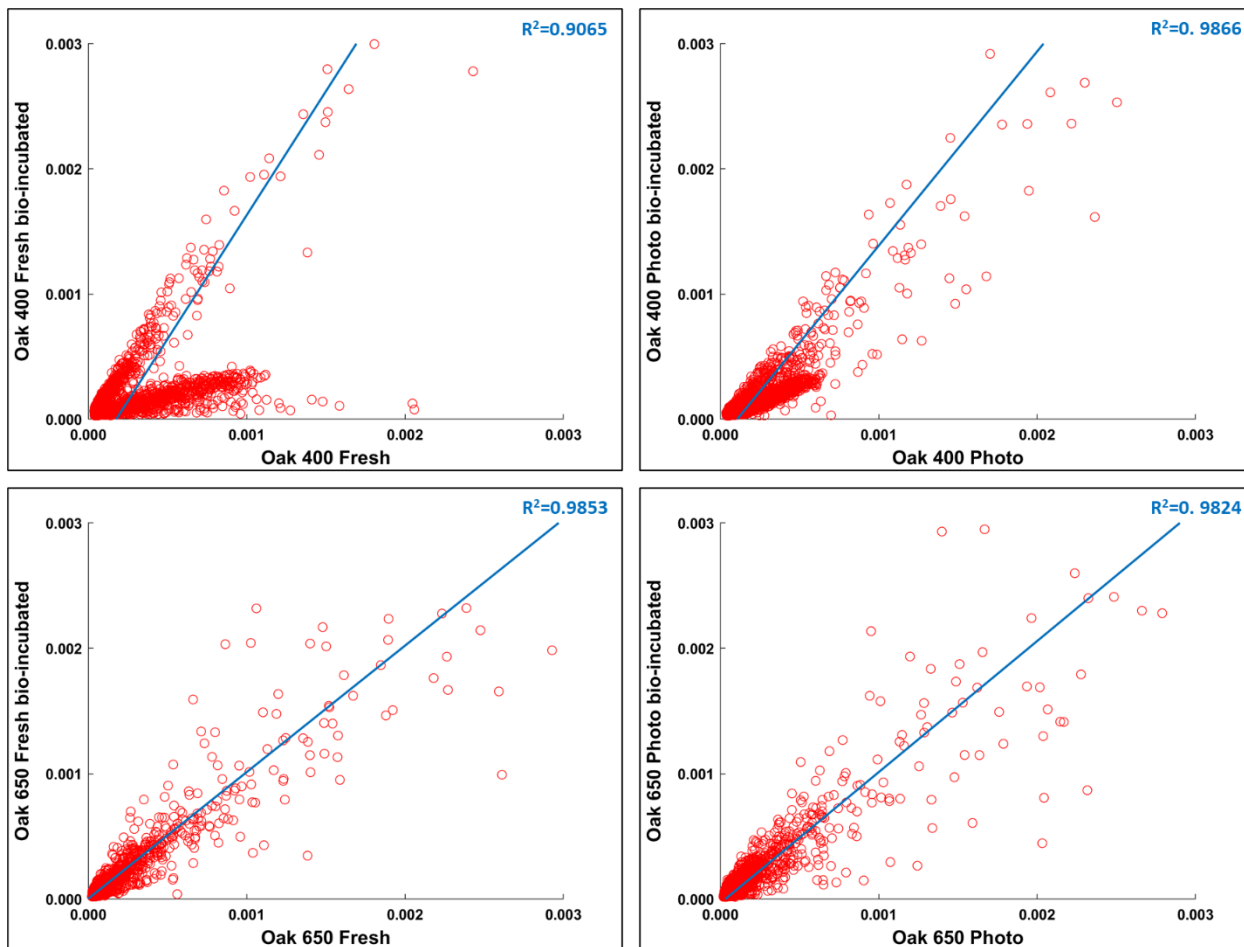
Figure 25. Abundance scatterplots of the bio-resistant formulas following Sleighter et al. (2012). This approach evaluates the similarity in relative abundance of each common formula among the control and its corresponding bio-incubated sample. A high R^2 value indicates a high similarity in the abundance of these formulas.

The use of hydrogen-to-carbon ratio (H/C) versus molecular weight (MW) plots has also been useful in interpreting ultrahigh resolution mass spectrometry data (e.g., (Gonsior et al., 2018; Powers et al., 2019; Valle et al., 2020), and such plots using the presence-absence approach are shown in Figure 26. These graphics help evaluate how different types of compounds (aliphatic vs aromatic) change relative to their MW.

For both Oak 400 leachates, it is clear that large aromatic molecules (H/C < 1.5, MW > 550 Da) are removed during the biotic degradation, and smaller (300 < MW < 550) aromatic compounds are produced. These aromatic molecules that are being degraded into smaller ones are mainly ligninaceous and not ConAC, in agreement with the BPCA data published by Bostick et al. (2020a). With regards to the aliphatic molecules (H/C > 1.5), it is clear that molecules of a wide range of sizes are removed and created during the incubation suggesting that molecular weight is not a critical factor in their bio-lability. This is in apparent disagreement with the general knowledge that microbes preferentially consume low molecular weight substrates (e.g., Søndergaard and Middelboe, 1995), which was also concluded for these samples by Bostick et al. (2020a). The consumption of large molecules indicates that microbes utilize extracellular enzymes to degrade them into smaller substrates (Billen et al., 1990) or secondary degradative pathways are also at play.
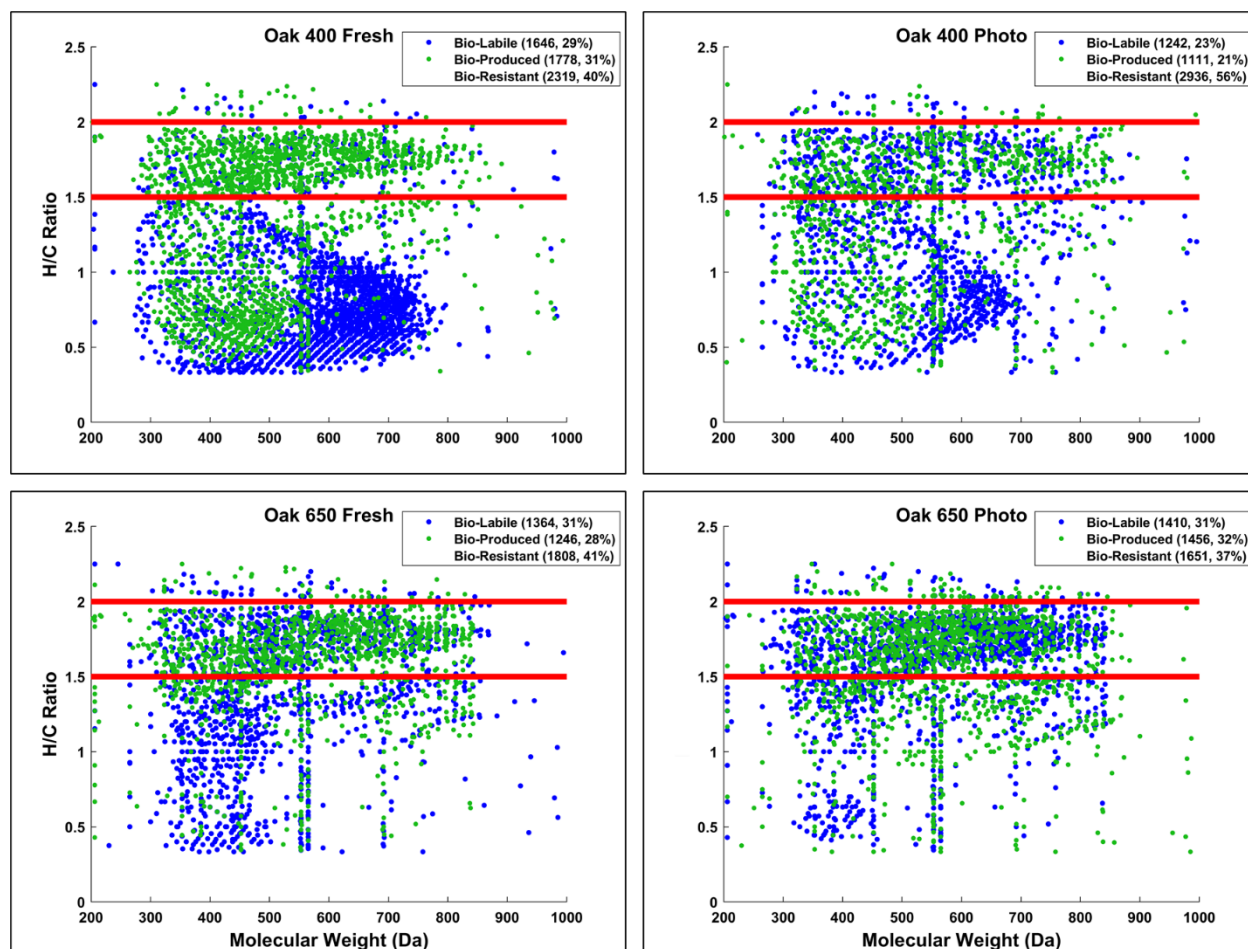
Figure 26. Hydrogen-to-carbon (H/C) ratio versus molecular weight plots of microbially incubated pyDOM leachates. Formulas are classified as **bio-labile** (molecular formulas only found in the "killed" control pyDOM leachates) and **bio-produced** (formulas that are only found in the bio-incubated samples). Formulas that are present in both the control and bio-incubated samples are operationally classified as bio-resistant and not shown for clarity. These classes are also individually plotted on Figures C4-6 in Appendix C. The number of formulas of each of these pools is shown in the legends (along with corresponding percentages). The red lines indicate where peptide-like formulas would plot.

3.2. Composition of bio-produced organic matter

The bio-produced organic compounds can be evaluated in various ways to examine the processes that may have occurred during the incubations. Using a presence/absence approach (Sleighter et al., 2012), the bio-produced formulas of each sample are compared with those of the other samples (Table 2). No significant overlap was found (2 – 320 formulas, 0 – 12%) among the molecules produced in the incubated pyDOM samples. Furthermore, no significant match was found between the bio-produced formulas of incubated pyDOM and those of the incubated sucrose control sample (63 – 94 formulas, 3%, Table 2). These observations indicate that the products of the incubations were either vastly different for each sample and may depend on the starting substrate or were further altered post-exudation to result in their diversification.

Table 2. Overlap of bio-produced molecular formulas among samples. The number of formulas corresponds to the formulas in common between the two samples being compared, and the percentage is relative to the total number of formulas in the two formula sets.

Sample	Oak 400 Fresh	Oak 400 Photo	Oak 650 Fresh	Oak 650 Photo
Oak 400 Fresh	-	-	-	-
Oak 400 Photo	320 (12%)	-	-	-
Oak 650 Fresh	126 (4%)	104 (5%)	-	-
Oak 650 Photo	165 (5%)	81 (3%)	2 (0%)	-
Sucrose	94 (3%)	63 (3%)	68 (3%)	83 (3%)

A significant fraction of the bio-produced organic matter was characterized as peptide-like (N-containing, $1.5 \leq H/C \leq 2.0$, $0.1 \leq O/C \leq 0.67$). This indicates that microbes convert a part of pyDOM into labile DOM (Moran et al., 2016; Vorobev et al., 2018), a process hereafter referred to as "microbial labilization". Given that the pyDOM samples used in this study were poor in organic nitrogen, the microbes must have used the inorganic nitrogen (NH_4^+) that was provided as a nutrient and converted some or all of it into microbial biomass. The peptide-like microbially-produced formulas comprise 23 – 40

% of the bio-produced formulas (Table 3), and the results of the comparative analyses described above also imply that these proteinaceous formulas are of highly variable composition.

The peptide-like formulas in the four samples were evaluated using one-way ANOVA to extract the variability in their composition. Averages of molecular parameters were derived from the formula lists – average number of elements (C, H, O, N), elemental ratios (O/C, H/C, N/C, H/N, O/N), molecular weight, double-bond equivalencies (DBE, DBE/C, DBE-O), modified aromaticity index (AI_{MOD}) and nominal oxidation state of carbon (NOSC). While the peptide-like formulas seem similar when plotted in the vK space (Figures 23 and Figure C3 in Appendix C), significant differences ($p < 0.05$) in the means of all molecular parameters were observed. When each metric was evaluated using ANOVA, there was at least one sample among the five being compared that had a significantly different mean. Using Scheffé's post-hoc test, it was observed that it was not the same sample that was statistically different each time, which indicated the vast diversity of bio-produced peptide-like molecules after these five incubations. The results from these statistical assessments support the findings by the presence/absence comparisons presented earlier (Table 2) and these findings collectively conclude that the microbial incubations of pyDOM created pools of new, very diverse molecules, a process hereafter referred to as "microbial diversification". As FT-ICR-MS was performed with soft electrospray ionization with no fragmentation, the structure of the observed molecules is inferred from the elemental composition of the assigned molecular formulas. Another possibility for these N-containing molecules is that they were formed by radical processes that coupled pyDOM molecules with the NH_4^+ nutrient that was added to support microbial growth. A preliminary experiment (data not shown) showed that mixing pyDOM with NH_4^+ did not result in abiotic formation of new molecules (for example via Michael addition; McKee et al., 2014), but abiotic formation was not tested in the presence of radicals.

To confirm that these formulas were associated with proteinaceous structures and are not just compounds that coincidentally plotted in the 'peptide region', spectrofluorometric analysis was performed to obtain excitation-emission matrices (EEMs) of the pyDOM samples before and after bio-incubation (Figure 27). The data for Oak 650 Photo is not reported as its EEM spectra were of questionable quality, and as

the sample was in limited amounts, analytical validation and quality assessment were not possible.

Table 3. Molecular metrics of peptide-like bio-produced formulas (N-containing, 1.5 ≤ H/C ≤ 2.0, 0.1 ≤ O/C ≤ 0.67) found in pyDOM samples after the 10-day incubation. The metrics below are reported as number-weighed mean ± standard deviation. The molecular metrics colored in **red** correspond to the means that were found to be significantly different ($p < 0.05$) from at least one of the other four means (evaluation done by ANOVA followed by Scheffé's post-hoc test).

	Oak 400 Fresh	Oak 400 Photo	Oak 650 Fresh	Oak 650 Photo	Sucrose
Number of bio-produced formulas	1778	1111	1246	1456	1339
Number of peptide-like bio-produced formulas	541 (30%)	261 (23%)	497 (40%)	314 (22%)	160 (12%)
Number of identified oligopeptides	14	5	11	18	2
C number	**28.5 ± 7.6**	30.9 ± 10.9	30.7 ± 7.6	30.3 ± 8.7	31.7 ± 9.6
H number	**49.8 ± 14.4**	54 ± 20.6	53.7 ± 14.8	54 ± 16.5	55.4 ± 18.5
O number	7.8 ± 2.6	7.8 ± 3.2	7.8 ± 2.9	**9.0 ± 2.8**	7.9 ± 3.1
N number	2.4 ± 1.1	**2.8 ± 1.3**	2.5 ± 1.2	2.4 ± 1.2	2.4 ± 1.3
O/C ratio	**0.28 ± 0.08**	0.26 ± 0.09	0.25 ± 0.08	**0.31 ± 0.10**	0.25 ± 0.08
H/C ratio	1.74 ± 0.12	1.74 ± 0.13	1.74 ± 0.13	**1.78 ± 0.16**	1.74 ± 0.14
N/C ratio	0.085 ± 0.037	**0.094 ± 0.045**	0.082 ± 0.038	0.083 ± 0.045	0.078 ± 0.042
H/N ratio	24.8 ± 11.4	23.5 ± 13.4	26 ± 13.2	**28.6 ± 16.7**	**29.4 ± 16**
O/N ratio	4.0 ± 2.2	**3.5 ± 2.2**	3.8 ± 2.5	**5.1 ± 3.5**	4.3 ± 2.7
MW[a]	**550 ± 140**	589 ± 188	582 ± 147	596 ± 143	597 ± 172
DBE[b]	5.81 ± 1.78	6.28 ± 2.17	6.13 ± 2.06	**5.51 ± 2.59**	6.2 ± 2.33
DBE/C[c]	0.211 ± 0.065	0.215 ± 0.071	0.206 ± 0.069	**0.189 ± 0.083**	0.203 ± 0.071
DBE-O[d]	-2.27 ± 2.75	-1.75 ± 3.52	-1.90 ± 3.55	**-3.82 ± 4.26**	-1.86 ± 3.65
AI_{MOD}[e]	0.077 ± 0.05	0.090 ± 0.052	0.083 ± 0.049	**0.089 ± 0.057**	**0.116 ± 0.049**
NOSC[f]	-0.929 ± 0.239	-0.933 ± 0.259	**-0.984 ± 0.227**	-0.903 ± 0.269	**-1.002 ± 0.218**

[a]Molecular Weight (Da); [b]Double-bond equivalency; [c]Carbon-normalized DBE; [d]Oxygen-corrected DBE; [e]Modified Aromaticity Index; [f]Nominal Oxidation State of Carbon
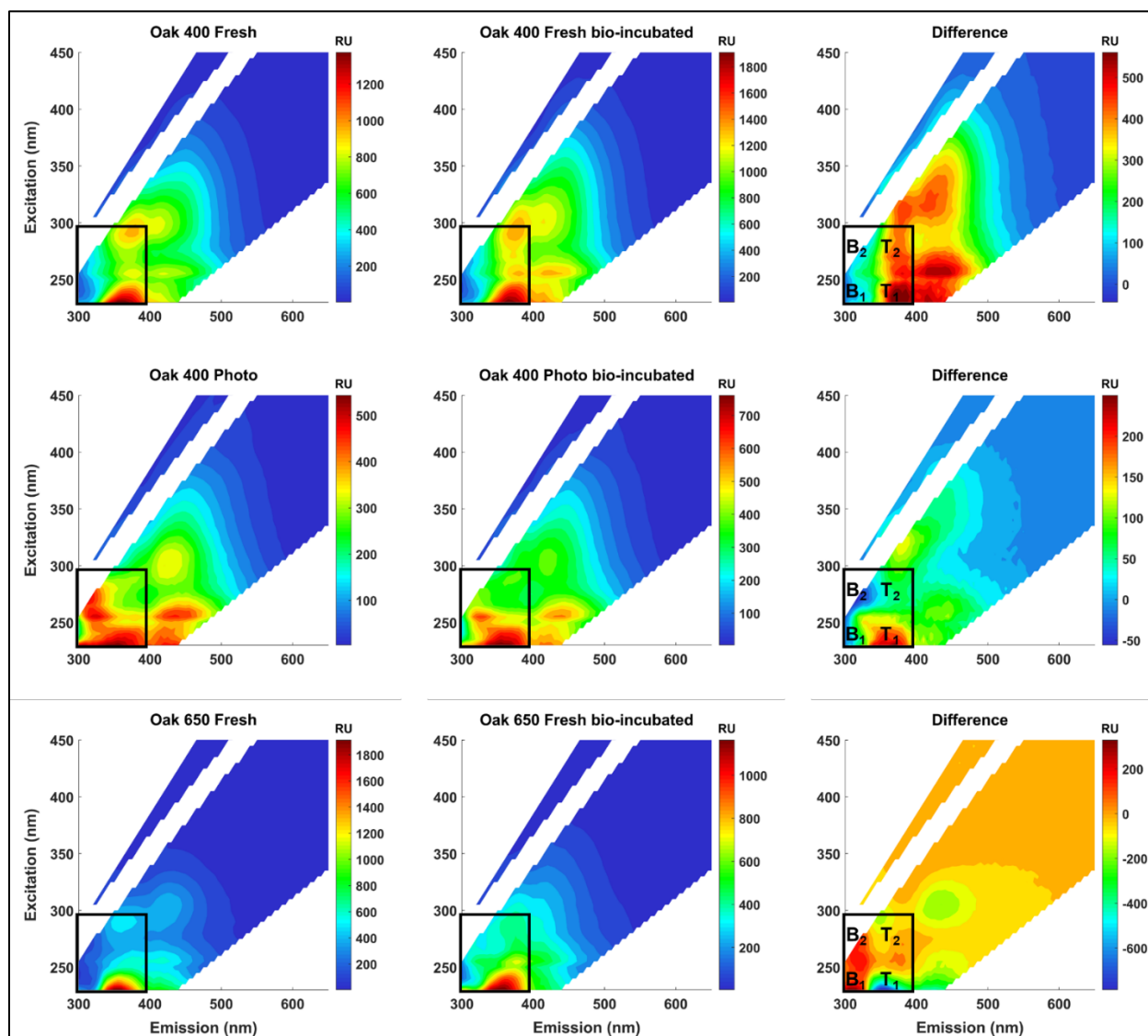
Figure 27. Fluorescence excitation-emission matrices (EEMs) of control (left panels) and bio-incubated (middle panels) pyDOM samples. Difference spectra are shown in the right panels. The black box indicates the region where compounds of proteinaceous and autochthonous/microbial origin fluoresce (Coble, 1996; Coble et al., 2014), with tyrosine-like (B_1 and B_2) and tryptophan-like (T_1 and T_2) peaks labeled on the difference plots (right panels).

Proteinaceous organic matter has a highly characteristic fluorophoric signature due to the distinguishable signals of the aromatic amino acids tyrosine and tryptophan. The short Stokes' shifts of these fluorophores allow them to spectroscopically separate on the EEM plot allowing for identification of related labile substances (Wünsch et al., 2019). Other amino acids, namely histidine and phenylalanine, are also fluorophoric, but are not easily identified in EEM data of complex matrices. A simplistic approach to evaluate the change after the bio-incubation is to use difference plots (e.g., Hemmler et al., 2019). For all samples, strong proteinaceous signals evolve after biotic incubations indicating that molecules of proteinaceous and autochthonous/microbial origin are produced (Coble, 1996; Coble et al., 2014). This indicated that peptide-like molecules observed using FT-ICR-MS are not an artifact due to charge competition in the source, but are truly bio-produced, validating the findings of the presence/absence analysis. There are subtle differences among the EEMs of all control and bio-incubated samples indicative of the high variability in fluorophoric content of these samples. This agrees with the observed variability in molecular composition described earlier. An interesting observation is that in the two Oak 400 pyDOM incubations, tyrosine-like fluorescence (peaks B_1 and B_2) decreases after biotic incubation while tryptophan fluorescence (peaks T_1 and T_2) increases. In contrast, the tryptophan-like fluorophores are degraded and tyrosine-like ones are produced after biotic incubation of Oak 650 Fresh pyDOM. It must be noted that there are proteinaceous fluorophores (and peptide-like formulas) in the control samples resulting from the addition of the microbial inoculate, but the associated fluorophores were present in low amounts. Thus, proteinaceous fluorescence signals in the control samples are not unexpected. However, a decrease in proteinaceous fluorophores is opposite of what is expected after significant microbial growth. Therefore, it is possibly due to fluorophoric compounds in this system being highly bio-labile and/or susceptible to oxidation by specific ROS, but the residual post-oxidation by-products would be still detectable by FT-ICR-MS and classified as peptide-like compounds. The loss of tyrosine-like fluorophores in the Oak 400 samples, and loss of tryptophan-like fluorophores in Oak 650 Fresh, are indicative of different microbial physiology and exudates in these incubations. The complexity of these EEM spectra and the compound-specific changes observed here indicate that proteomic and/or metabolomic analyses

(e.g., Nalven et al., 2020) are necessary in future microbiological studies of pyDOM in order to fully understand the changes in molecular composition during such incubations.

To determine if the bio-produced formulas are from true proteins, or are compounds with residual proteinaceous fluorophores, the formulas were evaluated in the context of possible combinations of amino acids that would be singly charged. Given that microbes exude large proteins (molecular weight > 30 kDa) such as lignin peroxidases, manganese peroxidases, and laccases (Higuchi, 2004), the peptide-like formulas observed by FT-ICR-MS (analytical window of 200-1000 Da) may have resulted from hydrolysis of the above-mentioned enzymes (or other proteinaceous exudates). If that is the case, the hydrolysates would likely have had a simple oligomeric composition. To test this, the bio-produced peptide-like formulas in each sample were compared to a library of 888,009 possible combinations of 20 amino acids (oligomeric sequences of 2-7 residues). Only a small number of oligopeptides were identified (5 – 18 oligopeptides of 2 – 5 amino acids, Tables 3 and C1 in Appendix C) which is counter to the proposed idea that hydrolysis of microbial exudates produced these newly observed peptide-like formulas. The lack of identified oligopeptides also calls into question the idea that microbial processes were solely responsible for the high variability of the bio-produced organic matter observed after the microbial incubation of pyDOM.

In an attempt to further elucidate the composition of these bio-produced N-containing substances, the previously published ^{1}H NMR data of these samples (Bostick et al., 2020a) were re-evaluated in greater detail. Additionally, to further elucidate the connectivity between observed functional groups, two-dimensional ^{1}H-^{1}H total correlation NMR spectroscopy (TOCSY) was utilized on a select sample. Figure 28 shows the TOCSY spectra of the bio-incubated Oak 650 Fresh sample.
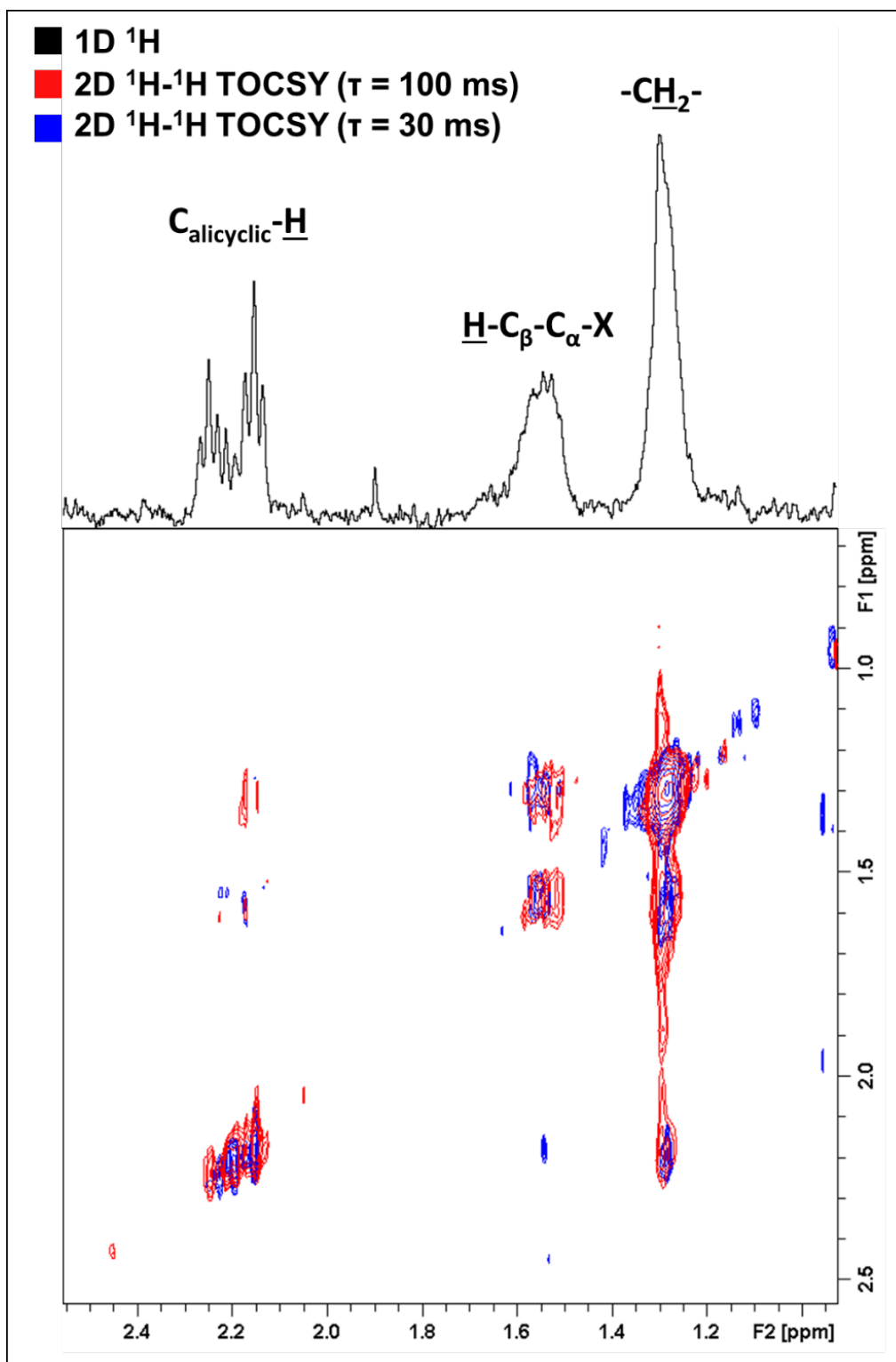
Figure 28. Two-dimensional ^{1}H-^{1}H total correlation spectroscopy (TOCSY) NMR spectra of the bio-incubated Oak 650 Fresh sample. Short- and long-range couplings were allowed to evolve during mixing times (τ) of 30 (**blue**) and 100 ms (**red**), respectively. The 1D ^{1}H spectrum is shown as a projection on top (**black**).

There are three groups of resonances that were found in all samples, even in the controls (although of small contributions relative to the total spectral signal). These resonances have not been previously observed in the ^{1}H NMR spectra of these pyDOM samples (Bostick et al., 2018; Goranov et al., 2020) indicating that they represent by-products of the microbial incubations, likely microbial biomass. In the control samples, the compounds associated with these resonances must be from the soil inoculant that was added. The three resonances are also observed to be in the same coupling network indicating that they are a part of the same or similar structures. Due to the very low concentration of these samples (3.5 – 4 $mgC \cdot L^{-1}$), the NMR analysis did not allow for a high-resolution structural elucidation, but some distinct signatures were nonetheless observed. The deshielded aliphatic peaks at δ = 2.1 – 2.3 ppm have a complex multiplicity pattern, a characteristic feature of alicyclic structures. These are likely residual carbohydrate moieties which have lost most of their O-containing groups through various cleavage processes and their backbone $C_{alicyclic}$-**H** resonances have been shifted upfield. The peak at 1.55 ppm is from β-hydrogens to a heteroatom (**H**-C_β-C_α-X, where X = O, N, S), and these are known to be associated with peptidoglycans (Spence et al., 2011). The TOCSY analysis was performed with two different mixing times (τ = 30 and τ = 100 ms) in order to evaluate short-range (2 – 3 bond) and long-range (4 – 6 bond) connectivities. Based on the observed couplings the observed resonances are vicinal to each other (3 bonds away). This indicates that these functional groups are closely bound in the peptidoglycan substances they likely represent.

All of these analyses of the molecules observed after the biotic incubation of the four pyDOM samples conclude that the observed biochemical processes in these systems are complex and difficult to unambiguously interpret. Based on the findings above it is clear that these formulas can originate from three different sources:

1) exoenzymes, which microbes use to extracellularly degrade larger molecules into smaller ones (Hyde and Wood, 1997; Higuchi, 2004);

2) peptidoglycans, which likely leached into solution after bacterial death and cell lysis (Yavitt and Fahey, 1984); and

3) other metabolites and exudates involved in the physiology of the different microbes in the used consortium (e.g., signaling compounds).

The significant degradation of pyDOM and production of these biological compounds indicates that microbes successfully converted the presumably carbon-rich recalcitrant pyrogenic molecules into more labile substances, a process hereafter refer to as "microbial labilization". However, the fact that the observed bio-produced labile molecules are not identifiable as simple oligopeptides, and are present in significantly different composition among the four samples, suggests that this molecular diversity may not be caused by predictable biotic reactions but by random radical-driven processes. Further evidence for the random radical-driven processes comes from the observed degradation of molecules across the whole vK space (Figures 23 and C1 in Appendix C), which is unusual because microbes generally preferentially consume smaller aliphatic species (Berggren et al., 2010a,b; Kirchman, 2018).

3.3. Radical Oxygenation as a potential source of molecular diversity

Microbial physiology has been associated with the production of reactive oxygen species (ROS), which have been shown to be important in the degradation of various types of organic compounds (e.g., Scully et al., 2003; McNally et al., 2005; Porcal et al., 2013; Trusiak et al., 2018; Xiao et al., 2020). A recent study showed that radicals can degrade various types of ligninaceous molecules (Waggoner et al., 2017) suggesting that microbially induced radical reactions can target a variety of pyDOM molecules. While there were no ROS measurements made in this study, Kendrick Mass Defect (KMD) analysis of the FT-ICR-MS data (Kendrick, 1963; Hughey et al., 2001) was performed to seek evidence for radical action. The KMD analysis identifies formulas that differ by any repeating structural moiety (e.g., $-CH_2-$). To identify potential products of radical attack, the FT-ICR-MS data was evaluated in the context of oxygenation, i.e., the mass lists were searched for formulas differing by one oxygen atom (addition of hydroxyl group), carbonyl group (addition of aldehydes or ketones), and carboxyl groups (Figure 29).
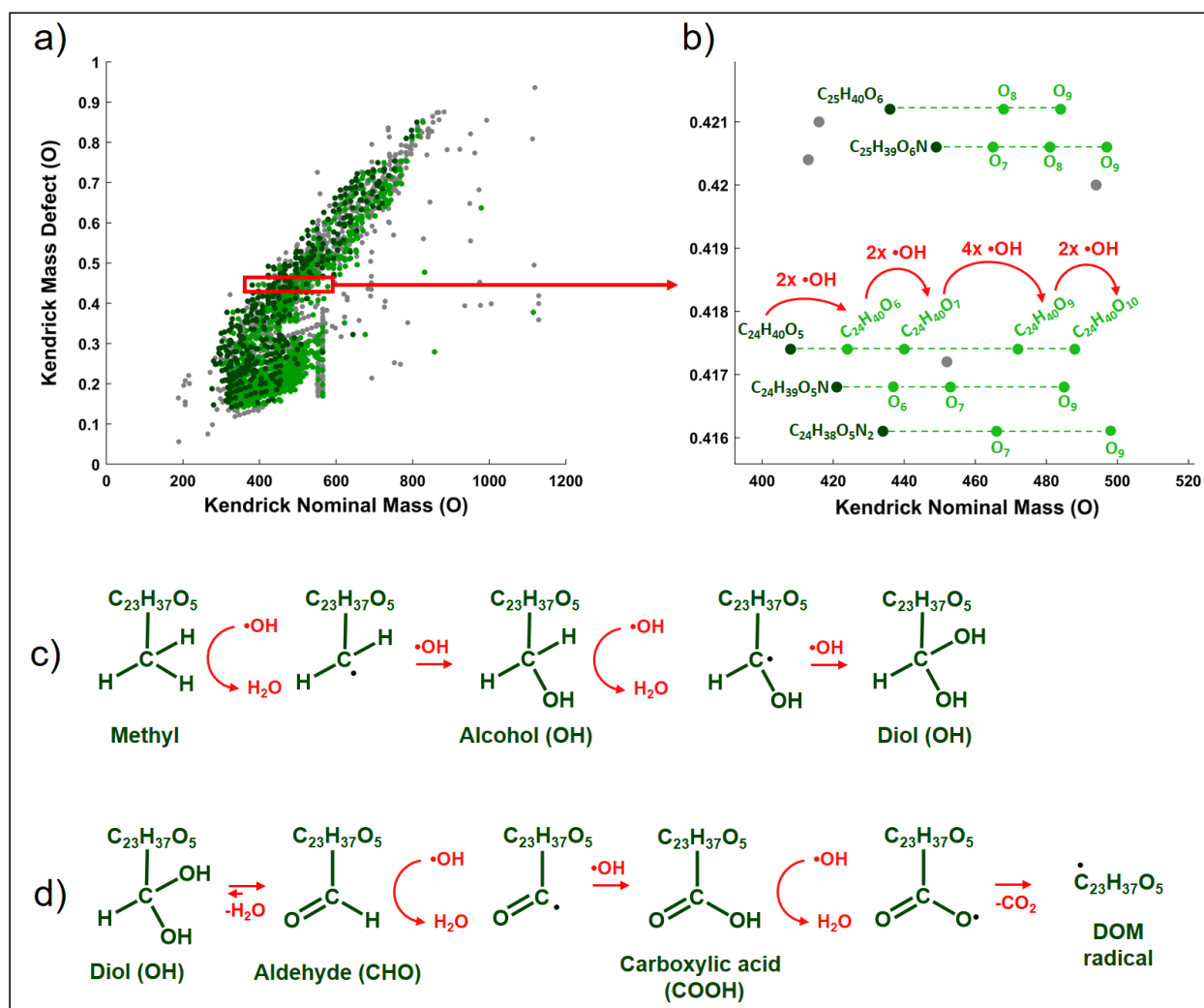
Figure 29. Kendrick Mass Defect (KMD) analysis using oxygen (O) series of the bio-produced formulas of Oak 400 Fresh pyDOM. Panel a) shows the whole KMD plot while panel b) shows an expanded region of it. Formulas not part of the O KMD series are colored in **gray**. Formulas in **dark green** are proposed substrates, and their oxygenation products are colored in **light green**. Only the molecular formulas for one of the series (KMD = 0.4174 Da) are labeled on panel b), while for the rest of the molecules, only the substrate formula and the number of oxygens in the oxygenation products are listed for clarity. The red arrows in panel b) show the formation of the four oxygenation products of the $C_{24}H_{40}O_5$ substrate after a sequential attack by hydroxyl radicals (•OH). Panel c) shows possible chemical reactions that can cause an increase of number of oxygens. Panel d) shows further oxidative processes involving the formation of keto and carboxyl groups which can contribute to the degradation of pyDOM, as well as to the formation of DOM radicals. The KMD plots for the O series are shown on Figure 30 below.
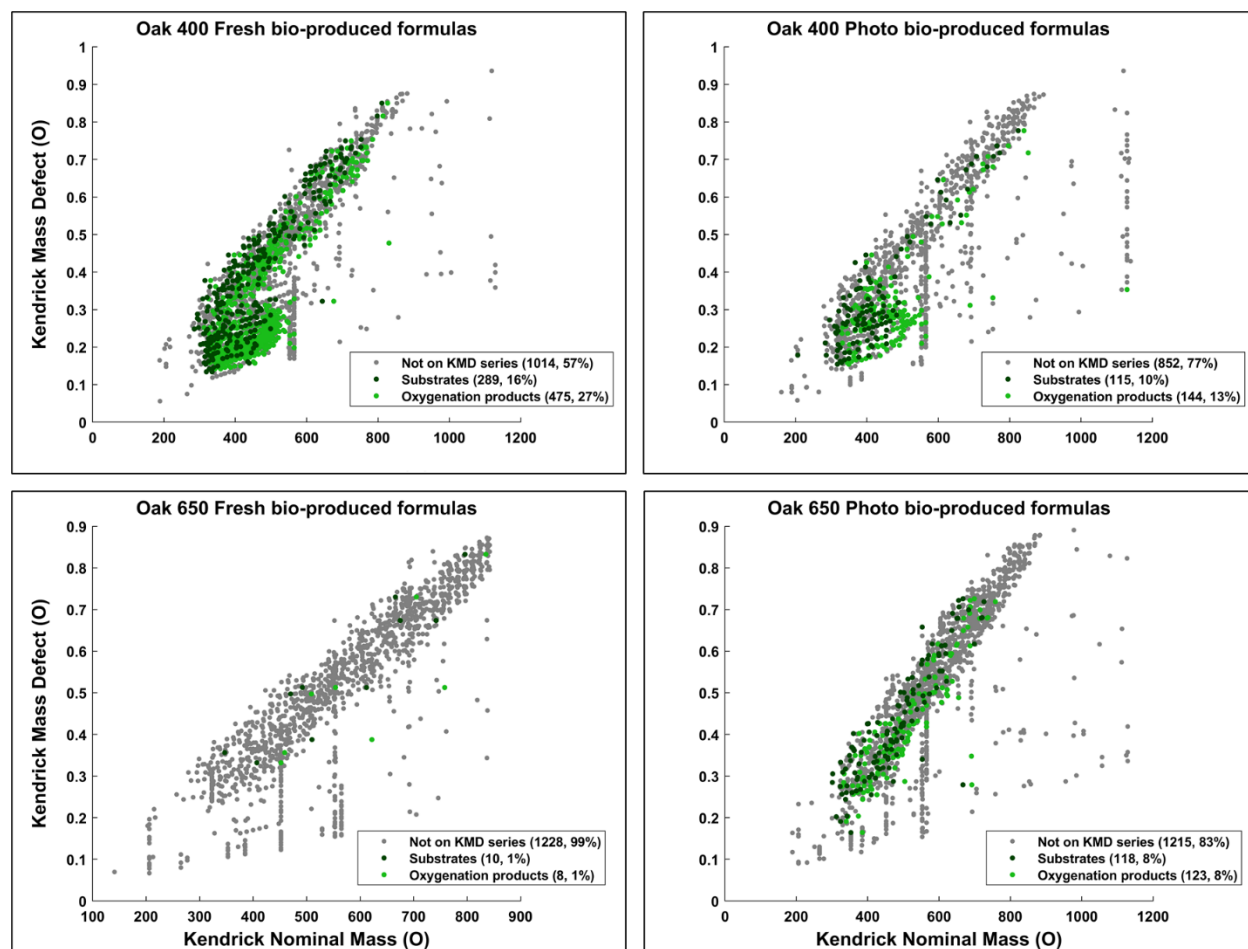
Figure 30. Kendrick Mass Defect versus Kendrick Nominal Mass plots for the Oxygen (O) series within the bio-produced formulas of the four pyDOM samples. Formulas not part of the O KMD series are colored in **gray**. Formulas in **dark green** are substrates with their oxygenation products colored in **light green**. The number of formulas of each of these pools are shown in the legends (along with corresponding percentages).

The mathematics behind the KMD analysis (see Section 2.4 of this Chapter) convert the mass of the molecular formula (also known as the IUPAC mass) to a "Kendrick" mass, whose mass is on a different scale which is specific for the selected structural moiety. On Figure 29a, an example is shown with the KMD analysis for molecules differing by one oxygen (-O-). On the regular (IUPAC) mass scale, such formulas would differ by 15.994915 Da, but on the Kendrick "O" mass scale, they differ by 16 Da. The difference between the Kendrick Mass, KM (e.g., 408.2876 Da) and the Kendrick Nominal Mass, KNM (408 Da) is the Kendrick Mass Defect, KMD (i.e., 0.2876 Da), and formulas with the exact same KMD differ by one or more oxygens, and lie on a KMD series. Visually these formulas would plot on horizontal lines on the KMD plot as indicated by the dashed lines in Figure 29b. Taking the series of KMD = 0.4174, this evaluation shows that there are five formulas in this particular KMD series that differ in number of oxygens ($C_{24}H_{40}O_{5-10}$). This implies that once $C_{25}H_{40}O_5$ is produced, it acts as a substrate and the other four formulas ($C_{24}H_{40}O_{6-10}$) are produced by oxygenation (likely in a sequential manner: $C_{24}H_{40}O_5 \rightarrow C_{24}H_{40}O_6 \rightarrow C_{24}H_{40}O_7 \rightarrow C_{24}H_{40}O_9 \rightarrow C_{24}H_{40}O_{10}$). This can happen via oxygenation by hydroxyl radical ($\bullet$OH) attacks. This ROS can abstract a hydrogen from C-H bonds and the hydrogen is substituted with an OH-group, resulting in the formation of alcohols (C-OH) as shown in Figure 29c. This is likely how the oxygenation products shown in Figures 29a and 29b have formed. Evidence for such reactions will be found on the KMD plots as evolution of a new molecule within the same KMD series, but with a different number of oxygens. Further radical attack results in formation of polyols (Figure 29c). In the case of formation of geminal diols (two alcohol groups on the same carbon atom), they can rearrange to aldehydes or ketones via keto-enol tautomerism (Figure 29d). Further radical attack would produce carboxyl groups, which can also be radically cleaved, and DOM radicals be formed. These radicals (as well as any other radical intermediate in this pathway) can be then further paired with hydrogen radicals ($\bullet$H) from the solution, other $\bullet$OH radicals, or other radicalized pyDOM or proteinaceous species.

Using KMD analysis, formulas produced by oxygenation were identified and plotted individually (Figure 31). It is assumed that the smallest molecule in each series is the substrate and any molecules with more oxygens are oxygenation products.
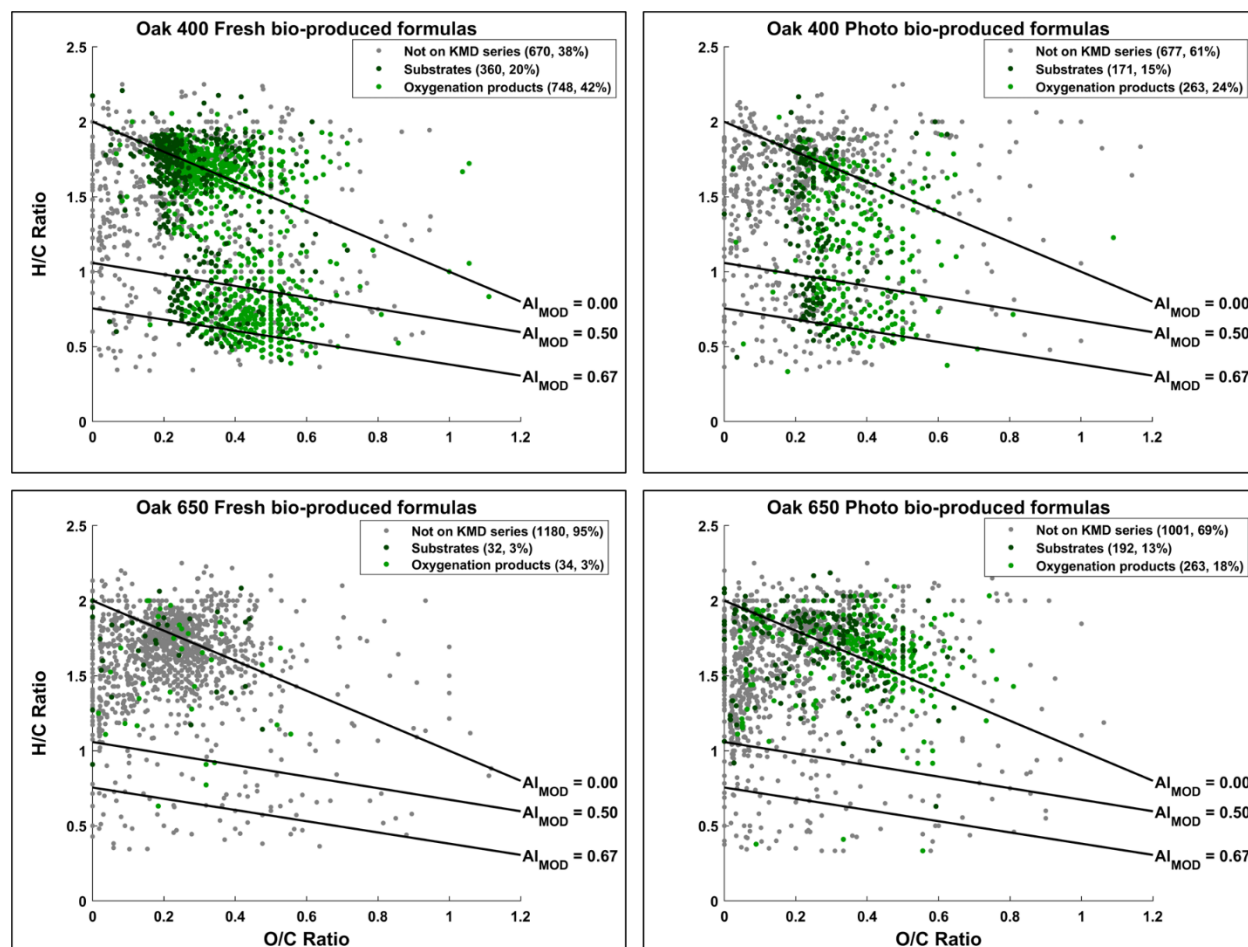
Figure 31. Van Krevelen diagrams evaluating oxygenation products among the bio-produced formulas of the four incubated pyDOM samples. Formulas not part of any of the oxygenation KMD series (O, CO, or COO) are colored in **gray**. Formulas in **dark green** are substrates with their oxygenation products colored in **light green**. The number of formulas in each of these pools are shown in the legends (along with corresponding percentages). The black lines indicate modified aromaticity index cutoffs (AI_{MOD}; Koch and Dittmar, 2006, 2016).

KMD analysis revealed that up to nearly a third (34 – 748, 3 – 42%) of the bio-produced formulas in these pyDOM samples could be classified as products of oxygenation reactions, likely driven by ROS species such as the hydroxyl radical (•OH). This is in agreement with previously observed cross-linking of microbial compounds through oxidative processes (Sun et al., 2017). The majority of the formulas, however, were not found to be products of oxidation as they did not lie on neither of the evaluated KMD series (O, CO, nor COO). Therefore, these compounds are likely formulas of exudates which were resistant to radical attacks or are formulas of compounds which have already been radically coupled with other compounds to result in unrecognizable molecules by the KMD analysis.

Additional evidence for intense radical processes in these systems is evolution of bio-produced unsaturated aliphatic compounds (1 < H/C < 2, O/C <2) on the van Krevelen diagrams (Figures 23 and C3 in Appendix C). ROS can attack aliphatic and aromatic compounds, open aromatic and alicyclic rings, cleave oxygen- or nitrogen-containing functionalities, and produce highly aliphatic molecules, as previously observed after photo-irradiation of pyDOM (Goranov et al., 2020), ConAC (Zeng et al., 2000a,b), and radical-based degradation studies of lignin (Waggoner et al., 2015, 2017; Waggoner and Hatcher, 2017; Khatami et al., 2019a,b). ROS can also attack any of the proteinaceous exudates and peptidoglycans cleaving them from many of their functional groups and converting them into the observed unsaturated aliphatic compounds. These produced aliphatic compounds could also contribute to the newly produced N-containing ("peptide-like") compounds observed by FT-ICR-MS if they are oxygenated by ROS post-formation. However, this seems unlikely as data from the supplementary fluorescence and NMR analyses support the formation of microbial biomass. These indirect observations of intense radical processes indicate that the microbial incubations of pyDOM are extremely complex systems, and future studies need to employ more specialized bio-analytical techniques to fully understand the processes occurring in them.

While FT-ICR-MS peak magnitudes are considered to be semi-quantitative, making it generally impossible to quantify the different bio-labile and bio-produced compounds, the ultrasensitivity of this technique ensures detection of all compounds that are within its analytical window. Here, the number of molecular formulas can be used as

a quantitative measure for molecular diversity (e.g., Gurganus et al., 2015). Previously published liquid-state ^{1}H NMR data for the same samples (Bostick et al., 2020a) provide a quantitative measure of functional group content. Strong positive and negative correlations were observed between the numbers of bio-labile and bio-produced formulas and the percent NMR spectral signal accounted for by olefinic functionalities and methanol, respectively (Figure 32 and Table C2 in Appendix C). These correlations suggest that the diversity of bio-degraded (bio-labile) and bio-produced molecules was related in some way with a process related to the availability of methanol (CH_3OH) and olefinic functionalities (C=C) in pyDOM.
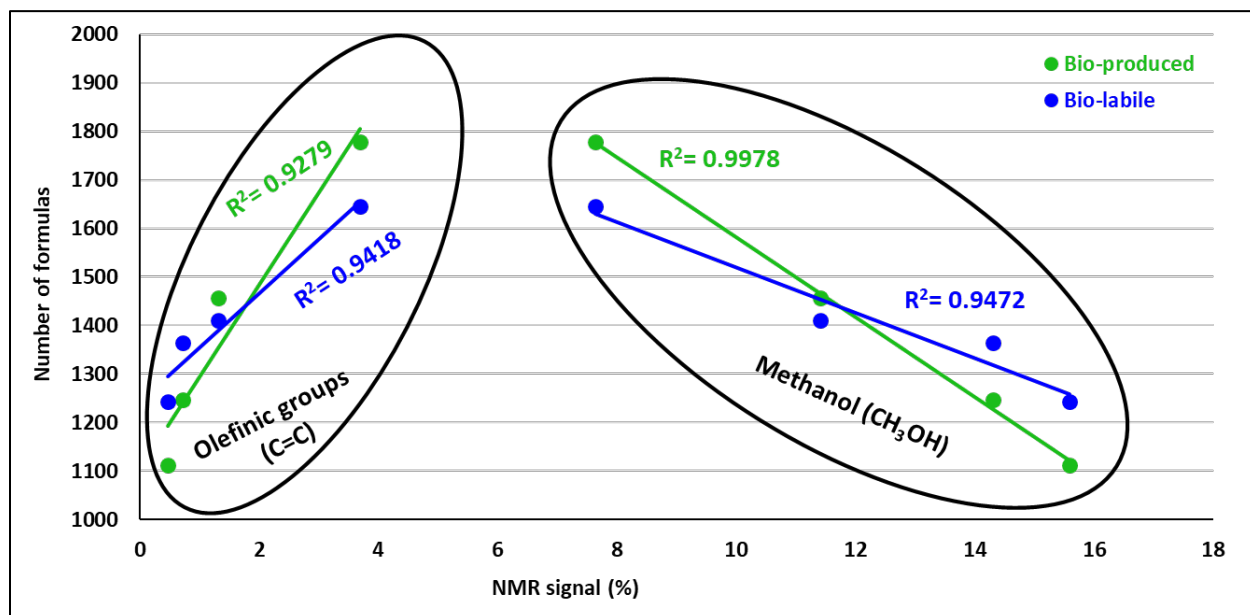
Figure 32. Correlation analysis between the number **bio-labile** and **bio-produced** formulas detected by FT-ICR-MS and relative intensity (%) of olefinic functionalities (C=C) and methanol (CH_3OH) as measured by liquid-state ^{1}H NMR and reported by Bostick et al. (2020a). No significant correlations were found between other functional groups and the number of bio-produced and bio-labile formulas (Table C2 in Appendix C).

Olefinic functionalities have been recently identified as important structural motifs in the composition of pyDOM and were observed to degrade in photochemical experiments due to their high reactivity with ROS species (Goranov et al., 2020). Although

they are in low abundance in pyDOM (< 10%), it is likely they act as important intermediates in the degradative pathways of pyDOM. The olefinic bonds can be homolytically cleaved by radicals and effectively act as radical-accelerators that further propagate radical-mediated organic matter transformations. Thus, the abundance of olefins can further increase the abundance of radicals and contribute to the elevated molecular diversity resulting in the linear relationship shown in Figure 32.

The other correlation between molecular diversity and NMR data is observed to be with methanol (CH_3OH), a very sharp highly distinguishable singlet at δ = 3.34 ppm in ^1H NMR spectra (Gottlieb et al., 1997). As it is a common contaminant in NMR analysis, special precautions were taken to obtain ultraclean spectra (see Section 2.5 of this Chapter). Methanol is a species that is naturally present in pyDOM (Bostick et al., 2018), and while it is generally considered to be toxic to microbes (Dyrda et al., 2019), there are methylotrophic bacteria and fungi (microbes of the families *methylococcaceae* and *methylobacteriaceae*) that can utilize it as a substrate (Chistoserdova et al., 2003; Kolb and Stacheter, 2013; Chistoserdova and Kalyuzhnaya, 2018). These species have been previously observed in the soil from the area where the microbial inoculum was extracted from (Khodadad et al., 2011), suggesting that the degradation of methanol may be biotic. In fact, in these samples, methanol, along with the other two measured low molecular weight substances, acetate and formate, was nearly completely degraded over the 10-day incubation (Bostick et al., 2020a).

The inverse relationship between the content of methanol and molecular diversity (Figure 32) can be interpreted in several ways. Firstly, methanol could be exhibiting toxicity to the microbes that assimilate pyDOM, as has been observed previously (Dyrda et al., 2019). This, however, is unlikely for the pyDOM systems studied here because the sample with the highest amount of methanol (Oak 400 Photo, ~3.7% CH_3OH) was the second most bio-reactive (Bostick et al., 2020a). Instead, the observed strong negative correlation may be explained by the fact that methanol is a known radical-scavenger (Múčka et al., 2013). If, as I propose, the molecular diversity results from the activity of radical processes, an increasing concentration of methanol would quench these radicals thereby decreasing their activity and limiting the molecular diversity. This would explain the negative relationship depicted by the correlation shown in Figure 32.

4. DISCUSSION

4.1. Multiple pathways for the alteration of pyDOM by microbes

Using a variety of analytical platforms in this and the parallel study (Bostick et al., 2020a), significant quantitative and qualitative losses were observed when pyDOM was subjected to incubation with a microbial consortium collected from a site impacted by forest fires. Additionally, labile and diverse compounds were produced during these incubations. Due to the high complexity of pyDOM, the changes are not straightforward, and there are at least two important pathways at play, 1) degradation through microbial assimilation (consumption of pyDOM), and 2) degradation/transformation via radical-mediated reactions (e.g., oxygenation) by ROS produced from microbial exoenzymes. These two pathways are discussed in the context of degradation of pyDOM and formation of new labile and diverse molecules.

4.1.1. Molecular degradation of pyDOM

A surprising observation in this study is that there was a uniform loss of pyDOM molecules from all regions of the vK diagrams. Microbes, it is generally presumed, preferentially assimilate small non-aromatic substances such as carbohydrates, proteins, low molecular weight acids (Berggren et al., 2010a,b; Kirchman, 2018). Thus, the aromatic fraction of pyDOM, mainly the ConAC, are generally considered to be bio-recalcitrant (Goldberg, 1985; Masiello, 2004). In addition to the condensed character of many of the molecules, there are significant numbers of potentially toxic organochlorine compounds, of both aliphatic and aromatic character, in pyDOM (Wozniak et al., 2020). Thus, the finding of the major biological activity in these samples and the significant amount of carbon, including aromatic carbon, that was mineralized, is a very significant finding for the wildfire biogeochemistry community (Bostick et al., 2020a).

Although pyDOM is highly heterogeneous (Wozniak et al., 2020), the observation of diverse molecular consumption is not unique to it. In a recent microbial degradation study of snow DOM, Antony et al. (2017) observed that both aromatic (including ConAC,

lignin, and tannins) and aliphatic formulas were bio-degraded. This is likely due to microbes evolving chemical mechanisms to thrive in the extreme conditions of glaciers (Antony et al., 2016). Analogously, as there have been previous prescribed fires in the area from which the microbes for this study were extracted (Johns, 2016), it is also possible that these organisms have adapted to the presence of ConAC and other pyrogenic substances, developing mechanisms for their assimilation (Judd et al., 2007).

While microbial assimilation of pyDOM compounds certainly occurred, the molecular data from this study show that there was a second degradative pathway which likely contributed to the extensive molecular alteration, and to the significant loss of carbon that was quantified in the parallel study (Bostick et al., 2020a). While some microbial exoenzymes operate via hydrolytic pathways (amylases, lipases, proteases, cellulases, β-galactosidases, etc.), many other enzymes operate through oxidative (electron-withdrawing) pathways. Examples of such enzymes are the various lignin-modifying enzymes in the peroxidase (lignin peroxidases, manganese peroxidases, etc.) and phenoloxidase (e.g., laccases) families (Higuchi, 2004). Thus, reactive oxygen species are usually produced and involved in the microbial degradation of organic matter in the environment.

The bio-labile molecules in the studied pyDOM samples are of highly variable degree of oxygenation, aromaticity, and size (some MW > 550 Da). Thus, microbial exoenzymes would have been needed to reduce the size of substrates into smaller units that could pass through microbial cell membranes (Sinsabaugh et al., 1997; Fuchs et al., 2011; Burns et al., 2013) and be consumed by the biota. The presence of enzymatic compounds is confirmed by observation of peptide-like compounds (FT-ICR-MS analysis) and proteinaceous fluorophores (spectrofluorometric analysis). An important finding is that a preferential degradation of ConAC of smaller molecular weights was observed (Bostick et al., 2020a). As small ConAC (i.e., oxygenated PAHs) are known to be toxic (e.g., Idowu et al., 2019), it is unlikely that they were directly consumed by the microbes. These substances are highly susceptible to attacks by ROS, which is likely how they were degraded in these samples. Thus, I speculate that microbes are most likely not directly consuming ConAC, but rather, are degrading them indirectly using ROS. These radicals can oxygenate pyDOM with various functional groups (e.g., hydroxy, aldehyde/keto,

carboxyl), and can also cleave functional groups (e.g., methoxy functionalities), open aromatic rings, and completely mineralize compounds to inorganic carbon (CO, CO_2, HCO_3^- and CO_3^{2-}) as shown on Figure 29. ROS have been previously shown to be very important in pyDOM photochemistry (Ward et al., 2014; Fu et al., 2016; Goranov et al., 2020; Wang et al., 2020), and it is likely that they play an important role in the microbial degradation of pyDOM as well.

More evidence for radical species involvement is provided by the peptidoglycan molecules produced during pyDOM incubation. While these molecules are generally large (Vollmer et al., 2008) and would not be detected as singly-charged molecules using FT-ICR-MS (analytical window covering m/z 200-1000), their hydrolytic products (small oligopeptides) would be observed. Very few oligopeptide sequences (5 – 18 oligopeptides of 2 – 5 residues) were identified among the bio-produced formulas indicating that such hydrolysates did not exist in the samples at the time of measurement. However, if there were abundant radical reactions occurring in the system, as I suggest, it is very possible that these hydrolysates were altered into unrecognizable organic structures that would still be classified as "peptide-like" but would have different molecular composition than the predicted linear peptide sequences. It is also possible that instead of peptidoglycan hydrolysis followed by consecutive oxygenation, ROS directly cleaved the peptidoglycans into smaller substances of peptide-like molecular composition.

4.1.2. Labilization and Diversification of pyDOM

The production of labile unrecognizable biological substances during these incubations correlates well with previous findings showing the formation of thousands of new biological compounds during biotic incubations unrelated to microbial metabolic pathways (Lechtenfeld et al., 2015; Wienhausen et al., 2017). However, in difference with previous studies, an insignificant overlap of bio-produced formulas was observed among the four pyDOM samples after the incubations (2 – 320 formulas, 0 – 12%). Insignificant numbers of matching formulas from pyDOM were also found in the bio-produced formulas of an incubation of sucrose with the same soil microbes (63 – 94 formulas, 3%). This indicates that microbes diversified the composition of these pyDOM samples.

The observed diversity can be explained by a scenario wherein the microbes secreted labile molecules whose identities differed depending on the growth medium and/or food source, yielding high variability among bio-produced formulas after the incubation of pyDOM. Additionally, it is possible that different microbial species (different bacteria, fungi, archaea, etc.) have proliferated in response to the sample-specific pyDOM composition, yielding different microbial populations growing during each different incubation, sequentially producing different bio-produced compounds (Fitch et al., 2018).

The finding of extreme molecular diversity contrasts with previous observations made by Lechtenfeld et al. (2015) in a study evaluating the molecular composition of microbially produced DOM. In their study, marine microbes were supplied with two different substrates (glucose and glutamic acid; and a mixture of oligosaccharides and oligopeptides), and a significant overlap (67 – 69 %) in the bio-produced organic matter was observed. The difference in observations between the work presented in this Chapter and by Lechtenfeld et al. (2015) is likely caused by a large difference in the composition of the pyDOM substrates relative to those in the Lechtenfeld et al. (2015) study. While the four pyDOM samples used here are highly heterogeneous to one another (Goranov et al., 2020; Wozniak et al., 2020), the substrates by Lechtenfeld et al. (2015) were of much higher similarity. Another possible reason is that the physiology of the soil microbes used here may be producing more diverse molecules than the marine microbes used by Lechtenfeld et al. (2015). It is likely that that aquatic microbes have a much different degradation strategy. As soils are far less rich in labile molecules, it is possible that soil microbes have adapted to produce much higher fluxes of ROS to degrade the more recalcitrant soil organic matter, which can also explain the larger dissimilarity in bio-produced organic molecules after the incubations of pyDOM.

An important observation using the H/C vs molecular weight plots (Figure 26) was that the bio-produced compounds after incubation of pyDOM were of various molecular weights. Thus, it is likely that that the microbial biomass produced during the incubation is radically coupled with pyDOM molecules. This has been recently proposed as an important process in marine DOM cycling (Hach et al., 2020). In that study, when isotopically ^{13}C-labeled organisms were incubated with oceanic surface waters, microbially produced compounds were quickly coupled to the ambient marine DOM

molecules. This "recombination" process occurred within hours of the production of microbial exudates, followed by the observation of a highly diversified DOM pool. This process is likely driven by radical coupling reactions, and such pathways have also been observed in incubations in the presence of sunlight (Sun et al., 2017). Another possible explanation is that chemically reactive species, such as quinones, reacted with microbially produced compounds via nucleophile-driven reactions (such as the Michael addition; McKee et al., 2014) to produce highly diverse pools of molecules after each incubation.

The observations from this study are compared to previous work by Waggoner et al. (2017) where a ligninaceous sample was treated with three different ROS: hydroxyl radical ($\cdot$OH), singlet oxygen ($^1O_2$), and superoxide ($O_2^{-\cdot}$). Each different radical degraded a specific pool of ligninaceous compounds, which showed that different ROS can degrade a variety of types of organic matter. However, there was a significant overlap observed between the three pools of molecules that were degraded indicating that degradation pathways solely based on ROS attacks are still ordered. Thus, because ROS on their own do not produce completely diversified molecular pools, the combination of the two pathways I describe here must have occurred to produce the great variability in the bio-produced microbial biomass observed in this study.

Clearly, the chemistry behind these microbially induced compositional changes of pyDOM is highly complex, and the observed molecular diversity after these biotic incubations contrasts with previous studies. These discrepancies cannot be interpreted unambiguously using the employed analytical approaches, and future studies need to involve measurements of radicals and their effects, as well as various DNA sequencing and "omics" approaches.

4.2. Implications for the cycling of pyDOM in the environment

The present study provides a detailed evaluation of the compounds that microbes degrade and produce in samples mimicking pyDOM in hydrologically dynamic environmental systems such as riverine and groundwater systems. It brings new knowledge about the properties and reactivity of pyDOM and challenges the conventional idea that pyDOM is stable towards biotic degradation. Several studies have already

shown that pyrogenic substances have soluble DOM components (Hockaday et al., 2007; Mukherjee and Zimmerman, 2013; Wagner et al., 2017; Bostick et al., 2018) and that more soluble components are produced with environmental aging (Abiven et al., 2011; Ascough et al., 2011; Roebuck et al., 2017; Quan et al., 2020). A recent study incubated pyDOM using riverine microbes and observed a significant degree of degradation as well (Qi et al., 2020). However, rather than using an extracted inoculate, in that work, the authors directly incubated pyOM in riverine water. Therefore, these incubations can be considered primed by the more labile riverine molecules (Guenet et al., 2010; Bianchi, 2011). The experiments presented in this study, in parallel with Bostick et al. (2020a), show that a large portion of pyDOM can be respired (bio-degraded) without priming, which indicates that these pyrogenic molecules may be far less resistant to degradation than previously presumed.

The involvement of pyDOM within the global carbon cycle is complex, and in many cases poorly understood. There is a growing body of literature showing that significant amounts of pyOM are solubilized and exported to the global ocean (Dittmar et al., 2012; Jaffé et al., 2013; Wang et al., 2016; Marques et al., 2017; Jones et al., 2020). However, the estimated pyDOM production and seepage rates of 1440 TgC·y^{-1} (Bostick et al., 2018) are greater than previously reported riverine flux estimates (203 TgC·y^{-1}; Jaffé et al., 2013; rescaled by Bostick et al., 2018). In addition to the implied 86% loss of carbon during export, a recent study also reported that the stable carbon isotopic signature (δ^{13}C) of oceanic ConAC are not terrigenous, but rather, marine-like (Wagner et al., 2019). This suggests that either all of the riverine-exported ConAC are being mineralized before reaching the global ocean or are chemically altered significantly to change their δ^{13}C isotopic signature (Jones et al., 2020). Furthermore, microbial and photochemical processes have been found to transform DOM with characteristic terrigenous DOM composition (compounds with lower H/C and higher O/C ratios) into compounds having characteristics of marine-derived DOM (compounds with higher H/C, lower O/C ratios; Rossel et al., 2013). Thus, pyDOM may simply be losing its diagnostic molecular and isotopic fingerprints during riverine export due to a variety of degradative post-production processes, as shown by the diversification observed in our study.

The cycling of organic matter in the environment has always been an enigma, and there has been a long-standing effort to explain the fate of land-derived DOM (terrigenous DOM including pyDOM) in the global ocean (Hedges et al., 1997). In Chapter III it was hypothesized that biotic consumption of photo-degradation products of pyDOM ("small aliphatic compounds") could result in the formation of marine-like DOM. This hypothesis was tested by comparing the incubation products from this study (the bio-produced formulas) to FT-ICR-MS formulas of several marine DOM samples (Table 4). An insignificant number of CRAM-like marine formulas (Hertkorn et al., 2006) was observed in these comparisons (4 – 272 common formulas, 0 – 6% overlap) contrasting with this proposition and suggesting that biotic incubations of photo-degraded pyDOM do not produce significant numbers of marine-like molecules.

An alternative idea is that the bio-produced molecules observed in this study are part of the fast-cycling, labile DOM pool per Hansell's model (Hansell and Carlson, 2015), and are quickly depleted in the natural environment. This parallels the findings of a recently published study (Hach et al., 2020) observing that microbially produced molecules are extremely labile and are, within hours, broken down and recombined with ambient DOM molecules. The closed laboratory systems in the study of this Chapter, may have enabled the observation of these highly labile molecules, whereas in the natural environment, they would have been quickly transformed, diluted, or mineralized to inorganic carbon resulting in their removal from analytical detection. The richness in nitrogen and peptide-like character of these new molecules suggest greater potential lability (Hach et al., 2020), and it is likely that the by-products of biotic degradation of pyDOM are readily incorporated into microbial food webs. This is consistent with the idea that terrigenous DOM is either mineralized to CO_2 or incorporated into food webs (Berggren et al., 2010a; Ward et al., 2013; Fasching et al., 2014). It is also consistent with the fact that the majority of organic nitrogen in the oceans is derived from microbial peptidoglycans (McCarthy et al., 1997, 1998; Simpson et al., 2011), and with observations of nitrogen from peptidoglycans in soil and sedimentary porewater systems (Schulten and Schnitzer, 1998; Hu et al., 2018, 2020).

Table 4. Overlap of bio-produced formulas of pyDOM with marine DOM samples.

Sample Name	Number of Formulas	Number of formulas in common with all bio-produced formulas of pyDOM
DS[a]	1752	4 (~0%)
GB[a]	1727	6 (~0%)
TP[a]	1303	4 (~0%)
CCB[a]	1079	4 (~0%)
OSC[a]	1189	4 (~0%)
DOM411[b]	2402	3 (~0%)
DOM412[b]	3524	6 (~0%)
DOM417[b]	3312	3 (~0%)
DOM 1, RO/ED[c,d]	1697	249 (~5%)
DOM 1 rep, RO/ED[c,d]	1756	272 (~6%)
DOM 2, RO/ED[c,d]	1918	223 (~5%)
DOM 2 rep, RO/ED[c,d]	1950	219 (~5%)
DOM 3, PPL[d]	2226	223 (~5%)
DOM 3 rep, PPL[d]	2256	235 (~5%)
DOM 4, PPL[d]	2325	246 (~5%)
DOM 4 rep, PPL[d]	2429	244 (~5%)

[a]Sleighter and Hatcher (2008)
[b]Unpublished data from samples obtained during the WACS-2 cruise (R/V Knorr) as part of the Western Atlantic Climate Study (WACS).
[c]Chen et al. (2014)
[d]Sleighter et al. (2012)

The production of these highly variable and diverse molecules, compositionally, is likely a contributing factor to the large complexity of natural organic matter (Hertkorn et al., 2007; Hawkes et al., 2018). They contribute to the highly variable microbial exometabolomes observed previously (Antón et al., 2013; Watrous et al., 2013; Romano et al., 2014) and stimulate further questions about their function and fate within the global carbon cycle. In this study, soil microbes were used, as the corresponding degradation by-products can be observed in both soil, groundwater, and partially in the upstream of rivers. Therefore, it would be critical to perform further studies with different microbial consortia (riverine, estuarine, marine, etc.) to fully understand the biological degradation of pyDOM in different environments.

5. CONCLUSIONS

This study probing the molecular changes occurring after biotic degradation of pyDOM revealed that soil microbes can effectively recycle and transform a significant portion of pyDOM molecules into labile microbial biomass. After the 10-day incubations, it appears that a wide range of molecules, both aromatic and aliphatic, were degraded, forming a highly diverse pool of compounds, including N-containing compounds with proteinaceous signatures and a peptidoglycan-like backbone. These observations are consistent with the previous identification of nitrogen from peptidoglycans in soils and oceans. These bio-produced compounds were highly specific for each pyDOM sample (very few common bio-produced molecular formulas among samples). The observed molecular labilization and diversification have implications for the studies of wildfire biogeochemistry, as this shows that microbial reworking of pyDOM can contribute to the large complexity and variability of natural organic matter. This study reveals that 1) pyDOM can be a medium for microbial growth, and 2) previously considered "recalcitrant" pyrogenic molecules can be incorporated into microbial food webs. This suggests that pyDOM is a much more active component in the global carbon and nitrogen cycles, and future studies need to further evaluate the bio-reactivity of pyDOM with microbial consortia of different environments, as well as in the context of wetted soils, groundwater processes, cycling within the riverine and marine water columns, and other aspects of the global carbon and nitrogen cycles.

CHAPTER V

CONCLUSIONS AND DIRECTIONS FOR FUTURE RESEARCH

1. CONCLUSIONS

Wildfires have always been present and have interacted with other biogeochemical components of the environment. However, only recently scientists have started to critically evaluate their environmental impact to expand the knowledge about their chemistry. In this Dissertation, I have presented numerous novel findings in regards of the sourcing and fate of pyrogenic organic matter in the environment, enhancing the knowledge of wildfire biogeochemistry. In Chapter II, I present quantitative evidence of the recently proposed abiotic non-pyrogenic formation of ConAC via electrocyclization reactions of lignin after exposure to the Fenton reaction (Chen et al., 2014; Waggoner et al., 2015). My findings indicate that this process can be a source of condensed molecules in soils, as well as any radical-rich systems. These pyrogenic-like compounds can then leach and contribute to the constant distributions of ConAC in the aquatic environments, thus potentially resulting in an overestimation in the quantitative constraining of the pyrogenic carbon fluxes and reservoirs in the environment.

The fluxes of pyrogenic dissolved organic matter (a significant portion of which are made of ConAC) from the terrestrial environment to the global ocean have been quantified in multiple studies (Dittmar et al., 2012; Jaffé et al., 2013; Wang et al., 2016; Marques et al., 2017; Jones et al., 2020). It has been estimated that during this export, 86% of pyDOM degrades (Bostick et al., 2018). The photochemical study in Chapter III allows for a better understanding of the degradative pathway of ConAC in such systems: sunlight photo-irradiation excites ConAC and they are photo-oxygenated with various functionalities such as hydroxyl and aldehyde groups. These moieties are then further photo-oxidized to carboxyl groups, which are then mineralized as inorganic carbon (e.g., CO_2) leaving smaller ConAC with aliphatic residues. Upon continuous exposure to sunlight, this cycle is repeated until all aromatic rings are degraded, and the molecular composition becomes highly aliphatic, less oxygenated, with smaller molecular weight,

and enriched in nitrogen (marine-like composition). These photo-produced molecules are likely to be highly bio-labile in natural systems, but in sterile conditions (as in the performed experiments presented in Chapter III) they are further cleaved out of oxygen-containing functional groups and polymerized into straight-chain alkanes. It is proposed that the kinetics of this pathway are controlled by the abundance (concentration) of ConAC in pyDOM, the degree of condensation of ConAC, and the additional matrix species such as inorganic nutrients or low molecular weight organic compounds. The abundance of the aforementioned pyDOM constituents is likely related to the char pyrolysis temperature and original biomass (e.g., oak vs grass). Additionally, reactive oxygen species produced by the photo-excitation of ConAC appear to degrade other light-unreactive structures within pyDOM such as the polysubstituted olefinic moieties that are found in char leachates from higher temperature chars (Oak 400, Oak 525, Oak 650).

Biotic incubation of pyDOM also revealed significant degradation. Molecules of various compound classes (ConAC, lignin-like, lipid-like, etc.) were bio-mineralized while many aliphatic, including peptide-like, labile molecules were produced. Microbial degradation appears to be through a combination of an assimilation (microbial consumption) and radical-mediated pathways. The microbially produced new molecules are associated with proteinaceous fluorophores and have peptidoglycan-like backbones as determined by NMR and fluorescence spectroscopies. It is also evident that their composition is unique in each pyDOM sample, and evidence suggests that there may be a dependence on the starting composition of the incubated pyDOM leachate. One possibility is that the microbial consortium produced different exudates when microbes consumed the different compounds from each different pyDOM medium. Alternatively, microbial exudates could be paired via nucleophile-driven (e.g., Michael addition) or radical-driven reactions with pyDOM compounds present in the incubation matrix, producing a highly complex pool of diverse and labile substances. The observed labilization and diversification of pyDOM is an important finding for understanding how pyDOM is coupled with the actively cycling pools of carbon and nitrogen in the environment. My results suggest that microbes are actively incorporating ("recycling") pyDOM in the global carbon and nitrogen cycles, contributing to its large molecular diversity. While the studies shown in Chapters II and III did not evaluate any natural

samples (e.g., charcoal samples from forests where wildfires have occurred in the past), the tight experimental control allowed for eliminating confounding variables in these experiments from environmental aging or admixture with DOM from non-pyrogenic sources. These *in vitro* laboratory experiments allow for simulating environmental processes which can directly test hypotheses and provide better understanding of the complex processes occurring in the environment.

Results from the research presented in this Dissertation enhance the knowledge of ConAC sources in the environment, as well as of the degradative pathways of pyDOM. While many new insights in wildfire biogeochemistry are presented here using numerous advanced analytical techniques, their application revealed numerous new aspects of research in regards of pyOM and pyDOM to be explored in future studies.

2. DIRECTIONS FOR FUTURE RESEARCH

The complex sourcing and degradative pathways of pyOM and pyDOM are recently discovered avenues of research in organic geochemistry. A significant focus of many experts in the field has been on the cycling of these organic compounds in the environment. It has been conceived that ConAC continuously leach in the aquatic environment after solubilization from soils (Hockaday et al., 2006, 2007; Dittmar et al., 2012; Jaffé et al., 2013) which leads to their accumulation and sequestration in the deep sea (Dittmar and Paeng, 2009; Ziolkowski and Druffel, 2010). This continuous export of pyDOM has been studied in more detail since then (Wang et al., 2016; Marques et al., 2017; Roebuck et al., 2017; Wagner et al., 2017b; Bostick et al., 2018; Coppola et al., 2019; Li et al., 2019; Drake et al., 2020; Jones et al., 2020). Interestingly, fire history (fire frequency and time since last burn) does not affect these dynamics (Ding et al., 2013). Additionally, recent findings by Wagner et al. (2019a) show that the terrestrial stable isotopic signature of ConAC ($\approx$ -30 ‰) is not preserved after their riverine-to-marine transfer. These studies indicate that sourcing and fate of ConAC in the environment is much more complex than originally thought.

There are numerous possibilities of why the isotopic signature of ConAC in the world ocean ($\approx$ -24 ‰) is significantly enriched with about 6 ‰ than that in the terrestrial

environment. This finding certainly questions many of the above-mentioned studies and indicates that reassessment of the terrestrial-to-marine transfer of ConAC is needed. The immediate hypothesis would be that photochemical alteration, as exposure to sunlight, preferentially degrades ^{13}C-depleted compounds such as ligninaceous aromatics (Benner et al., 1987; Spencer et al., 2009; Lalonde et al., 2014). This is additionally coupled with observations using compound-specific radiocarbon dating (Δ^{14}C) of ConAC (Ziolkowski and Druffel, 2010). It was observed that rivers export highly condensed and young (< 500 ^{14}C years old) ConAC while these compounds were found to be much less aromatic but ancient (~18000 ^{14}C years old) in the deep sea. These observations were also attributed to photochemistry as larger ConAC would be degraded allowing for the LMW ConAC to be preserved and accumulated in time. In the aforementioned study by Wagner et al. (2019a), compound-specific δ^{13}C signatures of ConAC from photo-irradiated surface waters and from the dark abyssal ocean were evaluated, and no statistically significant difference in δ^{13}C was observed. These findings suggest that photochemistry does not cause the discrepancy in stable isotopic composition of ConAC. However, as the authors conclude in their study: "the impact of sun exposure upon riverine BPCA-specific δ^{13}C signatures must be directly tested to confirm isotopic stability during photo-degradation [sic]" (Wagner et al., 2019a). As discussed in Chapter III and previous studies (Stubbins et al., 2010, 2012; Ward et al., 2014; Wagner and Jaffé, 2015; Fu et al., 2016; Li et al., 2019; Bostick et al., 2020b; Wang et al., 2020), photo-irradiation can significantly alter the structure of pyDOM and ConAC. Moreover, the complete (or nearly complete) mineralization of ConAC has been observed in some systems (Yuan et al., 2019; Bostick et al., 2020b). The terrestrial-to-marine export of ConAC should be re-evaluated in the context of photochemistry and other degradative pathways of ConAC, as it is possible that all ConAC are degraded even before they reach the mouths of rivers, which would leave their degradation by-products and inorganic carbon (e.g., CO_2) to enter the ocean and be undetected by the ConAC-specific methodology (Wagner et al., 2017a) used by Wagner et al. (2019a).

Additionally, in Chapter III it was suggested that high fluxes of ROS radicals are in part responsible for the degradation of pyDOM in addition to the photo-excitation of ConAC and other aromatic molecules. ROS are of essential importance for the

degradation and alteration of non-light-absorbing molecules or molecular moieties such as olefins. A recent study showed that hydroxyl radical ($\cdot$OH), singlet oxygen ($^1O_2$), and superoxide (O_2^{-}) degrade lignin differently (Waggoner et al., 2017), an observation which suggests that this is also possible for ConAC and pyDOM. No such comparative study has been carried out with pyDOM, and it is therefore not known if ROS have the capacity to significantly degrade and alter the isotopic signature of ConAC. In the context of structural examination, it is also critical to compare how molecules are altered by different ROS in comparison with direct photo-irradiation (i.e., degradation by photo-excitation). This will enhance the understanding and help deconvolute the complexity of the degradation pathway(s) of ConAC (and pyDOM) in sunlit environments.

Chapter IV shows evidence of molecular degradation and structural alterations in a biologically active system. The soil microbes that were used degraded pyDOM effectively (Bostick et al., 2020a), and it appears to happen through a combination of assimilation (consumption) and radical-mediated pathways. This biotic removal of ConAC and pyDOM from the environment must also be evaluated using isotopic techniques. Given that it is the first report of such high levels of biotic degradation of pyDOM in the environment, it must be carefully evaluated in the context of quantitative carbon and nitrogen cycles. Additionally, it was found that microbes do not produce significant number of molecules typical for marine environments (such as carboxyl-rich alicyclic molecules, CRAM; Hertkorn et al., 2006) after growing in pyDOM media, defying one of the hypotheses proposed in Chapter II. However, they were found to produce many peptidoglycan-like molecules, correlating with the previous observations of peptidoglycan nitrogen in soils and the global ocean. This is plausible as the microbial consortium used in these incubations was extracted from a forest soil, thus these organisms would produce soil-related substances, which can either accumulate on land or be leached and transported to the marine environment. Future studies should perform similar incubations with other consortia (riverine, oceanic, glacial, etc.) to evaluate the fate of pyDOM and ConAC in these different environments. Related to the hypothesis from Chapter II, it would also be necessary to incubate pyDOM with riverine, estuarine, and marine microbes to properly evaluate if pyDOM before or after photo-degradation could be a source of marine DOM. Additionally, integrating bio-analytical techniques (omics, cell

counting, etc.) would be necessary to fully decipher the microbial interactions with pyDOM and effectively deconvolute the different reactions occurring during these incubations.

While exposure of pyDOM to sunlight and microbes (separately or altogether) during terrestrial-to-marine export alters the quantity and quality of its molecules, there are other processes that must be explored to fully decipher the complex cycling of pyOM and pyDOM. Several non-pyrogenic processes have been discussed as avenues for future research, especially in terms of sourcing of ConAC to the environment (Wagner et al., 2019a; Jones et al., 2020): non-pyrogenic sourcing of ConAC by biotic (autochthonous) excretion, as suggested by Wagner et al. (2019a); production of ConAC at hydrothermal vents (Dittmar and Koch, 2006; Rossel et al., 2017; Estes et al., 2019); seepage of petrogenic ConAC from the ocean floor or through other openings, as suggested by Ziolkowski and Druffel (2010); as well as deposition of aerosols (Szidat et al., 2007; Mouteva et al., 2017; Coppola et al., 2019; Wagner et al., 2019b). The research study presented in Chapter II suggests that another non-pyrogenic process can also contribute to these non-pyrogenic ConAC in the environment. The proposed radical-mediated cyclopolymerization of lignin is very applicable for soil and sedimentary systems and must also be considered in the proper re-evaluation of pyOM, pyDOM, and ConAC fluxes in the environment.

Besides the necessity to improve the constraints of pyOM, pyDOM, and ConAC within the global carbon (and heteroelement, for example, nitrogen) cycles, current literature needs more comprehensive structural and molecular analyses of these materials. Pyrogenic organic matter in both its solid (pyOM) and dissolved (pyDOM) forms is a challenging environmental matrix to analyze, which likely contributes to the scarcity of structural and molecular studies. The high mineral (ash) content (Etiégni and Campbell, 1991; Xu et al., 2017; Bostick et al., 2018; Zhao et al., 2019; Li et al., 2020) and the high abundance of ConAC (making the sample matrix conductive, Freitas et al., 2001) are the reasons why these matrices are very difficult for solid-state structural NMR analysis. Infrared spectroscopy is another classical technique for analysis of solid samples, however the low oxygenation and high molecular rigidity of ConAC (graphene-like sheets) create serious limitations for this technique as well. After extraction of organics in liquid medium for liquid-state analyses, another set of challenges become present: low solubility

of ConAC (Wagner et al., 2017b), lability towards formation of colloids (Liu et al., 2018), and molecular chlorination (Wozniak et al., 2020). All these issues complicate and alter the analytical windows of any liquid-state/gel-state NMR or mass spectrometric analyses used for structural and molecular characterization (Wozniak et al., 2020). In contrast with marine DOM, for example, there have been numerous studies that have pinpointed exact structures of the molecules that are present in the ocean (e.g., Aluwihare et al., 1997; Hertkorn et al., 2006; Arakawa et al., 2017; Powers et al., 2019). Wildfire biogeochemists in the future should pair their expertise with that of analytical chemists to resolve the complexity of pyOM, develop new analytical methods, or find ways to refine current techniques to improve them for the analysis of pyOM and pyDOM. An important aspect of future work would be multi-dimensional NMR, which is becoming more and more useful in deciphering the structure of natural organic matter.

Clearly, there is a long path to fully understand and decipher the complexity of pyrogenic organic matter in the environment, both in structural and cycling contexts. The research presented in this Dissertation addresses many questions about these compounds, but it also presents numerous new avenues of research for wildfire biogeochemists to pursue in the next decades of scientific research.

REFERENCES

Abboudi, M., Jeffrey, W.H., Ghiglione, J.F., Pujo-Pay, M., Oriol, L., Sempéré, R., Charrière, B. and Joux, F. (2008) Effects of photochemical transformations of dissolved organic matter on bacterial metabolism and diversity in three contrasting coastal sites in the Northwestern Mediterranean Sea during summer. *Microb Ecol* **55**, 344-357.

Abdel-Fattah, T.M., Mahmoud, M.E., Ahmed, S.B., Huff, M.D., Lee, J.W. and Kumar, S. (2015) Biochar from woody biomass for removing metal contaminants and carbon sequestration. *J Ind Eng Chem* **22**, 103-109.

Abiven, S., Hengartner, P., Schneider, M.P.W., Singh, N. and Schmidt, M.W.I. (2011) Pyrogenic carbon soluble fraction is larger and more aromatic in aged charcoal than in fresh charcoal. *Soil Biol Biochem* **43**, 1615-1617.

Adams, R.W., Holroyd, C.M., Aguilar, J.A., Nilsson, M. and Morris, G.A. (2013) "Perfecting" WATERGATE: Clean proton NMR spectra from aqueous solution. *Chem Commun* **49**, 358-360.

Alexandri, E., Ahmed, R., Siddiqui, H., Choudhary, M.I., Tsiafoulis, C.G. and Gerothanassis, I.P. (2017) High resolution NMR spectroscopy as a structural and analytical tool for unsaturated lipids in solution. *Molecules* **22**, 1-71.

Aluwihare, L.I., Repeta, D.J. and Chen, R.F. (1997) A major biopolymeric component to dissolved organic carbon in surface sea water. *Nature* **387**, 166-169.

Antón, J., Lucio, M., Peña, A., Cifuentes, A., Brito-Echeverría, J., Moritz, F., Tziotis, D., López, C., Urdiain, M., Schmitt-Kopplin, P. and Roselló-Móra, R. (2013) High Metabolomic Microdiversity within Co-Occurring Isolates of the Extremely Halophilic Bacterium Salinibacter ruber. *PLoS ONE* **8**, 1-14.

Antony, R., Sanyal, A., Kapse, N., Dhakephalkar, P.K., Thamban, M. and Nair, S. (2016) Microbial communities associated with Antarctic snow pack and their biogeochemical implications. *Microbiol Res* **192**, 192-202.

Antony, R., Willoughby, A.S., Grannas, A.M., Catanzano, V., Sleighter, R.L., Thamban, M. and Hatcher, P.G. (2018) Photo-biochemical transformation of dissolved

organic matter on the surface of the coastal East Antarctic ice sheet. *Biogeochemistry* **141**, 229-247.

Antony, R., Willoughby, A.S., Grannas, A.M., Catanzano, V., Sleighter, R.L., Thamban, M., Hatcher, P.G. and Nair, S. (2017) Molecular insights on dissolved organic matter transformation by supraglacial microbial communities. *Environ Sci Technol* **51**, 4328-4337.

Arakawa, N., Aluwihare, L.I., Simpson, A.J., Soong, R., Stephens, B.M. and Lane-Coplen, D. (2017) Carotenoids are the likely precursor of a significant fraction of marine dissolved organic matter. *Sci Adv* **3**, 1-11.

Arruda, B.C., Smith, B., Spears, K.G. and Sension, R.J. (2013) Ultrafast ring-opening reactions: A comparison of α-terpinene, α-phellandrene, and 7-dehydrocholesterol with 1,3-cyclohexadiene. *Faraday Discuss* **163**, 159-171.

Ascough, P.L., Bird, M.I., Francis, S.M., Thornton, B., Midwood, A.J., Scott, A.C. and Apperley, D. (2011) Variability in oxidative degradation of charcoal: Influence of production conditions and environmental exposure. *Geochim Cosmochim Ac* **75**, 2361-2378.

Badr, Y., Abd El-Wahed, M.G. and Mahmoud, M.A. (2008) Photocatalytic degradation of methyl red dye by silica nanoparticles. *J Hazard Mater* **154**, 245-253.

Bae, E., Yeo, I.J., Jeong, B., Shin, Y., Shin, K.-H. and Kim, S. (2011) Study of double bond equivalents and the numbers of carbon and oxygen atom distribution of dissolved organic matter with negative-mode FT-ICR MS. *Anal Chem*, 4193-4199.

Baldock, J.A. and Smernik, R.J. (2002) Chemical composition and bioavailability of thermally, altered *Pinus resinosa* (Red Pine) wood. *Org Geochem* **33**, 1093-1109.

Bange, H.W. and Uher, G. (2005) Photochemical production of methane in natural waters: Implications for its present and past oceanic source. *Chemosphere* **58**, 177-183.

Bao, H., Niggemann, J., Luo, L., Dittmar, T. and Kao, S.-J. (2017) Aerosols as a source of dissolved black carbon to the ocean. *Nat Commun* **8**, 1-7.

Bax, A. and Davis, D.G. (1985) MLEV-17-based two-dimensional homonuclear magnetization transfer spectroscopy. *J Magn Reson* **65**, 355-360.

Beaupré, S.R. (2014) The carbon isotopic composition of marine DOC. In: *Biogeochemistry of Marine Dissolved Organic Matter* (eds. Hansell, D.A., Carlson, C.A.), Elsevier, Oxford, pp. 335–364.

Beltrán, F.J., Encinar, J.M. and Alonso, M.A. (1998) Nitroaromatic hydrocarbon ozonation in water. 1. Single ozonation. *Ind Eng Chem Res* **37**, 25-31.

Benner, R. and Biddanda, B. (1998) Photochemical transformations of surface and deep marine dissolved organic matter: Effects on bacterial growth. *Limnol Oceanogr* **43**, 1373-1378.

Benner, R., Fogel, M.L., Sprague, E.K. and Hodson, R.E. (1987) Depletion of ^{13}C in lignin and its implications for stable carbon isotope studies. *Nature* **329**, 708-710.

Benner, R., Pakulski, J., McCarthy, M., Hedges, J.I. and Hatcher, P.G. (1992) Bulk chemical characteristics of dissolved organic matter in the ocean. *Science* **255**, 1561-1564.

Berggren, M., Laudon, H., Haei, M., Ström, L. and Jansson, M. (2010a) Efficient aquatic bacterial metabolism of dissolved low-molecular-weight compounds from terrestrial sources. *ISME J* **4**, 408-416.

Berggren, M., Ström, L., Laudon, H., Karlsson, J., Jonsson, A., Giesler, R., Bergström, A.-K. and Jansson, M. (2010b) Lake secondary production fueled by rapid transfer of low molecular weight organic carbon from terrestrial sources to aquatic consumers. *Ecol Lett* **13**, 870-880.

Bertilsson, S. and Tranvik, L.J. (2000) Photochemical transformation of dissolved organic matter in lakes. *Limnol Oceanogr* **45**, 753-762.

Bianchi, T.S. (2011) The role of terrestrially derived organic carbon in the coastal ocean: A changing paradigm and the priming effect. *roc Natl Acad Sci USA* **108**, 19473-19481.

Billen, G., Servais, P. and Becquevort, S. (1990) Dynamics of bacterioplankton in oligotrophic and eutrophic aquatic environments: Bottom-up or top-down control? *Hydrobiologia* **207**, 37-42.

Bird, M.I., Moyo, C., Veenendaal, E.M., Lloyd, J. and Frost, P. (1999) Stability of elemental carbon in a savanna soil. *Global Biogeochem Cy* **13**, 923-932.

Bird, M.I., Wynn, J.G., Saiz, G., Wurster, C.M. and McBeath, A. (2015) The Pyrogenic Carbon Cycle. *Annu Rev Earth Pl Sc* **43**, 273-298.

Blough, N.V. and Zepp, R.G. (1995) Reactive oxygen species in natural waters. In: *Active Oxygen in Chemistry* (eds. Foote, C.S., Valentine, J., Greenberg, A., Liebman, J.F.), Chapman & Hall, New York, pp. 280-333.

Bostick, K.W., Zimmerman, A.R., Goranov, A.I., Mitra, S., Hatcher, P.G. and Wozniak, A.S. (2020a) Biolability of fresh and photodegraded pyrogenic dissolved organic matter from laboratory-prepared chars. *Earth and Space Science Open Archive (Pre-Print)*, 1-36.

Bostick, K.W., Zimmerman, A.R., Goranov, A.I., Mitra, S., Hatcher, P.G. and Wozniak, A.S. (2020b) Photolability of pyrogenic dissolved organic matter from a thermal series of laboratory-prepared chars. *Sci Total Environ* **724**, 1-14.

Bostick, K.W., Zimmerman, A.R., Wozniak, A.S., Mitra, S. and Hatcher, P.G. (2018) Production and composition of pyrogenic dissolved organic matter from a logical series of laboratory-generated chars. *Front Earth Sci* **6**, 1-14.

Botto, R.E., Wilson, R. and Winans, R.E. (1987) Evaluation of the reliability of solid ^{13}C NMR spectroscopy for the quantitative analysis of coals: study of whole coals and maceral concentrates. *Energ Fuel* **1**, 173-181.

Bowman, D.M.J.S., Balch, J.K., Artaxo, P., Bond, W.J., Carlson, J.M., Cochrane, M.A., D'Antonio, C.M., DeFries, R.S., Doyle, J.C., Harrison, S.P., Johnston, F.H., Keeley, J.E., Krawchuk, M.A., Kull, C.A., Marston, J.B., Moritz, M.A., Prentice, I.C., Roos, C.I., Scott, A.C., Swetnam, T.W., van der Werf, G.R. and Pyne, S.J. (2009) Fire in the Earth System. *Science* **324**, 481-484.

Bruun, S., Jensen, E.S. and Jensen, L.S. (2008) Microbial mineralization and assimilation of black carbon: Dependency on degree of thermal alteration. *Org Geochem* **39**, 839-845.

Burns, R.G., DeForest, J.L., Marxsen, J., Sinsabaugh, R.L., Stromberger, M.E., Wallenstein, M.D., Weintraub, M.N. and Zoppini, A. (2013) Soil enzymes in a changing environment: Current knowledge and future directions. *Soil Biol Biochem* **58**, 216-234.

Buxton, G.V., Greenstock, C.L., Helman, W.P. and Ross, A.B. (1988) Critical Review of rate constants for reactions of hydrated electrons, hydrogen atoms and hydroxyl radicals ($^\bullet$OH/$^\bullet$O$^-$) in Aqueous Solution. *J Phys Chem Ref Data* **17**, 513-886.

Chang, Z., Tian, L., Li, F., Zhou, Y., Wu, M., Steinberg, C.E.W., Dong, X., Pan, B. and Xing, B. (2018) Benzene polycarboxylic acid - A useful marker for condensed organic matter, but not for only pyrogenic black carbon. *Sci Total Environ* **626**, 660-667.

Chen, H.M., Abdulla, H.A.N., Sanders, R.L., Myneni, S.C.B., Mopper, K. and Hatcher, P.G. (2014) Production of black carbon-like and aliphatic molecules from terrestrial dissolved organic matter in the presence of sunlight and iron. *Environ Sci Tech Let* **1**, 399-404.

Chen, H.M., Stubbins, A., Perdue, E.M., Green, N.W., Helms, J.R., Mopper, K. and Hatcher, P.G. (2014) Ultrahigh resolution mass spectrometric differentiation of dissolved organic matter isolated by coupled reverse osmosis-electrodialysis from various major oceanic water masses. *Mar Chem* **164**, 48-59.

Chen, M. and Jaffé, R. (2014) Photo- and bio-reactivity patterns of dissolved organic matter from biomass and soil leachates and surface waters in a subtropical wetland. *Water Res* **61**, 181-190.

Chen, X., Ye, X., Chu, W., Olk, D.C., Cao, X., Schmidt-Rohr, K., Zhang, L., Thompson, M.L., Mao, J. and Gao, H. (2020) Formation of Char-Like, Fused-Ring Aromatic Structures from a Nonpyrogenic Pathway during Decomposition of Wheat Straw. *J Agric Food Chem* **68**, 2607-2614.

Chistoserdova, L., Chen, S.-W., Lapidus, A. and Lidstrom, M.E. (2003) Methylotrophy in *Methylobacterium extorquens* AM1 from a genomic point of view. *J Bacteriol* **185**, 2980-2987.

Chistoserdova, L. and Kalyuzhnaya, M.G. (2018) Current trends in methylotrophy. *Trends Microbiol* **26**, 703-714.

Clifton, C.L. and Huie, R.E. (1989) Rate constants for hydrogen abstraction reactions of the sulfate radical, SO_4^-. Alcohols. *Int J Chem Kinet* **21**, 677-687.

Coble, P.G. (1996) Characterization of marine and terrestrial DOM in seawater using excitation-emission matrix spectroscopy. *Mar Chem* **51**, 325-346.

Coble, P.G., Lead, J., Baker, A., Reynolds, D.M. and Spencer, R.G.M. (2014) *Aquatic Organic Matter Fluorescence*. Cambridge University Press, New York, NY.

Coppola, A.I., Seidel, M., Ward, N.D., Viviroli, D., Nascimento, G.S., Haghipour, N., Revels, B.N., Abiven, S., Jones, M.W., Richey, J.E., Eglinton, T.I., Dittmar, T. and Schmidt, M.W.I. (2019) Marked isotopic variability within and between the Amazon River and marine dissolved black carbon pools. *Nat Commun* **10**, 1-8.

Crawford, R.L. (1981) *Lignin biodegradation and transformation*. John Wiley and Sons Ltd, New York, NY.

Cusack, D.F., Chadwick, O.A., Hockaday, W.C. and Vitousek, P.M. (2012) Mineralogical controls on soil black carbon preservation. *Global Biogeochem Cy* **26**, 1-10.

Czimczik, C.I. and Masiello, C.A. (2007) Controls on black carbon storage in soils. *Global Biogeochem Cy* **21**, 1-8.

Czimczik, C.I., Preston, C.M., Schmidt, M.W.I. and Schulze, E.-D. (2003) How surface fire in Siberian Scots pine forests affects soil organic carbon in the forest floor: Stocks, molecular structure, and conversion to black carbon (charcoal). *Global Biogeochem Cy* **17**, 1-14.

Dai, Y., Zhang, N., Xing, C., Cui, Q. and Sun, Q. (2019) The adsorption, regeneration and engineering applications of biochar for removal organic pollutants: A review. *Chemosphere* **223**, 12-27.

Dalcanale, E. and Montanari, F. (1986) Selective oxidation of aldehydes to carboxylic acids with sodium chlorite-hydrogen peroxide. *J Org Chem* **51**, 567-569.

D'Andrilli, J., Fischer, S.J. and Rosario-Ortiz, F.L. (2020) Advancing critical applications of high resolution mass spectrometry for DOM assessments: Re-engaging with mass spectral principles, limitations, and data analysis. *Environ Sci Technol* **54**, 11654-11656.

Decesari, S., Mircea, M., Cavalli, F., Fuzzi, S., Moretti, F., Tagliavini, E. and Facchini, M.C. (2007) Source attribution of water-soluble organic aerosol by nuclear magnetic resonance spectroscopy. *Environ Sci Technol* **41**, 2479-2484.

Derbyshire, H. and Miller, E.R. (1981) The photodegradation of wood during solar irradiation. *Holz Roh Werkst* **39**, 341-350.

DiDonato, N., Chen, H., Waggoner, D. and Hatcher, P.G. (2016) Potential origin and formation for molecular components of humic acids in soils. *Geochim Cosmochim Ac* **178**, 210-222.

DiDonato, N. and Hatcher, P.G. (2017) Alicyclic carboxylic acids in soil humic acid as detected with ultrahigh resolution mass spectrometry and multi-dimensional NMR. *Org Geochem* **112**, 33-46.

Diels, O. and Alder, K. (1928) Synthesen in der hydroaromatischen Reihe. *Liebigs Ann Chem* **460**, 98-122.

Ding, Y., Yamashita, Y., Dodds, W.K. and Jaffé, R. (2013) Dissolved black carbon in grassland streams: Is there an effect of recent fire history? *Chemosphere* **90**, 2557-2562.

Dittmar, T. (2008) The molecular level determination of black carbon in marine dissolved organic matter. *Org Geochem* **39**, 396-407.

Dittmar, T., de Rezende, C.E., Manecki, M., Niggemann, J., Coelho Ovalle, A.R., Stubbins, A. and Bernardes, M.C. (2012) Continuous flux of dissolved black carbon from a vanished tropical forest biome. *Nat Geosci* **5**, 618-622.

Dittmar, T., Koch, B., Hertkorn, N. and Kattner, G. (2008) A simple and efficient method for the solid-phase extraction of dissolved organic matter (SPE-DOM) from seawater. *Limnol Oceanogr Meth* **6**, 230-235.

Dittmar, T. and Koch, B.P. (2006) Thermogenic organic matter dissolved in the abyssal ocean. *Mar Chem* **102**, 208-217.

Dittmar, T. and Paeng, J. (2009) A heat-induced molecular signature in marine dissolved organic matter. *Nat Geosci* **2**, 175-179.

Drake, T.W., Wagner, S., Stubbins, A., Wabakanghanzi, J.N., Dinga, J.B., Six, J. and Spencer, R.G.M. (2020) Du feu à l'eau: source and flux of dissolved black carbon from the Congo River. *Global Biogeochem Cy* **34**, 1-13.

Druffel, E. (2004) Comments on the importance of black carbon in the global carbon cycle. *Mar Chem* **92**, 197-200.

Dvorski, S.E., Gonsior, M., Hertkorn, N., Uhl, J., Muller, H., Griebler, C. and Schmitt-Kopplin, P. (2016) Geochemistry of dissolved organic matter in a spatially highly

resolved groundwater petroleum hydrocarbon plume cross-section. *Environ Sci Technol* **50**, 5536-5546.

Dyrda, G., Boniewska-Bernacka, E., Man, D., Barchiewicz, K. and Słota, R. (2019) The effect of organic solvents on selected microorganisms and model liposome membrane. *Mol Biol Rep* **46**, 3225-3232.

Earl, W.L. and Vanderhart, D.L. (1982) Measurement of ^{13}C chemical shifts in solids. *J Magn Reson* **48**, 35-54.

Estes, E.R., Berti, D., Coffey, N.R., Hochella, M.F., Wozniak, A.S. and Luther, G.W. (2019) Abiotic synthesis of graphite in hydrothermal vents. *Nat Commun* **10**, 1-6.

Etiégni, L. and Campbell, A.G. (1991) Physical and chemical characteristics of wood ash. *Bioresource Technol* **37**, 173-178.

Fasching, C., Behounek, B., Singer, G.A. and Battin, T.J. (2014) Microbial degradation of terrigenous dissolved organic matter and potential consequences for carbon cycling in brown-water streams. *Sci Rep* **4**, 4981.

Fasnacht, M.P. and Blough, N.V. (2002) Aqueous photodegradation of polycyclic aromatic hydrocarbons. *Environ Sci Technol* **36**, 4364-4369.

Fasnacht, M.P. and Blough, N.V. (2003a) Kinetic analysis of the photodegradation of polycyclic aromatic hydrocarbons in aqueous solution. *Aquat Sci* **65**, 352-358.

Fasnacht, M.P. and Blough, N.V. (2003b) Mechanisms of the aqueous photodegradation of polycyclic aromatic hydrocarbons. *Environ Sci Technol* **37**, 5767-5772.

Fenton, H.J.H. (1894) LXXIII.—Oxidation of tartaric acid in presence of iron. *J Chem Soc, Trans* **65**, 899-910.

Fitch, A., Orland, C., Willer, D., Emilson, E.J.S. and Tanentzap, A.J. (2018) Feasting on terrestrial organic matter: Dining in a dark lake changes microbial decomposition. *Global Biogeochem Cy* **24**, 5110-5122.

Forbes, M.S., Raison, R.J. and Skjemstad, J.O. (2006) Formation, transformation and transport of black carbon (charcoal) in terrestrial and aquatic ecosystems. *Sci Total Environ* **370**, 190-206.

Freeman, M.H. and McIntyre, C. (2008) A comprehensive review of copper-based wood preservatives with a focus on new micronized or dispersed copper systems. *Forest Prod J* **58**, 6-27.

Freitas, J.C.C., Emmerich, F.G., Cernicchiaro, G.R.C., Sampaio, L.C. and Bonagamba, T.J. (2001) Magnetic susceptibility effects on ^{13}C MAS NMR spectra of carbon mterials and graphite. *Solid State Nucl Magn Reson* **20**, 61-73.

Fu, H.Y., Liu, H.T., Mao, J.D., Chu, W.Y., Li, Q.L., Alvarez, P.J.J., Qu, X.L. and Zhu, D.Q. (2016) Photochemistry of dissolved black carbon released from biochar: Reactive oxygen species generation and phototransformation. *Environ Sci Technol* **50**, 1218-1226.

Fuchs, G., Boll, M. and Heider, J. (2011) Microbial degradation of aromatic compounds — from one strategy to four. *Nat Rev MIcrobiol* **9**, 803-816.

Fulmer, G.R., Miller, A.J.M., Sherden, N.H., Gottlieb, H.E., Nudelman, A., Stoltz, B.M., Bercaw, J.E. and Goldberg, K.I. (2010) NMR chemical shifts of trace impurities: Common laboratory solvents, organics, and gases in deuterated solvents relevant to the organometallic chemist. *Organometallics* **29**, 2176-2179.

George, B., Suttie, E., Merlin, A. and Deglise, X. (2005) Photodegradation and photostabilisation of wood - the state of the art. *Polym Degrad Stabil* **88**, 268-274.

Gerke, J. (2018) Concepts and misconceptions of humic substances as the stable part of soil organic matter: A review. *Agronomy* **8**, 1-16.

Gerke, J. (2019) Black (pyrogenic) carbon in soils and waters: A fragile data basis extensively interpreted. *Chem Biol Technol Agric* **6**, 1-8.

Gheysen, K., Mihai, C., Conrath, K. and Martins, J.C. (2008) Rapid identification of common hexapyranose monosaccharide units by a simple TOCSY matching approach. *Chem Eur J* **14**, 8869-8878.

Gil, A.M. and Neto, C.P. (1999) Solid-state NMR studies of wood and other lignocellulosic materials. *Ann R NMR S* **37**, 75-117.

Glaser, B., Haumaier, L., Guggenberger, G. and Zech, W. (1998) Black carbon in soils: The use of benzenecarboxylic acids as specific markers. *Org Geochem* **29**, 811-819.

Goldberg, E.D. (1985) *Black carbon in the environment: Properties and distribution*. J. Wiley, New York, NY.

Goldstone, J.V., Pullin, M.J., Bertilsson, S. and Voelker, B.M. (2002) Reactions of hydroxyl radical with humic substances: Bleaching, mineralization, and production of bioavailable carbon substrates. *Environ Sci Technol* **36**, 364-372.

Gomez-Saez, G.V., Pohlabeln, A.M., Stubbins, A., Marsay, C.M. and Dittmar, T. (2017) Photochemical alteration of dissolved organic sulfur from sulfidic porewater. *Environ Sci Technol* **51**, 14144-14154.

Gonsior, M., Hertkorn, N., Hinman, N., Dvorski, S.E., Harir, M., Cooper, W.J. and Schmitt-Kopplin, P. (2018) Yellowstone hot springs are organic chemodiversity hot spots. *Sci Rep* **8**, 1-13.

Gonsior, M., Peake, B.M., Cooper, W.T., Podgorski, D., D'Andrilli, J. and Cooper, W.J. (2009) Photochemically induced changes in dissolved organic matter identified by ultrahigh resolution Fourier transform ion cyclotron resonance mass spectrometry. *Environ Sci Technol* **43**, 698-703.

Goranov, A.I., Wozniak, A.S., Bostick, K.W., Zimmerman, A.R., Mitra, S. and Hatcher, P.G. (2020) Photochemistry after fire: Structural transformations of pyrogenic dissolved organic matter elucidated by advanced analytical techniques. *Geochim Cosmochim Ac* **290**, 271-292.

Gottlieb, H.E., Kotlyar, V. and Nudelman, A. (1997) NMR chemical shifts of common laboratory solvents as trace impurities. *J Org Chem* **62**, 7512-7515.

Green, S.A. and Blough, N.V. (1994) Optical absorption and fluorescence properties of chromophoric dissolved organic matter in natural waters. *Limnol Oceanogr: Methods* **39**, 1903-1916.

Griesbeck, A.G., Kramer, W. and Oelgemöller, M. (1999) Photoinduced decarboxylation reactions. Radical chemistry in water. *Green Chem* **1**, 205-208.

Guenet, B., Danger, M., Abbadie, L. and Lacroix, G. (2010) Priming effect: Bridging the gap between terrestrial and aquatic ecology. *Ecology* **91**, 2850-2861.

Güereña, D.T., Lehmann, J., Walter, T., Enders, A., Neufeldt, H., Odiwour, H., Biwott, H., Recha, J., Shepherd, K., Barrios, E. and Wurster, C. (2015) Terrestrial pyrogenic carbon export to fluvial ecosystems: Lessons learned from the White Nile watershed of East Africa. *Global Biogeochem Cy* **29**, 1911-1928.

Guggenberger, G. (2005) Humification and mineralization in soils. In: *Microorganisms in soils: Roles in genesis and functions* (eds. Varma, A., Buscot, F.), Springer, Berlin, Heidelberg, pp. 85-106.

Guieysse, B., Viklund, G., Toes, A.C. and Mattiasson, B. (2004) Combined UV-biological degradation of PAHs. *Chemosphere* **55**, 1493-1499.

Gurganus, S.C., Wozniak, A.S. and Hatcher, P.G. (2015) Molecular characteristics of the water soluble organic matter in size-fractionated aerosols collected over the North Atlantic Ocean. *Mar Chem* **170**, 37-48.

Hach, P.F., Marchant, H.K., Krupke, A., Riedel, T., Meier, D.V., Lavik, G., Holtappels, M., Dittmar, T. and Kuypers, M.M.M. (2020) Rapid microbial diversification of dissolved organic matter in oceanic surface waters leads to carbon sequestration. *Sci Rep* **10**, 1-10.

Hammes, K., Schmidt, M.W.I., Smernik, R.J., Currie, L.A., Ball, W.P., Nguyen, T.H., Louchouarn, P., Houel, S., Gustafsson, O., Elmquist, M., Cornelissen, G., Skjemstad, J.O., Masiello, C.A., Song, J., Peng, P., Mitra, S., Dunn, J.C., Hatcher, P.G., Hockaday, W.C., Smith, D.M., Hartkopf-Froeder, C., Boehmer, A., Luer, B., Huebert, B.J., Amelung, W., Brodowski, S., Huang, L., Zhang, W., Gschwend, P.M., Flores-Cervantes, D.X., Largeau, C., Rouzaud, J.N., Rumpel, C., Guggenberger, G., Kaiser, K., Rodionov, A., Gonzalez-Vila, F.J., Gonzalez-Perez, J.A., de la Rosa, J.M., Manning, D.A.C., Lopez-Capel, E. and Ding, L. (2007) Comparison of quantification methods to measure fire-derived (black/elemental) carbon in soils and sediments using reference materials from soil, water, sediment and the atmosphere. *Global Biogeochem Cy* **21**, 1-18.

Hansell, D.A. and Carlson, C.A. (2015) *Biogeochemistry of marine dissolved organic matter*, Second ed. Academic Press, Amsterdam.

Hatcher, P.G., Waggoner, D.C. and Chen, H. (2019) Evidence for the existence of humic acids in peat soils based on solid-state ^{13}C NMR. *J Environ Qual* **48**, 1571-1577.

Hawkes, J.A., Patriarca, C., Sjöberg, P.J.R., Tranvik, L.J. and Bergquist, J. (2018) Extreme isomeric complexity of dissolved organic matter found across aquatic environments. *Limnol Oceanogr Lett* **3**, 21-30.

He, Z., Sleighter, R.L., Hatcher, P.G., Liu, S., Wu, F., Zou, H. and Olanya, O.M. (2019) Molecular level comparison of water extractives of maple and oak with negative and positive ion ESI FT-ICR mass spectrometry. *J Mass Spectrom* **54**, 655-666.

Hedges, J.I., Cowie, G.L., Ertel, J.R., James Barbour, R. and Hatcher, P.G. (1985) Degradation of carbohydrates and lignins in buried woods. *Geochim Cosmochim Ac* **49**, 701-711.

Hedges, J.I., Eglinton, G., Hatcher, P.G., Kirchman, D.L., Arnosti, C., Derenne, S., Evershed, R.P., Kögel-Knabner, I., de Leeuw, J.W., Littke, R., Michaelis, W. and Rullkötter, J. (2000) The molecularly-uncharacterized component of nonliving organic matter in natural environments. *Org Geochem* **31**, 945-958.

Hedges, J.I., Keil, R.G. and Benner, R. (1997) What happens to terrestrial organic matter in the ocean? *Org Geochem* **27**, 195-212.

Helms, J.R., Stubbins, A., Ritchie, J.D., Minor, E.C., Kieber, D.J. and Mopper, K. (2008) Absorption spectral slopes and slope ratios as indicators of molecular weight, source, and photobleaching of chromophoric dissolved organic matter. *Limnol Oceanogr* **53**, 955-969.

Hemmler, D., Gonsior, M., Powers, L.C., Marshall, J.W., Rychlik, M., Taylor, A.J. and Schmitt-Kopplin, P. (2019) Simulated sunlight selectively modifies Maillard reaction products in a wide array of chemical reactions. *Chem Eur J* **25**, 13208-13217.

Hertkorn, N., Benner, R., Frommberger, M., Schmitt-Kopplin, P., Witt, M., Kaiser, K., Kettrup, A. and Hedges, J.I. (2006) Characterization of a major refractory component of marine dissolved organic matter. *Geochim Cosmochim Ac* **70**, 2990-3010.

Hertkorn, N., Frommberger, M., Witt, M., Koch, B.P., Schmitt-Kopplin, P. and Perdue, E.M. (2008) Natural organic matter and the event horizon of mass spectrometry. *Anal Chem* **80**, 8908-8919.

Hertkorn, N., Harir, M., Cawley, K.M., Schmitt-Kopplin, P. and Jaffé, R. (2016) Molecular characterization of dissolved organic matter from subtropical wetlands: A comparative study through the analysis of optical properties, NMR and FTICR/MS. *Biogeosciences* **13**, 2257-2277.

Hertkorn, N., Harir, M., Koch, B.P., Michalke, B. and Schmitt-Kopplin, P. (2013) High-field NMR spectroscopy and FTICR mass spectrometry: Powerful discovery tools for the molecular level characterization of marine dissolved organic matter. *Biogeosciences* **10**, 1583-1624.

Hertkorn, N., Ruecker, C., Meringer, M., Gugisch, R., Frommberger, M., Perdue, E., Witt, M. and Schmitt-Kopplin, P. (2007) High-precision frequency measurements: Indispensable tools at the core of the molecular-level analysis of complex systems. *Anal Bioanal Chem* **389**, 1311-1327.

Higuchi, T. (1990) Lignin biochemistry: Biosynthesis and biodegradation. *Wood Sci Technol* **24**, 23-63.

Higuchi, T. (1993) Biodegradation mechanism of lignin by white-rot basidiomycetes. *J Biotechnol* **30**, 1-8.

Higuchi, T. (2004) Microbial degradation of lignin: Role of lignin peroxidase, manganese peroxidase, and laccase. *Proc Jpn Acad Ser B Phys Biol Sci* **80**, 204-214.

Hockaday, W.C., Grannas, A.M., Kim, S. and Hatcher, P.G. (2006) Direct molecular evidence for the degradation and mobility of black carbon in soils from ultrahigh-resolution mass spectral analysis of dissolved organic matter from a fire-impacted forest soil. *Org Geochem* **37**, 501-510.

Hockaday, W.C., Grannas, A.M., Kim, S. and Hatcher, P.G. (2007) The transformation and mobility of charcoal in a fire-impacted watershed. *Geochim Cosmochim Ac* **71**, 3432-3445.

Hu, Y., Zheng, Q., Noll, L., Zhang, S. and Wanek, W. (2020) Direct measurement of the in situ decomposition of microbial-derived soil organic matter. *Soil Biol Biochem* **141**, 1-10.

Hu, Y., Zheng, Q., Zhang, S., Noll, L. and Wanek, W. (2018) Significant release and microbial utilization of amino sugars and d-amino acid enantiomers from microbial cell wall decomposition in soils. *Soil Biol Biochem* **123**, 115-125.

Hughey, C.A., Hendrickson, C.L., Rodgers, R.P., Marshall, A.G. and Qian, K. (2001) Kendrick mass defect spectrum: a compact visual analysis for ultrahigh-resolution broadband mass spectra. *Anal Chem* **73**, 4676-4681.

Hyde, S.M. and Wood, P.M. (1997) A mechanism for production of hydroxyl radicals by the brown-rot fungus *Coniophora Puteana*: Fe(III) reduction by cellobiose dehydrogenase and Fe(II) oxidation at a distance from the hyphae. *Microbiology* **143**, 259-266.

Idowu, O., Semple, K.T., Ramadass, K., O'Connor, W., Hansbro, P. and Thavamani, P. (2019) Beyond the obvious: Environmental health implications of polar polycyclic aromatic hydrocarbons. *Environ Int* **123**, 543-557.

Jacobs, L.E., Weavers, L.K. and Chin, Y.-P. (2008) Direct and indirect photolysis of polycyclic aromatic hydrocarbons in nitrate-rich surface waters. *Environ Toxicol Chem* **27**, 1643-1648.

Jaffé, R., Ding, Y., Niggemann, J., Vähätalo, A.V., Stubbins, A., Spencer, R.G.M., Campbell, J. and Dittmar, T. (2013) Global charcoal mobilization from soils via dissolution and riverine transport to the oceans. *Science* **340**, 345-347.

Johns, G. (2016). Austin Cary Forest Prescribed Burn, 33/8S/21E. *Prescribed Burn Prescription, School of Forest Resources and Conservation, UF/IFAS*, 1-5.

Johnson, R.L. and Schmidt-Rohr, K. (2014) Quantitative solid-state ^{13}C NMR with signal enhancement by multiple cross polarization. *J Magn Reson* **239**, 44-49.

Jones, M.W., Coppola, A.I., Santín, C., Dittmar, T., Jaffé, R., Doerr, S.H. and Quine, T.A. (2020) Fires prime terrestrial organic carbon for riverine export to the global oceans. *Nat Commun* **11**, 1-8.

Judd, K.E., Crump, B.C. and Kling, G.W. (2007) Bacterial responses in activity and community composition to photo-oxidation of dissolved organic matter from soil and surface waters. *Aquat Sci* **69**, 96-107.

Kahan, T.F. and Donaldson, D.J. (2007) Photolysis of polycyclic aromatic hydrocarbons on water and ice surfaces. *J Phys Chem A* **111**, 1277-1285.

Kaiser, E., Simpson, A.J., Dria, K.J., Sulzberger, B. and Hatcher, P.G. (2003) Solid-state and multidimensional solution-state NMR of solid phase extracted and ultrafiltered riverine dissolved organic matter. *Environ Sci Technol* **37**, 2929-2935.

Kane, E.S., Hockaday, W.C., Turetsky, M.R., Masiello, C.A., Valentine, D.W., Finney, B.P. and Baldock, J.A. (2010) Topographic controls on black carbon accumulation

in Alaskan black spruce forest soils: Implications for organic matter dynamics. *Biogeochemistry* **100**, 39-56.

Kapaev, R.R. and Toukach, P.V. (2016) Simulation of 2D NMR spectra of carbohydrates using GODESS software. *J Chem Inf Model* **56**, 1100-1104.

Kappenberg, A., Bläsing, M., Lehndorff, E. and Amelung, W. (2016) Black carbon assessment using benzene polycarboxylic acids: Limitations for organic-rich matrices. *Org Geochem* **94**, 47-51.

Kendrick, E. (1963) A mass scale based on CH_2 = 14.0000 for high resolution mass spectrometry of organic compounds. *Anal Chem* **35**, 2146-2154.

Khatami, S., Deng, Y., Tien, M. and Hatcher, P.G. (2019a) Formation of water-soluble organic matter through fungal degradation of lignin. *Org Geochem* **135**, 64-70.

Khatami, S., Deng, Y., Tien, M. and Hatcher, P.G. (2019b) Lignin contribution to aliphatic constituents of humic acids through fungal degradation. *J Environ Qual* **48**, 1565-1570.

Khodadad, C.L.M., Zimmerman, A.R., Green, S.J., Uthandi, S. and Foster, J.S. (2011) Taxa-specific changes in soil microbial community composition induced by pyrogenic carbon amendments. *Soil Biol Biochem* **43**, 385-392.

Kieber, D.J., McDaniel, J. and Mopper, K. (1989) Photochemical source of biological substrates in sea water: Implications for carbon cycling. *Nature* **341**, 637-639.

Kim, S., Kaplan, L.A. and Hatcher, P.G. (2006) Biodegradable dissolved organic matter in a temperate and a tropical stream determined from ultra-high resolution mass spectrometry. *Limnol Oceanogr* **51**, 1054-1063.

Kim, S., Kramer, R.W. and Hatcher, P.G. (2003) Graphical method for analysis of ultrahigh-resolution broadband mass spectra of natural organic matter, the van Krevelen diagram. *Anal Chem* **75**, 5336-5344.

Kirchman, D.L. (2018) *Processes in microbial ecology*, Second ed. Oxford University Press.

Klevit, R.E. (1985) Improving two-dimensional NMR spectra by t_1 ridge subtraction. *J Magn Reson* **62**, 551-555.

Koch, B.P. and Dittmar, T. (2006) From mass to structure: An aromaticity index for high-resolution mass data of natural organic matter. *Rapid Commun Mass Sp* **20**, 926-932.

Koch, B.P. and Dittmar, T. (2016) From mass to structure: An aromaticity index for high-resolution mass data of natural organic matter (Erratum). *Rapid Commun Mass Sp* **30**, 1.

Koch, B.P., Dittmar, T., Witt, M. and Kattner, G. (2007) Fundamentals of molecular formula assignment to ultrahigh resolution mass data of natural organic matter. *Anal Chem* **79**, 1758-1763.

Kolb, S. and Stacheter, A. (2013) Prerequisites for amplicon pyrosequencing of microbial methanol utilizers in the environment. *Front Microbiol* **4**, 1-12.

Kothawala, D.N., Murphy, K.R., Stedmon, C.A., Weyhenmeyer, G.A. and Tranvik, L.J. (2013) Inner filter correction of dissolved organic matter fluorescence. *Limnol Oceanogr Meth* **11**, 616-630.

Kroll, J.H., Donahue, N.M., Jimenez, J.L., Kessler, S.H., Canagaratna, M.R., Wilson, K.R., Altieri, K.E., Mazzoleni, L.R., Wozniak, A.S., Bluhm, H., Mysak, E.R., Smith, J.D., Kolb, C.E. and Worsnop, D.R. (2011) Carbon oxidation state as a metric for describing the chemistry of atmospheric organic aerosol. *Nature Chem* **3**, 133-139.

Kuhlbusch, T.A.J. and Crutzen, P.J. (1996) Black carbon, the global carbon cycle, and atmospheric carbon dioxide. In: *Biomass Burning and Global Change* (eds. Levine, J.S.), The MIT Press, Cambridge, pp. 160-169.

Kujawinski, E.B. and Behn, M.D. (2006) Automated analysis of electrospray ionization Fourier transform ion cyclotron resonance mass spectra of natural organic matter. *Anal Chem* **78**, 4363-4373.

Kujawinski, E.B., Del Vecchio, R., Blough, N.V., Klein, G.C. and Marshall, A.G. (2004) Probing molecular-level transformations of dissolved organic matter: Insights on photochemical degradation and protozoan modification of DOM from electrospray ionization Fourier transform ion cyclotron resonance mass spectrometry. *Mar Chem* **92**, 23-37.

Kuzyakov, Y., Bogomolova, I. and Glaser, B. (2014) Biochar stability in soil: Decomposition during eight years and transformation as assessed by compound-specific ^{14}C analysis. *Soil Biol Biochem* **70**, 229-236.

Kuzyakov, Y., Subbotina, I., Chen, H., Bogomolova, I. and Xu, X. (2009) Black carbon decomposition and incorporation into soil microbial biomass estimated by ^{14}C labeling. *Soil Biol Biochem* **41**, 210-219.

Laird, D.A., Chappell, M.A., Martens, D.A., Wershaw, R.L. and Thompson, M. (2008) Distinguishing black carbon from biogenic humic substances in soil clay fractions. *Geoderma* **143**, 115-122.

Lalonde, K., Vähätalo, A.V. and Gélinas, Y. (2014) Revisiting the disappearance of terrestrial dissolved organic matter in the ocean: a δ^{13}C study. *Biogeosciences* **11**, 3707-3719.

Lam, B. and Simpson, A.J. (2008) Direct ^{1}H NMR spectroscopy of dissolved organic matter in natural waters. *The Analyst* **133**, 263-269.

LaRowe, D.E. and Van Cappellen, P. (2011) Degradation of natural organic matter: A thermodynamic analysis. *Geochim Cosmochim Ac* **75**, 2030-2042.

Laszakovits, J.R., Somogyi, A. and MacKay, A.A. (2020) Chemical alterations of dissolved organic matter by permanganate oxidation. *Environ Sci Technol* **54**, 3256-3266.

Latch, D.E. and McNeill, K. (2006) Microheterogeneity of singlet oxygen distributions in irradiated humic acid solutions. *Science* **311**, 1743-1747.

Laurent, F., Cébron, A., Schwartz, C. and Leyval, C. (2012) Oxidation of a PAH polluted soil using modified Fenton reaction in unsaturated condition affects biological and physico-chemical properties. *Chemosphere* **86**, 659-664.

Lechtenfeld, O.J., Hertkorn, N., Shen, Y., Witt, M. and Benner, R. (2015) Marine sequestration of carbon in bacterial metabolites. *Nat Commun* **6**, 1-8.

Lehmann, J. (2007) A handful of carbon. *Nature* **447**, 143-144.

Lemaire, J., Laurent, F., Leyval, C., Schwartz, C., Buès, M. and Simonnot, M.O. (2013) PAH oxidation in aged and spiked soils investigated by column experiments. *Chemosphere* **91**, 406-414.

Li, J., Chen, Y., He, L., Liang, N., Wang, L., Zhao, J. and Pan, B. (2020) Sorption of sulfamethoxazole on biochars of varying mineral content. *Environ Sci Proc Imp* **22**, 1287-1294.

Li, M., Bao, F., Zhang, Y., Sheng, H., Chen, C. and Zhao, J. (2019) Photochemical aging of soot in the aqueous phase: Release of dissolved black carbon and the formation of $^1O_2$. *Environ Sci Technol* **53**, 12311-12319.

Li, M.D., Yeung, C.S., Guan, X., Ma, J., Li, W., Ma, C. and Phillips, D.L. (2011) Water- and acid-mediated excited-state intramolecular proton transfer and decarboxylation reactions of ketoprofen in water-rich and acidic aqueous solutions. *Chem Eur J* **17**, 10935-10950.

Liitiä, T.M., Maunu, S.L., Hortling, B., Toikka, M. and Kilpeläinen, I. (2003) Analysis of technical lignins by two- and three-dimensional NMR spectroscopy. *J Agric Food Chem* **51**, 2136-2143.

Lindell, M.J., Granéli, W. and Tranvik, L.J. (1995) Enhanced bacterial growth in response to photochemical transformation of dissolved organic matter. *Limnol Oceanogr* **40**, 195-199.

Liu, G., Zheng, H., Jiang, Z., Zhao, J., Wang, Z., Pan, B. and Xing, B. (2018) Formation and physicochemical characteristics of nano biochar: Insight into chemical and colloidal stability. *Environ Sci Technol* **52**, 10369-10379.

Liu, H., Zhou, P., Wu, X., Sun, J. and Chen, S. (2015) Radical scavenging by acetone: A new perspective to understand laccase/ABTS inactivation and to recover redox mediator. *Molecules* **20**, 19907-19913.

Liu, M., Mao, X.-a., Ye, C., Huang, H., Nicholson, J.K. and Lindon, J.C. (1998) Improved WATERGATE pulse sequences for solvent suppression in NMR spectroscopy. *J Magn Reson* **132**, 125-129.

Lorenz, K. and Lal, R. (2014) Biochar application to soil for climate change mitigation by soil organic carbon sequestration. *J Plant Nutr Soil Sci* **177**, 651-670.

Macko, S.A. and Estep, M.L.F. (1984) Microbial alteration of stable nitrogen and carbon isotopic compositions of organic matter. *Org Geochem* **6**, 787-790.

Mamy, L., Patureau, D., Barriuso, E., Bedos, C., Bessac, F., Louchart, X., Martin-laurent, F., Miege, C. and Benoit, P. (2015) Prediction of the fate of organic compounds in

the environment from their molecular properties: A review. *Crit Rev Env Sci Tec* **45**, 1277-1377.

Mangin, F., Banaszak-Léonard, E. and Len, C. (2015) One-step Barton decarboxylation by micellar catalysis - Application to the synthesis of maleimide derivatives. *RSC Adv* **5**, 69616-69620.

Mao, J., Cao, X., Olk, D.C., Chu, W. and Schmidt-Rohr, K. (2017) Advanced solid-state NMR spectroscopy of natural organic matter. *Prog Nucl Magn Reson Spectrosc* **100**, 17-51.

Marques, J.S.J., Dittmar, T., Niggemann, J., Almeida, M.G., Gomez-Saez, G.V. and Rezende, C.E. (2017) Dissolved black carbon in the headwaters-to-ocean continuum of Paraíba Do Sul River, Brazil. *Front Earth Sci* **5**, 1-12.

Marquès, M., Mari, M., Audí-Miró, C., Sierra, J., Soler, A., Nadal, M. and Domingo, J.L. (2016) Photodegradation of polycyclic aromatic hydrocarbons in soils under a climate change base scenario. *Chemosphere* **148**, 495-503.

Masiello, C.A. (2004) New directions in black carbon organic geochemistry. *Mar Chem* **92**, 201-213.

Masiello, C.A. and Druffel, E.R.M. (1998) Black carbon in deep-sea sediments. *Science* **280**, 1911-1913.

Matsumoto, A., Matsumura, T. and Aoki, S. (1996) Stereospecific polymerization of dialkyl muconates through free radical polymerization: Isotropic polymerization and topochemical polymerization. *Macromolecules* **29**, 423-432.

Matsumoto, A., Yokoi, K., Aoki, S., Tashiro, K., Kamae, T. and Kobayashi, M. (1998) Crystalline-state polymerization of diethyl(Z,Z)-2,4-hexadienedioate via a radical chain reaction mechanism to yield an ultrahigh-molecular-weight and stereoregular polymer. *Macromolecules* **31**, 2129-2136.

McCarthy, M., Pratum, T., Hedges, J. and Benner, R. (1997) Chemical composition of dissolved organic nitrogen in the ocean. *Nature* **390**, 150-154.

McCarthy, M.D., Hedges, J.I. and Benner, R. (1998) Major bacterial contribution to marine dissolved organic nitrogen. *Science* **281**, 231-234.

McKee, G.A., Kobiela, M.E. and Hatcher, P.G. (2014) Effect of Michael Adduction on Peptide Preservation in Natural Waters. *Environ Sci Proc Imp* **16**, 2087-2097.

McNally, A.M., Moody, E.C. and McNeill, K. (2005) Kinetics and mechanism of the sensitized photodegradation of lignin model compounds. *Photochem Photobiol Sci* **4**, 268-274.

Miller, M.P., Simone, B.E., McKnight, D.M., Cory, R.M., Williams, M.W. and Boyer, E.W. (2010) New light on a dark subject: Comment. *Aquat Sci* **72**, 269-275.

Miranda, M.L., Osterholz, H., Giebel, H.A., Bruhnke, P., Dittmar, T. and Zielinski, O. (2020) Impact of UV radiation on DOM transformation on molecular level using FT-ICR-MS and PARAFAC. *Spectrochim Acta A Mol Biomol Spectrosc* **230**, 1-12.

Mitchell, P., Simpson, A., Soong, R. and Simpson, M. (2018) Nuclear magnetic resonance analysis of changes in dissolved organic matter composition with successive layering on clay mineral surfaces. *Soil Syst* **2**, 1-17.

Moody, G.J. (1963) The action of Fenton's reagent on carbohydrates. *Tetrahedron* **19**, 1705-1710.

Mopper, K. and Kieber, D.J. (2000) Marine photochemistry and its impact on carbon cycling. In: *The Effects of UV Radiation in the Marine Environment* (eds. Mora, S.D., Demers, S., Vernet, M.), Cambridge University Press, Cambridge, U.K., pp. 101-129.

Mopper, K. and Kieber, D.J. (2002) Photochemistry and the cycling of carbon, sulfur, nitrogen and phosphorus. In: *Biogeochemistry of Marine Dissolved Organic Matter* (eds. Hansell, D.A., Carlson, C.A.), Academic Press, San Diego, pp. 455-507.

Moran, M.A. and Covert, J.S. (2003) Photochemically mediated linkages between dissolved organic matter and bacterioplankton. In: *Aquatic Ecosystems* (eds. Findlay, S.E.G., Sinsabaugh, R.L.), Academic Press, Burlington, pp. 243-262.

Moran, M.A., Kujawinski, E.B., Stubbins, A., Fatland, R., Aluwihare, L.I., Buchan, A., Crump, B.C., Dorrestein, P.C., Dyhrman, S.T., Hess, N.J., Howe, B., Longnecker, K., Medeiros, P.M., Niggemann, J., Obernosterer, I., Repeta, D.J. and Waldbauer, J.R. (2016) Deciphering ocean carbon in a changing world. *Proc Natl Acad Sci USA* **113**, 3143-3151.

Morelli, R., Russo-Volpe, S., Bruno, N. and Lo Scalzo, R. (2003) Fenton-dependent damage to carbohydrates: Free radical scavenging activity of some simple sugars. *J Agric Food Chem* **51**, 7418-7425.

Mouteva, G.O., Randerson, J.T., Fahrni, S.M., Bush, S.E., Ehleringer, J.R., Xu, X., Santos, G.M., Kuprov, R., Schichtel, B.A. and Czimczik, C.I. (2017) Using radiocarbon to constrain black and organic carbon aerosol sources in Salt Lake City. *J Geophys Res Atmos* **122**, 9843-9857.

Múčka, V., Bláha, P., Čuba, V. and Červenák, J. (2013) Influence of various scavengers of •OH radicals on the radiation sensitivity of yeast and bacteria. *Int J Radiat Biol* **89**, 1045-1052.

Mukherjee, A. and Zimmerman, A.R. (2013) Organic carbon and nutrient release from a range of laboratory-produced biochars and biochar-soil mixtures. *Geoderma* **193-194**, 122-130.

Mukherjee, A., Zimmerman, A.R. and Harris, W. (2011) Surface chemistry variations among a series of laboratory-produced biochars. *Geoderma* **163**, 247-255.

Murphy, K.R. (2011) A note on determining the extent of the water Raman peak in fluorescence spectroscopy. *Appl Spectrosc* **65**, 233-236.

Murphy, K.R., Butler, K.D., Spencer, R.G.M., Stedmon, C.A., Boehme, J.R. and Aiken, G.R. (2010) Measurement of dissolved organic matter fluorescence in aquatic environments: An interlaboratory comparison. *Environ Sci Technol* **44**, 9405-9412.

Murphy, K.R., Stedmon, C.A., Graeber, D. and Bro, R. (2013) Fluorescence spectroscopy and multi-way techniques. PARAFAC. *Anal Methods* **5**, 6541–6882.

Nalven, S.G., Ward, C.P., Payet, J.P., Cory, R.M., Kling, G.W., Sharpton, T.J., Sullivan, C.M. and Crump, B.C. (2020) Experimental metatranscriptomics reveals the costs and benefits of dissolved organic matter photo-alteration for freshwater microbes. *Environ Microbiol* **22**, 3505–3521.

Neff, J.M. (1979) *Polycyclic aromatic hydrocarbons in the aquatic environment*. Applied Science Publishers, London, UK.

Obernosterer, I. and Benner, R. (2004) Competition between biological and photochemical processes in the mineralization of dissolved organic carbon. *Limnol Oceanogr* **49**, 117-124.

Opsahl, S. and Benner, R. (1998) Photochemical reactivity of dissolved lignin in river and ocean waters. *Limnol Oceanogr* **43**, 1297-1304.

Osterholz, H., Kirchman, D.L., Niggemann, J. and Dittmar, T. (2016) Environmental drivers of dissolved organic matter molecular composition in the Delaware estuary. *Front Earth Sci* **4**, 1-14.

Page, S.E., Kling, G.W., Sander, M., Harrold, K.H., Logan, J.R., McNeill, K. and Cory, R.M. (2013) Dark formation of hydroxyl radical in arctic soil and surface waters. *Environ Sci Technol* **47**, 12860-12867.

Page, S.E., Sander, M., Arnold, W.A. and McNeill, K. (2012) Hydroxyl radical formation upon oxidation of reduced humic acids by oxygen in the dark. *Environ Sci Technol* **46**, 1590-1597.

Patriarca, C., Balderrama, A., Može, M., Sjöberg, P.J.R., Bergquist, J., Tranvik, L.J. and Hawkes, J.A. (2020) Investigating the ionization of dissolved organic matter by electrospray ionization. *Anal Chem* **92**, 14210-14218.

Penning, T.M., Burczynski, M.E., Hung, C.-F., McCoull, K.D., Palackal, N.T. and Tsuruda, L.S. (1999) Dihydrodiol dehydrogenases and polycyclic aromatic hydrocarbon activation: Generation of reactive and redox active o-quinones. *Chem Res Toxicol* **12**, 1-18.

Pfeffer, P.E., Gerasimowicz, W.V. and Piotrowski, E.G. (1984) Effect of paramagnetic iron on quantitation in carbon-13 cross polarization magic angle spinning nuclear magnetic resonance spectrometry of heterogeneous environmental matrixes. *Anal Chem* **56**, 734-741.

Pham, A.N., Xing, G., Miller, C.J. and Waite, T.D. (2013) Fenton-like copper redox chemistry revisited: Hydrogen peroxide and superoxide mediation of copper-catalyzed oxidant production. *J Catal* **301**, 54-64.

Porcal, P., Dillon, P.J. and Molot, L.A. (2013) Photochemical production and decomposition of particulate organic carbon in a freshwater stream. *Aquat Sci* **75**, 469-482.

Powers, L.C., Hertkorn, N., McDonald, N., Schmitt-Kopplin, P., Del Vecchio, R., Blough, N.V. and Gonsior, M. (2019) *Sargassum sp.* act as a large regional surce of marine dissolved organic carbon and polyphenols. *Global Biogeochem Cy* **33**, 1423-1439.

Psillakis, E., Goula, G., Kalogerakis, N. and Mantzavinos, D. (2004) Degradation of polycyclic aromatic hydrocarbons in aqueous solutions by ultrasonic irradiation. *J Hazard Mater* **108**, 95-102.

Pullen, S.H., Anderson, N.A., II, L.A.W. and Sension, R.J. (1998) The ultrafast photochemical ring-opening reaction of 1,3-cyclohexadiene in cyclohexane. *J Chem Phys* **108**, 556-563.

Pullin, M.J., Bertilsson, S., Goldstone, J.V. and Voelker, B.M. (2004) Effects of sunlight and hydroxyl radical on dissolved organic matter: Bacterial growth efficiency and production of carboxylic acids and other substrates. *Limnol Oceanogr* **49**, 2011-2022.

Qi, Y., Fu, W., Tian, J., Luo, C., Shan, S., Sun, S., Ren, P., Zhang, H., Liu, J., Zhang, X. and Wang, X. (2020) Dissolved black carbon is not likely a significant refractory organic carbon pool in rivers and oceans. *Nat Commun* **11**, 1-11.

Qualls, R.G. and Richardson, C.J. (2003) Factors controlling concentration, export, and decomposition of dissolved organic nutrients in the Everglades of Florida. *Biogeochemistry* **62**, 197-229.

Quan, G., Fan, Q., Zimmerman, A.R., Sun, J., Cui, L., Wang, H., Gao, B. and Yan, J. (2020) Effects of laboratory biotic aging on the characteristics of biochar and its water-soluble organic products. *J Hazard Mater* **382**, 1-9.

Raymond, P.A. and Bauer, J.E. (2001) Use of ^{14}C and ^{13}C natural abundances for evaluating riverine, estuarine, and coastal DOC and POC sources and cycling: A review and synthesis. *Org Geochem* **32**, 469-485.

Reisser, M., Purves, R.S., Schmidt, M.W.I. and Abiven, S. (2016) Pyrogenic carbon in soils: A literature-based inventory and a global estimation of its content in soil organic carbon and stocks. *Front Earth Sci* **4**, 1-14.

Richter, H. and Howard, J.B. (2000) Formation of polycyclic aromatic hydrocarbons and their growth to soot - a review of chemical reaction pathways. *Prog Energ Combust* **26**, 565-608.

Riedel, T., Biester, H. and Dittmar, T. (2012) Molecular fractionation of dissolved organic matter with metal salts. *Environ Sci Technol* **46**, 4419-4426.

Riedel, T., Zark, M., Vähätalo, A.V., Niggemann, J., Spencer, R.G.M., Hernes, P.J. and Dittmar, T. (2016) Molecular signatures of biogeochemical transformations in dissolved organic matter from ten world rivers. *Front Earth Sci* **4**, 1-16.

Rivas, J., Gimeno, O., de la Calle, R.G. and Beltran, F.J. (2009) Ozone treatment of PAH contaminated soils: Operating variables effect. *J Hazard Mater* **169**, 509-515.

Roebuck, J.A., Podgorksi, D.C., Wagner, S. and Jaffé, R. (2017) Photodissolution of charcoal and fire-impacted soil as a potential source of dissolved black carbon in aquatic environments. *Org Geochem* **112**, 16-21.

Romano, S., Dittmar, T., Bondarev, V., Weber, R.J.M., Viant, M.R. and Schulz-Vogt, H.N. (2014) Exo-metabolome of *Pseudovibrio sp.* FO-BEG1 analyzed by ultra-high resolution mass spectrometry and the effect of phosphate limitation. *PLoS ONE* **9**, 1-11.

Rossel, P.E., Stubbins, A., Rebling, T., Koschinsky, A., Hawkes, J.A. and Dittmar, T. (2017) Thermally altered marine dissolved organic matter in hydrothermal fluids. *Org Geochem* **110**, 73-86.

Rossel, P.E., Vähätalo, A.V., Witt, M. and Dittmar, T. (2013) Molecular composition of dissolved organic matter from a wetland plant (*Juncus effusus*) after photochemical and microbial decomposition (1.25 yr): Common features with deep sea dissolved organic matter. *Org Geochem* **60**, 62-71.

Roth, V.-N., Lange, M., Simon, C., Hertkorn, N., Bucher, S., Goodall, T., Griffiths, R.I., Mellado-Vázquez, P.G., Mommer, L., Oram, N.J., Weigelt, A., Dittmar, T. and Gleixner, G. (2019) Persistence of dissolved organic matter explained by molecular changes during its passage through soil. *Nat Geosci* **12**, 755-761.

Santín, C., Doerr, S.H., Kane, E.S., Masiello, C.A., Ohlson, M., de la Rosa, J.M., Preston, C.M. and Dittmar, T. (2016a) Towards a global assessment of pyrogenic carbon from vegetation fires. *Glob Chang Biol* **22**, 76-91.

Santín, C., Doerr, S.H., Merino, A., Bryant, R. and Loader, N.J. (2016b) Forest floor chemical transformations in a boreal forest fire and their correlations with temperature and heating duration. *Geoderma* **264**, 71-80.

Santín, C., Doerr, S.H., Merino, A., Bucheli, T.D., Bryant, R., Ascough, P., Gao, X. and Masiello, C.A. (2017) Carbon sequestration potential and physicochemical

properties differ between wildfire charcoals and slow-pyrolysis biochars. *Sci Rep* **7**, 1-11.

Santín, C., Doerr, S.H., Preston, C.M. and Gonzalez-Rodriguez, G. (2015) Pyrogenic organic matter production from wildfires: A missing sink in the global carbon cycle. *Glob Chang Biol* **21**, 1621-1633.

Santschi, P.H., Guo, L., Baskaran, M., Trumbore, S., Southon, J., Bianchi, T.S., Honeyman, B. and Cifuentes, L. (1995) Isotopic evidence for the contemporary origin of high-molecular weight organic matter in oceanic environments. *Geochim Cosmochim Ac* **59**, 625-631.

Sato, K., Hyodo, M., Takagi, J., Aoki, M. and Noyori, R. (2000) Hydrogen peroxide oxidation of aldehydes to carboxylic acids: An organic solvent-, halide- and metal-free procedure. *Tetrahedron Lett* **41**, 1439-1442.

Schmidt, M.W.I. and Noack, A.G. (2000) Black carbon in soils and sediments: Analysis, distribution, implications, and current challenges. *Global Biogeochem Cy* **14**, 777-793.

Schneider, M.P.W., Hilf, M., Vogt, U.F. and Schmidt, M.W.I. (2010) The benzene polycarboxylic acid (BPCA) pattern of wood pyrolyzed between 200 ^{O}C and 1000 ^{O}C. *Org Geochem* **41**, 1082-1088.

Schulten, H.R. and Schnitzer, M. (1998) The chemistry of soil organic nitrogen: A review. *Biol Fertil Soils* **26**, 1-15.

Scully, N.M., Cooper, W.J. and Tranvik, L.J. (2003) Photochemical effects on microbial activity in natural waters: The interaction of reactive oxygen species and dissolved organic matter. *FEMS Microbiol Ecol* **46**, 353-357.

Sigman, M.E., Schuler, P.F., Ghosh, M.M. and Dabestani, R.T. (1998) Mechanism of pyrene photochemical oxidation in aqueous and surfactant solutions. *Environ Sci Technol* **32**, 3980-3985.

Sigman, M.E., Zingg, S.P., Pagni, R.M. and Burns, J.H. (1991) Photochemistry of anthracene in water. *Tetrahedron Lett* **32**, 5737-5740.

Silverstein, R.M., Webster, F. and Kiemle, D. (2005) *Spectrometric identification of organic compounds*. John Wiley & Sons, Inc., Hoboken, NJ.

Simpson, A. (2001) Multidimensional solution state NMR of humic substances: A practical guide and review. *Soil Sci* **166**, 795-809.

Simpson, A.J. (2002) Determining the molecular weight, aggregation, structures and interactions of natural organic matter using diffusion ordered spectroscopy. *Magn Reson Chem* **40**, S72-S82.

Simpson, A.J., McNally, D.J. and Simpson, M.J. (2011) NMR spectroscopy in environmental research: From molecular interactions to global processes. *Prog Nucl Magn Reson Spectrosc* **58**, 97-175.

Simpson, A.J. and Simpson, M.J. (2009) Nuclear magnetic resonance analysis of natural organic matter. In: *Biophysico-chemical processes involving natural nonliving organic matter in environmental systems* (eds. Senesi, N., Xing, B., Huang, P.M.), pp. 589-650.

Sinsabaugh, R.L., Findlay, S., Franchini, P. and Fischer, D. (1997) Enzymatic analysis of riverine bacterioplankton production. *Limnol Oceanogr: Methods* **42**, 29-38.

Skjemstad, J., Reicosky, D.C., Wilts, A. and McGowan, J. (2002) Charcoal carbon in U.S. agricultural soils. *Soil Sci Soc Am J* **66**, 1249-1255.

Sleighter, R.L., Chen, H., Wozniak, A.S., Willoughby, A.S., Caricasole, P. and Hatcher, P.G. (2012) Establishing a measure of reproducibility of ultrahigh-resolution mass spectra for complex mixtures of natural organic matter. *Anal Chem* **84**, 9184-9191.

Sleighter, R.L. and Hatcher, P.G. (2007) The application of electrospray ionization coupled to ultrahigh resolution mass spectrometry for the molecular characterization of natural organic matter. *J Mass Spectrom* **42**, 559-574.

Sleighter, R.L. and Hatcher, P.G. (2008) Molecular characterization of dissolved organic matter (DOM) along a river to ocean transect of the lower Chesapeake Bay by ultrahigh resolution electrospray ionization Fourier transform ion cyclotron resonance mass spectrometry. *Mar Chem* **110**, 140-152.

Sleighter, R.L., McKee, G.A., Liu, Z. and Hatcher, P.G. (2008) Naturally present fatty acids as internal calibrants for Fourier transform mass spectra of dissolved organic matter. *Limnol Oceanogr Meth* **6**, 246-253.

Smith, C.R., Hatcher, P.G., Kumar, S. and Lee, J.W. (2016) Investigation into the sources of biochar water-soluble organic compounds and their potential toxicity on aquatic microorganisms. *ACS Sustain Chem Eng* **4**, 2550-2558.

Søndergaard, M. and Middelboe, M. (1995) A cross-system analysis of labile dissolved organic carbon. *Mar Ecol Prog Ser* **118**, 283-294.

Spence, A., Simpson, A.J., McNally, D.J., Moran, B.W., McCaul, M.V., Hart, K., Paull, B. and Kelleher, B.P. (2011) The degradation characteristics of microbial biomass in soil. *Geochim Cosmochim Ac* **75**, 2571-2581.

Spencer, R.G.M., Mann, P.J., Dittmar, T., Eglinton, T.I., McIntyre, C., Holmes, R.M., Zimov, N. and Stubbins, A. (2015) Detecting the signature of permafrost thaw in Arctic rivers. *Geophys Res Lett* **42**, 2830-2835.

Spencer, R.G.M., Stubbins, A., Hernes, P.J., Baker, A., Mopper, K., Aufdenkampe, A.K., Dyda, R.Y., Mwamba, V.L., Mangangu, A.M., Wabakanghanzi, J.N. and Six, J. (2009) Photochemical degradation of dissolved organic matter and dissolved lignin phenols from the Congo River. *J Geophys Res* **114**, 1-12.

Spokas, K.A., Cantrell, K.B., Novak, J.M., Archer, D.W., Ippolito, J.A., Collins, H.P., Boateng, A.A., Lima, I.M., Lamb, M.C., McAloon, A.J., Lentz, R.D. and Nichols, K.A. (2012) Biochar: A synthesis of its agronomic impact beyond carbon sequestration. *J Environ Qual* **41**, 973-989.

Spokas, K.A., Novak, J.M., Stewart, C.E., Cantrell, K.B., Uchimiya, M., DuSaire, M.G. and Ro, K.S. (2011) Qualitative analysis of volatile organic compounds on biochar. *Chemosphere* **85**, 869-882.

Stenson, A.C., Marshall, A.G. and Cooper, W.T. (2003) Exact masses and chemical formulas of individual Suwannee River fulvic acids from ultrahigh resolution electrospray ionization Fourier transform ion cyclotron resonance mass spectra. *Anal Chem* **75**, 1275-1284.

Stenson, A.C., William, M., Marshall, A.G. and Cooper, W.T. (2002) Ionization and fragmentation of humic substances in electrospray ionization Fourier transform-ion cyclotron resonance mass spectrometry. *Anal Chem* **74**, 4397-4409.

Stevenson, F.J. (1994) *Humus chemistry: Genesis, composition, reactions*. John Wiley & Sons, Canada.

Stubbins, A., Hubbard, V., Uher, G., Law, C.S., Upstill-Goddard, R.C., Aiken, G.R. and Mopper, K. (2008) Relating carbon monoxide photoproduction to dissolved organic matter functionality. *Environ Sci Technol* **42**, 3271-3276.

Stubbins, A., Niggemann, J. and Dittmar, T. (2012) Photo-lability of deep ocean dissolved black carbon. *Biogeosciences* **9**, 1661-1670.

Stubbins, A., Silva, L.M., Dittmar, T. and Van Stan, J.T. (2017) Molecular and optical properties of tree-derived dissolved organic matter in throughfall and stemflow from live oaks and eastern red cedar. *Front Earth Sci* **5**, 1-13.

Stubbins, A., Spencer, R.G.M., Chen, H.M., Hatcher, P.G., Mopper, K., Hernes, P.J., Mwamba, V.L., Mangangu, A.M., Wabakanghanzi, J.N. and Six, J. (2010) Illuminated darkness: Molecular signatures of Congo River dissolved organic matter and its photochemical alteration as revealed by ultrahigh precision mass spectrometry. *Limnol Oceanogr* **55**, 1467-1477.

Stubbins, A., Spencer, R.G.M., Mann, P.J., Holmes, R.M., McClelland, J.W., Niggemann, J. and Dittmar, T. (2015) Utilizing colored dissolved organic matter to derive dissolved black carbon export by Arctic rivers. *Front Earth Sci* **3**, 1-11.

Sun, L., Xu, C., Zhang, S., Lin, P., Schwehr, K.A., Quigg, A., Chiu, M.-H., Chin, W.-C. and Santschi, P.H. (2017) Light-induced aggregation of microbial exopolymeric substances. *Chemosphere* **181**, 675-681.

Szidat, S., Prévôt, A.S.H., Sandradewi, J., Alfarra, M.R., Synal, H.-A., Wacker, L. and Baltensperger, U. (2007) Dominant impact of residential wood burning on particulate matter in Alpine valleys during winter. *Geophys Res Lett* **34**, 1-6.

Thevenot, M., Dignac, M.-F. and Rumpel, C. (2010) Fate of lignins in soils: A review. *Soil Biol Biochem* **42**, 1200-1211.

Tong, M., Yuan, S., Ma, S., Jin, M., Liu, D., Cheng, D., Liu, X., Gan, Y. and Wang, Y. (2016) Production of abundant hydroxyl radicals from oxygenation of subsurface sediments. *Environ Sci Technol* **50**, 214-221.

Toteva, M.M. and Richard, J.P. (2011) The generation and reactions of quinone methides. *Adv Phys Org Chem* **45**, 39-91.

Travis, B.R., Sivakumar, M., Hollist, G.O. and Borhan, B. (2003) Facile oxidation of aldehydes to acids and esters with oxone. *Org Lett* **5**, 1031-1034.

Tremblay, L.B., Dittmar, T., Marshall, A.G., Cooper, W.J. and Cooper, W.T. (2007) Molecular characterization of dissolved organic matter in a North Brazilian mangrove porewater and mangrove-fringed estuaries by ultrahigh resolution Fourier transform-ion cyclotron resonance mass spectrometry and excitation/emission spectroscopy. *Mar Chem* **105**, 15-29.

Trusiak, A., Treibergs, L., Kling, G. and Cory, R. (2018) The controls of iron and oxygen on hydroxyl radical (•OH) production in soils. *Soil Syst* **3**, 1-23.

Tynkkynen, T., Tiainen, M., Soininen, P. and Laatikainen, R. (2009) From proton nuclear magnetic resonance spectra to pH. Assessment of ^{1}H NMR pH indicator compound set for deuterium oxide solutions. *Anal Chim Acta* **648**, 105-112.

Umezawa, T. and Higuchi, T. (1987) Formation of a muconate in aromatic ring cleavage of a β-O-4 lignin substructure model by lignin peroxidase. *Agric Biol Chem* **51**, 2281-2284.

Umezawa, T., Nakatsubo, F. and Higuchi, T. (1983) Deradation pathway of arylglycerol-β-aryl ethers by *Phanerochaete chrysosporium*. *Agric Biol Chem* **47**, 2677-2681.

Vähätalo, A.V. and Wetzel, R.G. (2008) Long-term photochemical and microbial decomposition of wetland-derived dissolved organic matter with alteration of ^{13}C:^{12}C mass ratio. *Limnol Oceanogr* **53**, 1387-1392.

Valle, J., Harir, M., Gonsior, M., Enrich-Prast, A., Schmitt-Kopplin, P., Bastviken, D. and Hertkorn, N. (2020) Molecular differences between water column and sediment pore water SPE-DOM in ten Swedish boreal lakes. *Water Res* **170**, 1-11.

Van Krevelen, D.W. (1950) Graphical-statistical method for the study of structure and reaction processes of coal. *Fuel Process Technol* **29**, 269-228.

Vlahov, G. (1999) Application of NMR to the study of olive oils. *Prog Nucl Magn Reson Spectrosc* **35**, 341-357.

Vollmer, W., Blanot, D. and De Pedro, M.A. (2008) Peptidoglycan structure and architecture. *FEMS Microbiol Rev* **32**, 149-167.

Vorobev, A., Sharma, S., Yu, M., Lee, J., Washington, B.J., Whitman, W.B., Ballantyne, F.t., Medeiros, P.M. and Moran, M.A. (2018) Identifying labile DOM components in a coastal ocean through depleted bacterial transcripts and chemical signals. *Environ Microbiol* **20**, 3012-3030.

Waggoner, D.C., Chen, H., Willoughby, A.S. and Hatcher, P.G. (2015) Formation of black carbon-like and alicyclic aliphatic compounds by hydroxyl radical initiated degradation of lignin. *Org Geochem* **82**, 69-76.

Waggoner, D.C. and Hatcher, P.G. (2017) Hydroxyl radical alteration of HPLC fractionated lignin: Formation of new compounds from terrestrial organic matter. *Org Geochem* **113**, 315-325.

Waggoner, D.C., Wozniak, A.S., Cory, R.M. and Hatcher, P.G. (2017) The role of reactive oxygen species in the degradation of lignin derived dissolved organic matter. *Geochim Cosmochim Ac* **208**, 171-184.

Wagner, S., Brandes, J., Goranov, A.I., Drake, T.W., Spencer, R.G.M. and Stubbins, A. (2017a) Online quantification and compound-specific stable isotopic analysis of black carbon in environmental matrices via liquid chromatography-isotope ratio mass spectrometry. *Limnol Oceanogr Meth* **15**, 995-1006.

Wagner, S., Brandes, J., Spencer, R.G.M., Ma, K., Rosengard, S.Z., Moura, J.M.S. and Stubbins, A. (2019a) Isotopic composition of oceanic dissolved black carbon reveals non-riverine source. *Nat Commun* **10**, 1-8.

Wagner, S., Brantley, S., Stuber, S., Van Stan, J., Whitetree, A. and Stubbins, A. (2019b) Dissolved black carbon in throughfall and stemflow in a fire-managed longleaf pine woodland. *Biogeochemistry*, 191-207.

Wagner, S., Cawley, K.M., Rosario-Ortiz, F.L. and Jaffé, R. (2015a) In-stream sources and links between particulate and dissolved black carbon following a wildfire. *Biogeochemistry* **124**, 145-161.

Wagner, S., Ding, Y. and Jaffé, R. (2017b) A new perspective on the apparent solubility of dissolved black carbon. *Front Earth Sci* **5**, 1-16.

Wagner, S., Dittmar, T. and Jaffé, R. (2015b) Molecular characterization of dissolved black nitrogen via electrospray ionization Fourier transform ion cyclotron resonance mass spectrometry. *Org Geochem* **79**, 21-30.

Wagner, S. and Jaffé, R. (2015) Effect of photodegradation on molecular size distribution and quality of dissolved black carbon. *Org Geochem* **86**, 1-4.

Wagner, S., Jaffé, R. and Stubbins, A. (2018) Dissolved black carbon in aquatic ecosystems. *Limnol Oceanogr Lett* **3**, 168-185.

Walling, C. (1975) Fenton's reagent revisited. *Acc Chem Res* **8**, 125-131.

Wang, H., Zhou, H., Ma, J., Nie, J., Yan, S. and Song, W. (2020) Triplet photochemistry of dissolved black carbon and its effects on the photochemical formation of reactive oxygen species. *Environ Sci Technol* **54**, 4903-4911.

Wang, X., Xu, C., Druffel, E.M., Xue, Y. and Qi, Y. (2016) Two black carbon pools transported by the Changjiang and Huanghe Rivers in China. *Global Biogeochem Cy* **30**, 1778-1790.

Ward, C.P., Sleighter, R.L., Hatcher, P.G. and Cory, R.M. (2014) Insights into the complete and partial photooxidation of black carbon in surface waters. *Environ Sci Proc Imp* **16**, 721-731.

Ward, N.D., Keil, R.G., Medeiros, P.M., Brito, D.C., Cunha, A.C., Dittmar, T., Yager, P.L., Krusche, A.V. and Richey, J.E. (2013) Degradation of terrestrially derived macromolecules in the Amazon River. *Nat Geosci* **6**, 530-533.

Watrous, J., Roach, P., Heath, B., Alexandrov, T., Laskin, J. and Dorrestein, P.C. (2013) Metabolic profiling directly from the Petri dish using nanospray desorption electrospray ionization imaging mass spectrometry. *Anal Chem* **85**, 10385-10391.

Watts, R.J., Yu, M. and Teel, A.L. (2017) Reactive oxygen species and associated reactivity of peroxymonosulfate activated by soluble iron species. *J Contam Hydrol* **205**, 70-77.

Weishaar, J.L., Aiken, G.R., Bergamaschi, B.A., Fram, M.S., Fujii, R. and Mopper, K. (2003) Evaluation of specific ultraviolet absorbance as an indicator of the chemical composition and reactivity of dissolved organic carbon. *Environ Sci Technol* **37**, 4702-4708.

Wershaw, R.L. (1999) Molecular aggregation of humic substances. *Soil Sci* **164**, 803-813.

Wetzel, R.G., Hatcher, P.G. and Bianchi, T.S. (1995) Natural photolysis by ultraviolet irradiance of recalcitrant dissolved organic matter to simple substrates for rapidbacterial metabolism. *Limnol Oceanogr* **40**, 1369-1380.

Whitty, S.D., Waggoner, D.C., Cory, R.M., Kaplan, L.A. and Hatcher, P.G. (2019) Direct noninvasive ^{1}H NMR analysis of stream water DOM: Insights into the effects of lyophilization compared with whole water. *Magn Reson Chem,* 1-14.

Wienhausen, G., Noriega-Ortega, B.E., Niggemann, J., Dittmar, T. and Simon, M. (2017) The exometabolome of two model strains of the *Roseobacter* group: A marketplace of microbial metabolites. *Front Microbiol* **8**, 1-15.

Wischmann, H. and Steinhart, H. (1997) The formation of PAH oxidation products in soils and soil/compost mixtures. *Chemosphere* **35**, 1681-1698.

Wozniak, A., Bauer, J., Sleighter, R., Dickhut, R. and Hatcher, P. (2008) Technical note: Molecular characterization of aerosol-derived water soluble organic carbon using ultrahigh resolution electrospray ionization Fourier transform ion cyclotron resonance mass spectrometry. *Atmos Chem Phys* **8**, 5099–5111.

Wozniak, A.S., Goranov, A.I., Mitra, S., Bostick, K.W., Zimmerman, A.R., Schlesinger, D.R., Myneni, S. and Hatcher, P.G. (2020) Molecular heterogeneity in pyrogenic dissolved organic matter from a thermal series of oak and grass chars. *Org Geochem* **148**, 1-18.

Wünsch, U.J., Bro, R., Stedmon, C.A., Wenig, P. and Murphy, K.R. (2019) Emerging patterns in the global distribution of dissolved organic matter fluorescence. *Anal Methods* **11**, 888-893.

Xiao, Y., Carena, L., Näsi, M.-T. and Vähätalo, A.V. (2020) Superoxide-driven autocatalytic dark production of hydroxyl radicals in the presence of complexes of natural dissolved organic matter and iron. *Water Res*, 1-8.

Xu, X., Zhao, Y., Sima, J., Zhao, L., Mašek, O. and Cao, X. (2017) Indispensable role of biochar-inherent mineral constituents in its environmental applications: A review. *Bioresource Technol* **241**, 887-899.

Yavitt, J.B. and Fahey, T.J. (1984) An experimental analysis of solution chemistry in a lodgepole pine forest foor. *Oikos* **43**, 222-234.

Yu, H., Xia, Q., Yan, J., Herreno-Saenz, D., Wu, Y.-S., Tang, I.W. and Fu, P.P. (2006) Photoirradiation of polycyclic aromatic hydrocarbons with UVA light - a pathway leading to the generation of reactive oxygen species, lipid peroxidation, and DNA damage. *Int J Environ Res Public Health* **3**, 348-354.

Yuan, C., Sleighter, R.L., Weavers, L.K., Hatcher, P.G. and Chin, Y.P. (2019) Fast photomineralization of dissolved organic matter in acid mine drainage impacted waters. *Environ Sci Technol* **53**, 6273-6281.

Zeng, Y., Hong, P.K.A. and Wavrek, D.A. (2000a) Chemical-biological treatment of pyrene. *Water Res* **34**, 1157-1172.

Zeng, Y., Hong, P.K.A. and Wavrek, D.A. (2000b) Integrated chemical-biological treatment of benzo[a]pyrene. *Environ Sci Technol* **34**, 854-862.

Zepp, R.G. (1979) Assessing the photochemistry of organic pollutants in aquatic environments. In: *Dynamics Exposure and Hazard Assessment of Toxic Chemicals* (eds. Haque, R.), Ann Arbor Science Publications Inc., Ann Arbor, MI.

Zhang, X., Han, J., Zhang, X., Shen, J., Chen, Z., Chu, W., Kang, J., Zhao, S. and Zhou, Y. (2020) Application of Fourier transform ion cyclotron resonance mass spectrometry to characterize natural organic matter. *Chemosphere*, 1-10.

Zhao, J., Shen, X.-J., Domene, X., Alcañiz, J.-M., Liao, X. and Palet, C. (2019) Comparison of biochars derived from different types of feedstock and their potential for heavy metal removal in multiple-metal solutions. *Sci Rep* **9**, 1-12.

Zimmerman, A.R. (2010) Abiotic and microbial oxidation of laboratory-produced black carbon (biochar). *Environ Sci Technol* **44**, 1295-1301.

Zimmerman, A.R., Gao, B. and Ahn, M.-Y. (2011) Positive and negative carbon mineralization priming effects among a variety of biochar-amended soils. *Soil Biol Biochem* **43**, 1169-1179.

Zimmerman, A.R. and Mitra, S. (2017) Trial by fire: On the terminology and methods used in pyrogenic organic carbon research. *Front Earth Sci* **5**, 1-8.

Ziolkowski, L.A., Chamberlin, A.R., Greaves, J. and Druffel, E.R.M. (2011) Quantification of black carbon in marine systems using the benzene polycarboxylic acid method: a mechanistic and yield study. *Limnol Oceanogr Meth* **9**, 140-140.

Ziolkowski, L.A. and Druffel, E.R.M. (2010) Aged black carbon identified in marine dissolved organic carbon. *Geophys Res Lett* **37**, 1-4.

APPENDIX A

COPYRIGHT PERMISSION FOR CHAPTER III

This Agreement between Old Dominion University - Aleksandar Goranov ("You") and Elsevier ("Elsevier") consists of your license details and the terms and conditions provided by Elsevier and Copyright Clearance Center.

License Number	4927661459134
License Date	Oct 14, 2020
Licensed Content Publisher	Elsevier
Licensed Content Publication	Geochimica et Cosmochimica Acta
Licensed Content Title	Photochemistry after fire: Structural transformations of pyrogenic dissolved organic matter elucidated by advanced analytical techniques
Licensed Content Author	Aleksandar I. Goranov, Andrew S. Wozniak, Kyle W. Bostick, Andrew R. Zimmerman, Siddhartha Mitra, Patrick G. Hatcher
Licensed Content Date	Dec 1, 2020
Licensed Content Volume	290
Licensed Content Issue	n/a
Licensed Content Pages	22
Start Page	271
End Page	292
Type of Use	Post on a website
Requestor type	Academic/educational institute
Portion	Full article
Format	Electronic
Are you the author of this Elsevier article?	Yes
Will you be translating?	No
Home page URL	https://digitalcommons.odu.edu/etds/
Client / Sponsor	Old Dominion University
Expected posting date	Dec 2020

APPENDIX B

SUPPORTING INFORMATION TO CHAPTER III

Section 1. 1D ^{1}H NMR Analysis: Data processing
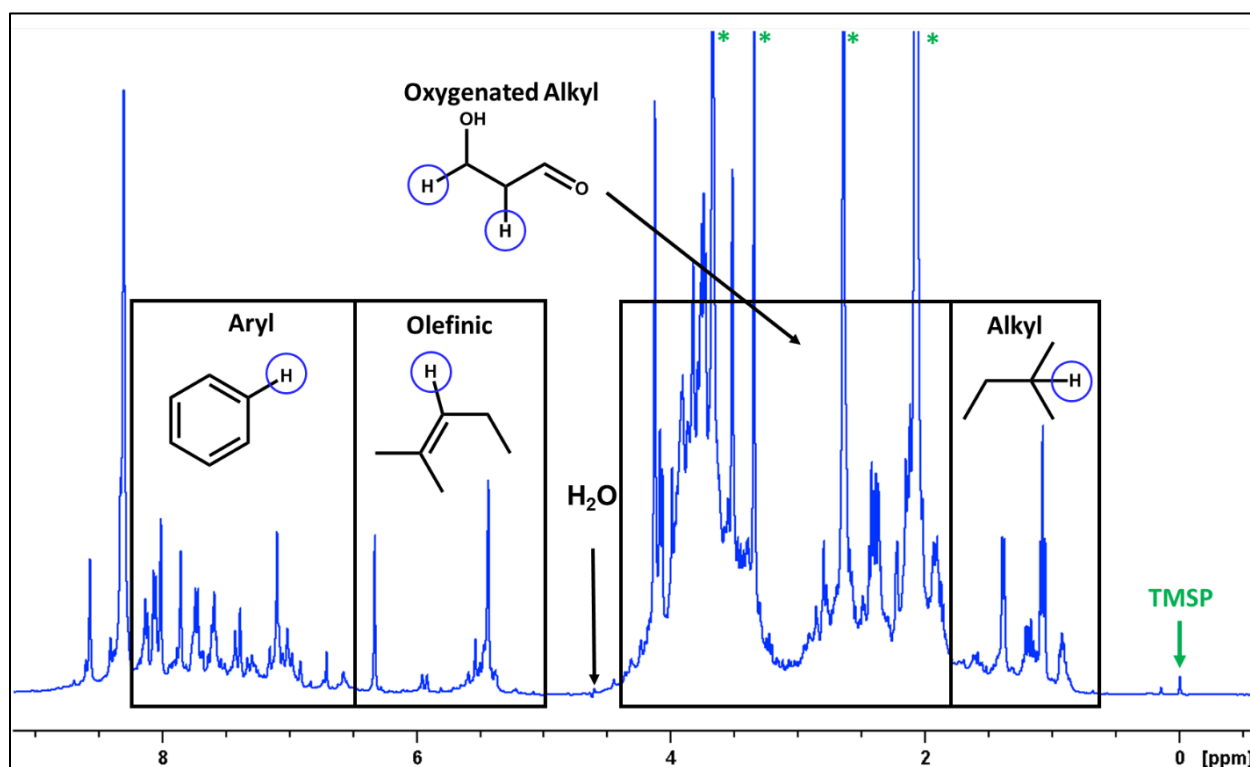
Figure B1. One-dimensional ^{1}H NMR spectrum of the control Grass 650 leachate. The four main functional group regions discussed in Chapter III are: aryl (6.50 – 8.30 ppm), olefinic (5.00 – 6.50 ppm), oxygenated alkyl (O-alkyl, 1.85 – 4.40 ppm) and alkyl (0.60 – 1.85 ppm). The water region (4.40 – 5.00 ppm) is not considered as signals in this area are heavily attenuated by the water suppression elements in the utilized pulse program. The peak of the TMSP internal reference (sodium 2,2,3,3-tetradeutero-3-trimethylsilylpropanoate) is also shown at δ ≈ -0.02 ppm. Asterisks (*) denote peaks that are off-scale.

NMR spectra are integrated over 0.00 – 10.00 ppm with exclusion of any signal between 4.40 - 5.00 ppm (water region). While there are certain functionalities that resonate in the water region, such as amine- an ester-^{1}H, their peaks are heavily attenuated by the Perfect Echo - WATERGATE and shaped presaturation water suppression elements (Adams et al., 2013; Whitty et al., 2019). Thus, the spectral intensity in this region is not quantitative. The utilized pulse program is highly effective in selectively saturating resonances in this region, and not attenuating resonances outside of it. This allows for quantitative observation of functionalities close-by, and if desired, quantification using a standard addition approach (e.g., Whitty et al., 2019). While resonances in the areas of 0.00 – 0.60 ("methane" region) and 8.30 – 10.00 ppm ("aldehyde" region) were measured and used for the normalization to total spectral intensity, these regions were not evaluated in Chapter III. Resonances in the "methane" region are either of dissolved methane (Fulmer et al., 2010) or poorly characterized silicates (Lam and Simpson, 2008), and due to the poor knowledge of these resonances in the context of pyDOM they were not considered in my interpretations. Resonances in the "aldehyde" region are generally from aldehydes (typical photo-products, Yu et al., 2006) and some highly deshielded aryl functionalities (Dvorski et al., 2016). Since these resonances can increase or decrease to unknown extents after to photo-irradiation, they have not been considered in this study either.

Low molecular weight compounds that resonate at highly characteristic chemical shifts (acetate, methanol, formate) are manually integrated and subtracted from their corresponding regions. After integration, the different chemical environments are divided by the H/C ratio typical for each functional group to convert the data to C-basis (Decesari et al., 2007; Bostick et al., 2018). This allows for a better approximation of the relative abundance of functional groups evaluated in Chapter III by discussing the data in terms of carbon (instead of hydrogen), which is helpful for interpreting the data regarding to the global carbon cycle. Each integral is then normalized to the total spectral intensity.

All data is also presented as percent change as shown for the aryl functionality of Oak 400 below. This is useful in comparing different samples and looking at extent of change, as shown previously (Mitchell et al., 2018).

$$\%\text{Change} = \frac{\text{Photo} - \text{Control}}{\text{Control}} \times 100 = \frac{7.04\,\% - 10.6\%}{10.6\,\%} = -33.8\,\% \qquad \text{Eq. B1}$$

Section 2. 1D ^{1}H NMR analysis: Analytical differences from Bostick et al. (2018)

Due to different instrumental parameters, there are notable differences in the ^{1}H NMR data obtained for these samples relative to their previous study, Bostick et al. (2018). In the previous study of these pyDOM leachates there was no clear trend observed for the olefinic moieties across the dataset. This was most likely due to the short relaxation delay that was used (2s) for the NMR analysis. In the current study I have employed a higher relaxation delay (4s) which allows for a more quantitative evaluation of olefinic resonances (e.g., Vlahov, 1999; Alexandri et al., 2017). This revealed a logical trend for these samples which has been described in Chapter III.

The change in relaxation delay also affected the functionality distribution of the Oak Biomass leachate. While Bostick et al. (2018) reported that aryl functionalities are higher in Oak Biomass than in Oak 250 (43% versus 30%), I report that aryl in Oak Biomass is 26% versus 34% in Oak 250. This is due to the larger acetone peak (C$\underline{H}_3$-CO-C$\underline{H}_3$, δ = 2.2 ppm, singlet) observed in the spectrum of Oak Biomass (35% of the total spectral intensity), which skews the functionality distribution in the spectrum.

It must be also noted that there is a slight variation in sample preparation. While Bostick et al. (2018) used biochar:water ratio of 1g:40 mL, here I have used 1g:20 mL to obtain more concentrated leachates. This most certainly has caused some differences between the two datasets, as discussed by Wozniak et al. (2020).

Section 3. Analytical caveats of ^{1}H-^{1}H Total Correlation NMR Spectroscopy (TOCSY NMR)

The obtained TOCSY spectra were noisy and exhibited many T_1-noise ridges that required extensive correction, which was not fully successful in some cases. Additionally, the spectra of the more thermally mature pyDOM exhibited only a few cross-peaks. This is likely because the samples were analyzed without pre-concentration (at total organic carbon content of 10-25 mgC·L^{-1}). Typically, high-quality multidimensional NMR spectra are achieved by analyzing samples at 30-100 mg/mL (30,000-100,000 mg/L) which is achieved using pre-concentration or dissolution of solid sample in solvent (Simpson, 2001; Simpson et al., 2011). This approach was avoided in order to observe the numerous photochemically important low molecular weight species (Whitty et al., 2019). Another surprising observation was that no cross-peaks were observed between aryl and aliphatic functional groups, in contrast with previous work showing that ConAC in the environment are typically functionalized with alkyl and O-containing functionalities (Dittmar and Koch, 2006). This may be due to one of the limitations of TOCSY, namely the inability to detect couplings between aryl-^{1}H and aliphatic-^{1}H nuclei due to their weak interactions (i.e., small J-coupling constants).

Section 4. Individual plots of the photo-labile and photo-produced formulas

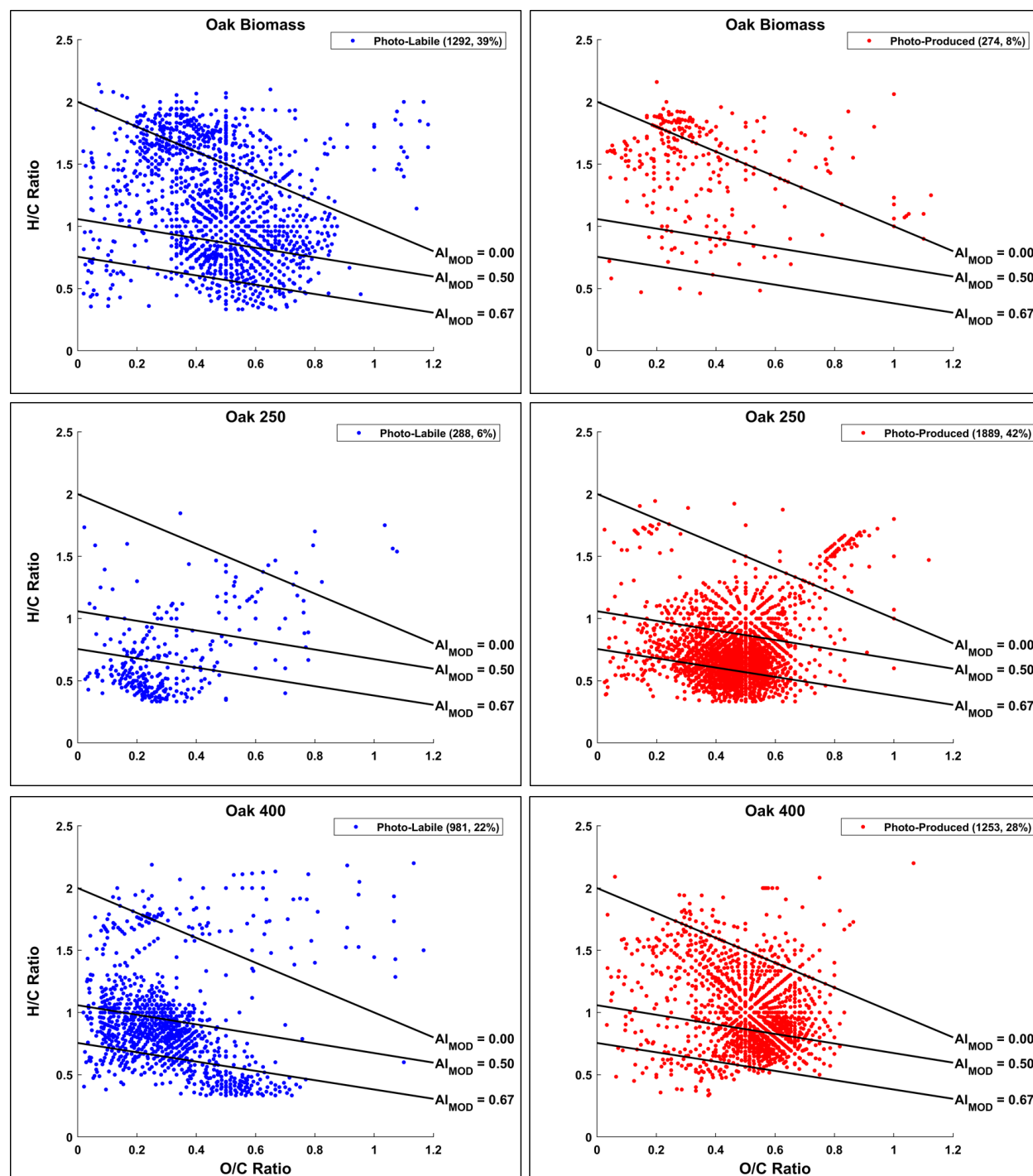**Figure B2.** Photo-labile (blue) and photo-produced formulas (red) for Oak Biomass DOM (top), Oak 250 pyDOM (middle), and Oak 400 pyDOM (bottom panels). The number of molecular formulas of each pool (and corresponding percentages) are given in parentheses in the legends. The black lines separate van Krevelen space based on the modified aromaticity index (AI_{MOD}, Koch and Dittmar, 2006, 2016).

Figure B3. Photo-labile (**blue**) and photo-produced formulas (**red**) for Oak 525 pyDOM (top), Oak 650 pyDOM (middle), and Grass 650 pyDOM (bottom panels). The number of molecular formulas of each pool (and corresponding percentages) are given in parentheses in the legends. The black lines separate the van Krevelen space based on the modified aromaticity index (AI_{MOD}, Koch and Dittmar, 2006, 2016).
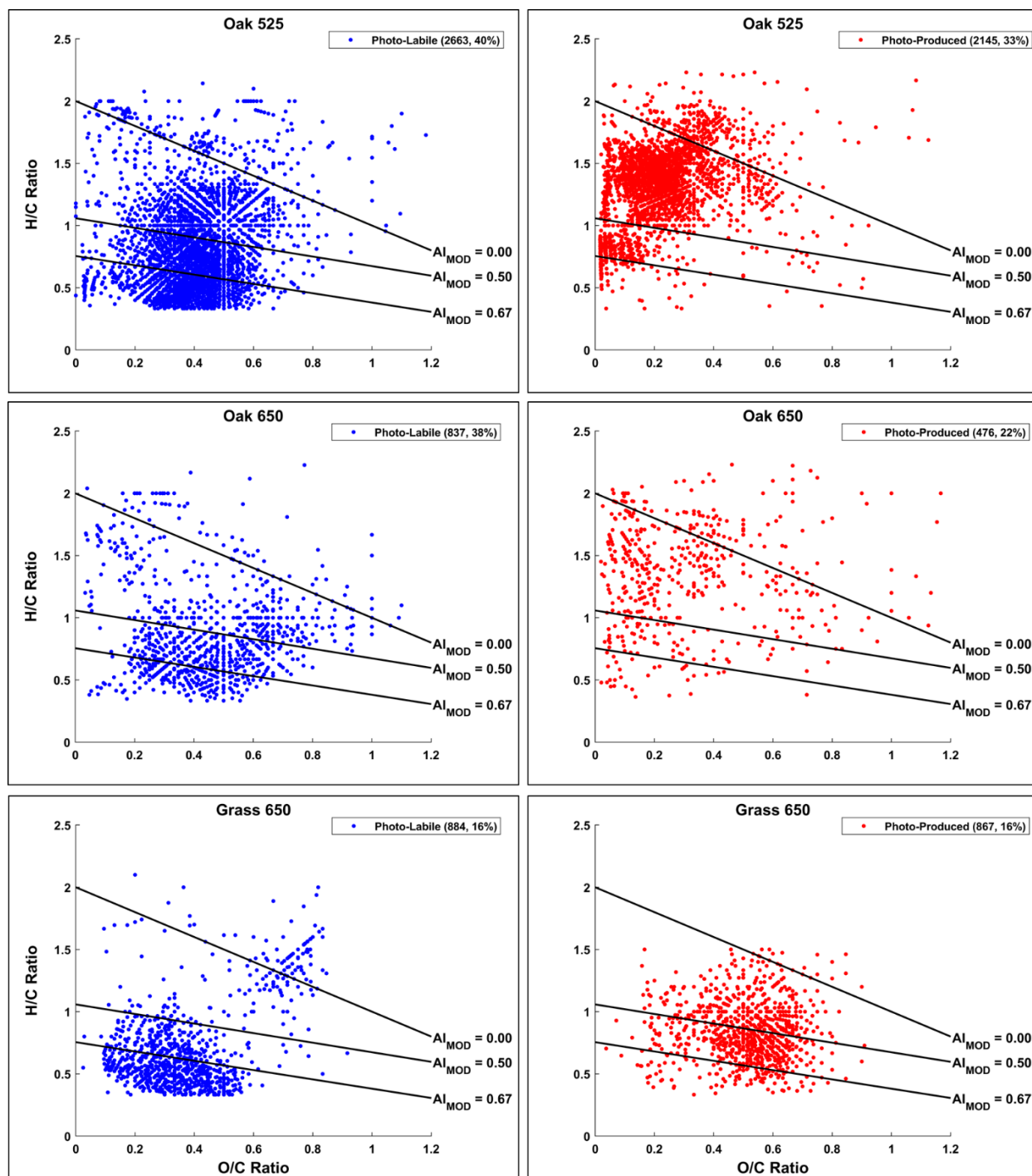
APPENDIX C

SUPPORTING INFORMATION TO CHAPTER IV

Section 1. Individually plotted bio-labile, bio-resistant, and bio-produced formulas on van Krevelen diagrams (H/C vs O/C)
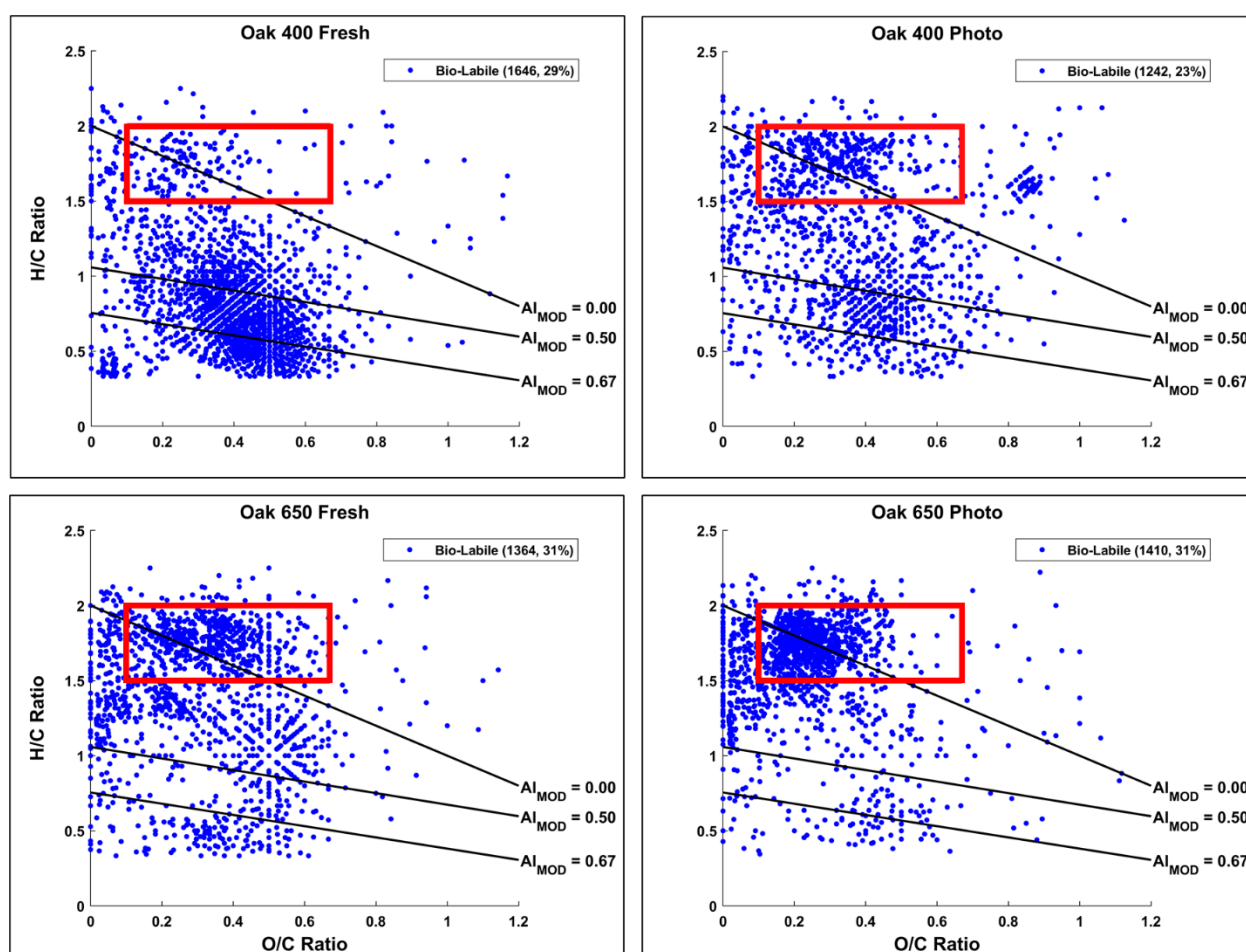
Figure C1. Van Krevelen diagrams of **bio-labile** formulas identified in the four pyDOM samples using presence/absence approach (Sleighter et al., 2012). The number of formulas and the corresponding percentage (relative to total number of formulas in the two samples being compared) are shown in the legends. The black lines indicate modified aromaticity index cutoffs (AI$_{MOD}$; Koch and Dittmar, 2006, 2016), and the red box indicates the peptide region (valid only for N-containing formulas).
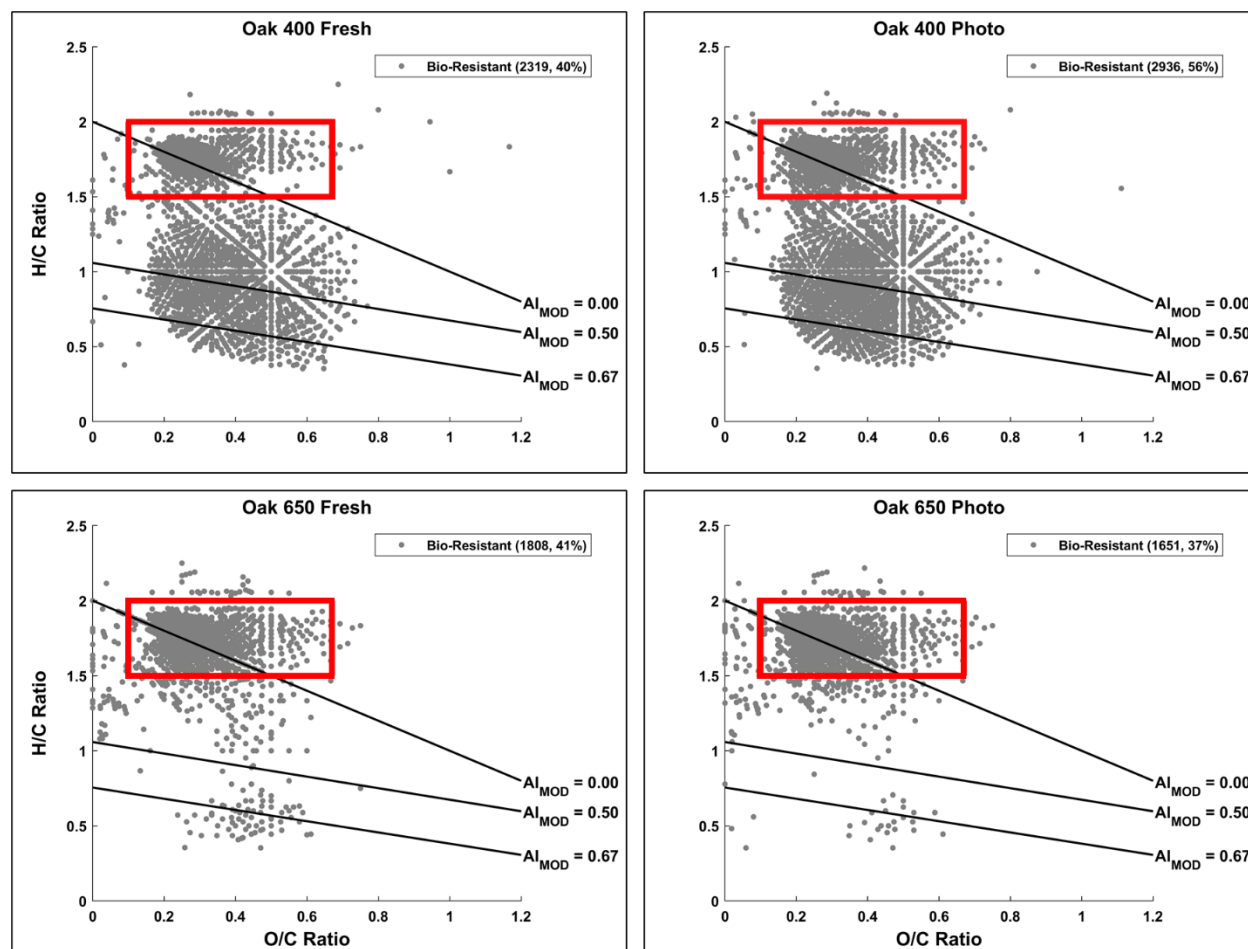
Figure C2. Van Krevelen diagrams of **bio-resistant** formulas identified in the four pyDOM samples using presence/absence approach (Sleighter et al., 2012). The number of formulas and the corresponding percentage (relative to total number of formulas in the two samples being compared) are shown in the legends. The black lines indicate modified aromaticity index cutoffs (AI_{MOD}; Koch and Dittmar, 2006, 2016), and the red box indicates the peptide region (valid only for N-containing formulas).
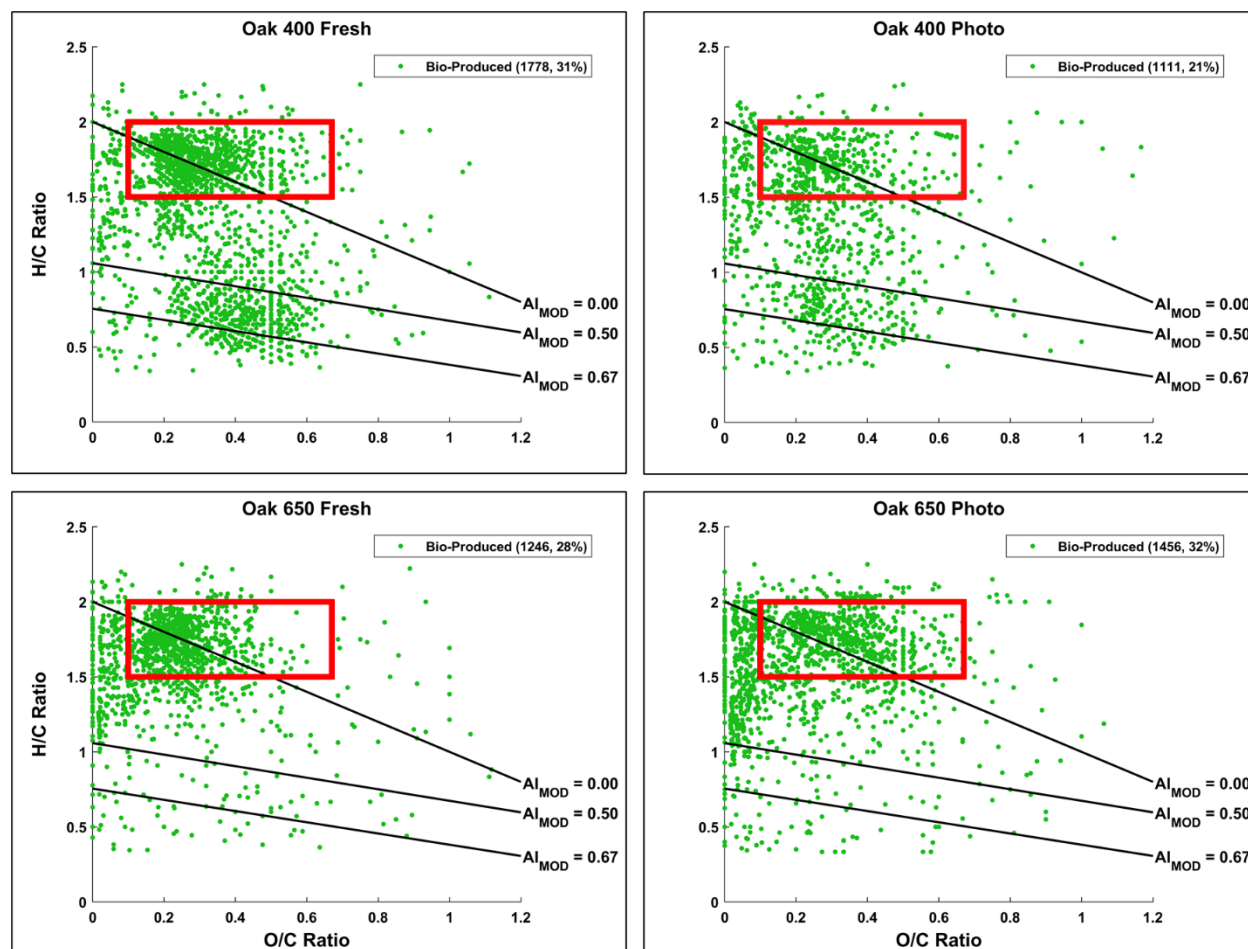
Figure C3. Van Krevelen diagrams of **bio-produced** formulas identified in the four pyDOM samples using presence/absence approach (Sleighter et al., 2012). The number of formulas and the corresponding percentage (relative to total number of formulas in the two samples being compared) are shown in the legends. The black lines indicate modified aromaticity index cutoffs (AI_{MOD}; Koch and Dittmar, 2006, 2016), and the red box indicates the peptide region (valid only for N-containing formulas).

Section 2. Individually plotted bio-labile, bio-resistant, and bio-produced formulas on H/C vs Molecular Weight plots

Figure C4. Hydrogen-to-carbon (H/C) ratio versus molecular weight plots of the **bio-labile** formulas. The number of formulas and the corresponding percentage (relative to total number of formulas in the two samples being compared) are shown in the legends. The red lines indicate where peptide-like formulas would plot.
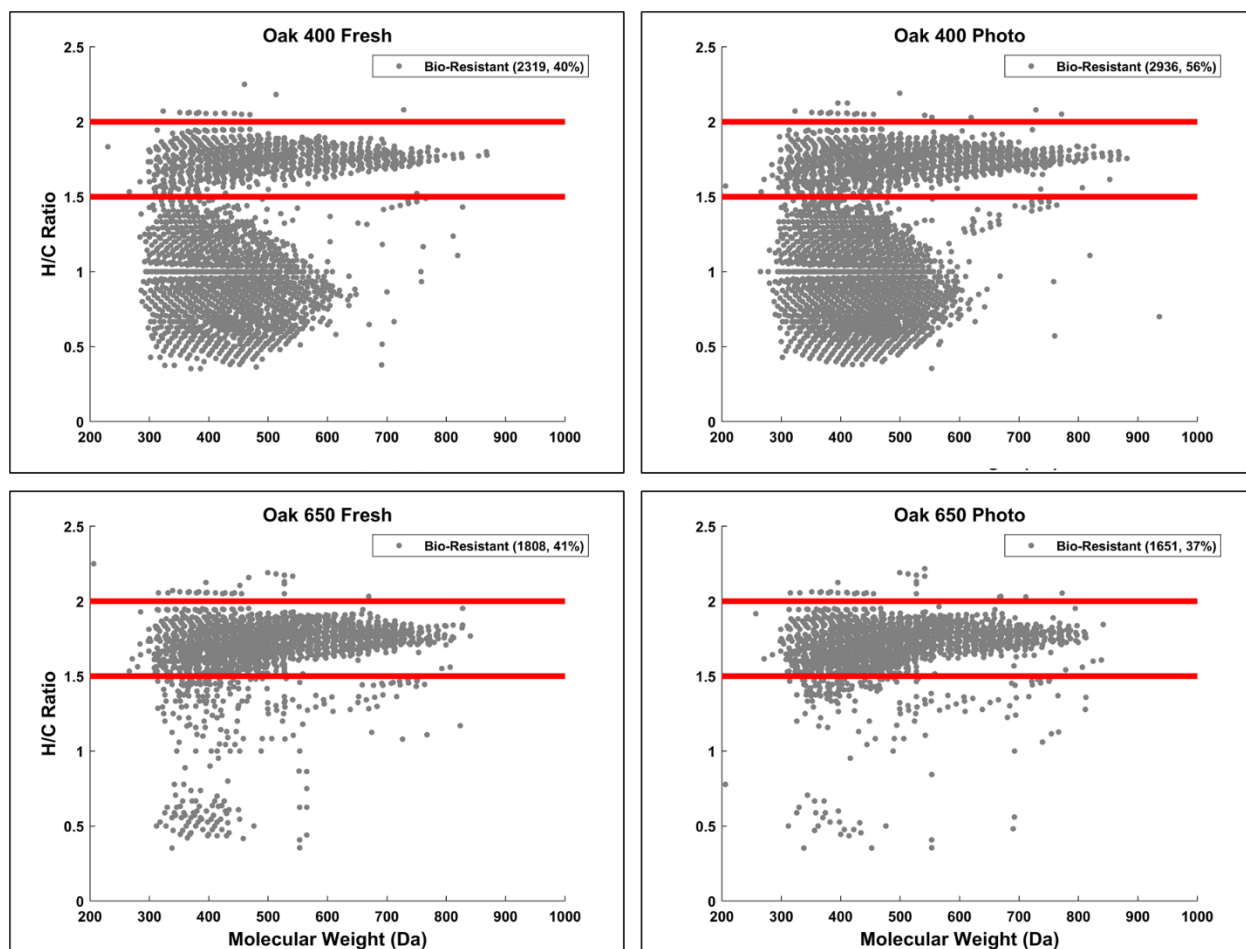
Figure C5. Hydrogen-to-carbon (H/C) ratio versus molecular weight plots of the **bio-resistant** formulas. The number of formulas and the corresponding percentage (relative to total number of formulas in the two samples being compared) are shown in the legends. The red lines indicate where peptide-like formulas would plot.
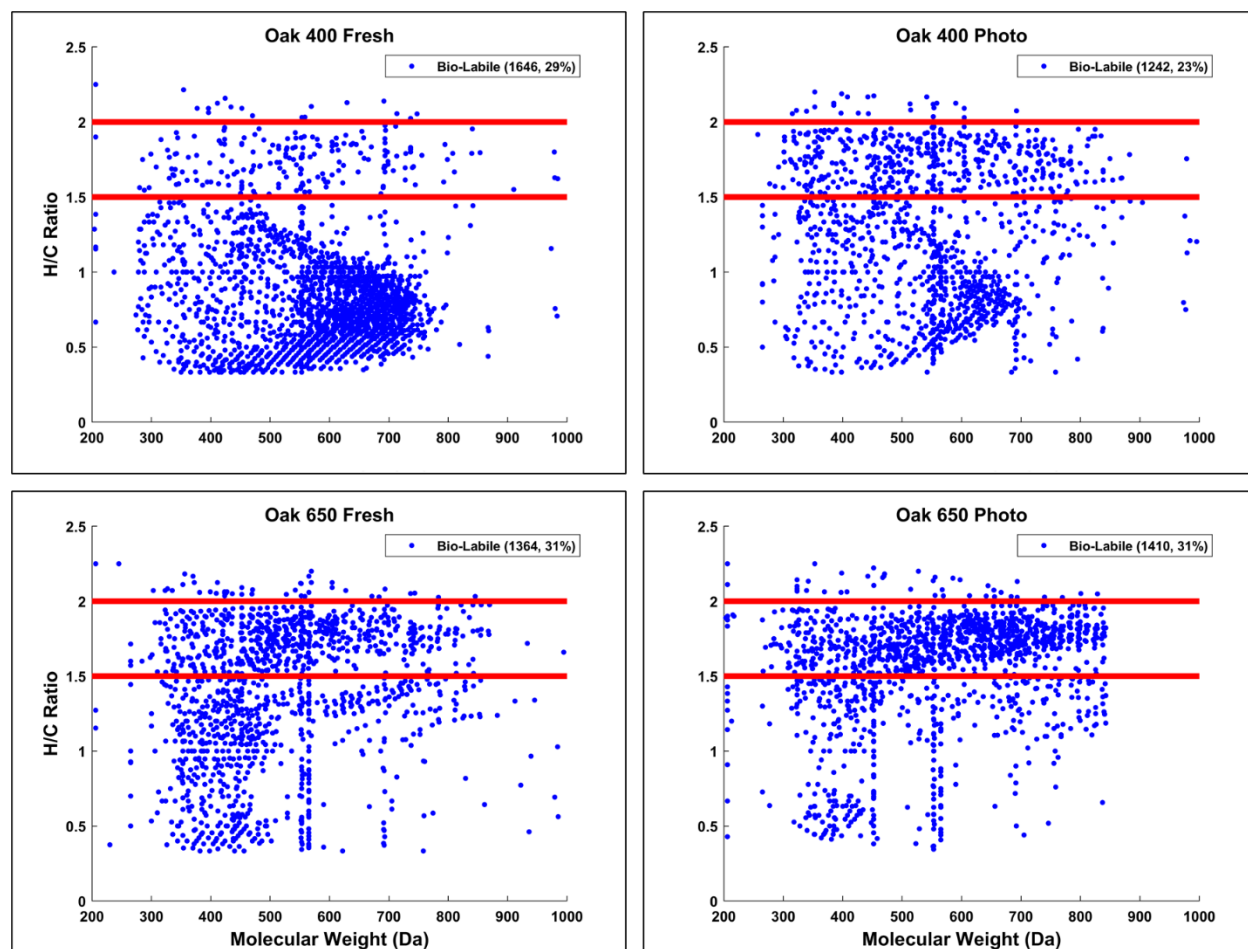
Figure C6. Hydrogen-to-carbon (H/C) ratio versus molecular weight plots of the **bio-produced** formulas. The number of formulas and the corresponding percentage (relative to total number of formulas in the two samples being compared) are shown in the legends. The red lines indicate where peptide-like formulas would plot.
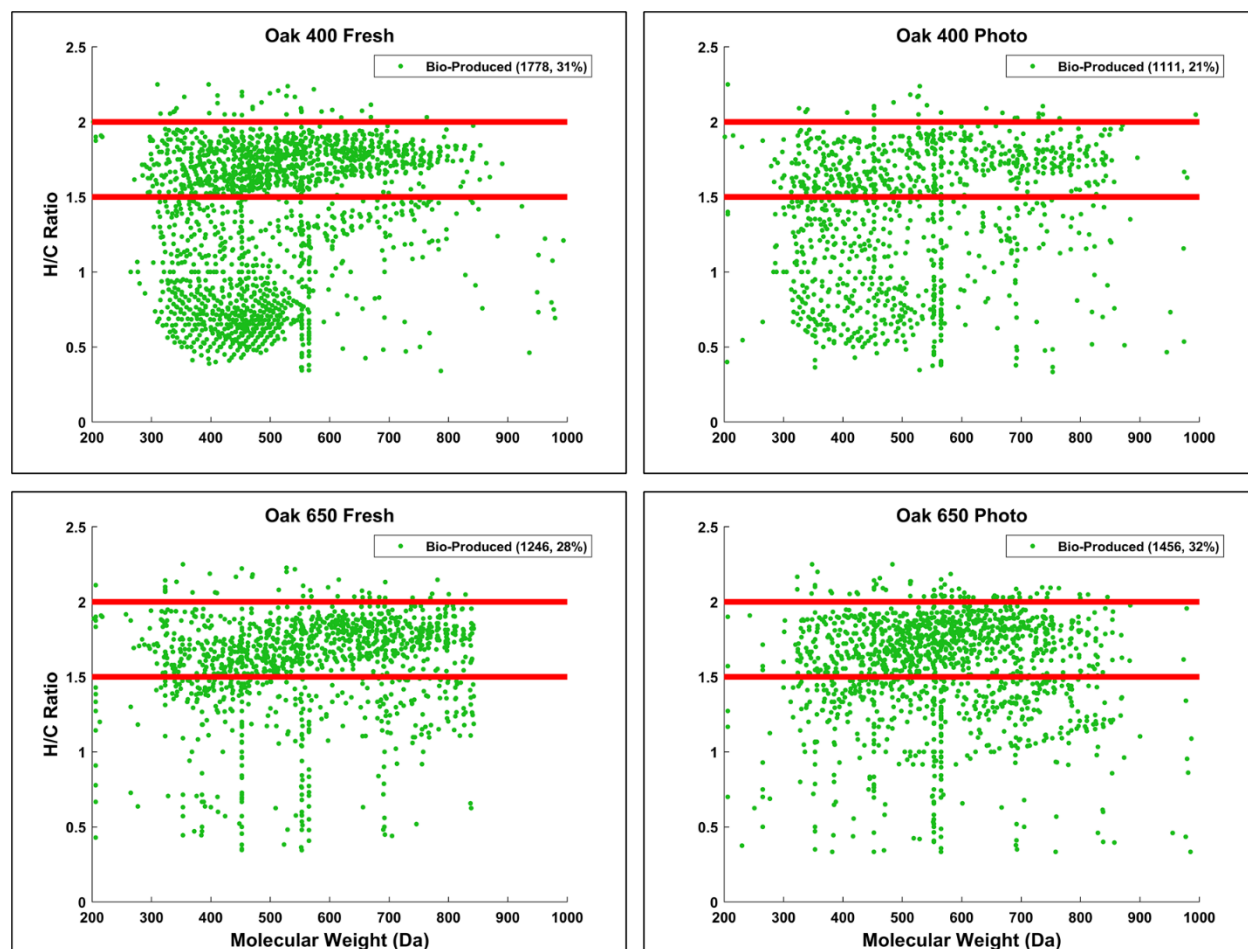
Section 3. Oligopeptide Sequences

Table C1. Oligopeptide sequences identified among the bio-produced formulas of each pyDOM sample.

Sample	Measured m/z	Amino Acid combination[#]	Molecular weight (Da)	Molecular Formula
Oak 400 Fresh	201.1246	AL	202.1317	$C_9H_{18}O_3N_2$
Oak 400 Fresh	356.2192	OLL	357.2264	$C_{17}H_{31}O_5N_3$
Oak 400 Fresh	455.2874	OLLV	456.2948	$C_{22}H_{40}O_6N_4$
Oak 400 Fresh	512.3457	ALLVV	513.3526	$C_{25}H_{47}O_6N_5$
Oak 400 Fresh	512.3457	GLLLV	513.3526	$C_{25}H_{47}O_6N_5$
Oak 400 Fresh	512.3457	VVVVV	513.3526	$C_{25}H_{47}O_6N_5$
Oak 400 Fresh	514.3251	ALLLS	515.3319	$C_{24}H_{45}O_7N_5$
Oak 400 Fresh	514.3251	ALLTV	515.3319	$C_{24}H_{45}O_7N_5$
Oak 400 Fresh	514.3251	GLLLT	515.3319	$C_{24}H_{45}O_7N_5$
Oak 400 Fresh	514.3251	LSVVV	515.3319	$C_{24}H_{45}O_7N_5$
Oak 400 Fresh	514.3251	TVVVV	515.3319	$C_{24}H_{45}O_7N_5$
Oak 400 Fresh	526.3607	ALLLV	527.3683	$C_{26}H_{49}O_6N_5$
Oak 400 Fresh	526.3607	GLLLL	527.3683	$C_{26}H_{49}O_6N_5$
Oak 400 Fresh	526.3607	LVVVV	527.3683	$C_{26}H_{49}O_6N_5$
Oak 400 Photo	341.2195	LPX	342.2267	$C_{16}H_{30}O_4N_4$
Oak 400 Photo	341.2195	KPV	342.2267	$C_{16}H_{30}O_4N_4$
Oak 400 Photo	350.1836	HPV	351.1907	$C_{16}H_{25}O_4N_5$
Oak 400 Photo	528.3188	LLWV	529.3264	$C_{28}H_{43}O_5N_5$
Oak 400 Photo	552.3768	LLLPV	553.3839	$C_{28}H_{51}O_6N_5$

179

Oak 650 Fresh	498.3293	AALLL	499.3370	$C_{24}H_{45}O_6N_5$
Oak 650 Fresh	498.3293	ALVVV	499.3370	$C_{24}H_{45}O_6N_5$
Oak 650 Fresh	498.3293	GLLVV	499.3370	$C_{24}H_{45}O_6N_5$
Oak 650 Fresh	512.3455	ALLVV	513.3526	$C_{25}H_{47}O_6N_5$
Oak 650 Fresh	512.3455	GLLLV	513.3526	$C_{25}H_{47}O_6N_5$
Oak 650 Fresh	512.3455	VVVVV	513.3526	$C_{25}H_{47}O_6N_5$
Oak 650 Fresh	552.3042	DLLPP	553.3112	$C_{26}H_{43}O_8N_5$
Oak 650 Fresh	552.3042	ELPPV	553.3112	$C_{26}H_{43}O_8N_5$
Oak 650 Fresh	552.3042	OOLPV	553.3112	$C_{26}H_{43}O_8N_5$
Oak 650 Fresh	552.3042	OLUVV	553.3112	$C_{26}H_{43}O_8N_5$
Oak 650 Fresh	552.3042	LLPUT	553.3112	$C_{26}H_{43}O_8N_5$

Oak 650 Photo	242.1508	KP	243.1583	$C_{11}H_{21}O_3N_3$
Oak 650 Photo	342.2034	OLV	343.2107	$C_{16}H_{29}O_5N_3$
Oak 650 Photo	356.2190	OLL	357.2264	$C_{17}H_{31}O_5N_3$
Oak 650 Photo	552.2676	ALSTY	553.2748	$C_{25}H_{39}O_9N_5$
Oak 650 Photo	552.2676	ATTYV	553.2748	$C_{25}H_{39}O_9N_5$
Oak 650 Photo	552.2676	DOLPP	553.2748	$C_{25}H_{39}O_9N_5$
Oak 650 Photo	552.2676	DLPUV	553.2748	$C_{25}H_{39}O_9N_5$
Oak 650 Photo	552.2676	EOPPV	553.2748	$C_{25}H_{39}O_9N_5$
Oak 650 Photo	552.2676	EPUVV	553.2748	$C_{25}H_{39}O_9N_5$
Oak 650 Photo	552.2676	GLTTY	553.2748	$C_{25}H_{39}O_9N_5$
Oak 650 Photo	552.2676	OOOPV	553.2748	$C_{25}H_{39}O_9N_5$

Oak 650 Photo	552.2676	OOUVV	553.2748	$C_{25}H_{39}O_9N_5$
Oak 650 Photo	552.2676	OLPUT	553.2748	$C_{25}H_{39}O_9N_5$
Oak 650 Photo	552.2676	LLUUS	553.2748	$C_{25}H_{39}O_9N_5$
Oak 650 Photo	552.2676	LFSST	553.2748	$C_{25}H_{39}O_9N_5$
Oak 650 Photo	552.2676	LUUTV	553.2748	$C_{25}H_{39}O_9N_5$
Oak 650 Photo	552.2676	FSTTV	553.2748	$C_{25}H_{39}O_9N_5$
Oak 650 Photo	552.2676	SSYVV	553.2748	$C_{25}H_{39}O_9N_5$

[#]Combination can be of any order

Section 4. Correlation analysis

Table C2. Data used for the correlation analysis between molecular diversity (as determined by FT-ICR-MS) and 1D NMR (Bostick et al., 2020a). Coefficients of determination (R^2 values) are listed for each functional group in the corresponding color.

	Oak 400 Fresh	Oak 400 Photo	Oak 650 Fresh	Oak 650 Photo
Number of bio-labile formulas	1646	1242	1364	1410
Number of bio-produced formulas	1778	1111	1246	1456
Aldehyde (O=CH) R^2=0.1263, R^2=0.2374	3.18%	4.52%	10.99%	4.24%
Aryl R^2=0.0094, R^2=0.0668	9.87%	8.47%	20.65%	7.54%
Olefinic (C=C) R^2=0.9472, R^2=0.9978	7.64%	15.60%	14.31%	11.41%
HC-O-R R^2=0.4217, R^2=0.3385	6.75%	23.64%	4.57%	9.41%
HC-C=Y R^2=0.0201, R^2=0.0511	12.33%	13.14%	4.49%	9.13%
HC-C-C-X R^2=0.4639, R^2=0.3968	3.98%	5.99%	6.52%	7.38%
Methylene (CH$_2$) R^2=0.1287, R^2=0.0997	6.46%	7.85%	11.57%	12.65%
Methyl (CH$_3$) R^2=0.0653, R^2=0.1664	0.89%	0.84%	0.25%	0.93%
Formate (HCOO$^-$) R^2=0.0033, R^2=0.0124	10.57%	3.51%	24.18%	33.91%
Methanol (CH$_3$OH) R^2=0.9418, R^2=0.9279	3.69%	0.47%	0.72%	1.31%
Acetate (CH$_3$COO$^-$) R^2=0.4217, R^2=0.3909	34.63%	15.97%	1.75%	2.10%

VITA

Aleksandar Ivaylov Goranov

Department of Chemistry and Biochemistry, Old Dominion University, Norfolk, VA

EDUCATION

- Doctor of Philosophy (Ph.D.) in Chemistry   December 2020
  Old Dominion University (ODU)
  Norfolk, VA

- Bachelor of Science (B.S.) in Chemistry   June 2017
  Ramapo College of New Jersey (RCNJ)
  Mahwah, NJ

RESEARCH EXPERIENCE

- Old Dominion University, Norfolk, VA   July 2017 – December 2020
  Organic Biogeochemistry Group
  Advisor: Dr. Patrick G. Hatcher

- Skidaway Institute of Oceanography, Savannah, GA   May – August 2016
  Organic Biogeochemistry Group
  Advisors: Drs. Aron Stubbins and Sasha J. Wagner

- Ramapo College of New Jersey, Mahwah, NJ   September 2015 – May 2017
  Fluorescence Spectroscopy Group
  Advisor: Dr. Loraine T. Tan

- Center for Marine Resource Studies   July – August 2015
  Cockburn Harbour, Turks and Caicos Islands
  Seagrass Ecology Group
  Advisor: Dr. Andrea E. Murray

- Macquarie University, Sydney, Australia   May – July 2015
  Marine Ecology Group
  Advisor: Dr. Jane E. Williamson

HONORS AND AWARDS

- Graduate Student Research Travel Award   Nov 2018
- Dominion Scholar Fellowship (2018 – 2020)   May 2018
- RCNJ Faculty-Student Research Award   May 2017
- American Institute of Chemists Award   April 2017
- American Chemical Society Division of Physical Chemistry Award   April 2017
- American Chemical Society Division of Analytical Chemistry Award   April 2016
- Arcadia University and Garmelle Le Vin Memorial Research Award   July 2015